The function of miR-324 in neurological and musculoskeletal biology

Daniel John Hayman

A thesis submitted for the degree of Doctor of Philosophy

Biosciences Institute

August 2022

Abstract

microRNAs are non-coding RNAs which modulate the expression of other RNA molecules. One microRNA can target many transcripts, allowing each microRNA to play key roles in many biological pathways. Our group has produced a global knockout model of miR-324, a microRNA previously implicated in bone and cartilage maintenance, defects of which result in common age-related diseases, such as osteoporosis or osteoarthritis. miR-324 has also been discussed in relation to epilepsy and therefore the neurological effects of miR-324 deletion were also investigated.

Ex vivo hippocampal electrophysiology revealed that miR-324-null mice show a hyperexcitability phenotype, and RNA sequencing in the murine hippocampus and neocortex revealed that *Suox*, a gene causal of the human disorder isolated sulfite oxidase deficiency, was a direct target of miR-324.

In vivo micro-computed tomography and histology revealed an increase in bone mineral density, trabecular thickness and cortical thickness in miR-324-null mice, while also displaying a decreased number of osteocytes and lipid droplets. *In vivo* TRAP staining revealed a decrease in osteoclasts and calcein/alizarin red-S double-labelling demonstrated an increased rate of bone formation in miR-324-null mice.

Ex vivo assays revealed that the high bone mass phenotype of the miR-324-null mice resulted from increased osteoblast activity and decreased osteoclastogenesis. miR-324 Target prediction and validation in osteoblasts, bone marrow macrophages and osteocytes, revealed that the osteoclast fusion regulator *Pin1* was a miR-324 target in the osteoclast lineage, *Hoxa9* and *Samd5* were osteocyte target genes and the master osteogenic regulator *Runx2* was a target of miR-324-5p in osteoblasts, the overexpression of which *in vitro* recapitulated the increased osteogenesis and decreased adipogenesis phenotype observed *in vivo*.

These data point to important roles of miR-324 in bone and neurological biology. Elucidation of pathways regulated by miR-324 offers promise for the treatment of bone diseases such as osteoporosis and neurological disorders such as epilepsy.

Acknowledgements

I would first like to thank my supervisor, Professor David Young, for his continued support and mentoring over the past four years. I would also like to thank my second supervisor, Dr Matt Barter, the self-proclaimed “SRG lifer”. Without the guidance and supervision of both, the work undertaken in this PhD project would not have been possible. I would also like to thank Dr Jamie Soul for his instruction in bioinformatics and RNA sequencing analysis. All of the above also deserve thanks for their generosity in buying rounds at lab socials!

I would also like to thank Professor Rob van 't Hof, Gemma Charlesworth, Mandie Prior and Dr Fran Johnson de Sousa Brito, for their tutorage in bone histomorphometry and for always being available to answer any questions. Gemma and Mandie additionally deserve an extra acknowledgement for their services in cutting and staining bone sections from the mice used in this project.

I would additionally like to thank Dr Kasia Piróg, Hua Lin and the Functional Genomics Unit at Newcastle University, for their assistance and advice in the *in vivo* mouse work over the course of this project. Hua deserves an extra thank you for her tutorage and work in sectioning and staining cartilage samples. Furthermore, I would like to thank Dr Fiona LeBeau, Dr Tamara Mondebadze and Dr Gavin Clowry for their excellent teaching of neuroscience (of which I had approximately zero knowledge of at the start of this PhD) and supervision of my electrophysiology experiments during this project.

I would like to my friends and family for their unconditional love and support throughout my time in Newcastle, especially Evie, who kept me going throughout the harder days of thesis writing, all whilst she was going through the same process. Of course, I would also like to thank the Skeletal Research Group for their friendly chats throughout the working day, as well as the Pub Fridays (when the whole world wasn’t in lockdown). I should particularly thank Jack Roberts for his excellent wit and “would you rather be…”s throughout our time in the shared office space.

Finally I would like to thank the Centre for Integrated Musculoskeletal Ageing for their funding of this research and for the network of support and opportunities they offered throughout the project.

Table of contents

List of tables

List of figures

Abbreviations

3'UTR	3’ untranslated region
α-MEM	α-Minimum essential media
aCSF	Artificial cerebrospinal fluid
AD	Alzheimer’s Disease
ADHD	Attention deficit hyperactivity disorder
AdiOst	Adipo-osteogenesis
AdiOst ratio	Ratio of adipogenesis to osteogenesis
ANOVA	Analysis of variance
App_{Swe}	Swedish mutant App allele
ATP	Adenosine triphosphate
BFR	Bone formation rate
BGP	β-glycerophosphate
BMD	Bone mineral density
BMM	Bone marrow macrophage
BMP	Bone morphogenetic protein
BRC	Bone remodelling compartment
BSA	Bovine serum albumin
CBFβ	Core binding factor-β
cDNA	Complementary DNA
CDS	Coding region
circRNA	Circular RNA
Ct	Cycle threshold
DMEM	Dulbecco's Modified Eagle Medium
DMM	Destabilisation of the medial meniscus
DO	Disease Ontology
DTT	Dithiothreitol
DV	Dorsal-ventral
ECM	Extracellular matrix
EDTA	Ethylenediaminetetraacetic acid
FLAG	Myc-DDK

GABA	Gamma-aminobutyric acid
GEO	Gene Expression Omnibus
GO	Gene Ontology
GOI	Gene of interest
GWAS	Genome-wide association studies
HBSS	Hanks' Balanced Salt Solution
Hh	Hedgehog
HITS-CLIP	High-throughput sequencing of ribonucleic acids isolated by crosslinking immunoprecipitation
hp	Hairpin inhibitor
hpCon	microRNA Hairpin Inhibitor Negative Control #1
hPIN1	Human Pin1
hRUNX2	Human Runx2
HSC	Haematopoietic stromal cell
Ihh	Indian Hedgehog
IID	Interictal discharge
ISOD	Isolated sulfite oxidase deficiency
KA	Kainate
LFP	Local field potential
lncRNA	Long noncoding ribonucleic acid
logFC	Log_2 fold-changes
µCT	Micro-computed tomography
MAR	Mineral apposition rate
M-CSF	Macrophage colony stimulating factor
MFC	Medial femoral condyle
miCon	miRIDIAN microRNA Mimic Negative Control #2
miR-23aC	miR-23a ~ 27a ~ 24–22 cluster
miRNA	Micro ribonucleic acid
MMA	Methyl methacrylate
MMP	Matrix metalloproteinase
mRNA	Messenger ribonucleic acid
MSC	Mesenchymal stromal cell

MTP	Medial tibial plateau
N.Oc	Osteoclast number
NCBI	National Center for Biotechnology Information
ncRNA	Noncoding ribonucleic acid
NFκB	Nuclear factor kappa B
NOF	Neck of femur fracture controls
OA	Osteoarthritis
OARSI	Osteoarthritis Society International
Oc.S.BS	Osteoclast surface area per bone surface area
OGM	Osteogenic media
OPG	Osteoprotegerin
P5P	Pyridoxal 5'-phosphate
PABP	Poly(A) binding protein
PBS	Phosphate-buffered saline
PCA	Principal component analysis
PCR	Polymerase chain reaction
PDGF-A	Platelet-derived growth factor A
PDGF-AA	Platelet-derived growth factor A homodimer
PDGF-AB	Platelet-derived growth factor A-B heterodimer
pDN6	Hexamers
PNP	Paranitrophenol
PNPP	Paranitrophenyl phosphate
PPDE	Pyridoxal phosphate-dependent epilepsy
PTH	Parathyroid hormone
PVDF	Polyvinylidene fluoride
RANK	Receptor activator of nuclear factor kappa-B
RANK-L	Receptor activator of nuclear factor kappa-B ligand
RISC	Ribonucleic acid-induced silencing complex
RNA-seq	RNA sequencing
RRHO	Rank-rank hypogeometric overlap
RT-qPCR	Real-time reverse transcriptase quantitative polymerase chain reaction

SD	Standard deviation
SDS	Sodium dodecyl sulfate
SMI	Structural model index
Sost	Sclerostin
TBE	Tris-Borate-EDTA
TBST	Tris-buffered saline with Tween-20 Detergent
TDMD	Target-directed micro ribonucleic acid degradation
TMD	Bone tissue mineral density
TRAP	Tartrate resistant acid phosphatase
UPL	Universal Probe Library
VOI	Volume of interest
WT	Wild-type

Chapter 1 - Introduction

1.1 microRNAs and disease

Noncoding RNAs (ncRNAs) are transcribed genetic elements which act to regulate the transcription or translation of other genes without ever being translated into protein themselves. microRNAs (miRNAs) are a class of single-stranded ncRNAs which modulate the expression of target RNA molecules. This regulation can be achieved through utilising sequences complimentary to the mature miRNA sequence, canonically within the 3' untranslated region (3'UTR) or less commonly the coding region (CDS) of target RNAs. The binding of miRNAs to these sequences allows downregulation of translation of the target mRNA [1-4]. miRNAs have been predicted to affect the expression of vast numbers of transcripts throughout the human genome [5, 6]; in fact, it has been estimated that over 60% of all protein-coding mRNAs in humans are miRNA targets [7]. Furthermore, the mechanism of gene regulation through miRNA activity is highly conserved across the plant and animal kingdoms [8-10], underpinning the importance of these small ncRNAs. As such, it is unsurprising that miRNAs have been found to play roles in many biological networks implicated in development and disease [11-16]. It is therefore crucial to understand the mechanisms behind biological processes not just at the level of the protein-coding genome, but also at the level of noncoding elements, such as miRNAs.

1.1.1 *microRNA biogenesis*

Canonical miRNAs can be transcribed either from intergenic or intragenic regions, producing a pri-miRNA molecule [17-19]. This is processed into a pre-miRNA molecule, a stem-loop structure of approximately 70nt, before eventually being cleaved in the cytoplasm by the Dicer endoribonuclease, producing a miRNA duplex, where each strand holds the potential to become a distinct mature miRNA arm. In most instances one arm is preferentially incorporated into an RNA-induced silencing complex (RISC) and therefore this arm is able to bind far more target RNA molecules, destabilise target transcripts and inhibit their translation far more than the other (Figure 1.1a). The other arm, known as the passenger arm, is frequently degraded, allowing the remaining strand to be processed into a mature miRNA of approximately 22nt in length [20, 21]. The process of miRNA arm choice relies upon the thermodynamic properties of the pre-miRNA duplex; generally, initiation of pre-miRNA unwinding occurs where the hydrogen bonds between the two strands are weakest, and the strand which is left with an exposed 5' terminus is subsequently taken up by the RISC, becoming a mature miRNA (Figure 1.1b) [1, 22]. Additionally, there is a distinct bias by the

RISC toward miRNA arms which begin with an adenosine or uridine residue, as these residues are more compatible at a structural level with the Argonaute protein within the RISC [23, 24]. Solely by mutating the terminal 5' residue of miR-140-5p, the miR-140 passenger arm, from cytidine to uridine in mice, Kobyashi et al. (2022) demonstrated an increase of greater than 10-fold in miR-140-5p expression in addition to a severe reduction in miR-140-3p expression in primary chondrocytes, therefore successfully inducing a switch in preference for miR-140 arm incorporation into the RISC [25]. Factors other than the miRNA sequence certainly also hold the potential to alter the choice between dominant and passenger arm, such as the availability of arm target mRNA transcripts. It has been suggested that specific target mRNAs may bind a complementary miRNA arm and in doing so stabilise that arm, in theory allowing a passenger arm in one tissue to be taken up by the RISC as a dominant arm in a different tissue solely due to increased target expression in the latter [26, 27]. However, there are also reports in the literature of target-directed miRNA degradation (TDMD), a process by which specific target mRNAs bind a RISC-incorporated miRNA arm and in doing so encourage dissociation between the 3' end of the arm and the RISC proteins [28-31]. Consequently, the 3' terminus becomes exposed, allowing oligouridylation by terminal uridyltransferases, a modification which marks miRNAs for degradation by the DIS3L2 exonuclease [32, 33]. Therefore, miRNA arm preference of the RISC is highly tissue-specific and dependent on the physiological expression of target mRNAs in addition to the actual miRNA arm sequences. It is also worth noting that the presence of a dominant and passenger arm is not ubiquitous for all miRNA species; it is entirely possible for both arms of a miRNA to undergo maturation at similar frequencies in a given tissue, such that both arms of the miRNA are found at almost identical concentrations, as is the case for miR-34b [34-36].

In addition to canonical miRNAs, an additional miRNA family exists, known as mirtrons, which are defined by their alternative point of entry into the miRNA processing pathway [37-39]. Mirtrons are less common than canonical miRNAs, but are still relatively abundant; according to mirtronDB, to date 1136 distinct mature human mirtons have been identified [40], compared to an estimated 2300 distinct human miRNAs [41]. Mirtrons are encoded from intron lariats spliced from messenger RNAs (mRNAs), which fold into a pre-miRNA-like secondary structure, such that Dicer recognises the structure and processes it into a miRNA duplex (Figure 1.1c) [42, 43]. Mirtrons may be more common in invertebrates such as *Drosophila melanogaster* than in mammals, due to invertebrate introns generally being closer

in size to a pre-miRNA than mammalian introns are [44, 45], although it has been suggested that the sheer number of introns in mammals relative to invertebrates may level this imbalance [37].

1.1.2 *The molecular activity of microRNAs*

Both canonical miRNAs and mirtrons act to regulate mRNA translation through the same mechanisms, namely via decapping and deadenylation of the target transcript [46-48]. Mature miRNAs guide the RISC to target genes through the binding of their seed sequence, a region between the 2nd and 8th nucleotides of the miRNA, which is perfectly complementary to a site within the target RNA, most commonly in the 3'UTR [5-7]. Subsequent decapping and deadenylation are both facilitated by the protein GW182 [49, 50]. Both of these processes severely negatively affect the stability and translational potential of the mRNA; the 5' cap is crucial to mRNA stability by protecting the transcript from exonuclease activity [51, 52], and therefore by stimulating decapping activity the RISC dramatically undermines the ability of the target mRNA to be translated. The poly(A) tail is also essential for transcript stability by allowing circularisation of the mRNA [53-55]. GW182 is crucial to miRNA-mediated repression and interacts with several key components; CCR4-NOT, PAN2-PAN3, EDD and the poly(A) binding protein (PABP) (Figure 1.2) [56]. CCR4-NOT and PAN2-PAN3 are the complexes thought to be largely responsible for the deadenylation activity of the RISC [57, 58]. PABP binding to GW182 is also thought to contribute to mRNA deadenylation. Ordinarily PABP helps to stabilise mRNA transcripts by binding proteins at the 5' cap of the mRNA from its position at the 3' poly(A) tail, thus circularising the transcript [59, 60]. However, interaction between GW182 and PABP destabilises the circularised mRNA by blocking the binding of PABP and eIF4G [61], one of the proteins positioned at the mRNA 5' cap. Additionally, this interaction may position the poly(A) tail beside the recruited deadenylation complexes, thus increasing deadenylation efficiency [46, 62]. Finally, GW182 recruits EDD, a protein which, together with the CCR4-NOT complex, interacts with the DDX6 RNA helicase, a protein reported to be essential for miRNA-mediated repression by enhancing decapping of the target mRNA [63-65].

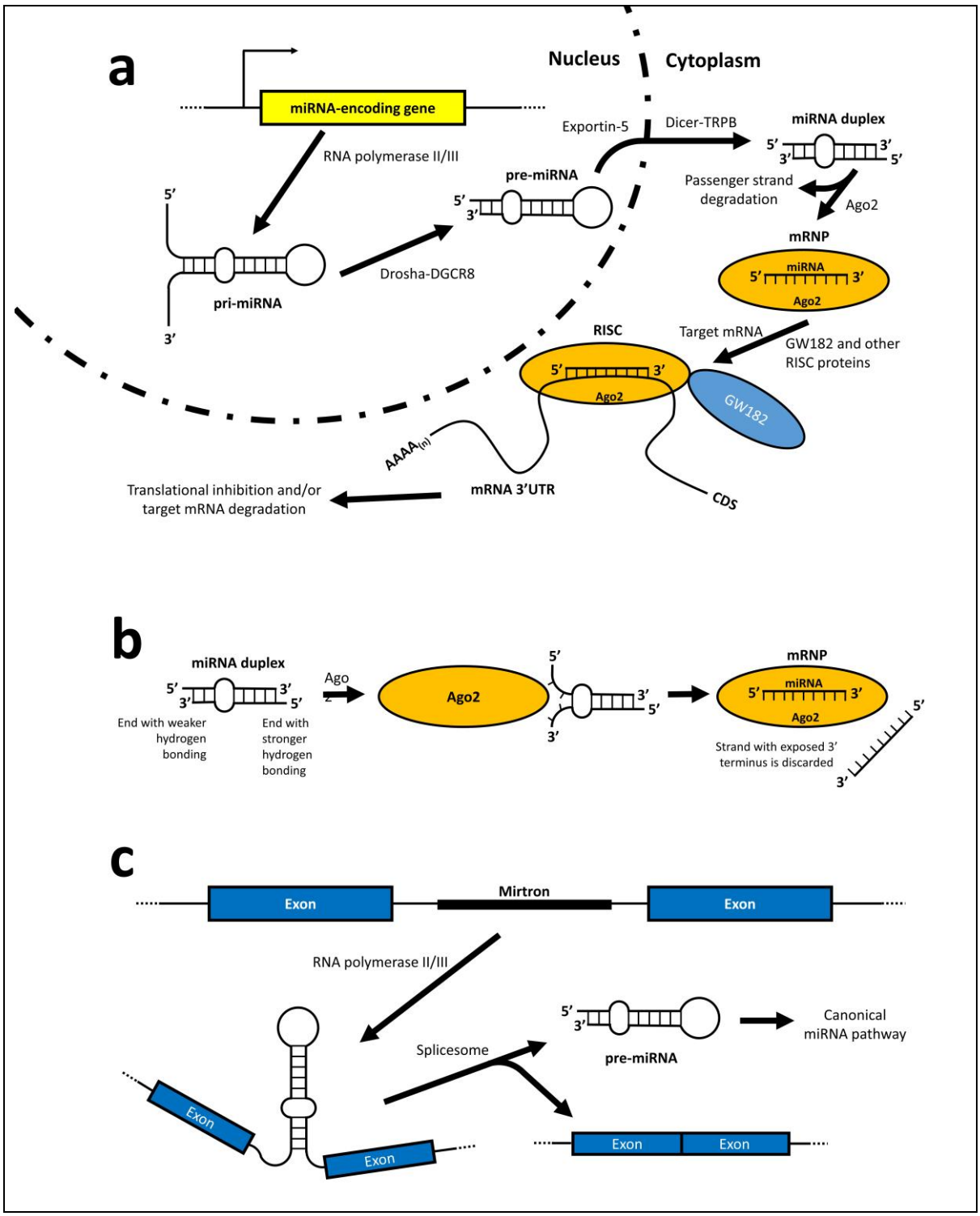
a
Nucleus
Cytoplasm
miRNA-encoding gene
RNA polymerase II/III
pri-miRNA
Drosha-DGCR8
pre-miRNA
Exportin-5
Dicer-TRPB
miRNA duplex
Passenger strand degradation
Ago2
mRNP
miRNA
Ago2
RISC
Target mRNA
GW182 and other RISC proteins
GW182
AAAA(n)
mRNA 3'UTR
CDS
Translational inhibition and/or target mRNA degradation
b
miRNA duplex
Ago2
End with weaker hydrogen bonding
End with stronger hydrogen bonding
mRNP
Strand with exposed 3' terminus is discarded
c
Exon
Mirtron
Exon
RNA polymerase II/III
Splicesome
pre-miRNA
Canonical miRNA pathway
Exon
Exon
Exon
Exon

Figure 1.1 - miRNA biogenesis pathways. (**a**) The canonical miRNA pathway, in which a pri-miRNA is transcribed from DNA, before being trimmed by the Drosha-DGCR8 complex and subsequently exported from the nucleus by Exportin-5. In most cases, one of the strands of this miRNA duplex becomes a mature miRNA and is incorporated into a RISC, going on to affect the expression of target genes. The other strand is known as the passenger strand and is degraded. (**b**) One miRNA arm is chosen to be matured and incorporated into a RISC whilst the other becomes the passenger strand. (**c**) The mirtron pathway is an alternative biogenesis mechanism in which a pri-miRNA-resembling intron is processed by the spliceosome and enters the biogenesis pathway as a pre-miRNA. miRNAs entering the processing pathway from this point of origin are known as mirtrons.

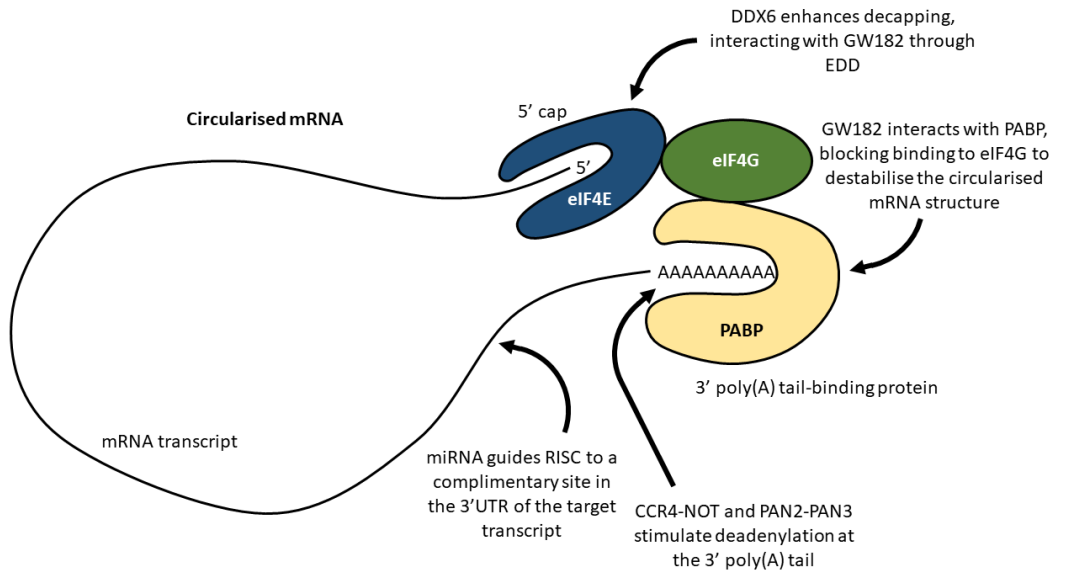

Figure 1.2 - RISC-mediated regulation of mRNA stability. A circularised mRNA transcript, illustrated with the activity of each component of the GW182 protein complex in relation to RISC-mediated translational inhibition and transcript destabilisation [54, 56, 57].

1.1.3 *miR-324 in human and murine biology*

miR-324 has been implicated in multiple diseases in human biology. In both humans and mice, miR-324 is encoded on the same sense strand as the *Dvl2* gene (*DVL2* in humans), antisense to *Acadvl* (*ACADVL* in humans). The murine *Mir324* locus is within a 3'UTR transcript variant of *Dvl2*, whereas in humans *MIR324* is located more than 1.5kb downstream of any annotated *DVL2* transcript [66] (Figure 1.3).

The two mature arms of miR-324, known as miR-324-5p and miR-324-3p (see Table 1.1 for details), are each predicted to target and repress a large number of genes; for both human and mouse, the miRNA target prediction algorithm TargetScan [5, 67] predicts well over 2000 targets for each arm, although some of these overlap. This large array of putative miR-324 targets suggests that this miRNA has the potential to play a role in a wide variety of processes in mammalian biology and therefore is likely to impact a large number of diseases. Based on evidence from the literature, this project aimed to investigate the function and activity of miR-324 in three primary tissues; brain, cartilage and bone.

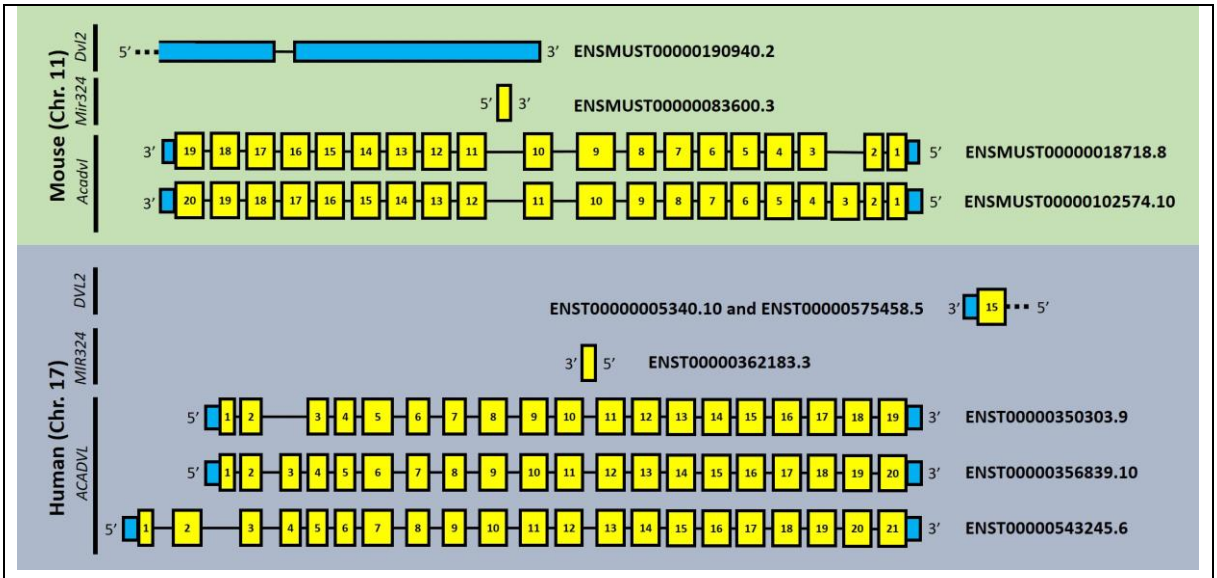

Figure 1.3 - The locus from which miR-324 is encoded in humans and in mice, shown in relation to neighbouring genes. The directionality of each gene illustrates which strand they are encoded from; the forward strand runs from left to right in a 5' to 3' direction. Exons are shown in yellow and UTRs are shown in blue. Ensembl transcript IDs are shown beside each transcript [68].

miR-324 arm	Human sequence (5’ to 3’)	Mouse sequence (5’ to 3’)
miR-324-5p	C**GCAUCCC**CUAGGGCAUUGGUG	C**GCAUCCC**CUAGGGCAUUGGUGU
miR-324-3p	CC**CACUGCC**CCAGGUGCUGCUGG	C**CACUGCC**CCAGGUGCUGCU

Table 1.1 - The mature sequences of miR-324-5p and -3p in human and mouse, based on miRBase deep sequencing reads [69]**.** The seed sequences within each mature sequence are shown in bold and red.

1.2 Epilepsy and neurological disease

The vertebrate brain is a complex organ comprised of three overarching regions; the forebrain, midbrain and hindbrain. Within each of which are multiple structures, separated from one another both spatially and functionally. For example, the hippocampus, a structure located in the forebrain, plays a role in memory production, whereas the nearby hypothalamus is largely responsible for regulation of important metabolic processes through the release of hormones [70-73]. Because of this functional distinction between spatially close structures, it is not always obvious precisely how an injury or developmental issue in a particular region of the brain will affect the afflicted individual. Complex regulatory networks between structures, such as the communication between the hippocampus and neocortex, complicate matters further still, as a slight dysregulation of a specific process in one structure could conceivably result in a harmful effect elsewhere [74-76]. Such complexity and interconnectedness suggests that these networks between neurological structures are likely to be highly susceptible to dysregulation of regulatory proteins and RNAs, including miRNAs, and in the case of many neurological disorders this has been shown to be the case [77, 78].

1.2.1 *Epilepsy*

Epilepsy is one of the most common neurological conditions, with an estimated prevalence of between 0.4 and 1% [79]. High numbers of cases are reported across the world with a fairly equal distribution between males and females (although the incidence is reportedly marginally higher in males). Cases are most frequent in the elderly and in young children [80-82]. The condition is defined as a predisposition to recurrent unexpected seizures, which commonly present as brief severe alterations to behaviour or perception of the surrounding environment [83]. Within the conditions that fall under the definition of epilepsy there is a

great deal of variation in factors such as the seizure severity, occurrence or length [83, 84]. These seizures are caused by prolonged periods of intense neuronal stimulation, a result of extended periods of neuronal depolarisation without a return to resting potential [85], which is the electric potential difference across a membrane whilst in a non-excited state. Although any single individual epileptic seizure is rarely lethal, epilepsy sufferers are more likely to die prematurely, on top of an increased risk of suicide; the reduction in life expectancy for epilepsy sufferers can be as much as 10 years [86-89]. Treatments are widely available for epilepsy and these are effective in approximately 70% of cases [79, 90, 91], although relapse and resistance to treatment are not uncommon [79, 92, 93]. Current pharmaceutical treatments include carbamazepine and tigabine, which block the usage of sodium channels (thus disrupting the axonal depolarization required for neuronal firing) and upregulate gamma-aminobutyric acid (GABA) production, the primary mammalian inhibitory neurotransmitter, respectively [94-97]. Both of these mechanisms result in a reduction of aberrant neuronal firing (summarised in Figure 1.4), which is the key component of epilepsy [85]. For many epilepsy treatments the precise molecular mechanisms of action are unclear, with most drugs identified in screening studies for molecules beneficial in animal models of epilepsy, rather than identification through predicted activity [94].

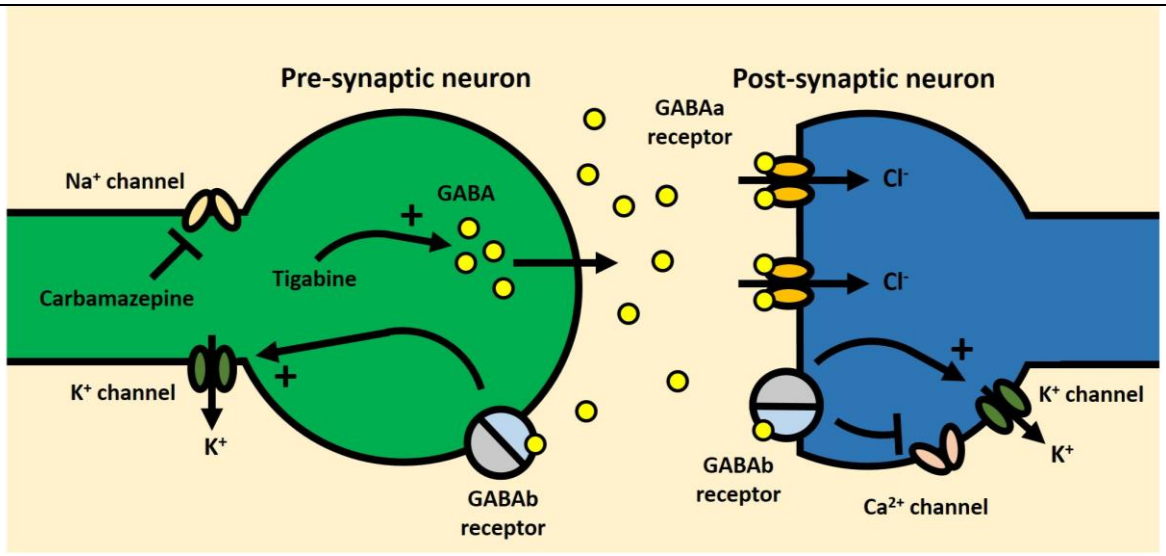

Figure 1.4 - Proposed mechanisms of action of the anti-epileptic pharmaceuticals carbamazepine and tigabine. The key component of signal transmission across a neuronal axon is depolarisation, where the electrical gradient at the axon membrane becomes more positive than the resting potential of -70 mV. Excessive prolonged periods of depolarisation without returning to a resting state is the underlying cause of a seizure [85], and therefore anti-epileptic pharmaceuticals are thought to target this mechanism. Depolarisation is achieved initially by the import of sodium ions (Na^+) along a chemical gradient. This sodium channel is the purported target of carbamazepine [94]. Tigabine is thought to upregulate the inhibitory activity of GABA at the neuronal synapse, and this results in increased binding of GABA to the receptors GABAa and GABAb [94, 98, 99]. Binding to GABAa at the post-synaptic neuron allows the entry of chloride ions (Cl^-) into the cell through the receptor, thus limiting the ability of the neuronal membrane to undergo depolarisation. Binding of GABA to GABAb results in a number of activities, but primarily increases export of potassium ions (K^+) and reduces entry of calcium ions (Ca^{2+}) to both the pre- and post-synaptic neuron. Once again, this results in an increased threshold required for neuronal depolarisation.

1.2.2 *microRNAs in neurological disease*

miRNAs are crucial components in normal brain development and neurological function. Several conditional knockout mouse models which lack *Dicer1*, an essential gene for miRNA processing, in specific neuronal populations present with severe neurological abnormalities [100-103]. Individual miRNAs too can impact severely on brain development; mice lacking miR-9, a highly expressed miRNA in the vertebrate brain, display impaired regulation of neural

progenitor cell proliferation [104-106], and upregulation of miR-34a promotes apoptotic pathways. miR-34a has also been purported to contribute to neuronal death in epilepsy rodent models following seizures [107, 108]. Individual miRNAs are therefore essential for normal neurological activity and modulation of these key miRNAs can produce detrimental effects to brain development and function.

1.2.3 *miR-324 in neurological disease*

miR-324 is expressed at higher levels in the brain than in any other tissue, in both humans and mice [109, 110], and has previously been implicated in the regulation of normal neural activity [111, 112]. Both miR-324-5p and -3p are each predicted to target many genes, although experimental validation of these is limited. *App*, the gene encoding the amyloid precursor protein [113], is one of the most confidently predicted miR-324-5p targets [5, 67], suggesting that miR-324-5p may play some role in Alzheimer's Disease onset or progression [114]. There is also evidence in the literature that miR-324-5p plays a role in epilepsy, as injection with a miR-324-5p antagomir in an epilepsy mouse model has been shown to reduce the frequency of epileptic seizure events [112]. This regulation may occur through the direct targeting of *Kcnd2* by miR-324-5p, which encodes an important potassium channel protein [111, 112]. Disruption of *Kcnd2* expression has been shown to impair normal functioning of potassium currents, which is essential for the normal regulation of neuronal excitability [115-117]. These studies therefore suggest a relationship between miR-324 and neurological activity.

1.3 Cartilage maintenance and osteoarthritis

Cartilage comprises of a single cell type, the chondrocyte, embedded within extracellular matrix (ECM), which is secreted by the chondrocytes themselves [118, 119]. In healthy cartilage, anabolism and catabolism are balanced, so that some components of the ECM are frequently turned over without losing volume. However, this balance can become shifted towards increased catabolism, due to injury or ageing-related processes, resulting in osteoarthritis (OA).

1.3.1 *The growth plate and endochondral ossification*

The growth plate is the region near each end of long bones at which longitudinal growth occurs, a process known as endochondral ossification. The growth plate is composed entirely of one cell type, the chondrocyte, and the ECM secreted by it [120, 121]. Chondrocytes are cells of mesenchymal lineage which form five highly structured zones in healthy growth plates, each composed of chondrocyte populations in a different stages of differentiation

(summarised in Figure 1.5) [121, 122]. Chondrocytes proliferate along the vertical axis of the growth plate in columnar organisation, such that chondrocytes in similar vertical positions in neighbouring columns will be at the same zone of chondrogenic differentiation in a healthy growth plate. Chondrocyte transition between zones is regulated by a complex network of morphogens, which in turn control the expression of genes encoding key transcription factors, such as *Sox9* and *Runx2*. These transcription factors then activate transcription of specific zonal genes, which in general encode ECM proteins [123-126]. Initially, chondrocytes are said to be in a resting phase, as they proliferate at a low rate. At this point they express *Col2a1*, the gene encoding type II collagen. Comparatively in the subsequent zone, the proliferative zone, chondrocytes rapidly undergo mitosis and express *Acan*, the gene encoding aggrecan, a key ECM proteoglycan, in addition to continued *Col2a1* expression. Further down the growth plate still, chondrocytes enter the pre-hypertrophic phase, in which the cells begin to expand in size and the expression of *Col2a1* and *Acan* begins to decrease, whereas *Col10a1* and *Ihh* become expressed for the first time, priming chondrocytes for the final active phase; the hypertrophic phase [120-122]. Indian hedgehog, encoded by *Ihh*, is key to the regulation of chondrocyte hypertrophy by upregulating the expression of *Pthrp* in pre-hypertrophic chondrocytes, which in turn inhibits hypertrophy [126]. This ensures that only chondrocytes distal enough from Indian hedgehog-secreting pre-hypertrophic chondrocytes undergo hypertrophy, thus maintaining the structure of the growth plate (Figure 1.5). In addition to a vastly increased volume, hypertrophic chondrocytes are essential in the precise regulation of bone development. This is achieved through their own apoptosis or transdifferentiation into osteoblasts as well as the precise coordination of bone remodelling cells [127, 128]. Chondrocytes deposit ECM throughout the hypertrophic phase, which is calcified in preparation for bone formation [129]. Thus, disruption of any phase of the growth plate in long bones can have severe consequences not just for diseases of the joint, but for the skeleton as well.

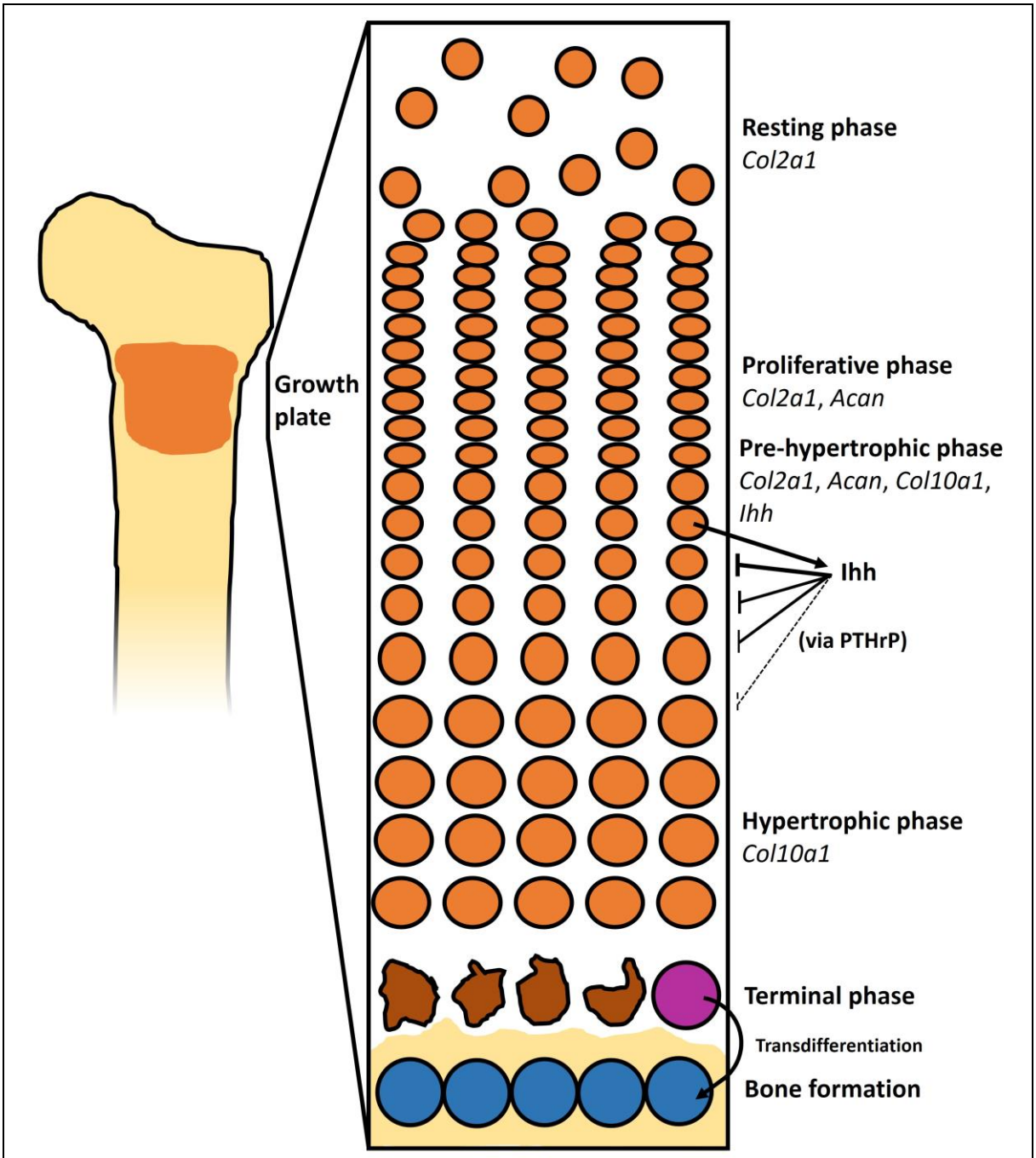

Figure 1.5 - The growth plate in long bones. Chondrocytes pass through five phases at the growth plate; resting, proliferative, pre-hypertrophic, hypertrophic and terminal. Proliferation occurs after the resting phase, in the proliferative phase, and at this point the growth plate becomes tightly ordered into columns of chondrocytes. After the proliferative stage, chondrocytes become larger, expanding throughout the pre-hypertrophic stage and depositing type X collagen in addition to type II collagen and aggrecan. Indian hedgehog is also secreted by pre-hypertrophic chondrocytes, which upregulates *Pthrp* in proximal chondrocytes, repressing the transition to hypertrophy. Thus, only once chondrocytes are distal enough from the pre-hypertrophic zone can they undergo the transition to the

hypertrophic phase. Finally, the hypertrophic chondrocytes either commit to apoptosis or undergo transdifferentiation into osteoblasts. Hypertrophic chondrocytes are also crucial in the coordination of the bone remodelling cells required for bone formation.

1.3.2 *Osteoarthritis*

Osteoarthritis (OA) is the most common disorder of the joint worldwide, and affected more than 300 million people in 2017 [130, 131], with the heritability of OA estimated to be as high as 50% [132, 133]. The prevalence of OA is greatest in the elderly population with more than half of those aged 65 years or older displaying radiographic evidence of OA. Of those 75 or older, 4 in every 5 people show OA symptoms [131]. To date there are no disease modifying drugs approved for widespread use in the treatment of OA [134], which holds harsh implications to countries with ageing populations such as the UK; by 2030 it has been predicted that OA will affect 17 million people within the UK [135]. The condition itself consists of severely decreased cartilage volume in concert with severely increased thickness of subchondral bone, resulting in severe pain and stiffening of joints [136-138]. At a molecular level, OA is the eventual consequence of increased catabolic activity in joint tissues, primarily resulting from increased matrix metalloproteinase (MMP) activity, such as MMP13, and other catabolic enzymes, such as ADAMTS5, which catalyse the breaking down of the key ECM components type II collagen and aggrecan respectively [139, 140]. In addition to this cartilage degradation, OA also causes severe bone remodelling, such that by the late stages of the condition, the subchondral bone of OA patients is severely thickened due to dysregulation of osteoblasts and osteoclasts, the cells responsible for bone formation and resorption respectively, with bony spurs known as osteophytes being clearly visible in affected individuals [141, 142].

The dysregulation of any single MMP can have a huge impact on cartilage homeostasis [132, 133]. For example, the knockout of *Mmp13* in mice improves resistance to cartilage degradation after surgical induction of OA [143]. In addition to this direct effect of MMP modulation, dysregulation of large gene networks are also thought to have a large impact on the transcriptomic profile of the chondrocyte; the activity of ncRNAs can affect the expression of a wide array of genes through complex networks and therefore can impact a process such as cartilage homeostasis through the dysregulation of many genes at once [144]. As such,

ncRNAs have been the focus of many recent studies into the regulation of OA and cartilage homeostasis [145-153].

It is worth mentioning that *Kcnd2*, a gene reported in the literature as a neurological target of miR-324 [111, 112], has also been posited as having importance in the differentiation of MSCs into chondrocyte precursor cells (CPCs). Human *KCND2* was reported as being significantly downregulated in CPCs relative to MSCs, therefore potentially indicating that *KCND2* is antagonistic to normal chondrogenic differentiation [154]. The reporting of murine *Kcnd2* being a direct miR-324 target is indicative that this regulatory axis could affect more than one of the processes investigated as part of this project.

1.3.3 *Animal models of osteoarthritis*

OA is a complex disorder that manifests itself at vastly different rates between patients as a result of a great number of risk factors, including age, weight and genetic predisposition [155-158]. Due to such confounding variables between human OA patients, *in vivo* animal models of the condition have been developed as pre-clinical models, although no single commonly used model is perfect in mimicking human OA progression [159-161]. Therefore, different animal models are commonly used to model different components of the condition. In the case of some animals OA occurs spontaneously, although the point at which onset begins is highly variable between species and strains. In the case of mice and a strain of guinea pig, Dunkin Hartley, small OA-like lesions have been found to occur as early as 3 months and 6 months respectively, with increasingly severe OA symptoms appearing with age [162]. However, in many cases waiting for spontaneous OA to occur in an animal is unacceptable because of financial, ethical or biological reasons, and therefore post-traumatic models of OA are more commonly used. These consist of either artificially damaging the meniscus, removing the meniscus completely or transection of the anterior cruciate ligament [162, 163]. After induction of OA, joints can be sectioned and stained, for example using Safranin-O to assess cartilage damage between induced animals and non-induced controls. Scoring systems such as the Osteoarthritis Society International (OARSI) histopathological scoring system [164] can be used to quantify and compare cartilage damage, allowing investigators to assess whether a particular condition impacts the onset of OA, therefore directing downstream research towards promising targets in animal models for future clinical trials in humans. It should be noted that this scoring system is adapted for use in mouse models, in which cartilage is approximately 50-fold thinner than human cartilage [165]. This important difference should

therefore be considered when progressing cartilage research from a mouse model in which this system of quantification has been used into translational studies.

1.3.4 *miRNAs in cartilage biology*

miRNAs are an important component of molecular networks involved in cartilage maintenance, and mice that conditionally lack Dicer, a key component of the miRNA processing pathway, in chondrocytes (deleted using Cre recombinase driven by a *Col2a1* promoter) display severe growth defects and often die prematurely [166]. Even individual miRNAs can have strong effects on musculoskeletal development; when the cartilage-specific miRNA miR-140 is knocked out in mice, craniofacial deformities and a short stature are observed [167], miR-455-null mice display severely reduced cartilage thickness [168] and miR-17/92-null mice display severe developmental abnormalities, recapitulating the Feingold syndrome observed in humans harbouring mutations in the miR-17/92 cluster [169, 170]. Other miRNAs, such as miR-29a, miR-29b and miR-1, have been found to regulate the expression of genes encoding the ECM components secreted by chondrocytes, such as *Acan* and *Col2a1* [171, 172], and all members of the miR-29 family have been shown to also downregulate other key cartilage development and maintenance pathways, such as the canonical Wnt and Nuclear factor kappa B (NFκB) signalling pathways [173]. Several miRNAs have been found to affect the migration of chondrocytes or precursor cells, including miR-375, miR-488 and miR-34a [174-176], and in the case of miR-34a, a knockout mouse model displayed a protective effect against Destabilisation of the medial meniscus (DMM)-induced OA [177]. This demonstrates the potential severity of modulating cartilage-associated miRNAs.

1.3.5 *miR-324 in osteoarthritis and cartilage maintenance*

miR-324 has been associated with diseases of the joint and pathways related to their onset in recent publications, including the Hedgehog (Hh) signalling pathway (the murine Hh signalling pathway is summarised in Figures 1.6a and 1.6b), which regulates several key musculoskeletal processes. These include endochondral ossification, whereby cartilage tissue is replaced by bone as the skeleton grows [178-180]. Alterations to the expression of any one of a number of Hh signalling genes can result in severe developmental abnormalities [181-185]. Multiple publications have reported the direct repression of *SMO* and *GLI1*, which encode two key human Hh signalling components, by miR-324-5p [151, 186, 187]. Interestingly however, despite the conservation of both miR-324-5p and its seed sequence in humans and mice, the

mechanism of Hh signalling regulation is not itself conserved; it has been shown that miR-324-5p instead targets *Gpc1* in mice, producing the same effect on the Hh pathway overall, albeit through a different target (Figure 1.6c) [151]. Additionally, miR-324-5p was found to be one of a small panel of miRNAs highly differentially expressed in osteoarthritis (OA) cartilage relative to neck of femur fracture controls (NOF) [151, 188]. miR-324-5p was significantly increased in expression in these OA cartilage samples, suggesting either that it plays some role in enhancing OA progression or that it is upregulated to protect against OA in response to the onset of the condition. In OA, the Hh signalling pathway is re-initiated, resulting in cartilage damage through a number of mechanisms [189-192] (summarised in Figure 1.6d). Perhaps therefore the Hh genes targeted by miR-324 are the reason for this association with the disorder.

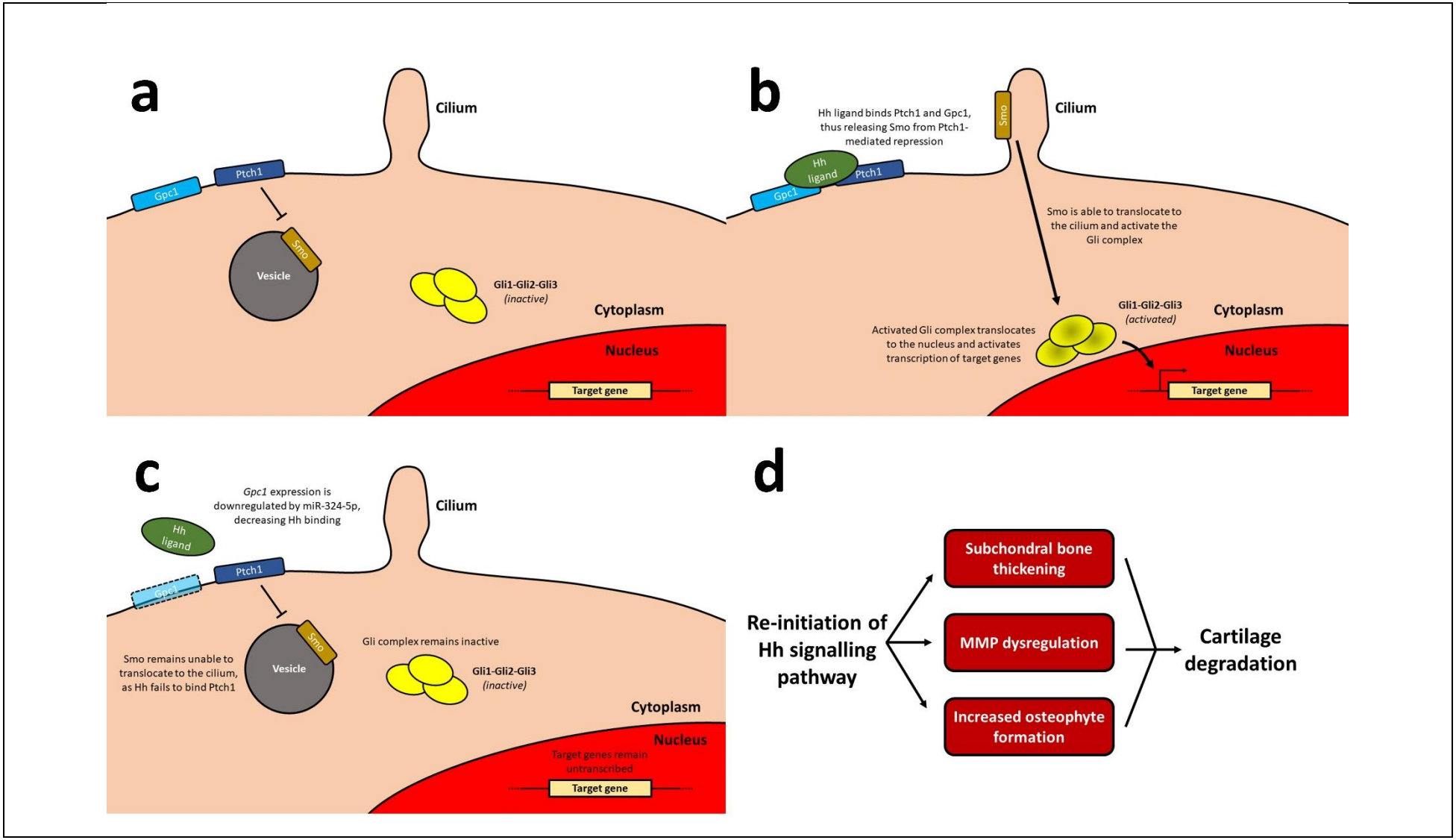
a
Cilium
Ptch1
Gpc1
Smo
Vesicle
Gli1-Gli2-Gli3
(inactive)
Cytoplasm
Nucleus
Target gene
b
Hh ligand binds Ptch1 and Gpc1, thus releasing Smo from Ptch1-mediated repression
Hh ligand
Smo
Cilium
Smo is able to translocate to the cilium and activate the Gli complex
Gli1-Gli2-Gli3
(activated)
Activated Gli complex translocates to the nucleus and activates transcription of target genes
Cytoplasm
Nucleus
Target gene
c
Gpc1 expression is downregulated by miR-324-5p, decreasing Hh binding
Hh ligand
Cilium
Ptch1
Gpc1
Smo
Vesicle
Smo remains unable to translocate to the cilium, as Hh fails to bind Ptch1
Gli complex remains inactive
Gli1-Gli2-Gli3
(inactive)
Cytoplasm
Nucleus
Target genes remain untranscribed
Target gene
d
Re-initiation of Hh signalling pathway
Subchondral bone thickening
MMP dysregulation
Increased osteophyte formation
Cartilage degradation

Figure 1.6 - The Hh signalling pathway. (**a**) The pathway in the absence of Hh ligand, whereby Ptch1 prevents the localisation of Smo from an intracellular vesicle to the cilium and therefore the Gli complex remains inactive. (**b**) Hh ligand binds Ptch1 and Gpc1, preventing the inhibitory effect of Ptch1 on Smo. Smo can therefore localise to the cilium and activate the Gli complex, allowing it to translocate to the nucleus and activate Hh target genes. (**c**) The effect of miR-324-5p on the Hh pathway in the presence of Hh ligand. Here, *Gpc1* is downregulated by miR-324-5p, preventing the binding of Hh ligand to Ptch1 and Gpc1. Therefore, the Gli complex remains inactive due to the inability of Smo to localise to the cilium. It should be noted that although Gpc1 is often referred to operate in combination with Ptch1 as a co-receptor of Hh ligand [151, 193] and therefore encouraging triggering of Hh signalling as shown in this schematic, there have also been reports of Gpc1 acting as a Hh signalling antagonist [194]. (**d**) Certain events caused by re-initiation of the Hh signalling pathway eventually result in cartilage loss and OA. These include thickening of subchondral bone, dysregulation of MMPs and increased formation of osteophytes [189-192].

1.4 Bone remodelling

Bone remodelling is the process by which bone is maintained. It is comprised of antagonistic effects provided by osteoblasts, which act to form new bone, osteoclasts, which resorb bone, and osteocytes, which are understood to play a large role in regulating the former cells [195]. The differentiation of these cells from mesenchymal and haematopoietic stem cells in the bone marrow is cross-regulated by mature bone cells, such that bone remodelling can be precisely modulated according to the need of the skeletal system at that particular time (Figure 1.7).

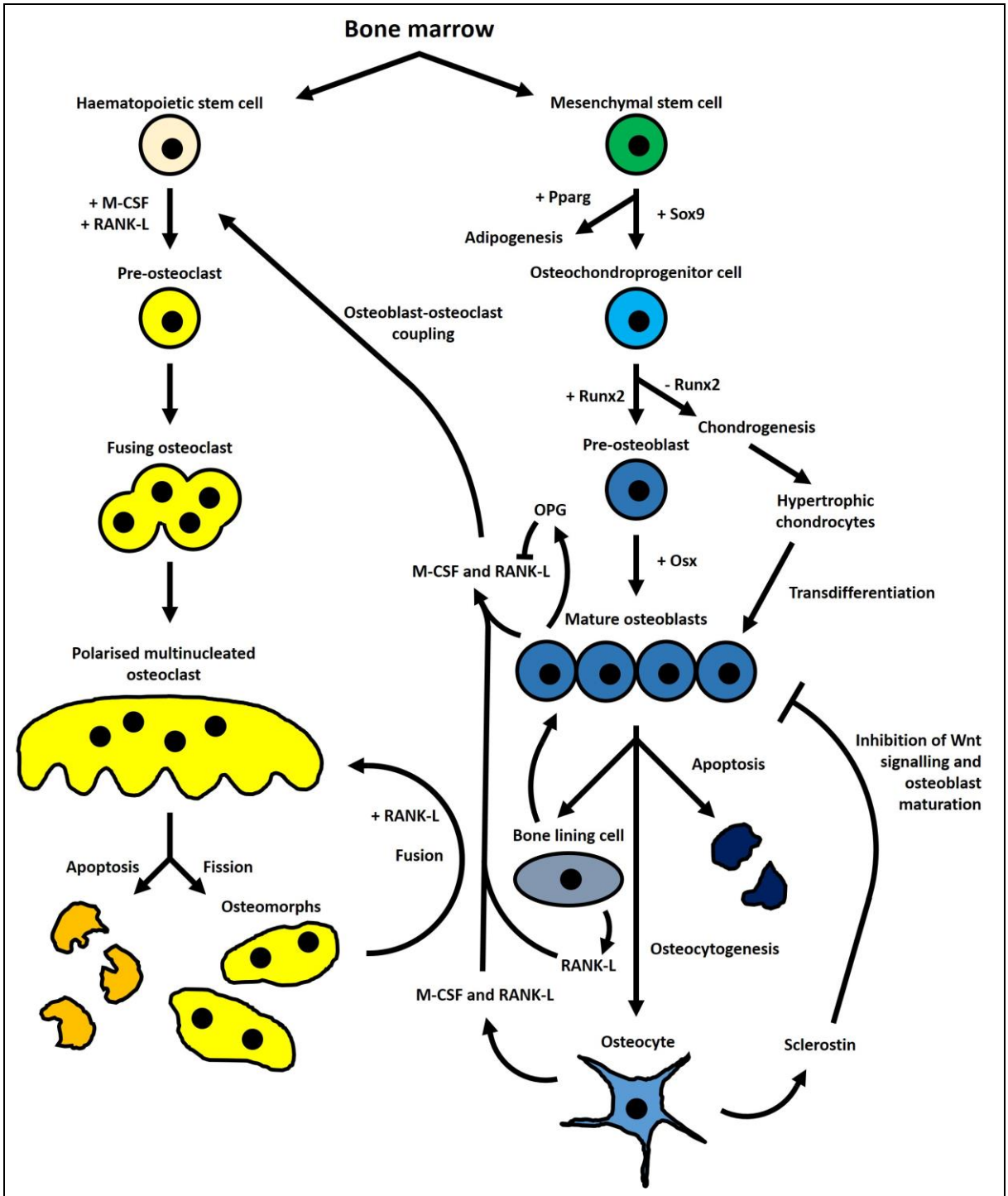

Figure 1.7 - A summary of bone cell differentiation from stromal cells. Haematopoietic stem cells commit to the osteoclast lineage upon stimulation with Receptor activator of nuclear factor kappa-B ligand (RANK-L) (which binds to the Receptor activator of nuclear factor kappa-B (RANK) cell surface receptor) and Macrophage colony stimulating factor (M-CSF), resulting in eventual fusion and polarisation to become a mature osteoclast. Mature osteoclasts have a relatively short life once activated, and eventually either commit to apoptosis or fission into osteomorphs, smaller inactive multinucleated cells which are able to re-fuse into mature osteoclasts again. RANK-L is essential for this re-fusion. Mesenchymal

stem cells comprise the origins of osteoblasts, bone lining cells and osteocytes. Expression of *Sox9* commits the stem cell to the osteochondroprogenitor lineage, rather than the adipogenic lineage, which is driven by *Pparg* expression. Subsequent *Runx2* expression in the osteochondroprogenitor lineage ensures that cells differentiate into pre-osteoblasts rather than chondrocytes. Expression of *Osx* subsequently allows further differentiation into mature osteoblasts, which function as a group of mature cells. Following on from bone formation, osteoblasts have three potential fates; a minority of cells undergo apoptosis, whereas the remainder either become bone lining cells, or become embedded in the newly formed bone and differentiate into osteocytes. Although osteocytogenesis is thought to be terminal, bone lining cells are able to reverse their differentiation and once again become mature osteoblasts able to form new bone. Osteocytes, osteoblasts and bone lining cells all contribute to the stimulation of osteoclastogenesis through the secretion of RANK-L, whilst osteoblasts and osteocytes additionally express *Csf1* (which encodes M-CSF), thus maintaining a balance between bone formation and resorption. In addition to secreting RANK-L, osteoblasts also secrete osteoprotegerin (OPG), a decoy receptor of RANK-L. Thus through altering the ratio between secreted RANK-L and OPG, osteoblasts can tightly regulate osteoclastogenesis and maturation. A final mechanism of intercellular regulation is through the use of sclerostin; osteocytes express and secrete *Sost*, which encodes sclerostin, a potent inhibitor of Wnt signalling, therefore allowing osteocytes to also regulate the maturation and activity of osteoblasts.

1.4.1 *Osteoclastic bone resorption*

Osteoclasts act to balance osteoblastic bone formation with bone resorption, thus releasing calcium from mineralised bone and in a healthy system ensuring that excessive bone formation does not occur. Osteoclasts are haematopoietic cells in origin (Figure 1.7) and thus differentiate from an entirely different pathway to osteoblasts, osteocytes and bone lining cells [196]. In osteoclastogenesis, pre-osteoclasts are recruited by expression of Receptor activator of nuclear factor kappa-B ligand (RANK-L) and Macrophage colony stimulating factor (M-CSF) in a space at the interface between the bone matrix and bone marrow known as a bone remodelling compartment (BRC) [196]. Both RANK-L and M-CSF are key for osteoclast differentiation, as proven in RANK-L-null mice and in M-CSF-null mice, where bone resorption is completely inhibited and severe high bone mass phenotypes are observed [197, 198]. It is

currently unclear exactly which bone cell is more important for the expression of *Tnfsf11* and *Csf1*, the murine genes encoding RANK-L and M-CSF, respectively, as their expression has been detected in both bone osteoblasts and osteocytes, with *Tnfsf11* also expressed by bone lining cells [199-205]. It is therefore possible that all three of these cell types are important in the initiation of osteoclastogenesis through M-CSF and RANK-L production. Once recruited and stimulated with M-CSF, pre-osteoclasts begin presenting Receptor activator of nuclear factor kappa-B (RANK) on their surface, and the binding of this RANK with the aforementioned RANK-L stimulates pre-osteoclasts to begin the process of fusion into giant multinucleated osteoclasts [206]. Exactly how the process of fusion is instigated at a molecular level following RANK/RANK-L binding is not well understood, although it is thought that upregulation of *Dcstamp*, a gene only expressed in macrophages undergoing osteoclastogenesis, may play a crucial role in osteoclast fusion, although not in subsequent resorption; *Dcstamp*-null mice are unable to produce multinucleate osteoclasts, but the immature mononucleate osteoclasts present in the BRCs of these mice are still able to resorb bone, albeit to a reduced level [196, 207]. Once multinucleate osteoclasts have matured, the process of resorption is able to begin within the BRC. Although bone resorption occurs fluidly, the process can be separated into several distinct steps; the first is the formation of a sealing zone, a region at the bone matrix-bone marrow interface spatially isolated from the bone marrow as a result of pre-osteoclasts binding to the bone surface via the surface receptor integrin $\alpha_V\beta_3$. This allows the recruited osteoclasts to become polarised, such that the resorption machinery is positioned towards the interface with the bone matrix [208, 209]. Following on from this, a ruffled border is formed at the osteoclast-bone matrix interface and insertion of an Adenosine triphosphate (ATP)ase at the osteoclast membrane adjacent to the sealing zone facilitates transport of protons towards the bone matrix. The increased acidity of this environment results in the dissolution of the mineralised inorganic component of the bone matrix, formed of calcium-containing hydroxyapatite. The exportation of vesicles containing the proteolytic enzyme cathepsin K produces the subsequent step in bone resorption, in which the organic component of the bone matrix, consisting primarily of type I collagen, is cleaved [196, 210-212]. The process of osteoclastic bone resorption is summarised in Figure 1.8. Once activated, the osteoclast lifespan was thought to be relatively short; until recently, osteoclasts were proposed to survive for a maximum of only 3 weeks in the bone marrow [213, 214], but recent advancements in this area have suggested that osteoclasts may actually survive for as long as

6 months [215]. However, recently an alternative end to osteoclast life has been demonstrated, introducing a new bone cell; the osteomorph [216].

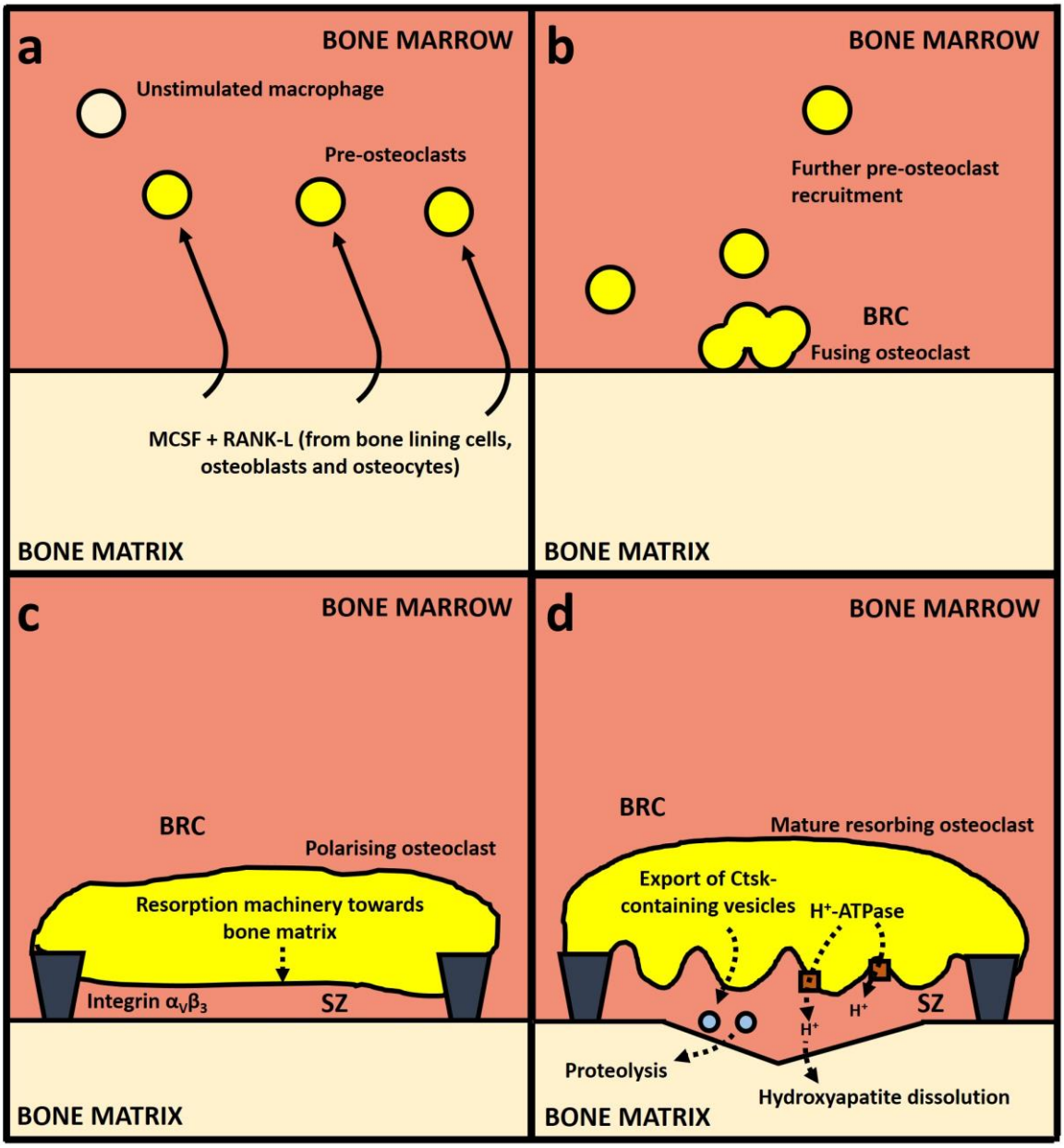

Figure 1.8 - Summary of osteoclastic bone resorption. (**a**) M-CSF and RANK-L are released from bone lining cells, osteoblasts and osteocytes, recruiting macrophages to the bone remodelling compartment (BRC) and stimulating the initial phase of the differentiation. (**b**) Within the BRC, the pre-osteoclasts begin to fuse into a giant multinucleate cell. (**c**) The multinucleate immature osteoclast expresses integrin $\alpha_V\beta_3$, allowing it to bind to the bone matrix and form a sealing zone (SZ). (**d**) Once polarisation of the osteoclast is complete, a ruffled border is formed against the SZ, through which the osteoclast pumps protons, allowing dissolution of the inorganic component of the bone matrix, and exports vesicles containing cathepsin K, allowing proteolysis of the organic components of the bone matrix.

1.4.2 *Osteomorphs and osteoclast recycling*

Although little is known regarding osteomorphs, their recent discovery [216] warrants them a brief mention. Osteomorphs are best described as non-resorbing multinucleate cells that are produced as a result of osteoclastic fission. Previously, osteoclasts were thought to initiate apoptosis at the end of their life, resulting in active osteoclasts possessing relatively short life spans [213-215]. However, a recent investigation authored by McDonald et al. (2021) utilised two-photon microscopy to prove that this is not the case; osteoclasts actually enter into a complex cycle of fusion and fission (Figure 1.7), allowing the energy spent by the skeletal system in the maturation and activation of an osteoclast to be recycled by way of storage in osteomorphs. This system allows, for example, an osteoclast to mature in one BRC, before undergoing fission into several osteomorphs, which can then re-enter the bone marrow and be ready to re-fuse into another maturing osteoclast at a spatially distinct BRC. Indeed, McDonald et al. (2021) even showed that osteomorphs can fuse together to form an osteoclast formed exclusively from osteomorphs. Despite the multinucleate similarity between osteomorphs and mature osteoclasts, there are a number of crucial differences; the most obvious distinction to make is that osteomorphs, unlike osteoclasts, are unable to resorb bone. Additionally, osteomorphs were shown using single-cell sequencing to express a distinct transcriptome from osteoclasts, and McDonald et al. (2021) advised that some of these differentially expressed genes encode cell-surface proteins, which could be used to distinguish the two cell types in future osteomorph work.

1.4.3 *Osteoblastic bone formation*

Osteoblasts are cells derived from the osteochondroprogenitor lineage and are responsible for the formation of bone. The transcription factor Sox9 commits mesenchymal stromal cells (MSCs) to differentiate into osteochondroprogenitor cells, and subsequent expression of *Runx2* ensures that osteochondroprogenitor cells are directed towards the osteoblast fate rather than the chondrocyte differentiation path, as occurs in healthy cartilage (Figure 1.7). At this stage, the cells are known as pre-osteoblasts, and expression of *Osx* drives the maturation of the cell into an osteoblast, regulated overall by the Wnt/β-catenin signalling pathway [217, 218]. Mature osteoblasts act in functional units and secrete proteins required to form the bone matrix, such as alkaline phosphatase and type I collagen. Hydroxyapatite is deposited alongside type I collagen, which is the mechanism through which calcium is added to the skeleton, strengthening the skeleton as it forms [218-220]. The activity of osteoblasts relative

to osteoclasts is regulated via a network of molecular signals, resulting in modulated activity depending on the levels of circulating calcium in the blood. In response to low calcium levels, parathyroid hormone (PTH) is released from the parathyroid gland, binding to the Pth1r receptor in osteoblasts. This binding triggers a molecular signalling cascade, resulting in increased production of osteoblastic M-CSF and RANK-L, therefore upregulating osteoclastogenesis, so also upregulating bone resorption, allowing more calcium to be released from mineralised bone and back into circulating blood [221, 222]. In addition to regulation by PTH, osteoblasts also produce a molecule known as osteoprotegerin (OPG), which is also used to modulate osteoclast activity. OPG is secreted by osteoblasts as a decoy receptor for RANK-L, and so by modulating the ratio of OPG to RANK-L, osteoblasts can regulate the amount of RANK-L available to be bound to by the RANK receptor on osteoclasts, a key interaction for osteoclastogenesis [223, 224]. At the end of the osteoblast life cycle, rather than committing to apoptosis, an osteoblast will in most cases either enter a quiescent state and become a bone lining cell or alternatively embed itself into the surrounding matrix and terminally differentiate into another bone cell known as an osteocyte in a process termed osteocytogenesis [225, 226].

1.4.4 *Osteocytes and bone lining cells*

Despite the shared mesenchymal lineage of osteoblasts, osteocytes and bone lining cells, each of the three cells is functionally, as well as spatially, distinct from the other two. Where the osteoblast acts as an effector cell in the process of bone remodelling, by actively forming and mineralising new bone, osteocytes and bone lining cells are thought to play more of a regulatory role.

Bone lining cells are flat quiescent cells differentiated from osteoblasts, and although their activity is not yet well understood, they have been shown to play key regulatory roles in bone remodelling [200, 227]. For example, bone lining cells are certainly important in stimulating osteoclastogenesis when the physiological conditions require increased bone resorption, by secreting RANK-L. Bone lining cells also participate in osteoclast inhibition through two mechanisms; physically, bone lining cells separate osteoclasts from the bone matrix they would otherwise resorb, and at a molecular level, bone lining cells have been shown to secrete OPG, thus inhibiting osteoclastogenesis through the same inhibitory mechanism as used by osteoblasts [200, 223, 227]. Interestingly, it has also been shown that the differentiation of osteoblasts into bone lining cells is not terminal; bone lining cells are able to reverse their

transition from osteoblasts and once again become bone forming osteoblasts [228], adding further complexity to the osteoblast differentiation path (Figure 1.7).

Osteocytes differentiate from osteoblasts embedded in bone matrix, a process known as osteocytogenesis, and are by far the most populous of the bone cells; it has been estimated that osteocytes comprise more than 90% of bone cells by number [229]. It is therefore unsurprising that they play important roles in a number of important bone regulatory activities. Perhaps the most well-known mechanism by which osteocytes act to regulate bone remodelling is through the osteocyte-specific gene *Sost*, which encodes sclerostin, a protein which exerts a negative regulatory effect on osteoblasts. It achieves this through binding to the key Wnt signalling receptors Lrp5 and Lrp6, thus repressing the Wnt signalling pathway in osteoblasts, both preventing their maturation and enhancing apoptotic pathways [230, 231]. The expression of *Sost* itself is also tightly regulated; PTH, released from the parathyroid gland in response to high levels of calcium in circulating serum, binds the osteocyte receptor Pth1r, which in turn represses *Sost* [226, 232]. Thus, when there is excess bone resorption and insufficient bone formation, resulting in high circulating calcium levels, the parathyroid gland can release osteoblasts from their osteocyte-mediated repression (Figure 1.9a). Interestingly, when the PTH target Pth1r is activated, osteoclast-mediated bone resorption is also upregulated, in addition to osteoblast-mediated bone formation; transgenic mice constitutively expressing *Pth1r* in osteocytes show decreased *Sost* expression in addition to a high bone mass phenotype, but also a high level of bone turnover. Furthermore, when *Lrp5* is deleted, the excess bone phenotype is absent, although the high rate of bone remodelling remains, suggesting that the regulation of bone remodelling via PTH may also act through a secondary mechanism independent of Lrp5, in addition to the Lrp5-dependent pathway that results in upregulation of osteoblast activity [233].

In addition to hormone-driven activity, osteocytes also play crucial regulatory roles through mechanosensory activity; osteocytes selectively activate and repress specific genes depending on the mechanical loading environment. The detection of mechanical stresses by osteocytes is thought to be driven by fluid flow shear stress; bone loading induces micro-deformation of the bone matrix, increasing interstitial fluid flow and thus also increasing the pressure experienced by osteocytes situated within the lacuno-canalicular space [234]. Many proteins have been suggested as important sensors of this increased stress, including spectrin, which is required for osteocytogenesis [235], and the gap-junction protein Connexin 43 [236]. It has

also been proposed that mechanical stress is sensed via the osteocyte cilia due to altered hydrostatic pressure. The subsequent transduction of this signal to molecular pathways is achieved through several mechanisms, including nitrogen oxide, Wnt signalling and calcium ion release [237, 238]. Downstream of mechanical sensing, osteocytes downregulate the expression of *Sost*, thus offering another route into the Sost-Lrp5/6 pathway, as well as *Dkk1* [239], a gene which, similar to *Sost*, inhibits Wnt signalling and therefore downregulates osteoblastic bone formation [240, 241]. Thus, upon mechanical loading, osteocytes release osteoblasts from *Sost*-mediated repression, so increasing bone formation. Upon mechanical unloading, osteocytes act to upregulate osteoclast activation pathways. Osteocytes proximal to microcracks, resulting from recent loading, commit themselves to apoptosis, whilst distal osteocytes upregulate the expression of *Tnfsf11* (RANK-L), thus priming the bone matrix for increased osteoclast-mediated bone resorption at specific sites at which bone remodelling is required [203, 242, 243] (Figure 1.9b).

Although the aforementioned regulatory networks are widely accepted, a great deal about osteocytes remains incompletely understood; several osteocyte-selective genes are thought to be highly important in bone biology, despite lacking a direct link to bone development or maintenance. *Fgf23* is one such gene, enabling essential coordination between osteocytes and the kidneys to regulate phosphate levels. The protein product of *Fgf23* is primarily secreted from osteocytes and although *Fgf23* is also expressed in other cells, it is most abundant in osteocytes [244-246]. Precise regulation of *Fgf23* is essential in mice, as both overexpression and lack of *Fgf23* leads to bone mineralisation defects in addition to skeletal abnormalities [247, 248]. In humans, gain-of-function *Fgf23* mutations result in hypophosphatemic rickets, whereas a missense loss-of-function mutation causes hyperphosphatemic tumoral calcinosis [249-252]. It is thought that in addition to causing these conditions through dysregulation of phosphate levels, *Fgf23* could directly regulate bone remodelling as well; the FGF23 receptors, FGFR1, FGFR2 and FGFR3, are expressed by osteoblasts and either transfection of osteoblasts with human *FGF23* or treatment with FGF23 protein severely inhibits osteogenesis and bone mineralisation *in vitro* [253, 254]. However, the precise mechanism behind this *Fgf23*-mediated osteoblast regulation is not fully understood. *Mepe* is another gene that holds great importance over osteocyte-mediated skeletal regulation. The gene is severely upregulated in human hypophosphatemic osteomalacia and mice lacking *Mepe* develop a severe high bone mass phenotype [255, 256]. Although the precise function of *Mepe* is not well understood, it

is highly expressed by osteocytes and its protein product has been found to be a component of the mineralised bone matrix within which osteocytes are embedded [257]. Due to the upregulation of *MEPE* in hypophosphatemic osteomalacia, it is perhaps unsurprising that MEPE serum levels have been found to correlate closely with bone mineral density (BMD) and serum phosphorus levels [258]. Osteocytes may therefore act through *Mepe* to regulate BMD and phosphate levels independently of *Fgf23*. A 23-amino acid fragment of human MEPE is currently undergoing clinical trials in regard to the ability of the fragment to limit the abnormal bone remodelling that occurs in OA patients [259, 260]. There may therefore be potential to ameliorate bone-related diseases through the exploitation of these lesser-known osteocyte regulatory pathways.

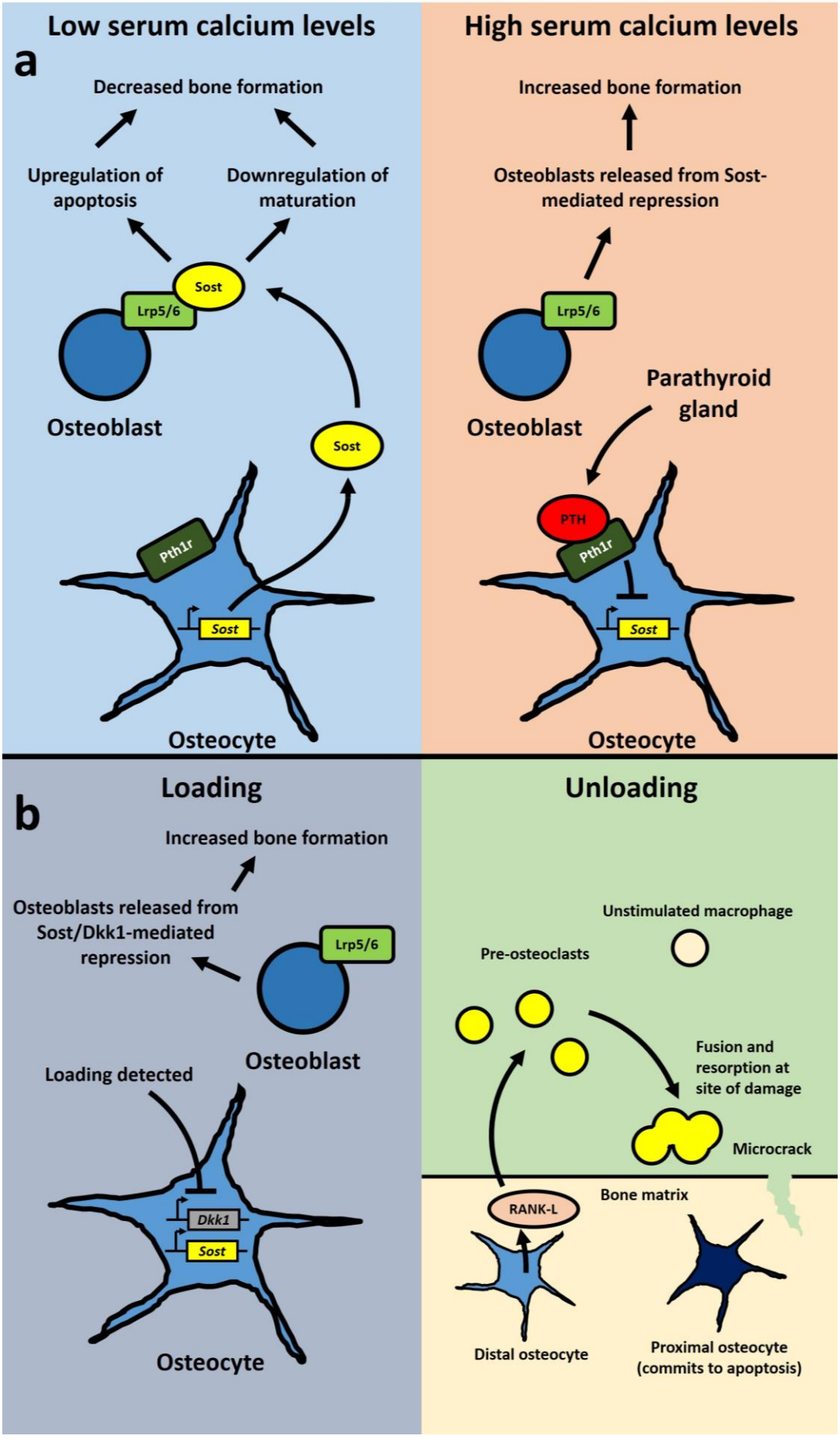
Low serum calcium levels
a
Decreased bone formation
Upregulation of apoptosis
Downregulation of maturation
Sost
Lrp5/6
Osteoblast
Sost
Pth1r
Sost
Osteocyte
High serum calcium levels
Increased bone formation
Osteoblasts released from Sost-mediated repression
Lrp5/6
Parathyroid gland
Osteoblast
PTH
Pth1r
Sost
Osteocyte
b
Loading
Increased bone formation
Osteoblasts released from Sost/Dkk1-mediated repression
Lrp5/6
Osteoblast
Loading detected
Dkk1
Sost
Osteocyte
Unloading
Unstimulated macrophage
Pre-osteoclasts
Fusion and resorption at site of damage
Microcrack
Bone matrix
RANK-L
Distal osteocyte
Proximal osteocyte (commits to apoptosis)

Figure 1.9 - Osteocytes can regulate the balance of bone remodelling in response to circulating calcium levels and mechanical loading. (**a**) In low serum calcium conditions, and therefore high bone formation rate, the gene encoding sclerostin, *Sost*, is expressed at high levels in osteocytes and binds to the Lrp5/6 receptor on osteoblasts. This interaction antagonises the Wnt signalling pathway, resulting in upregulation of osteoblast apoptosis and downregulation of osteogenesis, which in combination leads to a decreased rate of bone formation. Under high serum calcium conditions, and therefore low bone formation rates, parathyroid hormone (PTH) is released from the parathyroid gland and localises to osteocytes in bone, binding to the Pth1r receptor. This interaction inhibits the expression of *Sost*, thus releasing osteoblasts from their repression and therefore upregulating the rate of bone formation. (**b**) In response to mechanical loading, osteocytes repress *Sost* and *Dkk1*, releasing osteoblasts from Wnt signalling repression and thus increasing bone formation rate. In response to unloading, osteocytes proximal to points of bone microdamage undergo apoptosis, whereas distal osteocytes produce higher levels of RANK-L, stimulating fusion of pre-osteoclasts and recruitment to sites of microdamage, which therefore require bone remodelling.

1.4.5 *Diseases of bone remodelling*

Bone remodelling is a crucial process, responsible for the resorption and reformation of approximately one tenth of the human skeleton each year [261]. Therefore, it is unsurprising that dysregulation of the processes involved can result in severe diseases. In general, bone remodelling diseases are the result of an imbalance in the bone remodelling cycle, meaning that there is an upregulation of either osteoblast-mediated bone formation or osteoclast-mediated bone resorption, without being compensated for by the other. One of the most well-known diseases of bone remodelling is osteoporosis, which results from a relative increase in osteoclast activity, leading to severely weakened bone and an increased risk of fracture [262, 263]. Osteoporosis-related bone fracture is remarkably common, especially in the elderly population; approximately 1.5 million and 200,000 osteoporosis-related fractures are reported per year in the USA and UK, respectively [264, 265]. Diseases that increase relative osteoblast activity, rather than osteoclast activity, broadly have the opposite effect to that of osteoporosis, by increasing bone density, and are referred to in general as high bone mass diseases, or in particularly severe cases, osteopetrosis. Osteopetrotic diseases are far rarer

than those causing reduced bone mass such as osteoporosis, and although it is difficult to estimate overall osteopetrosis incidence due to the heterogeneous nature of the term, approximately 4 births per million inherit autosomal recessive forms of osteopetrosis and autosomal dominant osteopetrosis occurs in roughly 20 births per million [266, 267]. Autosomal recessive forms of osteopetrosis are more severe in general, emerging early in sufferers and causing many issues in growth and development; for example, craniofacial abnormalities caused by autosomal recessive osteopetrosis can severely impact neurological development and excess bone formation can supress haematopoiesis, therefore resulting in deficiency of blood cells, which can be fatal [268, 269]. Autosomal dominant osteopetrosis is in general less severe, although still increases fracture risk and incidence of OA, in addition to loss of hearing and sight due to suppression of the cranial nerve by excess bone in around 1 in every 20 autosomal dominant osteopetrosis sufferers [266, 270, 271]. At a cellular level, the cause of the increased relative osteoblast activity appears to not in fact be from upregulation of osteoblasts themselves, but instead from downregulation of osteoclasts; several genes that are important in the haematopoietic system, osteoclastogenesis and osteoclastic resorption (*CALDAGGEF1*, *CTSK*, *TNFRSF11A* and *TNFSF11*) have been implicated in human osteopetrosis, and mice lacking functional M-CSF, which is key for osteoclastogenesis, recapitulate the osteopetrotic phenotype [272-277].

Some bone remodelling diseases do not result from an increase in the activity of any one bone cell, but instead from increased overall bone turnover. Paget's disease is one such condition, producing disorganised bone microstructure due to rapid turnover, so reducing mechanical bone strength and increasing fracture risk. The disease is relatively common in the elderly population, estimated to affect between 1 and 2% of Caucasian adults over the age of 55, with the UK showing the highest prevalence worldwide [278, 279]. Several genes have been implicated in Paget's disease, including *SQSTM1* and *TNFRSF11A* [280-282], both of which are key in osteoclastogenesis and osteoclast maturation, therefore implying that through such genes, Paget's disease upregulates osteoclast activity, but does not uncouple osteoclast and osteoblast activity from one another, therefore resulting in the observed increased overall bone turnover.

1.4.6 *Pharmaceuticals in osteoporosis*

As one of the most prevalent bone disorders [264, 265], osteoporosis has presented an important challenge in identifying pharmaceuticals to prevent or minimise the impact of the

disease. Initially, most treatments for osteoporosis consisted of inhibition of bone resorption rather than upregulation of bone formation, such as with denosumab or treatment with bisphosphonates [283]. Over the past few decades, several anabolic pharmaceuticals have emerged. Teriparatide was the first bone formation-inducing pharmaceutical to be approved by the FDA, consisting of a 34 amino acid fragment of PTH. Upon subcutaneous injection, teriparatide increases the differentiation of osteoblast precursor cells into mature osteoblasts, thus increasing bone formation [284]. In contrast to the solely anabolic effects of teriparatide, romosozumab both enhances osteoblastic bone formation in addition to inhibiting osteoclast-mediated bone resorption. Romosozumab is a sclerostin antibody, such that treatment with it reduces the sclerostin-mediated negative regulation of osteoblast activity at the same time as inhibiting bone resorption. However, the potency of romosozumab decreases over time [285, 286]. There is therefore still a requirement for a pharmaceutical osteoporosis treatment which can be used for an extended period of time whilst also possessing the wide-reaching impact of romosozumab.

There is great interest in the use of miRNAs as pharmaceutical targets for disease treatment [287], and as such individual miRNAs could offer potential for osteoporosis treatment. For example, miR-182 is a miRNA which regulates osteoclastogenesis in mice. Upon inhibition of miR-182, bone loss is severely minimised in murine models of arthritis and osteoporosis [288]. Despite the promise of such RNA therapies and recent advancements in enhancing RNA stability for delivery into mammalian systems [289, 290], translation into humans is challenging; although it has been shown that the effects of treatment with small RNAs can be long-lasting [291], it is unknown how many off-target effects may be occurring upon treatment. For example, if one miRNA is able to target several different biological pathways, is it justifiable to assume that only the single intended target pathway is being affected? If not, then any number of unintended off-target effects could result from the treatment. This and accumulation of the therapeutic molecules in unintended tissues are at present the major concern of utilising small RNAs for pharmaceutical therapies [292], although specific delivery into target cells or tissues using virus- and nanoparticle-based delivery systems [293, 294] should reduce the risk of both of these issues. Therefore, although not currently commonplace, the utilisation of miRNAs and other small RNA molecules in the treatment of conditions such as osteoporosis is expected to become increasingly prevalent within the next few decades.

1.4.7 *microRNAs in bone remodelling*

miRNAs play a large role in the processes involved in bone remodelling; to date, more than 80 miRNAs have been reported to affect either osteogenesis, osteoclastogenesis or mediation of these processes by osteocytes [295]. Due to the complex networks allowing these three processes to communicate, a single miRNA knockout can have large implications on the underlying balance between bone formation and resorption. For example, the miR-185-null mouse exhibits dramatically increased bone formation due to dysregulation of the miR-185 target gene *Bgn*, which encodes biglycan, an important skeletal proteoglycan [296, 297]. Consequently, upregulation of *Bgn* results in increased osteogenesis due to Bgn-mediated enhancement of the key bone morphogenetic protein (BMP) Bmp2 [298]. Other miRNAs target components of bone remodelling directly, such as the miR-135a-5p-mediated repression of *RUNX2*, the central transcription factor in osteogenesis [299, 300], in order to downregulate the process of osteogenesis overall. miR-23a-5p, miR-137-3p and miR-155 have all also been found to directly target *RUNX2*, and therefore act as repressors of osteogenesis [301-303]. In addition to *RUNX2*, both miR-155 and miR-137-3p also target other genes involved in osteogenesis; miR-155 targets bone morphogenetic protein receptor 2 (encoded by *BMPR2*), a key component of the BMP signalling pathway, and miR-137-3p targets *CXCL12*, a purported regulator of the balance between osteogenesis and adipogenesis in differentiating MSCs [301, 302, 304]. Interestingly, the cluster from which miR-23a is expressed, known as the miR-23a ~ 27a ~ 24–22 cluster (miR-23aC), has also been implicated as a regulator of osteocytogenesis. It achieves this by the targeting of *Prdm16* by miR-27a-3p, which is also located in miR-23aC. *Prdm16* is a repressor of *Sost*, and therefore by repressing *Prdm16*, the miR-23aC enhances *Sost* expression and through this mechanism also enhances osteocytogenesis [305, 306].

Many miRNAs modulate the balance between bone formation and resorption by targeting genes important in osteoclastogenesis rather than in osteogenesis. The molecular components responsible for osteoclastogenesis upon binding of RANK-L are common direct targets of osteoclast-modulating miRNAs; miR-124 targets *NFATc1*, the transcription factor responsible for activation of osteoclastogenic genes, whereas miR-125a and miR-146a both target *TRAF6*, which is responsible for transduction of the RANK-RANK-L binding signal to stimulate the activity of *NFATc1* [307-311]. miRNAs have also been identified which directly target the gene encoding the RANK receptor, *TNFRSF11A*. miR-144-3p and miR-503 are two

such miRNAs, and through this direct repression of *TNFRSF11A* osteoclastogenesis can be severely attenuated, due to dramatically reduced levels of RANK-RANK-L binding in pre-osteoclasts and therefore reduced stimulation of the *TRAF*6-*NFATc1* signal transduction pathway [312, 313]. In pre-osteoclasts where this initial stimulation and transcriptional activation is allowed to proceed, the next key step in osteoclast maturation is the fusion of up to several hundred pre-osteoclasts to form a single multinucleate resorption-capable osteoclast. It is therefore unsurprising that the key gene in osteoclastogenic fusion, *DCSTAMP* [207], is also targeted by miRNAs in order to regulate maturation; miR-7b and miR-30a both directly target *DCSTAMP*, thus attenuating the osteoclast maturation process [314, 315].

These miRNA-mediated regulations highlight how essential the regulation of each individual bone cell type is on the bone remodelling network as a whole, and how the dysregulation of one miRNA could have a severe impact on the balance between bone formation and resorption.

1.4.8 *miR-324 in bone remodelling*

miR-324 may play a regulatory role in bone remodelling pathways. Significant positive correlations have been identified in humans between the abundance of miR-324-3p in serum and bone mineral density, mineral apposition rate, bone formation rate and mineralised bone surface, in addition to a significant negative correlation between serum abundance and cortical porosity [316, 317]. A decrease in miR-324-3p serum levels has also been reported in patients with osteoporotic fractures, although this did not achieve statistical significance [318]. It should however be noted that the levels of miR-324 in the serum is not necessarily representative of the levels experienced intracellularly by the relevant cells. Furthermore, an *in vitro* study using murine C3H10T1/2 cells, an MSC-like line, revealed that addition of miR-324-5p was able to reduce osteogenesis, both in terms of alizarin red-S staining and alkaline phosphatase level, which were reduced by approximately 30% and 50%, respectively [151]. Contrary to this, miR-324 has also been reported to enhance osteogenesis; Liang et al. (2021) recently reported that miR-324 is exported from osteoclasts in vesicles and transported to osteoblasts, in order to upregulate osteogenesis and thus couple bone formation and resorption [319]. The results of these studies imply that both arms of miR-324 may play a role in the activity of one or more of the cells involved in bone remodelling. Despite the fact that an in vivo knockout model will not enable a distinction between the effect of lacking one miR-

324 arm from the other, and the differential roles of miR-324 highlight the necessity for an *in vivo* knockout model of miR-324 to fully elucidate its function.

1.5 Aims and hypotheses

To summarise, miR-324 is a miRNA that may play important roles in multiple biological pathways and conditions, including OA and epilepsy. Despite the pathways and diseases associated with miR-324, no knockout model of miR-324 has been made according to published literature and therefore the activity of miR-324 *in vivo* is unknown. Prior to the initiation of this project, our group produced the first global miR-324-null mice, and due to the potential association of miR-324 with OA and epilepsy, I aim to use these miR-324-null mice to investigate whether key aspects of these conditions are altered relative to wild-type (WT) controls, by testing the following hypotheses:

- Knockout of *Mir324* in mice will affect cartilage maintenance, although it is unclear whether this effect will increase or decrease cartilage damage in miR-324-null mice relative to WT controls.
- miR-324-null mice will show a difference in thickness of subchondral bone; another key characteristic of OA alongside cartilage damage.
- miR-324-null mice will show differences in neurological activity, as has been previously suggested in the literature.

For all these areas of study I will endeavour to identify novel targets of miR-324 and suggest the biological pathways leading from direct target dysregulation to observed phenotypes in miR-324-null mice.

Chapter 2 - Materials and methods

2.1 Reagents

Reagent	Company	Catalogue number
Acetic acid	Sigma-Aldrich, USA	45754
Acid Phosphatase, Leukocyte (TRAP) Kit	Sigma-Aldrich, USA	387A
Agarose	Sigma-Aldrich, USA	A9539
Alamar Blue	Thermo Fisher Scientific, USA	DAL1025
Alizarin red-S	Sigma-Aldrich, USA	A5533
β-glycerophosphate	Sigma-Aldrich, USA	G9422
*Bam*HI restriction endonuclease	New England Biolabs	R0136S
Bovine serum albumin	Thermo Fisher Scientific, USA	23209
Bradford reagent	Sigma-Aldrich, USA	B6916
$CaCl_2 \cdot 2H_2O$	VWR International, USA	275844L
Calcein	Sigma-Aldrich, USA	C0875
Calf serum	Cytiva Life Sciences, USA	SH30073.02HI
Cells-to-cDNA II Kit	Thermo Fisher Scientific, USA	AM1722
Cetylpyridinium chloride	Sigma-Aldrich, USA	C0732
Collagenase Type I	Sigma-Aldrich, USA	SCR103
Dexamethasone	Sigma-Aldrich, USA	D4902
D-glucose	VWR International, USA	101176K
DharmaFECT 1 Transfection Reagent	Horizon Discovery, UK	T-2001
Diethanolamine	Sigma-Aldrich, USA	D8885
Dithiothreitol	Invitrogen, USA	D1532
dNTPs	Invitrogen, USA	10297018
DPX mountant	Sigma-Aldrich, USA	06522
Dulbecco's PBS	Gibco, USA	14190144
Dulbecco's Minimum Essential Medium (DMEM)	Gibco, USA	11995065
EcoMount	BioCare Medical, USA	EM897L
Ethanol	Sigma-Aldrich, USA	459836
Ethylenediaminetetraacetic acid	Sigma-Aldrich, USA	E9884
Fast Green FCF solution	Sigma-Aldrich, USA	F7258
Fast red-A	Advanced Cell Diagnostics, USA	324500
Fast red-B	Advanced Cell Diagnostics, USA	324500
Foetal bovine serum	Sigma-Aldrich, USA	F7524
Formalin solution, neutral buffered, 10%	Sigma-Aldrich, USA	HT501128
FuGENE® HD Transfection Reagent	Promega, USA	E2311
Glycerol	Sigma-Aldrich, USA	G5516
Glycine	Sigma-Aldrich, USA	G8898
Hanks' Balanced Salt Solution	Lonza, Switzerland	H6648
HCl	Sigma-Aldrich, USA	320331
Hoxa9 (NM_010456) Mouse Tagged ORF Clone	OriGene, USA	MR203609

ImmEdge hydrophobic barrier pen	Advanced Cell Diagnostics, USA	310018
Immobilon Western Chemiluminescent HRP Substrate	Merck Millipore, USA	WBKLS
In-Fusion HD cloning kit	Takara Bio, Japan	639650
Isopronanol	Sigma-Aldrich, USA	W292907
Kainate	Sigma-Aldrich, USA	K0250
KCl	VWR International, USA	101985M
Ketamine	Vetoquinol, France	
L-ascorbic acid	Sigma-Aldrich, USA	49752
L-glutamine	Sigma-Aldrich, USA	G8540
Marvel Original Dried Skimmed Milk Powder	Premier Foods, UK	
Mayer's haemotoxylin staining solution	Sigma-Aldrich, USA	MHS80
Methanol	Sigma-Aldrich, USA	34860
$MgCl_2$	Sigma-Aldrich, USA	M2670
$MgSO_4$	Sigma-Aldrich, USA	M7506-M
Minimum Essential Medium α (α-MEM)	Gibco, USA	12571063
miRIDIAN microRNA Hairpin Inhibitor Negative Control #1	Horizon Discovery, UK	IN-001005-01
miRIDIAN microRNA Mimic Negative Control #2	Horizon Discovery, UK	CN-002000-01
miRIDIAN microRNA mmu-mir-324-3p Hairpin Inhibitor	Horizon Discovery, UK	IH-310538-08
miRIDIAN microRNA mmu-mir-324-3p Mimic	Horizon Discovery, UK	C-310538-07
miRIDIAN microRNA mmu-mir-324-5p Hairpin Inhibitor	Horizon Discovery, UK	IH-310537-08
miRIDIAN microRNA mmu-mir-324-5p Mimic	Horizon Discovery, UK	C-310537-07
miRNAscope HD Assay Red	Advanced Cell Diagnostics, USA	324500
*mir*Vana miRNA Isolation Kit	Thermo Fisher Scientific, USA	AM1560
M-MLV Reverse Transcriptase and 5x First-strand buffer	Invitrogen, USA	28025013
NaCl	Sigma-Aldrich, USA	S7653
NaF	Sigma-Aldrich, USA	201154
NaH_2PO_4	VWR International, USA	307164T
$NaHCO_3$	Tocris, UK	3152
Nuclease-free water	Sigma-Aldrich, USA	W4502
NucleoSpin Gel and PCR Clean-up Kit	Macherey-Nagel, Germany	740609.10
Oil red-O	Sigma-Aldrich, USA	O0625
PageRuler™ Prestained Protein Ladder	Thermo Fisher Scientific, USA	26616
Paranitrophenyl phosphate	Thermo Fisher Scientific, USA	34045
pDN6	Invitrogen, USA	N8080127
Penicillin-Streptomycin	Sigma-Aldrich, USA	P4333
Phire Hot Start II DNA Polymerase	Thermo Fisher Scientific, USA	F122S

Phire reaction buffer	Thermo Fisher Scientific, USA	F524L
Phire Tissue Direct PCR Master Mix	Thermo Fisher Scientific, USA	F170S
pmirGLO Dual-Luciferase miRNA Target Expression Vector	Promega, USA	E1330
Polyvinylidene fluoride (PVDF) membrane	Thermo Fisher Scientific, USA	88518
Protease inhibitor cocktail tablets	Roche, Switzerland	04693132001
PureLink Genomic DNA Mini Kit	Thermo Fisher Scientific, USA	K182002
QIAzol Lysis Reagent	Qiagen, Germany	79306
QuikChange Lightning Site-Directed Mutagenesis Kit	Agilent, USA	210519
Recombinant Murine M-CSF	Peprotech, UK	315-02
Recombinant Murine SDF-1α (Cxcl12-α)	Peprotech, UK	250-20A
Recombinant Murine sRANK Ligand (CHO derived)	Peprotech, UK	315-11C
RNAscope® 1X Target Retrieval Reagent	Advanced Cell Diagnostics, USA	324500
RNAscope® Hydrogen Peroxide	Advanced Cell Diagnostics, USA	324500
RNAscope® Protease III	Advanced Cell Diagnostics, USA	324500
RNAscope® Wash Buffer	Advanced Cell Diagnostics, USA	324500
Runx2 (NM_001146038) Mouse Tagged ORF Clone	OriGene, USA	MR227321
Safranin O solution	Sigma-Aldrich, USA	HT90432
Samd5 (NM_177271) Mouse Tagged ORF Clone	OriGene, USA	MR216293
Scott's Tap Water Substitute Concentrate	Sigma-Aldrich, USA	S5134
Sodium dodecyl sulfate	Sigma-Aldrich, USA	L3771
Sucrose	Sigma-Aldrich, USA	16104
Superfrost Plus slides	Thermo Fisher Scientific, USA	10149870
System III Biopsy Cassettes	CellPath, UK	EAI-07
Thin Wall Borosilicate capiliary Tubes	Harvard Apparatus, UK	G120TF
Tris base	Sigma-Aldrich, USA	TRIS-RO
Tris-Borate-EDTA Buffer	BioBasic, Canada	A0026
TritonX	Sigma-Aldrich, USA	T8787
TruSeq Stranded mRNA sample preparation kit	Illumina, USA	20020594
Tween-20	Sigma-Aldrich, USA	8.17072
Weigert's Iron Haematoxylin solution	Sigma-Aldrich, USA	HT1079
*Xho*I restriction endonuclease	New England Biolabs, USA	R0146S
Xylazine	AnimalCare, UK	XVD704

2.2 Methods

2.2.1 *miR-324-null mouse models*

All animal experiments were performed under licenses granted from the Home Office (United Kingdom) in accordance with the guidelines and regulations for the care and use of laboratory animals outlined by the Animals (Scientific Procedures) Act 1986 according to Directive 2010/63/EU of the European Parliament, and conducted according to protocols approved by the Animal Ethics Committee of Newcastle University and the Home Office, United Kingdom. Breeding and subsequent phenotyping was performed under licence P8A8B649A. Initial deletion of the *Mir324* locus, injection into the cytoplasm of donor mouse zygotes and transfer into recipient foster mothers was performed prior to the initiation of this project, as previously described [320]. CRISPR/Cas9 guide RNAs (crRNAs) were designed using CHOPCHOP [321, 322]. crRNAs linked with TRACR (sgRNA) were amplified by PCR with a pLKO vector (Addgene_52628) as template, with a T7 TRACR R primer (5'-AAAAGCACCGACTCGGTGCC-3') in combination with a 5´ PCR primer that included a T7 sequence and specific crRNA (shown in bold; 5'-atgcatTTAATACGACTCACTATAgGGAGGCTTCCGACTTTGTAAAGGTTTTAGAGCTAGAAAT-3'; 5'-atgcatTTAATACGACTCACTATAgGGAGCTGGAGACCCACTGCCCCGTTTTAGAGCTAGAAAT-3').

This was converted to RNA using the MEGAshortscript T7 kit (Thermo Fisher Scientific). sgRNAs (50 ng/ml each) were mixed with recombinant Cas9 (ToolGen, CamBioScience Limited) and injected into the cytoplasm of donor mouse zygotes and transferred into recipient foster mothers. This resulted in a 133 bp deletion at the Mir324 locus. Mixed C57BL/6 and CBA/ca F_0 mice were backcrossed onto C57BL/6J and heterozygous animals crossed three times to eventually generate WT and miR-324-null lines. These lines were crossed to produce heterozygous mice every 4 generations in order to limit genetic drift between WT and miR-324-null lines and refresh the lines. miR-324-null mice harboured a 133bp deletion at the *Mir324* locus, which was confirmed by ear-notch PCR and Sanger sequencing (Forward primer: 5'-GTGCTGATCTACTCCTCCAACC-3'; reverse primer: 5'-AAATTCACAACTTTGGGGTGAT-3'). All experimentation was performed under licences P6EE54A50 or P8A8B649A. Throughout this project, several time points and both sexes of WT and miR-324-null animals were utilised for experiments. Experiments were always controlled with both miR-324-null and WT mice of the same age and sex, but limitations in mouse breeding as a result of the SARS-CoV-19 pandemic prevented additional time points from

being added to some experiments. For the same reason, sample numbers, which are stated throughout this thesis for each experiment, were also limited for some experiments.

2.2.2 *Extraction of DNA from murine tissues and cells*

Genomic DNA was extracted from murine ear notches (for genotyping purposes) using the Phire Tissue Direct PCR Master Mix (Thermo Fisher Scientific), and from murine C3H10T1/2 cells (for use as a polymerase chain reaction (PCR) template) using the PureLink Genomic DNA Mini Kit (Thermo Fisher Scientific), following the manufacturer's protocol for both methodologies.

2.2.3 *PCR amplification and agarose gels*

Phire Hot Start II DNA Polymerase (Thermo Fisher Scientific) was utilised to amplify specific regions of genomic DNA or complementary DNA (cDNA), following the manufacturer's protocol. The following components were added to each PCR reaction: 4 µl of 5x Phire reaction buffer, 0.2 mM dNTPs (final concentration), 0.4 µl of Phire Hot Start II DNA Polymerase (all Thermo Fisher Scientific), 3.75 ng μl^{-1} of genomic DNA (final concentration, or 2.5 µl of cDNA), 0.5 mM (final concentration) each of forward and reverse primer and nuclease-free water to a total volume of 20 µl. The reaction mixture was then heated to 98°C for 30 seconds, before undergoing 35 cycles of the following: 98°C for 5 seconds, optimum annealing temperature for 5 seconds and 72°C for 20 seconds. Subsequently, the mixture was heated to 72°C for 1 minute, before being cooled to 4°C. The optimum annealing temperature for each reaction was determined by undertaking each PCR amplification at a range of temperatures between 57°C and 70°C and identifying the temperature in which a band of the desired size was identified most clearly upon gel electrophoresis in a Tris-Borate-EDTA (TBE) 1.5% (w/v) agarose gel, run at 80 V for approximately 1 hour.

2.2.4 *Extraction of RNA from murine tissues and cells*

RNA was extracted from murine tissues and cells using the *mir*Vana miRNA Isolation Kit (Thermo Fisher Scientific), following the manufacturer's protocol to isolate total RNA. For RNA extraction from C3H10T1/2 and MLO-Y4 cells in 24-well plates or larger, QIAzol Lysis Reagent (Qiagen) was used, following standard protocols. A NanoDrop™ 1000 Spectrophotometer (Thermo Fisher Scientific) was used to measure the RNA concentration and purity. For cells plated in 96- or 48-well plates, the Cells-to-cDNA II Kit (Thermo Fisher Scientific) was utilised to isolate RNA and subsequently reverse transcribe this to cDNA.

2.2.5 *Reverse transcription*

cDNA was reverse transcribed from total RNA using M-MLV Reverse Transcriptase (Invitrogen), following the manufacturer's protocol for each gene of interest (GOI). Specifically, 3 µl of 10 mM dNTPs and 1 µl of 1 µg/µl of random hexamers (pDN6; both from Invitrogen) was added to 8 µl of RNA (normalised to equal concentrations between samples taken from the same experiment) and heated to 70°C for 5 minutes, before being cooled to 4°C. Subsequently, the following was also added to each sample: 4 µl of 5x First strand buffer, 2 µl of 0.1 M Dithiothreitol (DTT), 0.5 µl of M-MLV Reverse Transcriptase and 1.5 µl of nuclease-free water (all from Invitrogen). The samples were subsequently heated to 37°C for 50 minutes, then 75°C for 15 minutes and finally cooled at 4°C. Reverse transcription of *Mir324* and the housekeeping gene *U6* were undertaken essentially as previously described [151].

2.2.6 *Real-time reverse transcriptase quantitative PCR (RT-qPCR)*

cDNA was amplified using TaqMan Fast Advanced Master Mix (Applied Biosystems). GOI mRNA levels were quantified using a Quant Studio 3 (Thermo Fisher Scientific), using specific primers and Universal Probe Library (UPL; Roche Molecular Systems) probes (Appendix A) to measure the amplification of individual GOIs. Assays for several genes were ordered, where a UPL-based assay was not possible, including *Mir324-5p*, *-3p*, *U6*, and *18S*. Each sample was heated to 95°C for 20 seconds, before undergoing 40 cycles (or 50 cycles for very lowly expressed genes) of heating to 95°C for 1 second and 60°C for 20 seconds. Data was analysed using the ThermoFisher Cloud Design and Analysis software (Thermo Fisher Scientific). The ΔCt method of normalisation was used to account for any differences between the samples, using *U6* to normalise *Mir324* levels and either *Ndufa2* or *18S* (in brain and bone experiments, respectively), both of which are housekeeping genes, to normalise every other gene tested. *U6* is a highly-expressed non-coding RNA housekeeping gene, therefore making it an acceptable control for other non-coding RNAs, such as miRNAs. *Ndufa2* was selected for use in brain tissues as the housekeeping gene which had the lowest magnitude $\log_2$(fold-change) and which had an adjusted p-value of > 0.05 in the hippocampal and cortical RNA-sequencing experiments undertaken in this project. Therefore, the normalised Cts (cycle thresholds) were calculated as follows: $2^{-(Ct_{GOI}-Ct_{Normaliser})}$. The normalised Cts measured in miR-324-null samples were compared against those measured in WT samples to assess whether there was any statistically significant difference for each GOI, utilising Student's two-tailed *t*-tests to compute p-values.

2.2.7 *Protein extraction*

Murine tissue samples were ground into a fine powder on dry ice using a disposable pestle, before being resuspended in 150µl of a 1% (v/v) TritonX lysis buffer, which contained the following components: 50 mM Tris base, 150 mM NaCl, 5 mM NaF, 1 mM Ethylenediaminetetraacetic acid (EDTA), 1% (v/v) TritonX, 10% (v/v) glycerol (all Sigma-Aldrich) and 1 Protease inhibitor cocktail tablet (Roche). Prior to use, the buffer was made up to 50 ml with deionised water and the pH adjusted to 7.5 using dilute HCl. Cells were scraped from plates and also resuspended in the same TritonX-based lysis buffer. Samples were subsequently kept on ice for 25 minutes, before undergoing centrifugation at 13,000x*g* for 10 minutes at 4°C. The supernatant was quantified using a Bradford Assay, which consisted of adding 3 µl of protein lysate to 150 µl of Bradford reagent (Sigma-Aldrich) and measuring the absorbance at 595 nm using a Varioskan LUX Multimode Microplate Reader (Thermo Fisher Scientific). Increasing concentrations of Bovine serum albumin (BSA; Thermo Fisher Scientific) from 0 to 4 mg/ml, with 150 µl of Bradford reagent added to each, were also measured on the same plate, so as to accurately determine the protein lysate concentration from a calibration curve. Protein lysate was subsequently frozen at -80°C for storage.

2.2.8 *Western blotting*

10 µg of each sample was heated to 105°C for 5 minutes to denature the protein, before being loaded onto a 10% (w/v) Sodium dodecyl sulfate (SDS)-PAGE gel and separated using electrophoresis for approximately 1 hour at 140 V, alongside a PageRuler™ Prestained Protein Ladder (ThermoFisher Scientific). Protein separation was undertaken in a running buffer, composed of the following: 250 mM Tris base, 1920 mM glycine and 1% (v/v) SDS (both Sigma-Aldrich). Protein was subsequently transferred to a Polyvinylidene fluoride (PVDF) membrane using electroblotting for 90 minutes at 1 mA/cm^2, in transfer buffer, composed of the following: 48 mM Tris base, 39 mM glycine, 0.0325% (v/v) SDS and 20% (v/v) methanol. Subsequently, the membrane was blocked for 1 hour in 5% (w/v) milk, diluted in Tris-buffered saline with Tween-20 Detergent (TBST), consisting of the following: 10 mM Tris base, 150 mM NaCl and 0.1% (v/v) Tween-20 (Sigma-Aldrich). Following blocking, the membrane was incubated overnight at 4°C with the primary antibody (Table 2.1). Band visualisation was undertaken using HRP-conjugated secondary antibodies (Dako; used at 1:1000 dilution) and Immobilon Western Chemiluminescent HRP Substrate (Merck Millipore) and subsequent quantification was performed using Fiji [323].

Protein	Dilution/concentration	Host animal	Purchased from
Acadvl	1:500	Rabbit	Abcam, catalogue number ab155138
β-tubulin	1:1000	Mouse	Sigma-Aldrich, catalogue number T8328
CD300f/LMIR3	0.2 µg/mL	Goat	R&D Systems, catalogue number AF2788
Dvl2	1:500	Rabbit	LifeSpan BioSciences, catalogue number LS-C383215-50
FLAG (Myc-DDK)	1:2000	Mouse	Cell Signalling Technology, catalogue number 2276S
GAPDH	1:40,000	Mouse	Sigma-Aldrich, catalogue number MAB374
Runx2	1:500	Rabbit	Cell Signalling Technology, catalogue number 12556S (kindly donated by Dr Sarah Rice)
Suox	1:200	Rabbit	Invitrogen, catalogue number PA5-21705

Table 2.1 - Primary antibodies used for western blotting.

2.2.9 *miR-324-5p in situ hybridisation*

Murine brains were fixed in 10% (w/v) neutral-buffered formalin (Sigma-Aldrich) overnight before being washed twice with distilled water and stored in System III Biopsy Cassettes (CellPath) in 70% (v/v) ethanol. The samples were dehydrated in a tissue processor using a series of ethanol concentrations (70%, 90%, 95%, 100%, 100% and 100%), each for 45 minutes and subsequently cleared with xylene, before being embedded in paraffin blocks. A Microm HM355S Rotary Microtome (Thermo Fisher Scientific) was used to cut 5 µm coronal sections from the samples, taken at approximately -5 mm along the DV axis relative to the bregma [324, 325]. The miRNAscope HD Assay Red [326] (Advanced Cell Diagnostics, as used by Gan et al. [327]) was subsequently used to investigate levels of miR-324-5p. This consisted of the collection of tissue sections onto Superfrost Plus slides (Thermo Fisher Scientific) before being deparaffinised using xylene. Subsequently, 4 drops of RNAscope® Hydrogen Peroxide (Advanced Cell Diagnostics) were added to each slide and incubated at room temperature for 10 minutes, before being washed 3 times in distilled water. Slides were then inserted into distilled water in a HybEZ™ Oven (Advanced Cell Diagnostics) with a temperature set to ≥99°C

for 10 seconds, before being transferred to a container of RNAscope® 1X Target Retrieval Reagent (Advanced Cell Diagnostics) for 15 minutes, also in the HybEZ™ Oven. After this, slides were washed in distilled water and dried in a 60°C incubator. A hydrophobic barrier was subsequently drawn around each tissue section, using an ImmEdge hydrophobic barrier pen (Advanced Cell Diagnostics), and after leaving the barrier to dry, 5 drops of RNAscope® Protease III (Advanced Cell Diagnostics) were added and incubated for 30 minutes at 40°C. Slides were subsequently washed twice in distilled water. In order to detect miR-324-5p (using a custom probe) and *U6* (using the miRNAscope positive control probe), 4 drops of each probe were added to separate samples and incubated at 40°C for 2 hours, after which the slides were washed twice in 1x Wash buffer (Advanced Cell Diagnostics). A scrambled probe (miRNAScope negative control) was also used to confirm the assay was working. Subsequently, 6 sequential amplification steps using 6 different probes were undertaken for the signal, using the following incubation settings: 30 minutes at 40°C, 15 minutes at 40°C, 30 minutes at 40°C, 15 minutes at 40°C, 30 minutes at room temperature and finally 15 minutes at room temperature. Slides were washed twice between each signal amplification step. A solution of Fast red-A and Fast red-B (both Advanced Cell Diagnostics) was prepared (in a 60:1 ratio) and 100 µl of the solution was added to each tissue section. The slides were then incubated for 10 minutes at room temperature and washed twice with distilled water, before being counterstained for 1 second at room temperature using 50% (v/v) Mayer's haemotoxylin staining solution (Sigma-Aldrich). The slides were then washed 5 times in distilled water and the nuclei blued using Scott's Tap Water Substitute Concentrate (Sigma-Aldrich), before again washing in distilled water 5 times. Slides were subsequently dried at 60°C for 15 minutes before being mounted using EcoMount (BioCare Medical). Following mounting, samples were imaged using an Axiovert 200 Inverted Microscope (Zeiss). As previously mentioned, the SARS-CoV-19 pandemic severely limited animal breeding. Therefore, 13.5-month-old were used for this experiment as none aside from these were available at the time and these were required for another experiment at the same time.

2.2.10 *Hippocampus slice preparation*

Female miR-324-null and WT mice (aged 5 months) were anaesthetised by inhalation of 100% isoflurane, before intramuscular injections with ketamine (≥ 100 mg/kg, Vetoquinol) and xylazine (≥ 10 mg/kg, AnimalCare). After the pedal withdrawal reflex had ceased, the mice underwent a transcardial perfusion with 30 ml of sucrose artificial cerebrospinal fluid (aCSF),

via injection into the left ventricle, undertaken by Dr Tamara Mondebadze. The sucrose aCSF was composed of the following: 204.5 mM sucrose, 3.0 mM KCl, 1.25 mM NaH_2PO_4, 2.0 mM $MgSO_4$, 2.0 mM $CaCl_2 \cdot 2H_2O$, 10.0 mM of D-glucose and 24.0 mM $NaHCO_3$ (all from Sigma-Aldrich). The brain was excised and 450 µm horizontal hippocampal sections were cut using a vibratome (Model 5100 mz, Campden Instruments), also undertaken by Dr Tamara Mondebadze. The overlying cortex was trimmed from around the hippocampus, before being placed in a holding chamber at room temperature at an interface between carbogen gas (5% CO_2 and 95% O_2) and aCSF (with sucrose replaced by 126 mM NaCl) for 1 hour. In order to avoid any confounding issues due to dorsal-ventral (DV) differences within the hippocampus [328-330] only slices from the central portion of the hippocampus (between -3.24 mm and -5.04 mm along the DV axis relative to the bregma) were used [324, 325].

2.2.11 *Electrophysiology data acquisition*

Extracellular recording electrodes with resistances of 2-5 mΩ were produced from glass capillary tubes (Thin Wall Borosilicate with filament; Harvard Apparatus) using a micropipette puller (Model P-97, Sutter), before being filled with aCSF using a MicroFil syringe. The hippocampal slices were held in the holding chamber for approximately 40 minutes, transferred to a recording chamber, maintained at 30-32°C, through which 100 ml of aCSF was continuously recycled. The slices were left to acclimatise for 15 minutes, before local field potentials (LFPs) were measured from the *stratum radiatum* layer of the CA3 region. The signal was amplified 10x by an AI-2010 differential amplifier (Axon Instruments) and background noise was minimised using a 50Hz HumBug noise eliminator (Quest Scientific). Neurolog external filters (Digitimer) were used to filter the signal at 1 Hz high-pass and 300 Hz low-pass, with a sampling rate of 5000 Hz, and an ITC-18 (NPI Electronic) was used to convert the analogue signal to digital. Spontaneous LFP activity was recorded for 30 minutes, before bath application of 50 nM kainate (KA) (Sigma-Aldrich). The resulting activity was recorded for a further 30 minutes, before the concentration of KA was increased every 30 minutes to 100 nM, 150 nM, 200 nM, 400 nM, 600 nM, 800 nM and finally 1 µM. Trace recordings were performed using Axograph X v1.7.2 (Axograph Scientific).

2.2.12 *Electrophysiology data analysis*

Power spectra were generated from the last minute at each KA concentration, using Axograph (Axograph Scientific). The peak frequency, peak amplitude and power area (from 15-48 Hz) of oscillations from each trace were measured and compared between genotypes. For some

slices at high KA concentrations, an additional faster frequency was observed in the power spectra in addition to the gamma peak. For the purposes of assessing differences in gamma band activity, only the lower gamma-frequency peak was measured. At each KA concentration, only slices showing clear gamma-frequency oscillations were included for analysis. The standard deviation (SD) of the amplitude for the final minute of each trace was also measured and Axograph was used to detect peaks in the LFP at least 5 SDs from the baseline of that trace. These peaks were defined as "spikes" as they occurred during clear gamma activity and were not full interictal discharges (IIDs). A proportion of events were identified manually as IIDs, which are established biomarkers of epilepsy and which result from imbalance in the excitation and inhibition in neural networks [331-333]. Additionally, in order to summarise the data, slices that showed any IIDs were classed as displaying interictal activity, and those showing no IIDs but a higher number of spikes than the mean + 2 SDs of WT slice spikes at each KA concentration, were classed as showing a high number of spikes. The remaining slices were classed as showing no abnormal activity in response to KA. Measurements were taken from 6 miR-324-null mice and 6 WT mice, and multiple slices were taken from each of these mice, giving an overall sample size of 32, consisting of 16 WT slices and 16 miR-324-null slices. Each slice was treated as one sample, due to the considerable variability in the power of oscillations. For each metric, two-way mixed ANOVA tests or variants were used to assess statistical significance of the effect of genotype and KA concentration. Where the data was not normally distributed, it was either $\log_{10}$ transformed or a two-way mixed ANOVA of ranks was used in order to satisfy statistical assumptions.

2.2.13 *Murine behavioural analysis*

In order to investigate behavioural differences between miR-324-null and WT mice, the MouseTrapp system [334] was utilised. Each mouse was placed alone into an acrylic cage on top of a tablet (on which the MouseTrapp software was installed) and monitored for 50 minutes whilst the MouseTrapp software recorded the number of touches, distance travelled and number of rears in each 30 second interval over the 50 minutes. In order to allow for increased stress at the start of each 50-minute recording, the first 10 minutes of data were omitted, allowing the mice to acclimatise to the new conditions. Each parameter was compared between genotypes after the experiment was completed. Two additional parameters were also created from the parameters automatically returned by the MouseTrapp software; the maximum number of rears for each mouse was taken as the

maximum number of rears in a 30 second interval for each mouse, and the mean step length was estimated by dividing the distance travelled in each 30 second interval by the number of touches in the same interval. The resulting mean step length value was then additionally divided by 4, to account for the four limbs for which touches were being detected. Despite the ease of use of the MouseTrapp system, it should be noted that there are several limitations of this system; although time is allowed at the start of each recording so as to limit stress of the animal, it is still likely that the animal will be in a heightened state of stress relative to being housed in its cage, in which other animals were also housed. Furthermore, the system does not contain any form of enrichment for the animals, and so any behaviours observed only in the presence of such equipment will not be observed through the MouseTrapp system. The statistical significance of each parameter between genotypes was assessed using Student's two-sided *t*-tests.

2.2.14 *RNA sequencing and analysis*

Prior to RNA sequencing (RNA-seq), RNA samples were purified using the DNA-free DNA Removal Kit (Invitrogen) to remove any DNA contamination. Sequencing libraries for osteoblasts, osteoclasts, bone marrow macrophages (BMMs), hippocampus and neocortex were prepared using the TruSeq Stranded mRNA sample preparation kit (Illumina) following the manufacturer's protocol and subsequent sequencing was performed on an Illumina NextSeq 500. Kallisto [335] was used for pseudo-alignment and quantification, against the mouse GRCh38 (release 92) transcriptome [336]. Mapped transcripts were converted to a gene level using Tximport [337] and DESeq2 [338] was used to calculate p-values and $\log_2$ fold-changes (logFC), using the Benjamini-Hochberg method to adjust for multiple testing. Integrated Genomics Viewer [339, 340] was used to produce sashimi plots for each tissue, in order to analyse whether any splicing variation occurred upon removal of *Mir324* at the *Acadvl* and *Dvl2* loci. Rank-rank hypogeometric overlap (RRHO) [341] of the RNA-seq results from the hippocampus and neocortex was carried out using the RRHO package in R [342], with the logFC of each gene used as the comparison statistic. Sample permutation p-values were also computed using the RRHO package, calculated using the sum of the signal from genes sharing similar logFC values in both hippocampus and neocortex RNA-seq results. Putative miR-324 target genes were identified by filtering initial RNA-seq results for genes that were upregulated in miR-324-null tissue and that were predicted to be targets of either miR-324-5p or miR-324-3p by the TargetScan 7.2 algorithm [5, 67]. For the hippocampal and neocortical

RNA-seq experiments, other relevant GOIs were identified by utilising the Disease Ontology (DO) [343], using the term "epilepsy syndrome" to filter for relevant genes, with murine genes first converted to their human homologues using the BiomaRt R package [344]. For all tissues, the DO was also used to test for enrichment in specific diseases, using a Kolmogorov-Smirnov test for significant enrichment with the GOseq R package [345]. Gene Ontology analysis was undertaken using the same methodology in order to identify pathways enriched in each RNA-seq experiment. For these enrichment analyses, differentially expressed genes were defined as those with adjusted p-values ≤ 0.05.

2.2.15 *Micro-computed tomography*

After mice were sacrificed by cervical dislocation, the right hind legs were collected, the skin removed, and fixed at room temperature overnight in 10% (w/v) neutral-buffered formalin (Sigma-Aldrich). Only hind legs were used so as to provide consistency between biological samples. The following day, legs were washed twice in 1x Dulbecco's phosphate-buffered saline (PBS; Gibco) and stored in 70% (v/v) ethanol at 4°C. A SkyScan 1272 (Bruker) was used to scan the bones. For cortical scans, a resolution of 2016 x 1344, a pixel size of 9.0 µm, an aluminium filter thickness of 0.5 mm and a rotation step of 0.5° was used, whereas a resolution of 4032 x 2688, a pixel size of 4.5 µm, an aluminium filter thickness of 0.5 mm and a rotation step of 0.3° was used for trabecular bone. NRecon (Bruker) was used to construct cross-sectional slices from the scanned images and DataViewer (Bruker) was used to produce 3D computational models from these cross-sections. CTAn (Bruker) was used to quantify metrics in miR-324-null and wild-type mice, essentially as previously described [346]. For trabecular tibial measurements, a volume of interest (VOI) encompassing the tibia exactly 90-990 µm below the tibial growth plate proximal to the knee joint was used, whereas for trabecular femoral measurements a VOI 90-990 µm above the femoral growth plate proximal to the knee joint were used. For measuring tibial cortical bone, a VOI positioned 450-1350 µm above the point at which the fibula and tibia merge was analysed, whereas for tibial femoral bone, a 900 µm VOI at the vertical midpoint of the femur was used for analysis. In order to test the amount of bowing in murine leg bones, the horizontal distance between the fibula and tibia at the midpoint of the tibia (calculated at the exact vertical midpoint between the tibial plateau and the point at which the fibula joins the tibia) was measured on the transaxial plane. Bone tissue mineral density (TMD) was calculated from cortical scans using CtAn

(Bruker), calibrated against phantom rods supplied by Bruker, with known calcium hydroxyapatite densities of 0.25 and 0.75 $g \cdot cm^{-3}$.

2.2.16 *Double-injection of alizarin red-S and calcein*

Mice underwent intraperitoneal injections of alizarin red-S (3 mg/ml, dissolved in 1.4% $NaHCO_3$, Sigma-Aldrich) in addition to a subsequent injection with calcein (2 mg/ml, dissolved in 1.4% $NaHCO_3$, Sigma-Aldrich) 6 days later. For each injection, the mouse was injected with 0.1 ml/10 g of mouse weight. Mice were subsequently housed for 24 hours before being sacrificed for tissue collection. Injections were undertaken by Hua Lin.

2.2.17 *Methyl methacrylate embedding, histology and histomorphometry*

After micro-computed tomography was used to scan murine hind legs, flesh was removed from the bones and the femur and tibia were separated. The tibiae were embedded in methyl methacrylate (MMA) and a tungsten steel knife on a motorised rotary microtome (Leica) was utilised to cut 5 µm sections from each MMA-embedded block. Sections were stained either with Goldner's Trichrome, in order to analyse osteoid, lipid droplets and osteocyte abundance, or counterstained with calcein blue and used to quantify the amount of bone formed between the lines corresponding to injections of alazarin red-S and calcein, essentially as previously described [346]. Sections stained with Goldner's Trichrome were visualised at 10X magnification, whereas those visualised for double-labelling analysis were visualised at 20X magnification. For both groups, images were captured using an Axioscan Z1 slide scanner (Zeiss). Sectioning and imaging were performed by Gemma Charlesworth and Amanda Prior. The OsteoidHisto and CalceinHisto open-source image analysis programs were utilised to analyse osteoid thickness in Goldner's Trichrome-stained sections and histomorphometric parameters in the other sections, respectively [347]. Fiji [323] was utilised to quantify osteocyte abundance within the same trabecular bone area detected by OsteoidHisto and this area was used to normalise osteocyte numbers. A mean average of 3 sections from each mouse was used to represent N = 1 for each mouse.

2.2.18 *Histopathological scoring of murine joints and assessment of cartilage damage*

The left hind legs of miR-324-null and WT mice were collected and stored overnight in 10% (w/v) neutral-buffered formalin (Sigma-Aldrich), before being washed twice with distilled water and subsequently decalcified using Formical-2000 (American MasterTech Scientific) for 16 hours on a rocker. The young mouse cohort (aged 6-months at time of sacrifice) underwent destabilisation of the medial meniscus (DMM) surgery [348] aged 4-months (undertaken by

Hua Lin), whereas DMM surgery was not undertaken on the 14-month aged cohort. The joints were then washed with distilled water twice more, before being placed in System III Biopsy Cassettes (CellPath) and stored in 70% (v/v) ethanol. The samples were dehydrated in a tissue processor using a series of ethanol concentrations (70%, 90%, 95%, 100%, 100% and 100%), each for 45 minutes, and subsequently cleaned with xylene, before being infiltrated in paraffin wax and embedded with the main joint cavity facing downwards and the tibia flat relative to the cartridge surface, which corresponds to the front of the resulting wax block. For each joint, 100 5 µm sections were cut using an RM2235 microtome (Leica), and these were collected onto 25 slides, such that the first slide contained sections 1, 26, 51 and 75 and the final slide contained sections 25, 50, 75 and 100. Of the 25 slides, slides 1, 5, 10, 15, 20 and 25 were stained for histological analysis. For this, the sections were dewaxed using xylene, rehydrated through a series of ethanol concentrations (100%, 95%, 75% and 50%) and stained with Weigert's Iron Haematoxylin solution (Sigma-Aldrich), before being counterstained with 0.06% Fast Green FCF solution (Sigma-Aldrich) and rinsed briefly with 1% (v/v) acetic acid. Safranin O solution (Sigma-Aldrich; 0.1% (w/v) in distilled water) was used to stain cartilage, before the sections were dehydrated in a series of ethanol concentrations (95%, 100% and 100%) and cleared using xylene. Finally, the sections were fixed using DPX mountant (Sigma-Aldrich) and visualised at 5X magnification using an Axioscan Z1 slide scanner (Zeiss). Embedding, sectioning and Safranin O staining was performed by Hua Lin. The severity of OA in each section of each joint was assessed by three independent scorers, blinded to genotype, using the OARSI histopathological scoring system [164]. The five highest damage scores for each joint surface given by each scorer were averaged, and the means of these averages from the two scorers who were most closely correlated across all joints were used to assess the statistical significance of joint damage between miR-324-null samples and WT controls. The medial femoral condyle (MFC) and medial tibial plateau (MTP) of each joint were scored separately in addition to a separate summed score of the whole joint, consisting of the highest scoring overall joints.

2.2.19 *Isolation of murine osteoblasts from calvarial bone*

Osteoblasts were isolated from the calvariae of mouse pups essentially as previously described [346]. The calvariae of miR-324-null and WT mice aged 3-5 days were dissected, washed in PBS and subsequently with Hanks' Balanced Salt Solution (HBSS; Lonza), before undergoing digestion at 37°C in 1 mg/ml collagenase type I (Sigma-Aldrich) for 10 minutes, in

a shaking water bath. The supernatant was discarded, before the calvariae underwent a second collagenase digestion for 30 minutes. The supernatant from this and subsequent digestions was kept and combined. Calvariae were then washed in PBS and digested in 4 mM EDTA for 10 minutes, before being washed in HBSS and then undergoing a final collagenase digestion for 30 minutes. The supernatant was then centrifuged at 300*xg* for 3 minutes before being reconstituted in complete α-minimum essential media (α-MEM (Gibco) supplemented with 2 mM L-glutamine, 10% foetal bovine serum, 100 µg/ml streptomycin and 100 IU/ml penicillin (all Sigma-Aldrich)) and grown to confluency (14 days), at which point the cells were plated for osteogenesis assays.

2.2.20 *Isolation and culture of murine osteoblasts and haematopoietic stromal cells from leg bone chips and marrow*

Under sterile conditions, the femurs and tibiae of miR-324-null and WT mice aged 5-months were dissected and the flesh removed. The two bones were subsequently separated at the knee joint, and the epiphyses were removed so as to expose the marrow. The marrow was flushed from the bones by centrifugation at 800*xg* for 4 minutes and plated directly into 10 ml complete α-MEM, supplemented with 100 ng/ml M-CSF, and incubated for 3 days to obtain M-CSF-dependent bone marrow macrophages (BMMs) [346]. The remaining bone was chopped into small chips of approximately 2 mm^3 in volume, washed in HBSS, and digested using 1 mg/ml collagenase type I for 1 hour. Subsequently, the bone chips from one leg were plated in complete α-MEM and cultured for approximately 6 weeks to allow osteoblasts to grow out from the bone, with the media replaced every 3 days. All incubations were at 37°C and 5% (v/v) CO_2. It should be noted that two separate origins for osteoblasts (leg bone and calvariae) were used over the course of this project. Prior to the SARS-CoV-19 pandemic, I had planned to use solely leg bone chip-derived osteoblasts, so all data was directly comparable. However, in order to generate osteoblasts more quickly from the animals available at the time, which as previously mentioned were limited due to the SARS-CoV-19 pandemic, it was necessary to also obtain osteoblasts from calvariae, as these could be obtained at a much younger time point. The two osteoblast cell types were however never compared with one another; for example, miR-324-null carvarial osteoblasts were only compared with other calvarial osteoblasts.

2.2.21 *Isolation of murine osteocyte RNA from leg bone chips*

A protocol adapted from Qing *et al*., (2012) [349] was used to isolate pure osteocyte RNA from murine leg bones with minimal osteoblast contamination. As in the initial step of osteoblast and osteoclast isolation (section 2.2.20), the marrow and flesh of murine leg bones was removed, before the bones were chopped into chips. Bone chips were digested in a solution of 0.2% (w/v) collagenase type I and 0.05% (w/v) trypsin (both in complete α-MEM) for 30 minutes in a 37°C shaking incubator. The collagenase solution was removed and bone chips were washed with HBSS, before the digestion was repeated a further two times, with HBSS wash steps between each digestion. Subsequently, bone chips were incubated in a 0.6 mM EDTA solution (also containing 0.05% (w/v) trypsin, in PBS) for 30 minutes, before being washed in HBSS and undergoing a final 30 minute collagenase digestion. Following this, bone chips were ground on liquid nitrogen in 250 µl QIAzol Lysis Reagent (Qiagen) for 90 seconds at a frequency of 25 s^{-1} using a Mixer Mill MM 400 (Retsch). This was repeated, with the samples being replaced into liquid nitrogen between grinding steps to prevent thawing. The bone powder was left at room temperature to thaw for 20 minutes before resuspension in a further 250 µl QIAzol Lysis Reagent, from which RNA was isolated using the *mir*Vana miRNA Isolation Kit (Thermo Fisher Scientific), following the manufacturer's protocol.

2.2.22 *Osteoblast proliferation and alkaline phosphatase assays*

For cell proliferation and alkaline phosphatase assays, osteoblasts were plated in a 96-well plate at 1.5 x 10^4 cells/well in 200 µl/well of complete Dulbecco's Modified Eagle Medium (DMEM; supplemented with 2 mM L-glutamine, 10% foetal bovine serum, 100 µg/ml streptomycin and 100 IU/ml penicillin) and incubated at 37°C for 24 hours. Subsequently, 20 µl/well of Alamar Blue (Thermo Fisher Scientific) was added and the plate incubated at 37°C for 2.5 hours, before a Varioskan LUX multimode microplate reader (Thermo-Fisher Scientific) was used to quantify fluorescence (excitation 560 nm and emission 590 nm) as a measure of cell viability. Media was subsequently removed and cells were washed in PBS, before being fixed for 10 minutes in 10% (w/v) neutral-buffered formalin (Sigma-Aldrich) and frozen dry at -20°C. When all samples were collected and cell proliferation quantified, alkaline phosphatase assays were undertaken, adapted from Johnson de Sousa Brito and colleagues [346]. Briefly, cells were thawed at 4°C for 12 hours and washed in PBS, before 100 µl of 20mM paranitrophenyl phosphate (PNPP (Thermo Fisher Scientific); pH 9.8, solubilised in 1M diethanolamine and 1mM $MgCl_2$ (both Sigma-Aldrich)) was added to each well. This initiated

the dephosphorylation of PNPP by alkaline phosphatase and the production of paranitrophenol (PNP). Absorbance was measured at 405 nm after 30 minutes and the resultant measurements were quantified against serial dilutions of PNP and normalised against cell proliferation measurements.

2.2.23 *Osteogenesis assays and alizarin red-S staining in murine osteoblasts*

Osteoblasts underwent alizarin red-S staining, adapted from previously described methodology [346]. Cells were plated at 6 x 10^4 cells/well in 24-well plates in osteogenic medium (complete α-MEM, supplemented with 2 mM β-glycerophosphate (BGP) and 50 µg/ml L-ascorbic acid (both Sigma-Aldrich)). Osteoblasts isolated from murine calvariae were incubated for 7 days, whereas osteoblasts isolated from murine leg bones were incubated for 18 days, with media changes performed 3 times per week for both. Half of the wells were fixed for 10 minutes in 10% (w/v) neutral-buffered formalin (Sigma-Aldrich), then washed in distilled water and stained with 40 mM alizarin red-S for 30 minutes. Subsequently, cells were washed in distilled water overnight, air dried, and imaged using an Axiovert 200 Inverted Microscope (Zeiss). Cells were then incubated in a 10% (w/v) cetylpyridinium chloride solution in 10 mM sodium phosphate (pH 7.0) for 30 minutes at room temperature. The absorbance of the cetylpyridinium chloride solution was measured at 562 nm to quantify the Alizarin red-S staining intensity of each sample. The remaining wells were either lysed (as described in section 2.2.7) for protein or using the *mir*Vana miRNA Isolation Kit (Thermo Fisher Scientific), following the manufacturer's protocol, to isolate total RNA (as described in section 2.2.4).

2.2.24 *miR-324 titration and reintroduction in miR-324-null osteoblasts*

miR-324-null and WT calvarial osteoblasts were isolated and cultured as described in section 2.2.19. miR-324-null osteoblasts were transfected with miR-324-5p and -3p mimics (both Horizon Discovery) at final concentrations of 5 nM, 500 pM, 50 pM and 5 pM using DharmaFECT 1 (Horizon Discovery) transfection reagent and subsequently stimulated with osteogenic media for 7 days, as described in section 2.2.23. miR-324-null osteoblasts transfected with miRIDIAN microRNA Mimic Negative Control #2 (miCon; Horizon Discovery) were included as a negative control and osteoblasts obtained from WT mice were included as a positive control. RNA was extracted and reverse transcribed, before the levels of miR-324-5p and -3p were quantified using RT-qPCR (as described in sections 2.2.5 and 2.2.5). After identifying the optimal final transfection concentration to use for miR-324-5p and -3p mimics, the experiment was repeated using osteoblasts obtained from a separate cohort of miR-324-

null mice. Both gene expression analysis and alizarin red-S staining (as described in section 2.2.23) were undertaken after 7 days of stimulation with osteogenic media to assess whether the transient transfection with miR-324 mimics could rescue the miR-324-null phenotype.

2.2.25 *Osteoclastogenesis assays and TRAP staining*

M-CSF-dependent BMMs were seeded in 12-well plates at 5.5 x 10^4 cells/well. Cells were cultured in complete α-MEM, supplemented with 50 ng/ml RANK-L and 30 ng/ml M-CSF (both Peprotech) to stimulate osteoclastogenesis. In parallel, an equal number of cells were only stimulated with 30 ng/ml M-CSF to act as BMM controls. After 3 days, the media was replaced, and after a further 2 days, RNA was extracted or cells were fixed for Tartrate resistant acid phosphatase (TRAP) staining. All incubations were undertaken at 37°C and 5% (v/v) CO_2. For TRAP staining, cells were washed in PBS and fixed for 10 minutes in 10% (w/v) neutral-buffered formalin (Sigma-Aldrich). Subsequently, cells were washed in PBS, then washed 3 times in deionised water. The Acid Phosphatase, Leukocyte (TRAP) Kit (Sigma-Aldrich) was used to stain cells for TRAP for 30 minutes at 37°C. Subsequently, the staining solution was removed, and cells were washed 3 times in deionised water, before being stored at 4°C in 70% (v/v) EtOH until image analysis. An Axiovert 200 Inverted Microscope (Zeiss) was used to visualise the stained cells. The number of TRAP-positive cells with ≥3 nuclei in each sample were counted in addition to the number of nuclei in each of these cells. Fiji [323] was used to measure the total area covered by TRAP-positive cells with ≥3 nuclei, allowing calculation of the mean osteoclast area. All osteoclastogenesis assays were performed in triplicate and the mean of the triplicates was treated as N = 1 for each mouse from which cells were isolated.

2.2.26 *Prediction of novel miR-324 BMM and osteoblast targets*

The TargetScan algorithm [5, 67] was used to predict targets for miR-324-5p and -3p, and these putative targets were filtered by genes annotated to bone- and metabolism- related DO terms [343] (terms used for this filter are given in Appendix B). This subset of putative miR-324 target genes was then filtered for genes that were significantly upregulated (adjusted p-value ≤ 0.05 and $\log_2$ fold-change > 0) in miR-324-null samples relative to WT controls. Finally, the following thresholds were imposed on the remaining genes, in order to output the genes most likely to be direct miR-324 osteoblast targets: TargetScan total context score of < -0.25 and a $\log_2$ fold-change of > 0.35. These thresholds were not chosen for any biological reason, but instead such that they limited the number of putative miRNA targets generated, all of which necessarily required validating *in vitro*, to a number which could realistically be

manually tested. Additionally this reduced the risk of false negative results after *in vitro* validation due to multiple testing correction, which would certainly have been required if these TargetScan thresholds had not been utilised. The genes which passed all filters and thresholds were subsequently tested for direct interaction with miR-324-5p or -3p using 3'UTR-luciferase assays. miRmap identified an additional miR-324-3p binding site in *Cxcl12*-γ by allowing for a non-canonical G-U base pairing [350, 351] and therefore this was also validated using 3'UTR-luciferase assays.

2.2.27 *Prediction of novel miR-324 osteocyte targets*

A largely *in silico* approach was used to identify putative miR-324 osteocyte target genes. The TargetScan algorithm [5, 67] was utilised to predict targets of miR-324-5p and -3p and these were filtered using the osteocyte active transcriptome [352], in order to identify only targets which were expressed and likely important in osteocytes. Putative target genes were filtered further using previous miR-324-null RNA-seq datasets; only genes identified as being upregulated in at least one miR-324-null RNA-seq experiment (adjusted p-value ≤ 0.1) were kept in the putative miR-324 osteocyte target subset. The previous RNA-seq experiments were undertaken in hippocampus, neocortex (see Chapter 3) and rib chondrocytes (not shown). The osteoclast, osteoblast and BMM RNA-seq datasets (see Chapter 5) were not utilised for this purpose as the excess of differentially expressed genes would not have sufficiently reduced the osteocyte miR-324 target subset. Finally, the 5 most highly predicted miR-324 targets in the osteocyte active transcriptome were added to the subset, as were the 4 miR-324 target genes already validated from other tissues. The expression of each of these genes was subsequently measured in miR-324-null and WT osteocytes using RT-qPCR in order to identify which putative target genes behaved like real targets of miR-324. 3'UTR-luciferase assays were subsequently utilised to validate these putative targets. OATargets [353] was utilised in order to annotate whether each gene was associated with body height, bone mineral density or osteoarthritis through genome-wide association studies (GWAS).

2.2.28 *Construction of 3'UTR luciferase reporter plasmids*

Fragments of the 3'UTR regions of putative miR-324 targets, containing predicted miR-324 binding sites, were either amplified from murine genomic DNA, which was extracted from WT C57BL/6J mouse ear notches, or from cDNA reverse transcribed from RNA extracted from WT murine osteoblast (as described in sections 2.2.2, 2.2.3 and 2.2.4) where the 3'UTR contained intronic regions. PCR primers (Table 2.2) were designed for In-Fusion HD cloning (Takara Bio)

into the pmiRGLO luciferase reporter plasmid (Promega), which was pre-digested to completion with *Xho*I restriction endonuclease (New England Biolabs). Mutant 3'UTR constructs, which were identical to WT amplifications except for mutations of 2 nucleotides within the predicted miR-324 binding sites (Table 2.3), were ordered as gBlocks (Integrated DNA Technologies) where possible and cloned into pmiRGLO using In-Fusion HD, or otherwise were produced by site-directed mutagenesis of the WT plasmids using QuikChange Lightning (Agilent; Table 2.4). All constructs underwent confirmation by Sanger sequencing (Source Biosciences).

Gene	Forward primer (5' → 3')	Reverse primer (5' → 3')	Amplicon size (bp)	Length of full 3'UTR (bp)	Number of predicted miR-324 binding sites	
					miR-324-5p	miR-324-3p
App	GCTCGCTAGCCTC GAATTCTTGTGGT TTGTGGCCC	CGACTCTAGACTC GAAGAAATCAATG TGTATCCTC	287	5646	1	0
Bcl2	GCTCGCTAGCCTC GAGCCACAAGTG CCTGCTTTAT	CGACTCTAGACTC GACATCAGCCACG CCTAAAAGT	4012	8386	0	3
Ccne1	GCTCGCTAGCCTC GAAAGGAGGGT GCTACTTGACC	CGACTCTAGACTC GATGTTGGCTGAC AGTGGAGAA	233	531	1	0
Cd300lf	GCTCGCTAGCCTC GATGTACCTGCTT CCTTACCCG	CGACTCTAGACTC GAGCTCACGGAAC AGAACAGTC	634	687	2	0
Cxcl12-α	GCTCGCTAGCCTC GACCGAGGAAG GCTGACATCC	CGACTCTAGACTC GAGCCGGATCTTG TGTTGACTC	525	1488	0	2
Cxcl12-β	GCTCGCTAGCCTC GAGCAAGGAAGT GCAGC	CGACTCTAGACTC GACTGCATATAGG AAGC	545	2770	1	1
Cxcl12-γ	GCTCGCTAGCCTC GATAAAACGCTT CTGGAGGCCA	CGACTCTAGACTC GATGAACCCATCG CTGCTTAGA	3558	5129	3	2
Cxcl12-γ (unique part)	GCTCGCTAGCCTC GATAAAACGCTT CTGGAGGCCA	CGACTCTAGACTC GACAAGGAGCAC ATGACAAGGC	704	2419	2	1
Hoxa9	GCTCGCTAGCCTC GAAATTTGCTCTT CGTGTGGCA	CGACTCTAGACTC GACTCACTTCTCCT CTGGTGCA	521	1144	1	0
Icam1	GCTCGCTAGCCTC GAAGCATTTACC CTCAGCCACT	CGACTCTAGACTC GAAACCACTGCCA GTCCACATA	560	871	2	0
Ing1	GCTCGCTAGCCTC GACATGTCAGCG AGTGTCAGAC	CGACTCTAGACTC GAGCTGCACTTCC GGTTATGAT	490	1129	1	0
Klf7	GCTCGCTAGCCTC GAGCGGCTACTC TACTGTCCTT	CGACTCTAGACTC GAAGCATTTGTGA CAAAGCGGT	985	6266	1	0
Pdgfa	GCTCGCTAGCCTC GAACCAAACCAC ACCCAACAAC	CGACTCTAGACTC GAACGTTAAAGG GGCAGAGGAA	612	1203	1	0
Pin1	GCTCGCTAGCCTC GACCCTTCCTGCT ACTGTCACA	CGACTCTAGACTC GAGCTCTTGGTGT TGCAAGCTA	1514	3300	0	3

hPIN1	GCTCGCTAGCCTC GAGGGTGGGGA GCCCAGGCCTG	CGACTCTAGACTC GAGGAGCGTGGC CTAACTAGAA	414	490	0	1
Ptgs1	GCTCGCTAGCCTC GAAGTGGTTTTG TCTGCCTCCT	CGACTCTAGACTC GAGTCCATCTGTT CCCTCCACA	636	921	1	0
Rgs5	GCTCGCTAGCCTC GAGGGAAAATG GCAGCCTTTGA	CGACTCTAGACTC GACTGACCCTCAA CCCAGAACT	997	3473	1	1
Runx2	GCTCGCTAGCCTC GAATGGCGTCAA ACAGCCTCTT	CGACTCTAGACTC GAGACGACGACA GACTGCTCTA	636	3904	1	0
hRUNX2	GCTCGCTAGCCTC GACCCCTTGTTCT CTGGTCCTT	CGACTCTAGACTC GAGAGGGTGGAG GGAAGAAGTG	647	3777	1	0
Samd5	GCTCGCTAGCCTC GAACTGGATGGT GACTCTGCAA	CGACTCTAGACTC GAATTCTGTCATG AGCGCCTCT	1220	6051	0	2
Sp6	GCTCGCTAGCCTC GATGTCACATAC CTGCCGTTCT	CGACTCTAGACTC GAAAGGACAGGC AGCTGAGAAA	2034	2141	2	0
Spon1	GCTCGCTAGCCTC GAAAAAGATGGC GCTTCTGTCC	CGACTCTAGACTC GAGACGGGTTGT GATGGGTTTC	975	3406	1	1
Suox	GCTCGCTAGCCTC GATTGTACCCAA AGAACCACCTAG	CGACTCTAGACTC GAGGAAATCCCCT TGCATCCCA	581	623	1	0
Top1	GCTCGCTAGCCTC GAACAGTGTGGT TTGGGGAAGA	CGACTCTAGACTC GAATGTGGGAAT GGACTCTGCA	1121	1210	0	1

Table 2.2 - Primers used to amplify 3'UTR fragments of putative miR-324 target genes from murine genomic DNA. The overlaps with linearised pmiRGLO required for In-Fusion cloning are shown in red. *hPIN1* and *hRUNX2*, the human homologues of *Pin1* and *Runx2*, were amplified from human SW1353 cell cDNA, whereas all other 3'UTR fragments were amplified from WT murine ear notch genomic DNA or from WT murine osteoblast cDNA.

Gene	WT predicted binding site(s)	Mutated predicted binding site(s)	Position(s) of first nucleotide of predicted binding site(s) in 3'UTR
App	AAATCGATGGGGGATGCTTCTT GTGAA	AAATCGATGGGGCAGGCTTCTT GTGAA	415
Cd300lf	GGCTGCTTCAGGGATGCTGTGT AAATC; AGAAGGTGGAGGGATGCAGA AGGAGTCA	GGCTGCTTCAGGCAGGCTGTG TAAATC; AGAAGGTGGAGGCAGGCAGA AGGAGTCA	233; 576
Cxcl12-γ (unique part)	TGCTTAGAAAGGGATGCCCCA CCCTTA; CTGAGGCCTGGGGATGCCCAG GAACAC; CTAAGGTTAAGGCGGTGCGCC TTGTCA	TGCTTAGAAAGGCAGGCCCCA CCCTTA; CTGAGGCCTGGGCAGGCCCAG GAACAC; CTAAGGTTAAGGAGCTGCGCC TTGTCA	1509; 2026; 2102
Hoxa9	ATAGTTCTCCGGGATGCATAGA TTCAT	ATAGTTCTCCGGCAGGCATAGA TTCAT	696
Pdgfa	GAGCCCGCCTGGGATGCTGCC TGCCAG	GAGCCCGCCTGGCAGGCTGCC TGCCAG	480
Pin1	ACTTCAGAAGGGCAGTGGGGA TGGGGA; GCCTCAGGGTGCAGTGCAGCA CCCTA; GGGCTCAGGAGGCAGTGGCAG CCCTCC	ACTTCAGAAGGGAACTGGGGA TGGGGA; GCCTCAGGGTGCTGGGCAGCA CCCTA; GGGCTCAGGAGGAACTGGCAG CCCTCC	184; 363; 1454
Ptgs1	GGCCAGCCATGGATGCATAGT GAGACT	GGCCAGCCATGGTTCCATAGTG AGACT	406
Runx2	GGGAATAGAGGGGATGCATTA GTGCCTA	GGGAATAGAGGGCAGGCATTA GTGCCTA	2517
Samd5	TCAGGAGTAAGGCAGTGACCG ACCATC; TGTCGGCCTTGGCAGTGGGCA AGAGGA	TCAGGAGTAAGGAACTGACCG ACCATC; TGTCGGCCTTGGAACTGGGCA AGAGGA	193; 811
Suox	AATTGCCTCTGGGATGCAAGG GGATTTC	AATTGCCTCTGGCAGGCAAGG GGATTTC	552

Table 2.3 - Comparison of WT and mutant 3'UTR predicted miR-324 binding sites in putative miR-324 target genes. Predicted miR-324-5p binding sites are highlighted in red, -3p binding sites in turquoise and single nucleotide mutations are highlighted in yellow and formatted bold. The 10 nt sequences either side of each predicted binding site are shown for context. For the predicted binding site of *Cxcl12*-γ, a non-canonical G-U base pairing was predicted between the binding site and miR-324-3p. This G residue is underlined to highlight this non-canonical binding site prediction.

Gene	First site forward primer	First site reverse primer	Second site forward primer	Second site reverse primer
Cd300lf	AGGCAGGCTGCTTCAGGcAgGCTGTGTAAATCGTATC	GATACGATTTACACAGCcTgCCTGAAGCAGCCTGCCT	AGCAGAAGGTGGAGGcAgGCAGAAGGAGTCAGG	CCTGACTCCTTCTGCcTgCCTCCACCTTCTGCT
Ptgs1	AGAAAGAGTCTCACTATGgAaCCATGGCTGGCCTAGAAC	GTTCTAGGCCAGCCATGGtTcCATAGTGAGACTCTTTCT		

Table 2.4 - Primers utilised to introduce single nucleotide mutations at predicted miR-324 binding sites using QuikChange Lightning. Mutagenesis sites are shown in lower case. All primers are shown in a 5' to 3' orientation.

2.2.29 *3'UTR-luciferase assays*

Murine C3H10T1/2 cells, an immortalised MSC-like cell line, were cultured at 37°C and 5% (v/v) CO_2 in DMEM, supplemented with 2 mM L-glutamine, 10% foetal bovine serum, 100 µg/ml streptomycin and 100 IU/ml penicillin, using vented T75cm^2 flasks as previously described [151]. Cells were seeded onto 96-well plates at 5000 cells/well, before being incubated at 37°C for 18 hours. Subsequently, cells were transfected with the pmiRGLO-3'UTR constructs using FuGENE HD Transfection Reagent (Promega) at a 3:1 ratio (µl FuGene:µg DNA), following the manufacturer's protocol. These cells were incubated at 37°C for 4 hours, media was aspirated, and the cells were transfected with miCon or miR-324-5p or miR-324-3p mimics (all Horizon Discovery) at a final concentration of 50 nM using DharmaFECT 1 (Horizon Discovery) transfection reagent. The cells were incubated at 37°C for 24 hours, after which the media was aspirated, cells washed with PBS and lysed using 30 µl of Passive Lysis Buffer (Promega). Luciferase level of each well was determined relative to an internal Renilla control using a GloMax-Multi Detection System (Promega) and reagents from the Dual-Luciferase Reporter Assay System (Promega). For each pmiRGLO-3'UTR construct, at least 3 technical replicates were measured for each of miR-324-5p, miR-324-3p and miCon. The mean values from at least 3 independent experiments were used to calculate statistical significance using Student's two-tailed paired *t*-tests. The empty pmiRGLO plasmid was included in every experiment as a negative control and, after miR-324 targets were identified, one of these was used as a positive control for each subsequent experiment. For putative human target genes,

the same protocol was undertaken, but using the human Y201 cell line in place of murine C3H10T1/2 cells.

2.2.30 *Overexpression plasmids and construction of negative control*

Myc-DDK (FLAG)-tagged coding DNA sequence (CDS) clones of murine *Hoxa9*, *Samd5* and *Runx2* were purchased from Origene, within the pCMV-ENTRY overexpression vector (catalogue numbers MR203609, MR216293 and MR227321, respectively). To produce a negative control plasmid containing no CDS, the pCMV-ENTRY-*Hoxa9* plasmid was first digested using with *Bam*HI and *Xho*I. After separating the digestion products on a Tris-Borate-EDTA 0.8% (w/v) agarose gel, the band corresponding to the pCMV-ENTRY vector backbone was excised and purified using the NucleoSpin Gel and PCR Clean-up Kit (Macherey-Nagel). To circularise the empty plasmid, including additional restriction sites (shown in lower case) and overhangs required for In-Fusion HD cloning (shown in bold), the following gBlock was synthesised (Integrated DNA Technologies): 5'-**TAGGGCGGCCGGGAATTCGTCGACTGGATC**GATCCGGTACCGAGGAGATCTtctagaGCCGCCgctagcAAGcatatgACGAGACGCGTACGCGGCCGC**TCGAGCAGAAACTCATCTCAGAAGAGGATC**-3'. In-Fusion HD cloning (Takara Bio) was used to insert this sequence into the linearised pCMV-ENTRY backbone, following the manufacturer's protocol, to produce the negative control overexpression plasmid, pCMV-ENTRY-neg.

2.2.31 *Culture of MLO-Y4 cells and overexpression of miR-324 target genes*

The MLO-Y4 osteocyte model cell line [354] was utilised to investigate the effects of validated miR-324 target genes on the osteocyte phenotype *in vitro*. The MLO-Y4 cells were kindly gifted by Dr Mark Birch, University of Cambridge. MLO-Y4 cells were cultured in α-MEM supplemented with 5% calf serum (Cytiva Life Sciences), 5% foetal bovine serum, 2 mM L-glutamine, 100 µg/ml streptomycin and 100 IU/ml penicillin, using collagen I-coated vented T75cm^2 flasks (StemCell Technologies, catalogue number 100-0349) and 6-well plates (Thermo Fisher Scientific, catalogue number A1142801). Culture conditions were maintained at 37°C and 5% (v/v) CO_2. For experimental overexpression assays, MLO-Y4 cells were plated at 1.5 x 10^5 cells/well in 6-well plates in complete media. The following day, cells were transfected with an overexpression plasmid or pCMV-ENTRY-neg (the negative control) using Fugene HD (Promega), following the manufacturer's protocol, and were subsequently left in the transfection mix for 72 hours before being lysed for RNA or protein. Alternative to transfection, cells were stimulated with 50 ng/mL of Cxcl12-α chemokine (Peprotech,

catalogue number 250-20A), or left unstimulated as the negative control, and also lysed after 72 hours.

2.2.32 *Adipo-osteogenesis in murine C3H10T1/2 mesenchymal stromal cells*

Adipo-osteogenesis (AdiOst) co-differentiation assays were undertaken using murine C3H10T1/2 cells. Cells were plated in 96-well plates at 5 x 10^3 cells/well in 96-well plates in complete DMEM. Prior to stimulation with AdiOst co-differentiation media, C3H10T1/2 cells were transfected either with microRNA Hairpin Inhibitor Negative Control #1 (hpCon), hp-miR-324-5p hp-miR-324-3p, miCon, miR-324-5p mimic, miR-324-3p mimic (all Horizon Discovery), a pCMV-ENTRY-*Runx2* overexpression plasmid or pCMV-ENTRY-neg. miRNA mimics and hairpins were transfected at a final concentration of 50 nM using DharmaFECT 1 (Horizon Discovery), whereas overexpression plasmids and the negative control were transfected using FuGene HD (using a 3 µl FuGene:1 µg DNA ratio), following the standard manufacturer's protocol for each. Twenty-four hours after transfection, the media was aspirated and either fresh complete media (as negative controls) or AdiOst co-differentiation medium (complete α-MEM supplemented with 100 nM dexamethasone, 2 mM BGP and 50 µg/ml L-ascorbic acid [346, 355] (all Sigma-Aldrich)) was added. Two further conditions, unsupplemented AdiOst or AdiOst media supplemented with 50 ng/ml Cxcl12-α (Peprotech; catalogue number 250-20A), were also tested in order to assess the effect of high levels of the Cxcl12 chemokine on AdiOst differentiation. Media was replaced three times each week for a total of 18 days. The experimental wells were either stained with alizarin red-S (as described in section 2.2.23), oil red-O or RNA was extracted using the Cells-to-cDNA II Kit (Thermo-Fisher Scientific). Oil red-O staining was undertaken essentially as previously described [356]; at the experimental end point, cells were fixed for 1 hour in formalin solution (10%, neutral buffered; Sigma-Aldrich), washed in distilled water and subsequently in 60% (v/v) isopropanol (Sigma-Aldrich), before being dried and stained for 10 minutes with 21% (w/v) Oil red-O solution (Sigma-Aldrich). Cells were then washed, imaged with an Axiovert 200 Inverted Microscope (Zeiss), and destained using 100% (v/v) isopropanol. The stain intensity was quantified by measuring the absorbance at 500 nm.

2.2.33 *Statistical analysis*

Where data was of a normal distribution (tested using the Shapiro-Wilk test for normality), statistical significance was assessed using Student's two-tailed *t*-test (all unpaired unless indicated otherwise in the figure legends) for single comparisons or analysis of variance

(ANOVA) for testing the effects of multiple variables on a continuous variable output; the test used for each comparison is indicated in the corresponding figure legend. Where data was non-parametric, Mann-Whitney U tests were used to assess significance of single comparisons, and either $\log_{10}$ transformed two-way ANOVA tests or ANOVA of rank tests were used for the effects of multiple comparisons. Tukey's HSD tests were used for post-hoc ANOVA testing. All data analysis and statistical calculations were performed using R version 3.6.2 [357]. Relevant R packages used for statistical analysis are cited.

Chapter 3 - miR-324-null mice display increased hippocampal activity and mild behavioural abnormalities

Statement: Some of the data and writing presented in this chapter is part of a publication for which I am the first author [320]. Therefore, there is significant overlap between that publication and this chapter.

3.1 Introduction

3.1.1 *Neurological disease and microRNAs*

miRNAs are crucial components in normal brain development and neurological function and a complete lack of miRNAs results in severe consequences. *Dicer1* encodes an essential endoribonuclease for miRNA processing, and *Dicer1* conditional knockout models in individual neuronal populations present with severe neurological abnormalities [100-103]. These are most commonly due to upregulation of apoptotic pathways or downregulation of cell proliferation, resulting in reduced brain size. The impact of some individual miRNAs on brain development are so great that knockout of the individual miRNA can severely impact neurological function. For example, mice lacking miR-9, one of the most highly expressed miRNAs in vertebrate brains, present with severely abnormal telencephalic structures due to a lack of miR-9-mediated regulation of neural progenitor cell proliferation [104-106]. Double knockout of genes encoding the miR-34b/c and miR-449 clusters, which are functionally redundant to one another [358], mirrors *Dicer1* knockout models in that apoptosis is upregulated, resulting in a reduction in basal forebrain size [359]. A related miRNA, miR-34a, is also important in normal brain function, and produces an opposing effect to miR-34b/c in that it promotes apoptotic pathways when it is upregulated. Furthermore, miR-34a may contribute to the neuronal death that occurs in rodent models following seizures, as it has been shown to be upregulated following these events [107, 108]. Individual miRNAs are therefore essential for normal brain development and in general these key neurological miRNAs exert their effects through shifting the balance between neurogenesis and apoptosis.

3.1.2 *miR-324 in neurological disease*

miR-324 has previously been suggested to function in the regulation of normal neural activity [111, 112] and is expressed more abundantly in both the human and mouse brain than in other tissues [109, 110]. Experimentally validated target information for miR-324 is somewhat limited, but the two mature miR-324 arms, miR-324-5p and -3p, are each predicted to target and repress a large number of genes. Amongst the targets relevant for neurological activity, *App*, the gene encoding the amyloid precursor protein [113], is one of the most confidently predicted [5, 67], potentially linking miR-324-5p to Alzheimer's disease [114]. miR-324-5p has also been investigated in relation to epilepsy; in a murine model of epilepsy, whereby wild-type (WT) mice were injected with pilocarpine in order to evoke seizure activity, the use of a miR-324-5p antagomir was found to reduce the incidence of epileptic events [112],

purportedly by downregulating the expression of *Kcnd2*, a gene encoding the potassium channel protein Kv4.2 [111, 112]. Deletion or mutation of *Kcnd2* has been shown to severely impair A-type K^+ currents, the precise regulation of which is key maintaining normal levels of neuronal excitability [115-117, 360]. A detailed investigation into the cause of the association between miR-324 and epilepsy has however not yet been reported.

In this chapter, by utilising the global miR-324-null mouse model generated by our group, investigation into the function of miR-324 in the vertebrate brain was undertaken, using hippocampal slices for *ex vivo* electrophysiological analysis. Subsequent high-throughput RNA sequencing (RNA-seq) experiments were used in order to identify genes and biological pathways impacted by lack of *Mir324* in the murine hippocampus and neocortex, as well as 3'UTR-luciferase assays to confirm direct interactions between miR-324 and putative targets. Finally, behavioural analysis of miR-324-null and WT mice was undertaken to identify any *in vivo* phenotypes resulting from the transcriptomic changes identified.

3.1.3 *Chapter aims*

1. Compare *ex vivo* electrophysiological activity in hippocampal slices between genotypes.
2. Undertake behavioural analysis of miR-324-null and WT mice to identify if the lack of miR-324 results in an observable *in vivo* phenotype.
3. Published literature suggests that miR-324 is important in the regulation of neurological activity. I will therefore undertake RNA-seq to compare transcriptomic changes between genotypes in the hippocampus and the neocortex in order to elucidate miR-324-mediated regulatory pathways.

3.2 Results

3.2.1 *miR-324-5p is expressed in the murine hippocampus and neocortex*

To confirm *Mir324* expression in the brain (and validate the lack of miR-324-5p in the miR-324-null mouse brain), RT-qPCR was performed. The expression levels of *Mir324* in male 13.5-month old WT and miR-324-null mice were measured using RT-qPCR in hippocampus and neocortex, confirming that miR-324-null mice completely lack expression of *Mir324* (Figure 3.1a). Additionally, *in situ* hybridisation revealed that miR-324-5p is expressed across the murine hippocampus in WT mice, including the CA3 region (Figure 3.1b). miR-324-null mice

were born at the normal Mendelian ratio, were phenotypically normal with no obvious overt phenotype and survived with normal longevity.

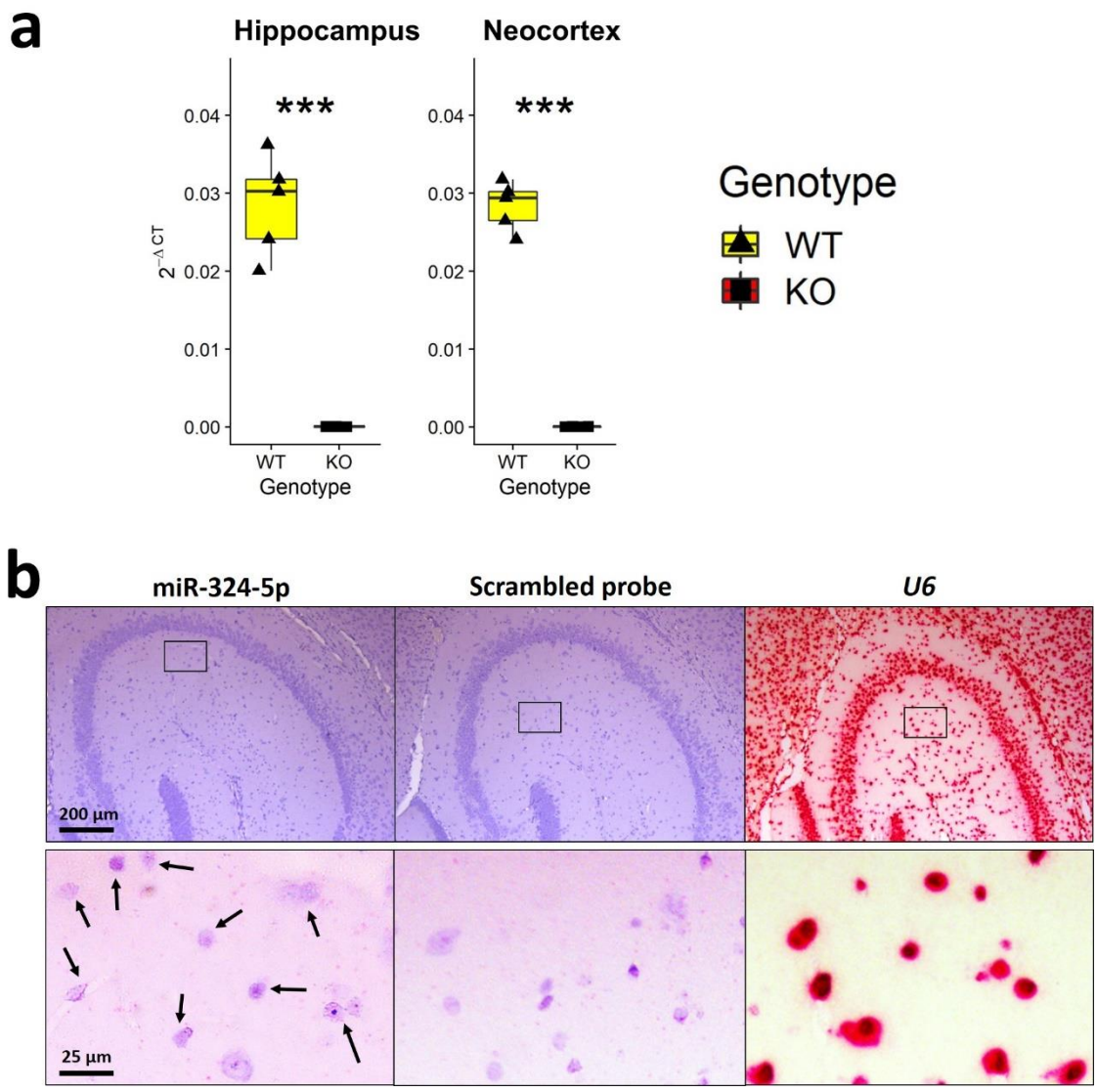

Figure 3.1 - miR-324-5p is expressed in the murine hippocampus and neocortex. (**a**) The expression levels of *Mir324* were measured in the hippocampus and neocortex tissue of miR-324-null and WT mice aged 13.5 months (N = 5). *Mir324* was detected in all WT samples and was not detected in any miR-324-null samples. *U6* was used as the control to normalise *Mir324* levels between samples. *** signifies p-value ≤ 0.001 (two-sided Student's *t*-tests). (**b**) miR-324-5p is shown to be expressed in the murine hippocampal CA3 region by *in situ* hybridisation. Representative images of the murine hippocampus are shown following hybridisation to probes against miR-324-5p, *U6* (positive control) or a scrambled probe sequence (negative control) and subsequent counterstaining with haematoxylin. Arrows indicate the cells in which miR-324-5p expression is detected as punctate red spots.

3.2.2 *miR-324-null mice display electrophysiological abnormalities in the hippocampus*

In order to determine whether global miR-324-null mice exhibited any deficits in the generation of network activity, the local field potential (LFP) was recorded from the CA3 *stratum radiatum* in hippocampal slices obtained from 5-month-old female miR-324-null and WT mice (each mouse contributed either 2 or 3 slices to the overall experimental population, depending on the tissue quality upon dissection). Kainate (KA), a neurotoxin commonly used to evoke acute brain seizures experimentally [361], was used to induce gamma-frequency oscillatory activity (20-80 Hz) at a range of concentrations between 50 nM and 1 µM. At 0 nM KA, no spontaneous gamma-frequency oscillation was observed. As the KA concentration was increased, the power of the gamma-frequency oscillation increased in amplitude and area until 400-600 nM KA, at which point the oscillation collapsed as previously reported [362]. Hippocampal KA-evoked oscillatory activity was recorded at each concentration for 30 minutes and the final minute of each trace was used to measure area power, peak amplitude and peak frequency. All slices, both WT and miR-324-null, showed gamma-frequency oscillatory activity during the course of the experiment. Over the range of KA concentrations, no statistically significant differences were observed between genotypes for any of the metrics (Figure 3.2), although area power showed a trend to be larger in the miR-324-null slices and was close to the significance threshold (p-value = 0.068). All three metrics were statistically significantly affected by the concentration of KA, independent of genotype (p-values for area power, peak amplitude and peak frequency = 2.4×10^{-25}, 1.8×10^{-20} and 1.0×10^{-20}, respectively). With regard to peak frequency, a shift to a higher frequency was observed between 400 nM and 600 nM KA in miR-324-null slices, whereas in WT slices this shift was less consistent.

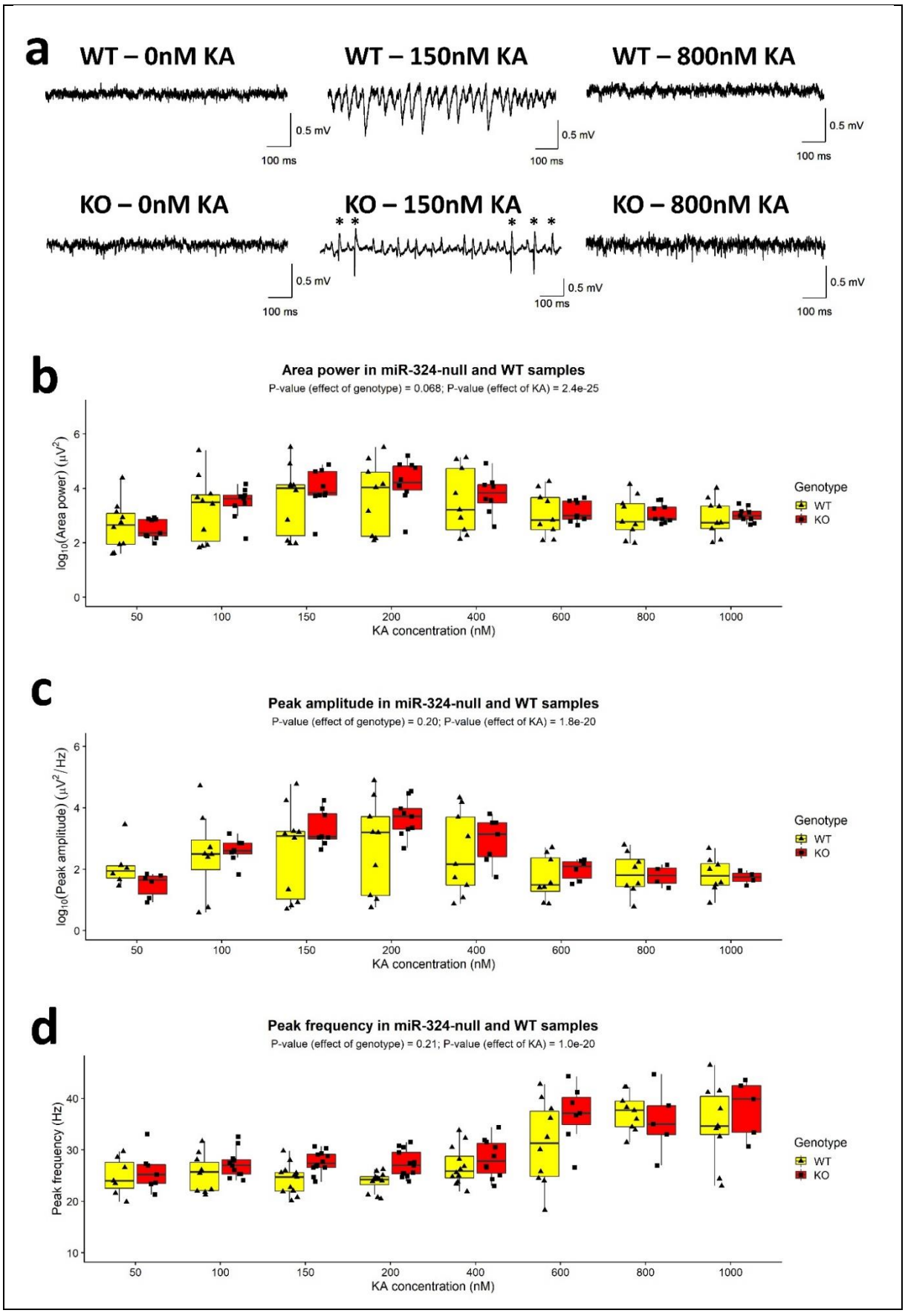
a
WT – 0nM KA
WT – 150nM KA
WT – 800nM KA
KO – 0nM KA
KO – 150nM KA
KO – 800nM KA
0.5 mV
100 ms
b
Area power in miR-324-null and WT samples
P-value (effect of genotype) = 0.068; P-value (effect of KA) = 2.4e-25
log10(Area power) (μV2)
KA concentration (nM)
Genotype
WT
KO
c
Peak amplitude in miR-324-null and WT samples
P-value (effect of genotype) = 0.20; P-value (effect of KA) = 1.8e-20
log10(Peak amplitude) (μV2/Hz)
d
Peak frequency in miR-324-null and WT samples
P-value (effect of genotype) = 0.21; P-value (effect of KA) = 1.0e-20
Peak frequency (Hz)

Figure 3.2 - No change in gamma-frequency oscillations was observed between hippocampal slices taken from 5-month-old female miR-324-null and WT mice. (**a**) Example 1 second traces of LFP which were each recorded from a single WT and miR-324-null slice in the absence of KA (baseline), at 150 nM, and at 800 nM KA bath application. In both genotypes, no spontaneous oscillations were seen before KA application, but clear gamma-frequency activity was evident at 150 nM. In the miR-324-null slices, "spikes" in the LFP are indicated by *****. Oscillations subsequently collapsed at higher KA concentrations (800 nM KA). (**b**-**d**) Comparisons between genotypes of area power, peak amplitude and peak frequency showed no significant differences, although area power was close to the 5% significance threshold (p-value = 0.068). KA concentration significantly affected all three metrics. N = 16 slices obtained from 6 mice per genotype. Slices that did not show clear gamma-frequency oscillatory activity at a particular concentration were omitted from analysis at that concentration, and therefore for some KA concentrations N < 16. P-values were calculated using two-way mixed ANOVAs, although for peak amplitude and area power, the data was first $\log_{10}$ transformed so as to satisfy statistical assumptions, as the initial data were not normally distributed.

Interestingly, in some hippocampal slices, particularly those obtained from miR-324-null mice, regular interictal discharges (IIDs) were evident following application of KA, which are defined as intermittent electrophysiological events which occur in patients affected by epileptic disorders [363]. In other slices, oscillations exhibited large so-called "spikes" in the field potential recordings, which were defined as peaks in the LFP at least 5 SDs from the baseline of that trace. Upon comparing the proportions of all slices exhibiting IIDs in miR-324-null and WT slices across the range of KA concentrations used, there was a noticeable increase in the number of slices showing IIDs in miR-324-null slices relative to WT slices, which was most apparent at 150 and 200 nM KA (Figure 3.3). All IIDs observed in WT slices were obtained from a single mouse, whereas slices taken from 4 of the 6 miR-324-null mice produced IIDs after KA application. The number of detected spikes and IIDs per minute were both significantly increased in miR-324-null mice relative to WT controls (p-values = 2.8×10^{-3} and 0.021, respectively), demonstrating that lack of *Mir324* increases the overall incidence of these hyperexcitable epilepsy-related events (Figure 3.4). In particular, the frequency of spikes was significantly increased in miR-324-null slices between 150 nM and 800 nM of KA and the

frequency of IIDs was significantly increased in miR-324-null slices between 150 nM and 400 nM of KA (p-values ≤ 0.05, using Tukey's HSD post-hoc tests). KA concentration was not found to significantly affect these metrics, independent of genotype.

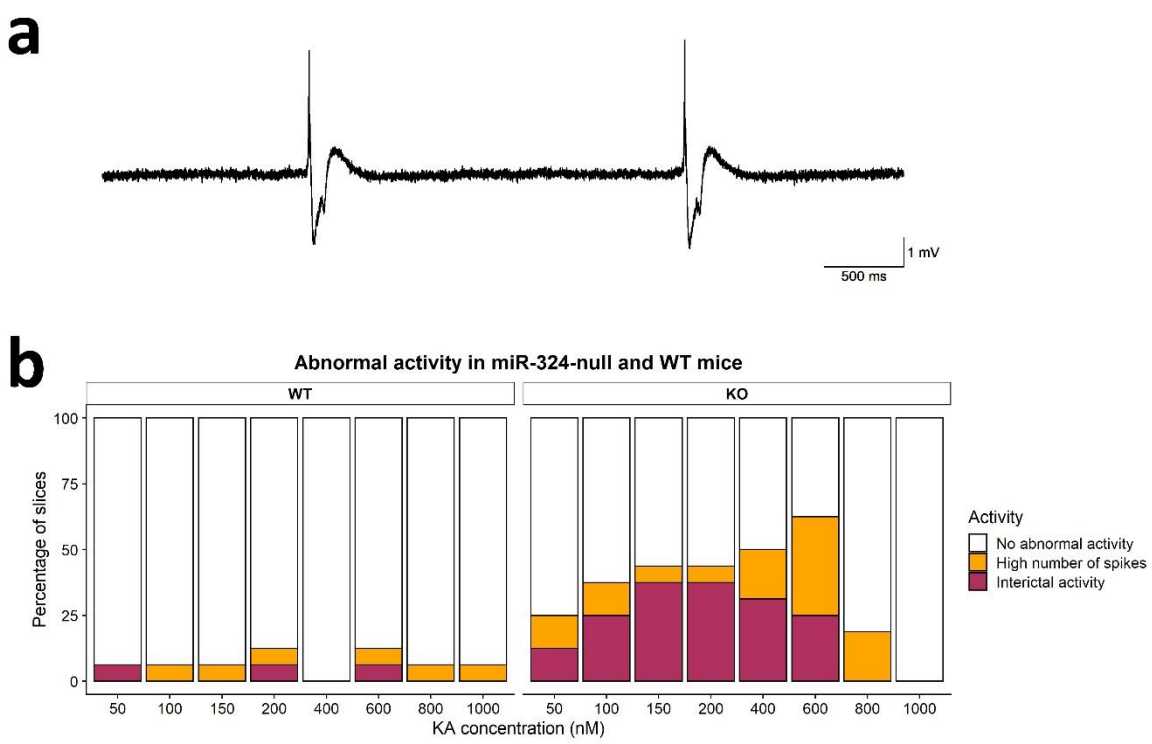

Figure 3.3 - Increased excitability in hippocampal slices obtained from female 5-month-old miR-324-null mice. (**a**) IIDs were observed in some slices from miR-324-null mice. (**b**) A higher proportion of miR-324-null hippocampal slices showed IIDs or a high number of spikes than WT slices (N = 16 slices obtained from 6 mice per genotype). Any slice displaying at least one IID was classed as showing interictal activity, whilst slices showing no interictal activity but a high number of spikes were also grouped together. Slices were classed as showing high number of spikes if they had a greater number of spikes than the mean plus 2 standard deviations (SDs) of spike number in the WT slices, for each KA concentration. For example, the mean plus 2 SDs of WT spikes at 150 nM KA was 15.0, and therefore any slices at 150 nM with more than 15 spikes were classed as having a high number of spikes. The most prominent distinction between genotypes is seen at 150 and 200 nM KA, at both of which 37.5% of miR-324-null slices displayed interictal activity, whereas the majority of WT slices at these concentrations showed no abnormal activity.

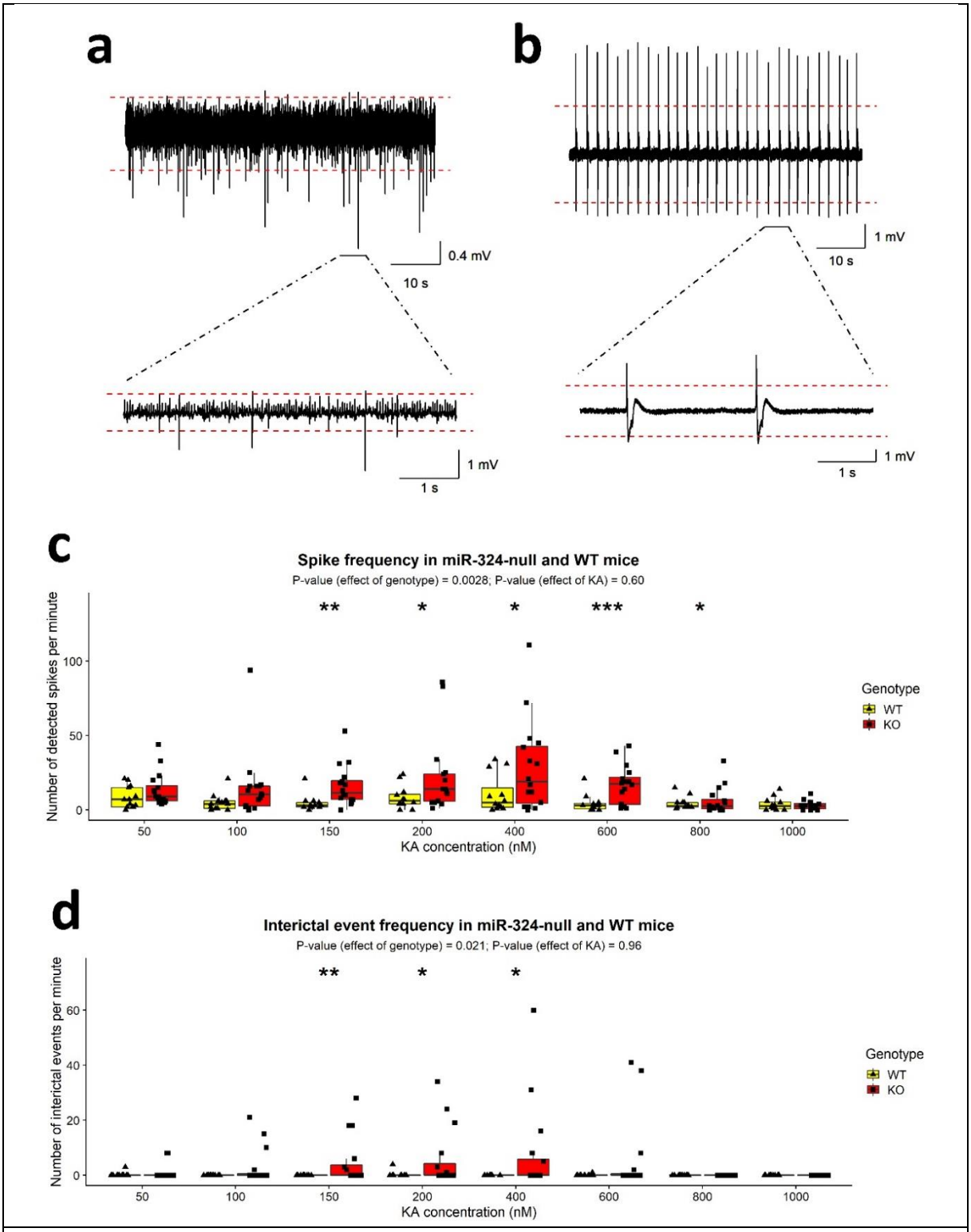

Figure 3.4 - Comparison of measures of excitability in electrophysiology data measured in hippocampal slices taken from 5-month -old female miR-324-null and WT mice. (**a** and **b**) Examples of traces following bath application of 150 nM KA which show large numbers of spikes (peaks more than 5 SDs from the baseline) and IIDs, respectively (both measured in miR-324-null slices). The red dashed lines indicate 5 standard deviations above and below the baseline. (**c** and **d**) Electrophysiological traces of miR-324-null mice contained a

significantly higher frequency of spikes and IIDs than WT control traces. The majority of slices obtained from WT mice showed no IIDs and therefore the frequency for these slices is 0. N = 16 slices obtained from 6 mice per genotype. P-values were calculated using two-way mixed ANOVAs of ranks, as the initial data was not normally distributed. *, ** and *** indicate p-values ≤ 0.05, 0.01 and 0.001, respectively, for post-hoc testing at each KA concentration, using Tukey's HSD tests.

3.2.3 *miR-324-null mice display mild in vivo behavioural abnormalities*

Considering the hippocampi of miR-324-null mice displayed increased excitability *ex vivo* relative to WT controls, we proceeded to investigate whether this abnormality affected the behaviour of the mice *in vivo*. For this, the MouseTrapp system [334] was utilised to record the number of touches, number of rears and distance travelled in 30 second intervals over the course of 50 minutes. No statistically significant difference between genotypes was observed in the mean number of touches, mean distance covered or mean number of rears per minute, but the maximum number of rears per minute was significantly increased in miR-324-null mice. Additionally, the mean step length of each mouse was approximated by dividing the distance travelled in each interval by the number of touches. Here too a significant difference is observed between genotypes; miR-324-null mice were found to have a reduced average step length relative to WT controls (Figure 3.5). These differences, although mild, suggest that the *ex vivo* electrophysiological abnormalities observed in miR-324-null mice may express as these observable behavioural changes *in vivo*.

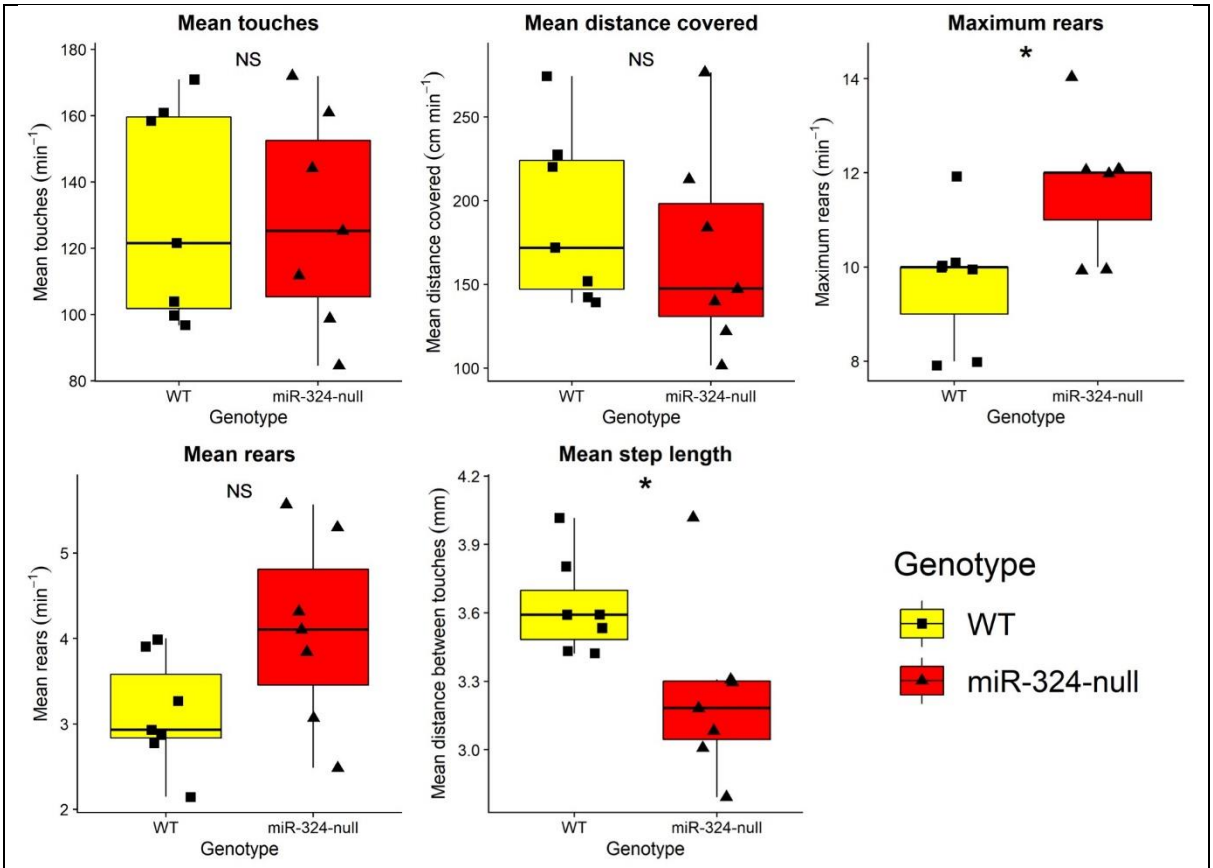

Figure 3.5 - Female miR-324-null mice aged 7 months display mild abnormalities in behaviour. The behaviour of miR-324-null and WT mice (N = 7) was analysed for 50 minutes, following 10 minutes of acclimatisation, using the MouseTrapp system [334], allowing a comparison of the number of touches, distance covered and number of rears between genotypes, with recordings split into 30 second intervals. Additionally, the mean distance between touches, approximating the mean step length, was calculated using the following formula for each 30 second interval: $\frac{Distance\ covered / Number\ of\ touches}{4}$. The mean number of touches, mean number of rears and mean distance covered showed no statistically significant difference between genotype, although the maximum number of rears per minute was significantly increased and the mean step length was significantly decreased in miR-324-null mice relative to WT controls. * signifies p-value < 0.05, assessed using two-sided Student's *t*-tests.

3.2.4 *Hippocampal and neocortical RNA sequencing of miR-324-null mice*

In order to identify genes and biological pathways dysregulated by lack of *Mir324* which may be responsible for the observed phenotypes, RNA-seq of RNA extracted from 13.5-month-old male miR-324-null and WT mouse hippocampus and neocortex was undertaken (dataset

freely available at National Center for Biotechnology Information (NCBI) Gene Expression Omnibus (GEO), accession GSE158337). The murine *Mir324* locus is within a predicted 3'UTR transcript variant of *Dvl2*, antisense to the *Acadvl* locus, but no reads from either genotype mapped to the predicted variant of *Dvl2* and reads that mapped to *Acadvl* differed only a minimal amount at the deletion locus between genotype (Figure 3.6a). Western blotting was utilised to confirm that *Mir324* deletion and the resulting minor alterations to read mapping did not affect the protein levels of Acadvl and Dvl2, thus confirming that the hippocampal hyperexcitability identified was due to the removal of miR-324 and not dysregulation of *Acadvl* and *Dvl2* (Figure 3.6b).

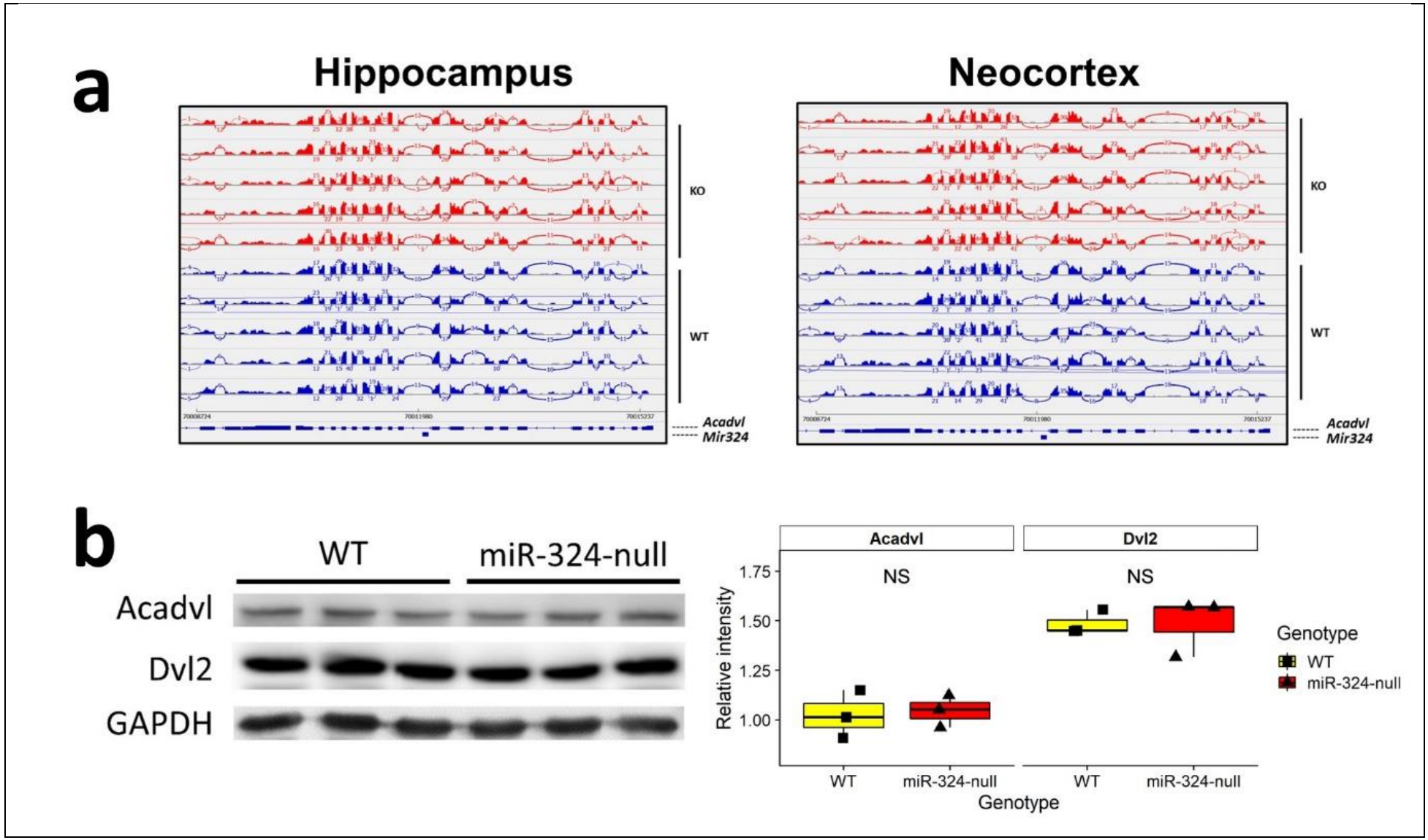
a
Hippocampus
Neocortex
KO
WT
Acadvl
Mir324
b
WT
miR-324-null
Acadvl
Dvl2
GAPDH
Acadvl
Dvl2
NS
NS
Relative intensity
1.75
1.50
1.25
1.00
WT
miR-324-null
WT
miR-324-null
Genotype
Genotype
WT
miR-324-null

Figure 3.6 - Mir324 deletion does not affect the expression of Acadvl or Dvl2. (**a**) A Sashimi plot of splicing at the *Mir324* locus showed that very little splicing variation is seen between miR-324-null and WT samples aged 13.5 months, both in hippocampus and neocortex. Red indicates miR-324-null samples and blue indicates WT samples. The region shown is at the coordinates chr11:70,008,183-70,017,428. (**b**) Western blotting revealed that no change to Acadvl or Dvl2 at a protein level resulted from *Mir324* deletion, relative to the housekeeping protein GAPDH. Quantification of the relative intensities of Acadvl and Dvl2 is also shown. Protein for this experiment was extracted from the hippocampi of female miR-324-null and WT mice (N = 3 per genotype) aged 7-months.

Principal component analysis (PCA) of the RNA-seq data showed variance corresponding to the different brain regions to be greater than the variance corresponding to the genotypes, due to the relatively low number of differentially expressed genes (Figure 3.7a). However, when comparing all genes ranked by fold-change the two datasets were highly correlative [342] (Figure 3.7b). The removal of the *Mir324* locus resulted in 126 genes significantly differentially expressed (adjusted p-value ≤ 0.05) in the hippocampus and 81 genes significantly differentially expressed in the neocortex. A total of 40 genes were differentially expressed in both tissues, all of which were regulated in the same direction in both hippocampus and neocortex (Figure 3.7c; list of shared differentially expressed genes shown in Table 3.1).

Disease Ontology (DO) enrichment analysis [343] showed that differentially expressed genes were significantly enriched for epilepsy syndrome in the hippocampus RNA-seq, but not in the neocortex (Figure 3.8a). Therefore, related genes of interest (GOIs) were identified by filtering for epilepsy-associated genes in the DO that were significantly differentially expressed in miR-324-null samples relative to WT controls, in either hippocampus or neocortex RNA-seq results (adjusted p-value ≤ 0.05). Only 4 genes fitted these criteria, each of which was only significantly differentially expressed in the hippocampus (Table 3.2). These GOIs were measured using RT-qPCR in both the 13.5-month-old (male) and the 7-month-old (male and female) hippocampal samples, with only *Pnpo* identified as significantly differentially downregulated in all three datasets (Figure 3.8b).

Gene	Hippocampus RNA-seq		Neocortex RNA-seq	
	logFC	Adjusted p-value	logFC	Adjusted p-value
Mrpl27	-1.45	3.84×10^{-60}	-1.26	1.99×10^{-44}
Sp6	2.25	1.81×10^{-24}	1.92	1.61×10^{-17}
Nme1	-1.03	6.26×10^{-25}	-0.786	1.59×10^{-13}
Gm4811	2.95	6.72×10^{-12}	2.80	2.17×10^{-9}
Phb	-0.567	3.54×10^{-10}	-0.531	7.00×10^{-9}
B230217C12Rik	-0.862	1.73×10^{-22}	-0.577	1.29×10^{-8}
Utp18	0.545	1.87×10^{-8}	0.564	1.04×10^{-8}
Mrpl10	0.421	1.32×10^{-7}	0.508	8.52×10^{-12}
Gm5540	2.44	1.85×10^{-7}	2.10	5.00×10^{-9}
Mllt6	-0.323	2.91×10^{-7}	-0.430	4.71×10^{-13}
Gm4875	2.68	8.15×10^{-11}	1.85	4.17×10^{-7}
Gm6304	2.07	1.68×10^{-6}	1.83	5.81×10^{-7}
Gm3555	-1.71	9.01×10^{-6}	-1.60	4.60×10^{-6}
Gm20390	0.428	1.12×10^{-5}	0.440	4.60×10^{-6}
Nme2	-1.55	1.98×10^{-28}	-0.705	4.71×10^{-5}
Gm10184	0.701	7.68×10^{-6}	0.559	4.88×10^{-5}
Dgke	-0.523	6.87×10^{-8}	-0.400	0.000355
Cbx8	0.762	0.00192	0.848	0.000296
Pigz	-1.18	8.79×10^{-6}	-0.904	0.00474
Cacng6	-1.27	0.000714	-1.18	0.00414
Chd9	-0.312	0.00533	-0.367	0.000236
Rapgefl1	-0.139	0.00594	-0.202	2.26×10^{-7}
Suox	0.476	0.00165	0.447	0.00474
Gm5898	1.05	0.00641	1.18	7.71×10^{-5}
Rnf157	-0.307	0.00397	-0.309	0.00386
AC102745.1	-0.632	0.00594	-0.784	0.00396
Acbd4	0.356	0.0160	0.389	0.00544
Ncor2	-0.248	0.0217	-0.393	1.31×10^{-6}
Ece1	-0.217	0.00371	-0.201	0.0267
C1qb	-0.260	0.0275	-0.305	0.00484
Spop	-0.232	0.000350	-0.174	0.0347
Cep85	-0.307	0.0169	-0.303	0.0198
Hif1an	-0.245	0.0233	-0.265	0.0140
Ccl28	0.987	0.0186	1.04	0.0198
Gm10282	0.942	0.0311	1.10	0.00830
Eno1b	0.215	0.0384	0.245	0.00111
Alpk1	0.996	0.00481	0.842	0.0386
Cd300lf	0.888	0.0275	0.916	0.0267
Smarce1	-0.402	0.0267	-0.397	0.0386
Mill2	-0.611	0.0380	-0.661	0.0305

Table 3.1 - Genes significantly differentially expressed in both the hippocampal and neocortical RNA-seq experiments in miR-324-null samples relative to wild-type controls.

Genes are ordered by mean adjusted p-value. All were regulated in the same direction in both hippocampal and neocortical samples.

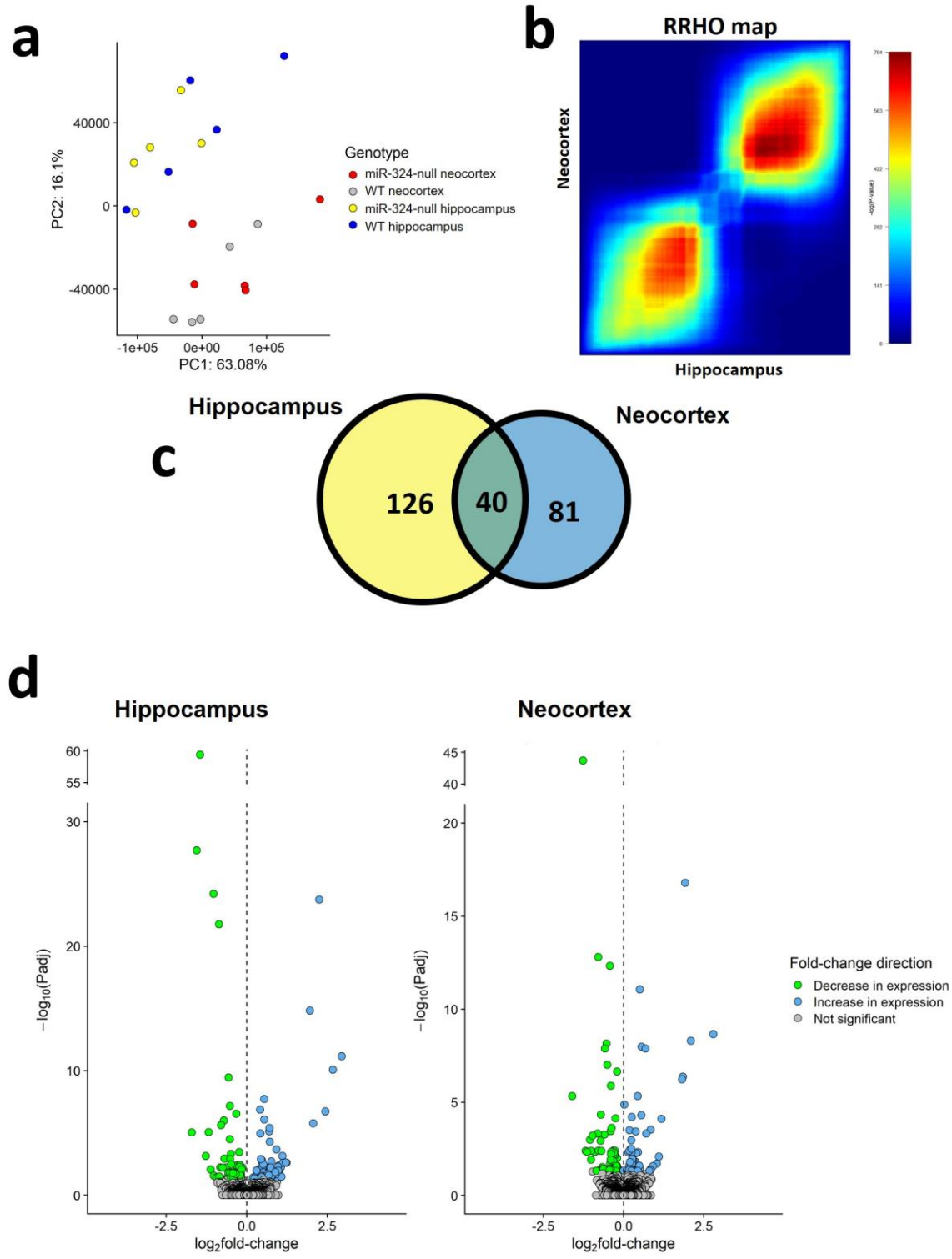

Figure 3.7 - Initial analysis of RNA-seq of hippocampus and neocortex in 13.5-month old male miR-324-null and WT mice. (**a** and **b**) PCA analysis does not show as strong a segregation of samples by genotype as it does by tissue, although the results of hippocampus and neocortex RNA-seq experiments are well correlated using RRHO (sample permutation p-value < 0.001). (**c**) Only 40 of the genes found to be differentially expressed

in miR-324-null samples relative to WT controls were found to be differentially expressed in both tissues. (**d**) Volcano plots for hippocampus and neocortex tissue showing the fold-change and adjusted p-value of each gene. Genes significantly increased in expression in miR-324-null samples are shown in blue, genes significantly decreased in expression are shown in green and genes showing no significant changes (adjusted p-value > 0.05) are coloured grey.

Gene	**Hippocampus RNA-seq**		**Neocortex RNA-seq**	
	logFC	**Adjusted p-value**	**logFC**	**Adjusted p-value**
Pnpo	-0.523	3.20×10^{-5}	-0.253	0.248
Scn5a	1.21	0.00240	0.0309	0.989
Gria1	0.295	0.0282	0.0678	0.850
Gad1	0.270	0.0466	0.186	0.315

Table 3.2 - Genes found to be differentially expressed (adjusted p-value ≤ 0.05) in either the hippocampus or neocortex RNA-seq experiments which are associated with epilepsy according to the Disease Ontology [343]**.**

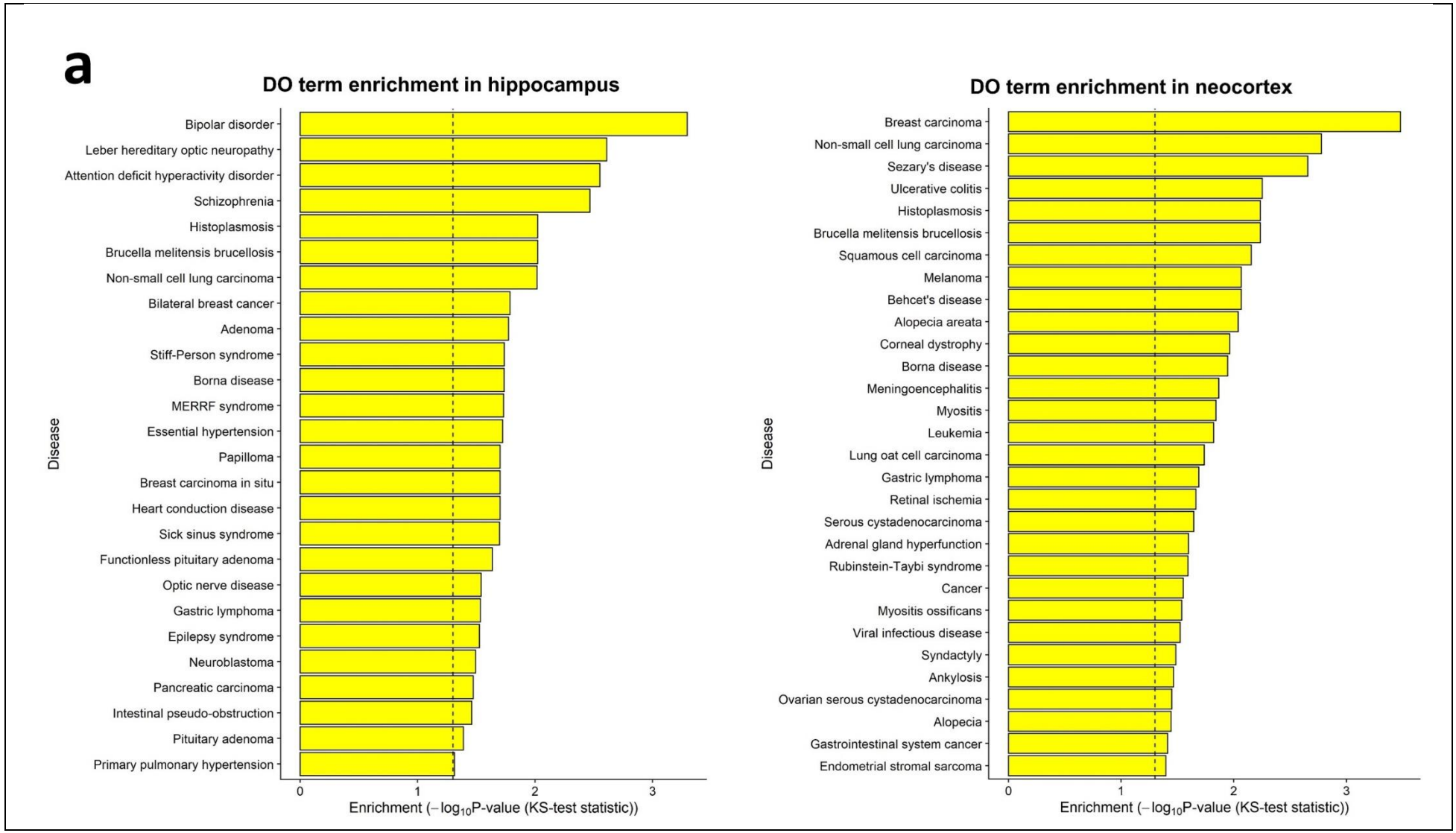
a
DO term enrichment in hippocampus
Bipolar disorder
Leber hereditary optic neuropathy
Attention deficit hyperactivity disorder
Schizophrenia
Histoplasmosis
Brucella melitensis brucellosis
Non-small cell lung carcinoma
Bilateral breast cancer
Adenoma
Stiff-Person syndrome
Borna disease
MERRF syndrome
Essential hypertension
Papilloma
Breast carcinoma in situ
Heart conduction disease
Sick sinus syndrome
Functionless pituitary adenoma
Optic nerve disease
Gastric lymphoma
Epilepsy syndrome
Neuroblastoma
Pancreatic carcinoma
Intestinal pseudo-obstruction
Pituitary adenoma
Primary pulmonary hypertension
Disease
0
1
2
3
Enrichment (−log10P-value (KS-test statistic))
DO term enrichment in neocortex
Breast carcinoma
Non-small cell lung carcinoma
Sezary's disease
Ulcerative colitis
Histoplasmosis
Brucella melitensis brucellosis
Squamous cell carcinoma
Melanoma
Behcet's disease
Alopecia areata
Corneal dystrophy
Borna disease
Meningoencephalitis
Myositis
Leukemia
Lung oat cell carcinoma
Gastric lymphoma
Retinal ischemia
Serous cystadenocarcinoma
Adrenal gland hyperfunction
Rubinstein-Taybi syndrome
Cancer
Myositis ossificans
Viral infectious disease
Syndactyly
Ankylosis
Ovarian serous cystadenocarcinoma
Alopecia
Gastrointestinal system cancer
Endometrial stromal sarcoma
Disease
0
1
2
3
Enrichment (−log10P-value (KS-test statistic))

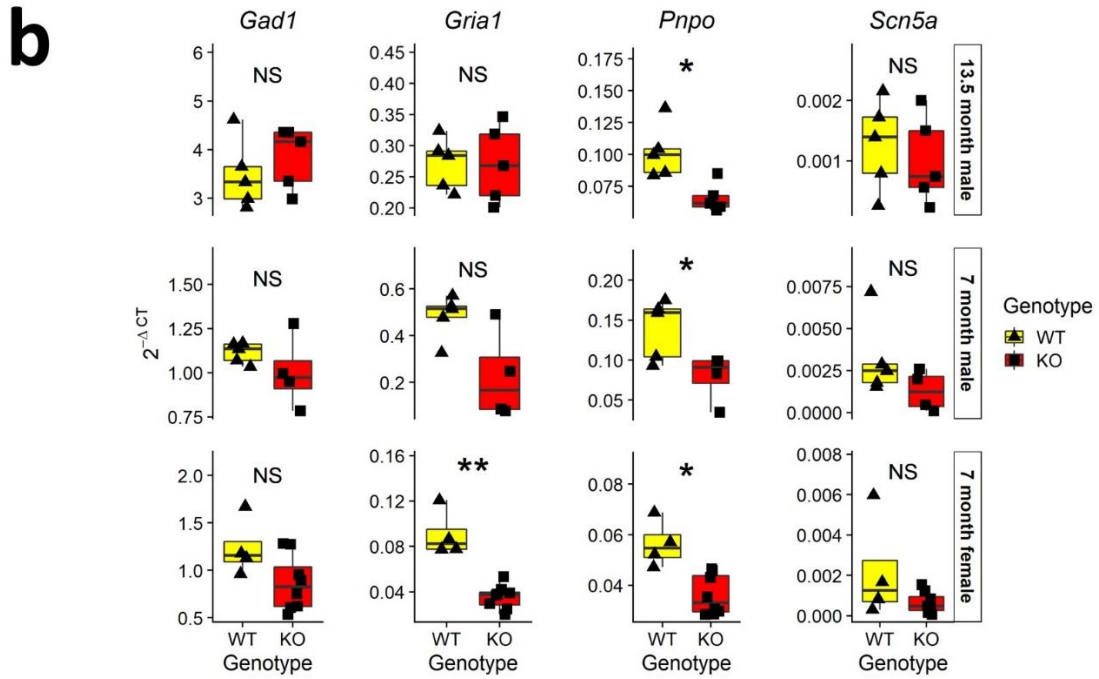

Figure 3.8 - Relation of RNA-seq results to epilepsy. (**a**) Epilepsy syndrome was significantly enriched in the hippocampus RNA-seq, but not in the neocortical experiment (p-values = 0.03 and 0.74 respectively), using terms and gene associations from the DO. Other neurological disorders, such as bipolar disorder, attention deficit hyperactivity disorder and schizophrenia, were also found to be statistically significantly enriched in the hippocampus but not in the neocortex. The significance of each DO term was established using a Kolmogorov-Smirnov test. The dotted line on each plot shows where the cut-off for significance at a 5% level is found. (**b**) RT-qPCR quantification of the expression of epilepsy-associated genes was undertaken in the hippocampus tissue of the 13.5-month-old male RNA-seq cohort and in 7-month-old male and female hippocampal validation cohorts, utilising *Ndufa2* as the housekeeping gene to normalise against. * and ** indicate p-values ≤ 0.05 and 0.01 respectively, using two-sided Student's *t*-tests to assess statistical significance.

3.2.5 *Identification of novel putative miR-324 targets in the hippocampus and cortex*

Both miR-324-5p and miR-324-3p are each predicted to target and repress a large number of genes; for both human and mouse, the miRNA target prediction algorithm TargetScan [5, 67] predicts over 3000 targets for each arm, although some of these overlap (Figure 3.9a). There are reportedly two distinct isomiRs of miR-324-3p, miR-324-3p.1 and -3p.2 [364-366], which alter the predicted seed binding sequence and therefore also the predicted targets (Figure 3.9b). Most miRNA target prediction databases are able to predict targets for both miR-324-3p.1 and -3p.2 and therefore in this project, miR-324-3p is used to refer to both isomiRs.

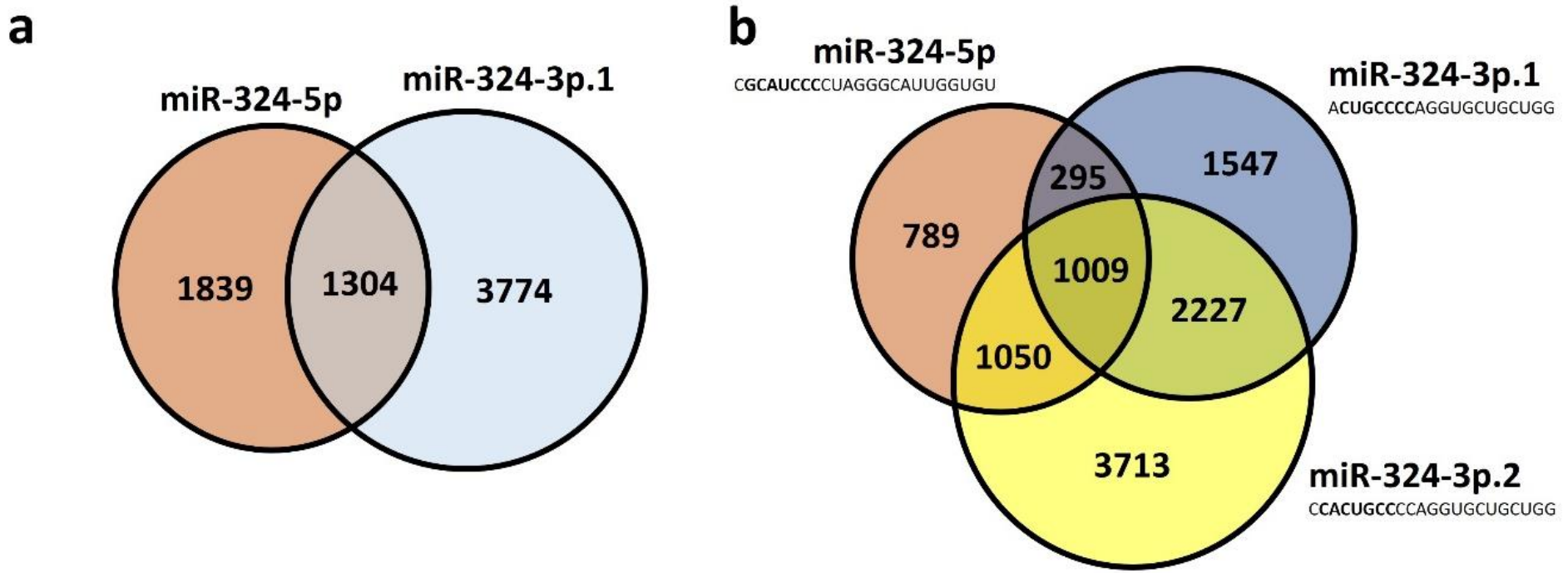

Figure 3.9 - Numbers of predicted targets for each mature arm of miR-324, according to the TargetScan algorithm [5, 67]**.** (**a**) Both miR-324-5p and miR-324-3p.1, often considered the canonical miR-324-3p isomiR, are each predicted to target over 3000 mRNAs, although 1304 of these putative targets are shared between the two arms. (**b**) There are two distinct mature miR-324-3p sequences called miR-324-3p.1 and -3p.2, and most target prediction algorithms predict targets for both isomiRs. The mature sequences of miR-324 are based on miRBase deep sequencing reads [365, 366] and within these, the seed sequences are shown in bold.

By utilising the TargetScan miRNA target prediction algorithm, a number of the genes identified as being differentially expressed between miR-324-null and WT tissue were also observed to be predicted targets of miR-324-5p or miR-324-3p [5, 67] (Figure 3.10a). Of these predicted targets, 6 were significantly upregulated (adjusted p-value ≤ 0.05) in miR-324-null samples in both hippocampus and cortex (Table 3.3). The expression of each of these genes was measured using RT-qPCR in the 13.5-month old male hippocampal samples and additionally in hippocampal samples from 7-month old male and female cohorts (Figure 3.10b), and the expression of *Cd300lf*, *Sp6* and *Suox* was confirmed to be consistently increased in miR-324-null samples.

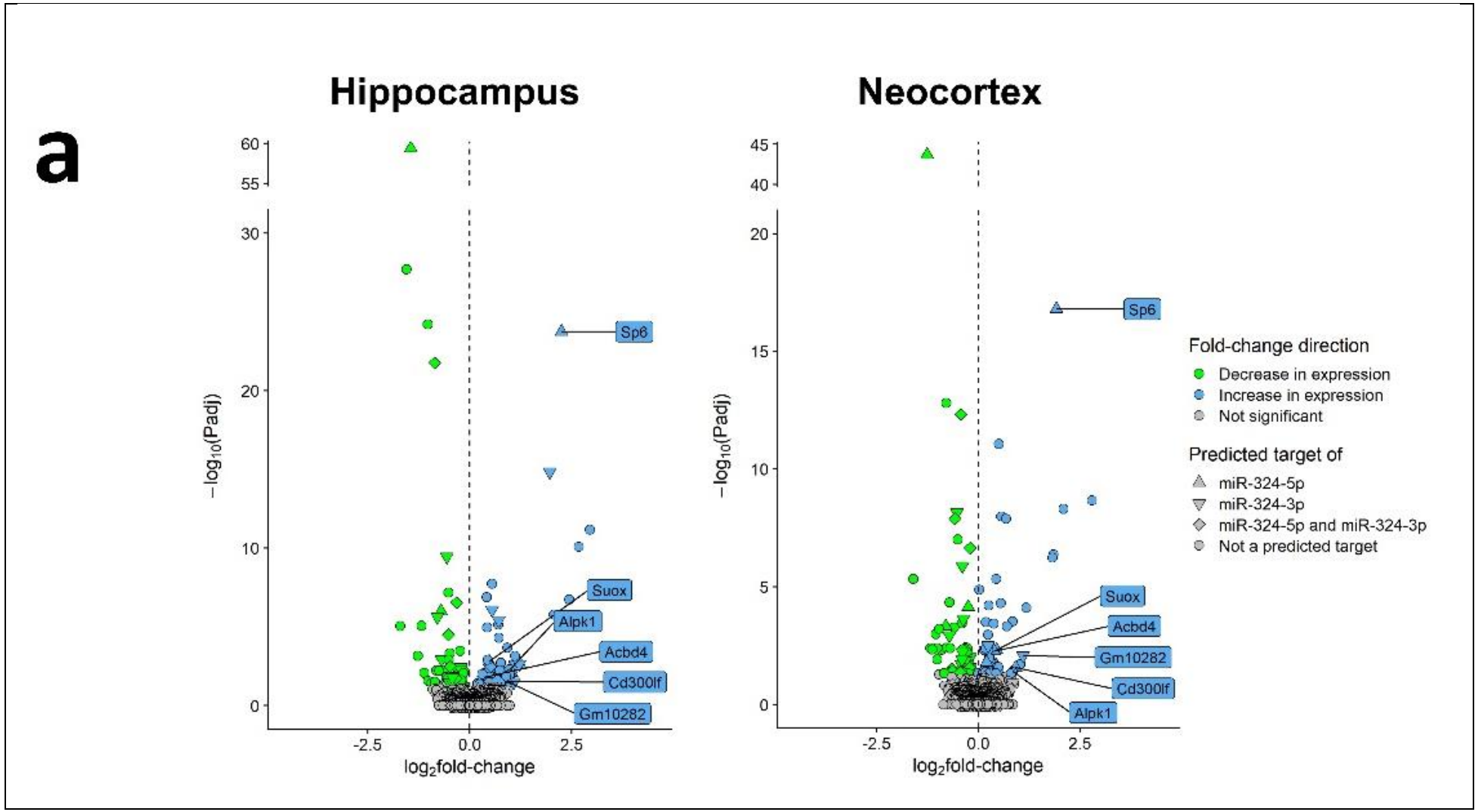
a
Hippocampus
Neocortex
−log10(Padj)
log2fold-change
Sp6
Suox
Alpk1
Acbd4
Cd300lf
Gm10282
Fold-change direction
Decrease in expression
Increase in expression
Not significant
Predicted target of
miR-324-5p
miR-324-3p
miR-324-5p and miR-324-3p
Not a predicted target

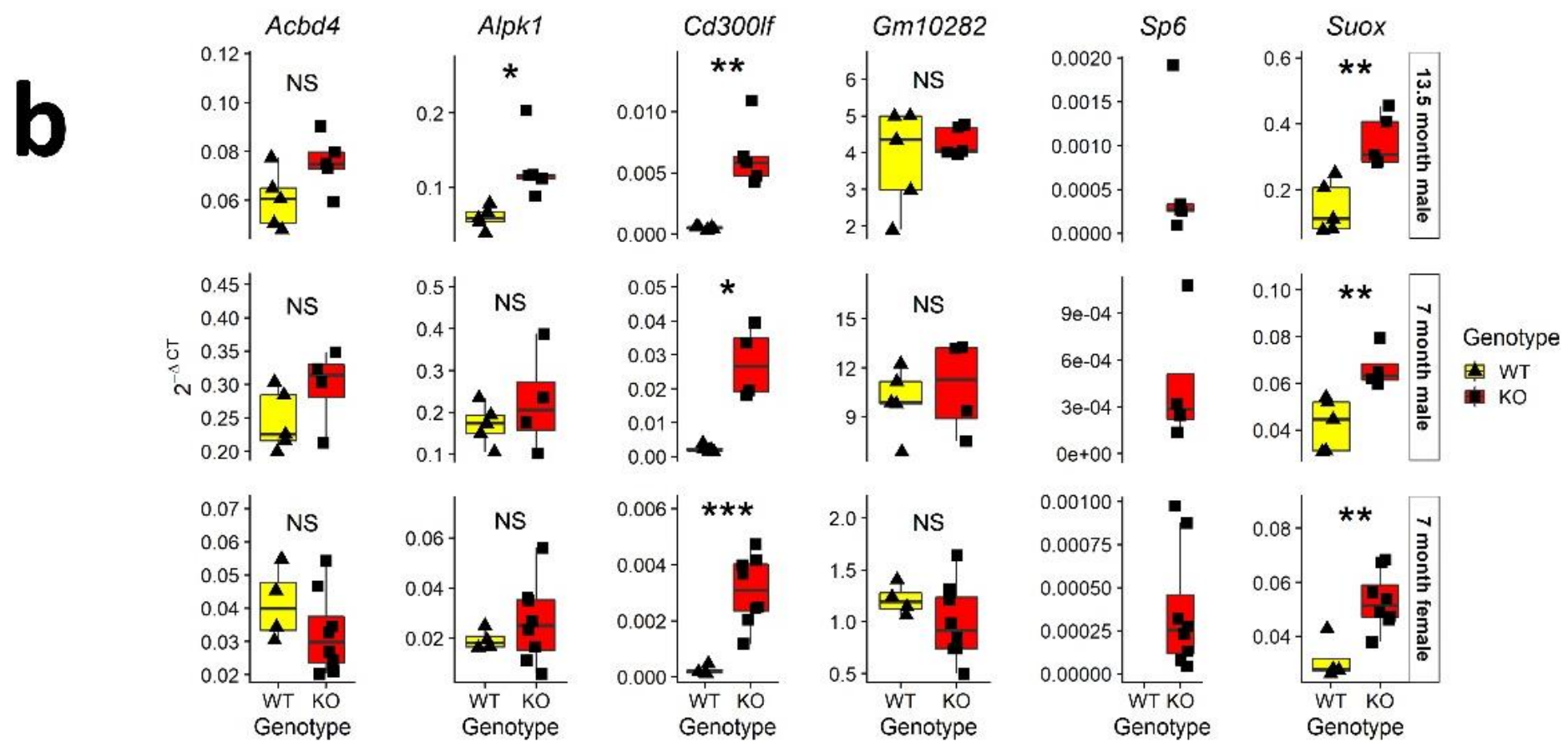

Figure 3.10 - Initial identification of putative miR-324 targets in murine hippocampus and cortex. (**a**) Volcano plots for hippocampus and neocortex tissue showing the fold-change and adjusted p-value of each gene in addition to whether it is a predicted target of either arm of miR-324, according to the TargetScan algorithm [5, 67]. Genes significantly increased in expression in miR-324-null samples are shown in blue, genes significantly decreased in expression are shown in green and genes showing no significant changes (p-value > 0.05) are coloured grey. Genes found to be

significantly upregulated in miR-324-null hippocampus and neocortex, in addition to being a miR-324 target, are labelled. (**b**) Of the genes that were predicted targets of miR-324 and significantly upregulated in both the hippocampus and neocortex RNA-seq, only *Cd300lf* and *Suox* were significantly differentially expressed in all cohorts. *Sp6* was also highly upregulated, but it was not detected in any of the WT samples in any cohort and so statistical significance could not be calculated. *Ndufa2* was utilised as the housekeeping gene to normalise against. *, ** and *** indicate p-values ≤ 0.05, 0.01 and 0.001 respectively, using two-sided Student's *t*-tests to assess statistical significance.

Gene	Hippocampus RNA-seq		Neocortex RNA-seq	
	logFC	**Adjusted p-value**	**logFC**	**Adjusted p-value**
Sp6	2.25	1.81×10^{-24}	1.92	1.61×10^{-17}
Suox	0.476	0.00165	0.447	0.00474
Acbd4	0.356	0.0160	0.389	0.00544
Gm10282	0.942	0.0311	1.10	0.00830
Alpk1	0.996	0.00481	0.842	0.0386
Cd300lf	0.888	0.0275	0.916	0.0267

Table 3.3 - Putative miR-324 targets in murine hippocampus and cortex. Of the 40 genes significantly differentially expressed in murine hippocampus and neocortex RNA-seq experiments (adjusted p-value ≤ 0.05), 6 were predicted as targets either of miR-324-5p or -3p by the TargetScan algorithm [5, 67]. Putative target genes are ordered by mean adjusted p-value.

Although *Cd300lf*, *Sp6* and *Suox* were validated to be significantly upregulated in miR-324-null mice at both 13.5- and 7-months of age and are predicted targets of miR-324, the interactions between miR-324 and the 3'UTRs of these genes were not necessarily direct. In order to test this, 3'UTR-luciferase reporter assays were undertaken in murine C3H10T1/2 cells. Both *Cd300lf* and *Suox* showed statistically significant reductions in relative luciferase activity in the presence of miR-324-5p but not miR-324-3p or a miRNA negative control mimic (miCon; Figure 3.11a). Additionally, when 2 nucleotides were mutated in the predicted binding sites of miR-324-5p in either of the *Cd300lf* and *Suox* 3'UTRs, the miR-324-5p-mediated downregulation was ablated, strongly indicating that miR-324-5p binds the *Cd300lf* and *Suox* 3'UTRs *in vitro* and mediates repression of *Cd300lf* and *Suox* through these interactions (Figure 3.11b). Western blotting of Suox and CD300lf from female murine hippocampal tissue aged 7-months revealed that the levels of both proteins increased in miR-324-null samples relative to WTs, although the increase in CD300lf levels did not achieve statistical significance at a 5% threshold (Figure 3.11c).

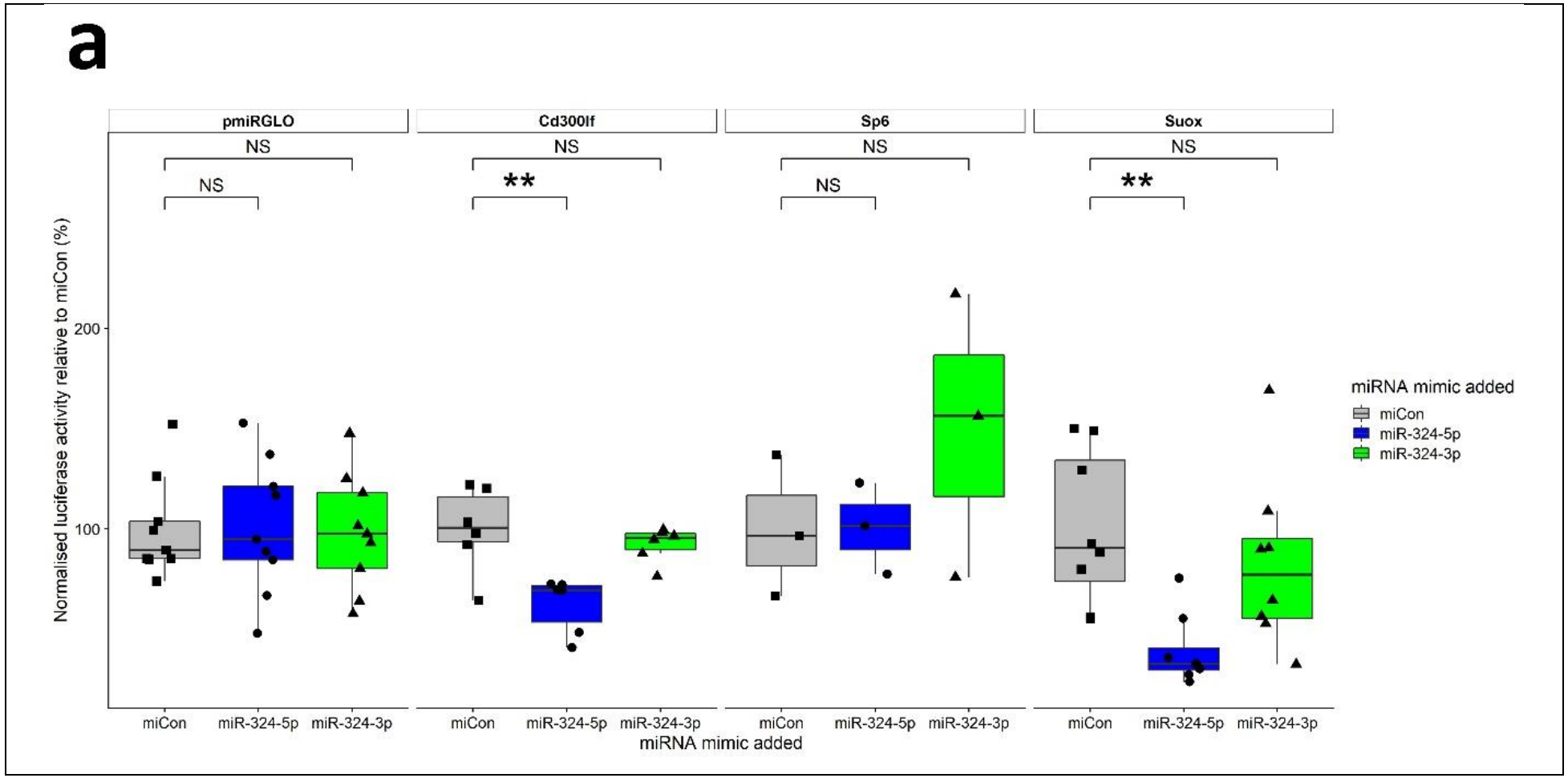
a
pmiRGLO
Cd300lf
Sp6
Suox
NS
NS
NS
**
NS
NS
**
Normalised luciferase activity relative to miCon (%)
200
100
miCon
miR-324-5p
miR-324-3p
miRNA mimic added

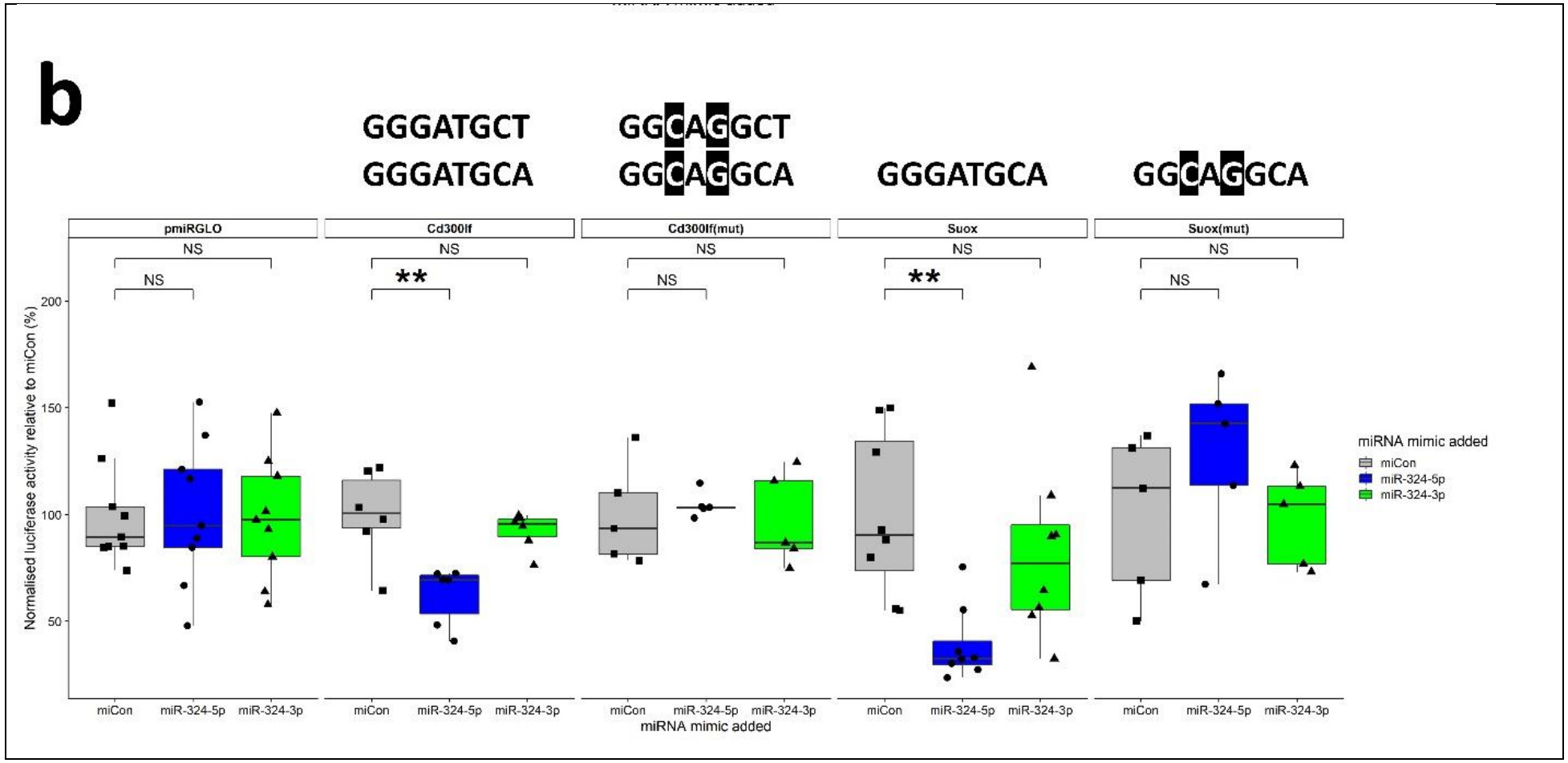
b
GGGATGCT
GGGATGCA
GGCAGGCT
GGCAGGCA
GGGATGCA
GGCAGGCA
pmiRGLO
Cd300lf
Cd300lf(mut)
Suox
Suox(mut)
NS
**
Normalised luciferase activity relative to miCon (%)
200
150
100
50
miCon
miR-324-5p
miR-324-3p
miRNA mimic added

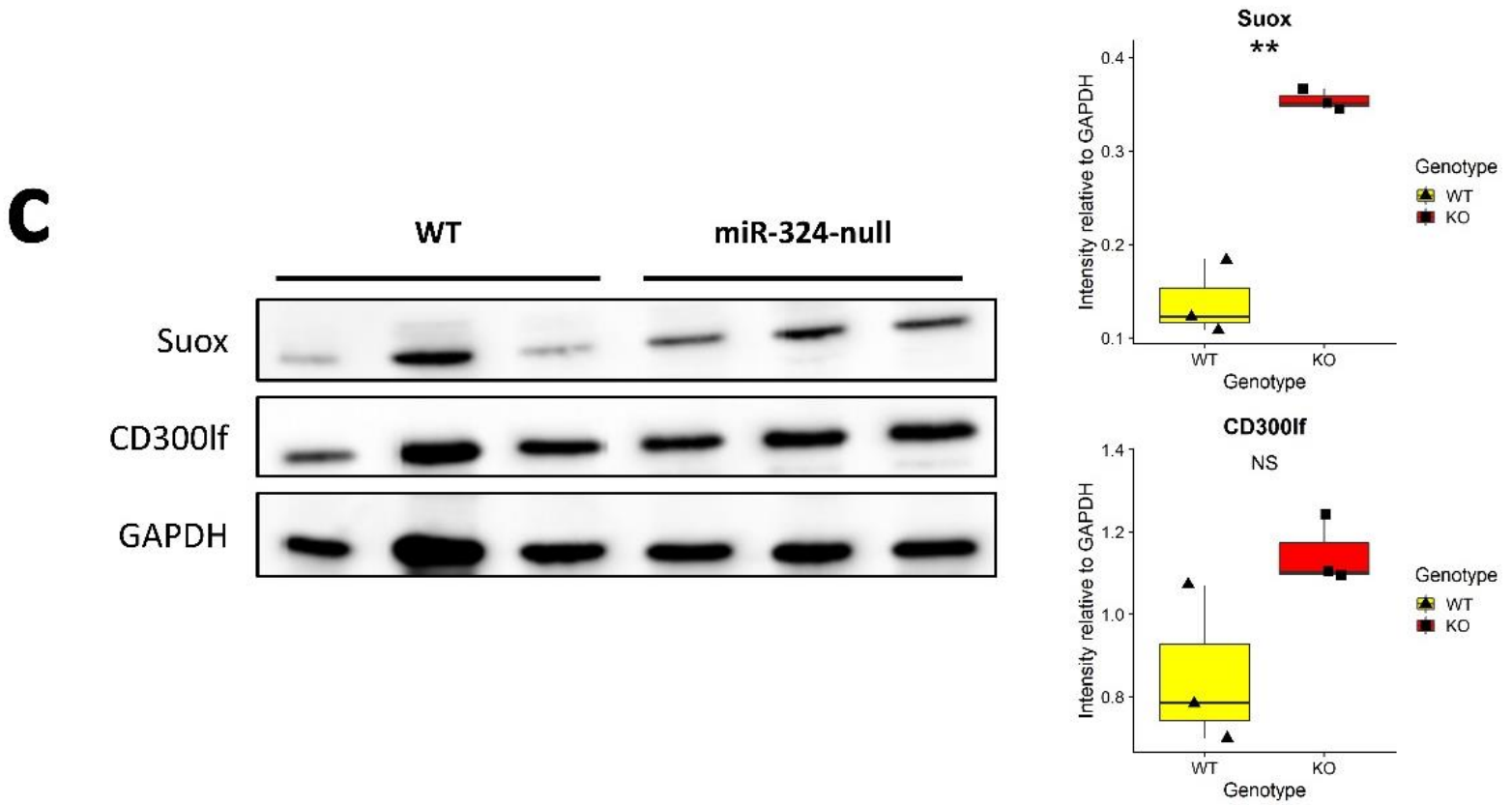

Figure 3.11 - Identification of novel miR-324-5p targets using 3'UTR luciferase assays. (**a**) C3H10T1/2 murine cells were transfected with 3'UTR-pmiRGLO constructs and subsequently also with either a negative control miRNA mimic (miCon) or a mimic of miR-324-5p or miR-324-3p. Luciferase activity was measured after cells were incubated at 37°C for 24 hours. Relative luciferase activity was calculated as a ratio of Renilla activity, an internal transfection control of pmiRGLO, and values were plotted as a percentage of mean miCon luciferase activity for each construct. *Suox* and *Cd300lf*, but not *Sp6*, were identified as direct miR-324-5p targets *in vitro*. (**b**) When 2 nt of the miR-324 binding sites of the *Cd300lf* and *Suox* 3'UTRs

were mutated, shown as *Cd300lf(mut)* and *Suox(mut)*, the miR-324-5p-mediated repression was inhibited in both cases. The predicted miR-324-5p binding sites of each 3'UTR are shown above the panel corresponding to that 3'UTR, with mutations highlighted in black. For panels **a** and **b**, the means of at least 3 independent experiments were used to test statistical significance in two-tailed Student's *t*-tests. A negative control was included for each independent experiment (pmiRGLO) in addition to miCon and, after miR-324 targets were identified, one of these was used as a positive control for each independent experiment. (**c**) Western Blotting was used to confirm that the changes to the quantity of target gene mRNAs affected levels of the corresponding proteins in female hippocampal tissue aged 7-months. Suox levels were significantly increased in miR-324-null samples relative to WT controls and, although levels of CD300lf were not statistically significantly increased at a 5% level (p-value = 0.077), there was a trend towards increased expression in miR-324-null samples. Suox and CD300lf band intensities were normalised against GAPDH. In all panels, ** indicates p-values ≤ 0.01.

3.3 Discussion

3.3.1 *miR-324-null mice display abnormal hippocampal electrophysiology and behaviour*

The electrophysiological analyses undertaken here illustrated a clear hippocampal hyperexcitability with an increase in epilepsy-associated events in mice lacking *Mir324*. However, the networks regulating oscillatory activity in the hippocampi of these mice are evidently not severely impaired, as no significant changes were observed in the area power, peak amplitude or peak frequency in slices obtained from miR-324-null animals. However, a mild behavioural phenotype is seen in these animals; an increased maximum number of rears and a decreased mean step length. Therefore, there is a mild observable effect *in vivo* resulting from the lack of *Mir324* in the brain. Furthermore, increased rearing behaviour is often an indicator of seizure-like activity in rodents [367-369] and therefore it is plausible that this is an *in vivo* manifestation of the hippocampal hyperexcitabilility which was observed *ex vivo* in miR-324-null mice. The altered step length is less clear in terms of a link to epilepsy, but it could be as a result of dysregulation of motor function in miR-324-null mice, as has been identified previously in many mouse models of neurological conditions, including Alzheimer's Disease [370-372]. However, it cannot be ruled out that the altered step length is actually nothing at all to do with neurological changes in miR-324-null mice; these animals lack *Mir324* expression in all tissues, and so it is feasible that miR-324-null mice may show abnormalities in tissues within the musculoskeletal system in addition to the tissues of the brain.

It is unclear at precisely which developmental time point the increased excitability and behavioural abnormalities emerge in the miR-324-null mice. In future studies it would therefore be beneficial to undertake electrophysiology and behavioural analyses at earlier time points. It would additionally be useful to develop a conditional knockout model of miR-324, in which the *Mir324* locus is flanked by loxP sites. Crossing these animals with, for example, the Fzd9-Cre mice, in which Cre recombinase expression is largely restricted the hippocampus and cortex [373, 374], would allow analysis of the effect of *Mir324* deletion only in these specific tissues, reducing the risk of any compensatory mechanisms. Furthermore, investigation into which specific neuronal populations have been affected in miR-324 null mice is also essential in order to assess whether the increased excitability is universal throughout the hippocampus or whether there are subregional differences. For example, it is possible although not likely that only neurons within the CA3 hippocampal region are abnormal in miR-324-null mice. It would therefore be beneficial to investigate whether similar hyperexcitability

effects are observed in for example the CA1 and CA2 regions, in order to understand how severely impacted the murine hippocampus is by the deletion of Mir324. Furthermore, miR-324 has previously been discussed in relation to neuronal populations such as astrocytes and primary neurons [375, 376], so it would be beneficial to investigate whether the same miR-324-null hyperactivity phenotype is observed in mice conditionally lacking Mir324 in these neuronal subpopulations.

3.3.2 *Gene dysregulation in the murine hippocampus and neocortex due to the lack of Mir324*

The genetic cause of the increase in hyperexcitability and behavioural abnormality is somewhat difficult to elucidate fully, but may stem from *Pnpo* and *Suox*, genes which were both found to be significantly differentially expressed in the hippocampus, both in RNA-seq and RT-qPCR, and which are both related to epilepsy. *Pnpo* expression was decreased in hippocampal miR-324-null samples. In humans, mutant *PNPO* results in a specific form of epilepsy known as pyridoxal phosphate-dependent epilepsy (PPDE). This presents due to the inability of affected individuals to produce sufficient levels of pyridoxal 5'-phosphate (P5P), a key cofactor for many neurotransmitter biosynthesis reactions [377, 378]. Patients affected by PPDE often present with neonatal epileptic encephalopathy, although some cases of later-onset epilepsy can also be effectively treated with P5P. This suggests that there may be a far broader spectrum of phenotypes for individuals lacking PNPO than is currently suggested in the literature [379, 380]. It is, therefore, conceivable that the decreased expression of *Pnpo* in miR-324-null mice could play a role in the generation of increased epileptic events identified here.

Suox was also identified to be differentially expressed in miR-324-null mice, in addition to being a novel direct target of miR-324-5p *in vitro*. In humans, *SUOX* is associated with isolated sulfite oxidase deficiency (ISOD), a disorder caused by lack of functional SUOX. ISOD, like PPDE, is associated with increased epileptic events in patients, although the relative gene expression of *SUOX* in ISOD is decreased [381], in contrast to the increased *Suox* expression identified in miR-324-null mice. It is possible that an excess of murine Suox results in a phenotype similar to that of human SUOX deficiency, although there are no studies in the literature testing this hypothesis, and so exactly what effect an increase in *Suox* expression may have is currently unknown.

The second novel miR-324-5p target identified in this study, *Cd300lf*, has no direct link to epilepsy in the literature. *Cd300lf* encodes a membrane receptor which is involved in the

regulation of immune response to infection, which in mice is the primary receptor of norovirus [382-384]. It has previously been reported that in the THP-1 human cell line, treatment with CD300LF results in reduced levels of MMP-9 [385], a matrix metalloproteinase (MMP) which, along with the 22 other human MMPs, is key to the maintenance of extracellular matrix across many biological processes [386, 387]. These include maintenance of the blood-brain barrier and homeostatic regulation of synaptic excitability, both of which have previously been demonstrated to be regulated in part by the activity of MMP-9 [388-391]. Thus, the lack of *Cd300lf* repression in miR-324-null mice may result in reduced levels of MMP-9, therefore contributing to the abnormal neurological activity seen *ex vivo* in hippocampal slices from miR-324-null mice. However, any CD300lf-mediated *Mmp9* repression would necessarily be subtle, considering we identified no significant change at a transcriptomic level. Further investigation is therefore required to identify whether this dysregulation of the CD300lf-MMP-9 axis can affect MMP-9 levels to any biologically meaningful extent.

In order to fully investigate whether lack of miR-324 effects the observed phenotypes through the regulation of either *Cd300lf* or *Suox*, it would be beneficial to assess how similar global or conditional *Suox*- and *Cd300lf*-overexpressor mice are in relation to the miR-324-null mice; presumably if the pathways involved in these disorders are shared between miR-324 and *Suox* or *Cd300lf* then a similar hyperexcitability phenotype would be observed in both miR-324-null and *Suox*- and *Cd300lf*-overexpressor mice.

3.3.3 *Previously identified miR-324 target genes*

Although the novel miR-324 targets identified and validated in this study appear to respond similarly to miR-324 in both murine tissue and the C3H10T1/2 cell line, it is possible that some targets of miR-324 were unable to be identified by the methodology we used. For example, *Gpc1* and *App*, the latter of which is one the most confidently predicted miR-324-5p targets [5, 67], were previously identified as direct targets of miR-324-5p using both transcriptomic and proteomic techniques in C3H10T1/2 cells [151]. However, in our RNA-seq experiment there is no significant increase in the expression of either gene. Another reported miR-324-5p target, *Kv4.2*, was identified using luciferase assays and proteomic analyses, but the authors reported that no changes in mRNA levels were identified [111]. We also identified no significant changes to *Kv4.2* mRNA levels between miR-324-null and WT mice using RNA-seq. All three of these genes have been implicated in neurological activity; *Gpc1* in relation to the developmental regulation of brain size [392], *App* in the amyloidogenesis pathway [113] and

Kv4.2 in the regulation of seizure activity and excitability [116, 117]. Given the close relationship of these genes to the phenotypes observed in miR-324-null mice, all of these genes may well also be direct miR-324-5p targets in the brain, and the fact that they were not identified in this study could be attributed to the lack of in-depth proteomic analyses in addition to the differences in models used. However, considering that the vast majority of protein level alteration can be attributed to a change in the amount of corresponding mRNA [393], it is reasonable to assume that the target identification analysis undertaken in this study should have detected most direct miR-324 target genes that were expressed at a reasonable level in the murine hippocampus and neocortex. It should also be considered that in the case of *Gpc1* and *App*, *Mir324* was removed rather than overexpressed, and therefore the possibility remains that although these genes fulfil all *in silico* miR-324-5p target requirements, very little regulation by miR-324-5p occurs *in vivo* under physiological miR-324-5p levels.

3.3.4 *The miR-324-null increased rearing phenotype bears similarity to models of epilepsy and other neurological diseases*

This chapter was focused on attempting to elucidate the link between miR-324 and epilepsy. Although a clear *ex vivo* hyperexcitability phenotype and mild *in vivo* behavioural phenotypes were observed, these are not necessarily unique to epilepsy. Other neurological conditions identified in the DO analysis included bipolar disorder, attention deficit hyperactivity disorder (ADHD) and schizophrenia, each of which have also been shown to be associated with cortical hyperexcitability [394-397]. The possibility that the increase in hippocampal excitability reported here could also point to a role of miR-324 in other neurological conditions therefore cannot be excluded. Interestingly, mouse models of both bipolar disorder and schizophrenia have been found to show increased rearing due to hyperactivity. Several bipolar disorder mouse models utilise the circadian rhythm to induce bipolar disorder-like symptoms. One method to achieve this is through a method called lateral hypothalamic kindling, which is achieved through frequent electrical stimulation of the lateral hypothalamus. This results in symptoms of mania in rats, including increased rearing [398], as was observed in the miR-324-null mice. Models of schizophrenia have also shown evidence of increased rearing when social isolation is used to induce schizophrenia-like symptoms, in addition to general hyperactivity relative to WT controls [399-403]. Considering this in combination with the gene dysregulation of genes annotated to bipolar disorder and schizophrenia in miR-324-null mice, it is possible that lack of miR-324 may be producing the observed phenotype of increased rearing through

bipolar disorder- and schizophrenia-related genes in addition to those associated with epilepsy.

3.3.5 *Transient inhibition of miR-324 may produce a distinct effect to that observed in miR-324-null mice*

Previously, *in vivo* downregulation of miR-324 using an antagomir has been associated with decreased epileptic activity, which was measured primarily as a decreased number of seizures and spikes [112]. In contrast to these results, in this chapter I have shown that *Mir324* deletion results in an increase in IIDs and spikes. However, there were several notable differences between the two studies; Tiwari *et al*. (2019) used an injectable miR-324-5p antagomir to produce a transient miR-324-5p downregulation, and tested the effect of this in mouse models of epilepsy where pilocarpine had been used to induce *status epilepticus*. It is therefore possible that different phenotypes are seen because miR-324-5p was only transiently downregulated. Additionally, pilocarpine treatment in mice has been shown to induce changes in a large number of genes [404, 405], which may also play a role in the difference between the results identified in our study and those identified by Tiwari and colleagues. Interestingly, the downregulation of *Kv4.2* by miR-324-5p observed by Gross *et al*. (2016) was observed only during or shortly after seizure activity [111] and therefore future studies should explore whether miR-324 targets different genes and therefore produces different effects in the hippocampus during *status epilepticus* compared to under non-seizure circumstances.

3.3.6 *Age and sex limitations*

The greatest limitations of the study presented here are the differences in age and sex between the mice used for each experiment. Although age and sex are always controlled for direct comparisons, there is a risk that the conclusions of each experiment do not necessarily hold for all time points, considering that there are notable increases in CA3 neuronal activity with age [406, 407] and many epilepsies are widely regarded as being more prevalent in either males or females; for example, Focal cortical dysplasia is more commonly found in male patients, whereas Idiopathic generalized epilepsy and Photosensitive epilepsy are both more commonly observed in female patients [408-411]. Additionally it is possible that the expression of *Mir324* is altered with age or sex; many key miRNAs are upregulated in the ageing brain [412], including miR-34a [413], which also shows differential expression by sex [414]. The RT-qPCR validation of putative miR-324 target genes shows that, at least at a transcriptomic level, the novel miR-324 target genes identified here respond similarly to lack

of *Mir324* in samples obtained from 13.5-month males, 7-month old females and 7-month old males, thus minimising these limitations, but not eliminating them entirely.

3.4 Summary

In this chapter I have shown using RT-qPCR that global miR-324-null mice do not express *Mir324* in the hippocampus or neocortex and that *Mir324* is expressed at detectable levels in WT controls. I have additionally used *in situ* hybridisation to show that miR-324 can be detected specifically in the CA3 hippocampal region of WT mice.

Additionally, hippocampal slices from miR-324-null mice showed increased excitability with an increased frequency of IIDs and spikes in the LFP relative to WT controls. These are both indicative of epileptic seizures or related neurological conditions, and suggest that the hippocampal networks regulating oscillatory activity in miR-324-null mice may be impaired. However, this impairment is not severe, considering that no statistically significant changes to area power, peak amplitude or peak frequency were observed in miR-324-null mice.

I have also shown that miR-324-null mice present with a mild behavioural abnormality *in vivo*, consisting of a decreased mean step length and an increased number of maximum rears per minute. No obvious difference was however observed in regard to the mean number of touches, mean number of rears or mean distance covered per minute. Despite this phenotype being relatively mild, it is interesting that increased rearing has previously been found in epilepsy mouse models, in addition to models of bipolar disorder and schizophrenia, both of which were significantly enriched for in the Disease Ontology analysis undertaken in this chapter. Therefore, the *ex vivo* miR-324-null phenotype may not exclusively be the result of dysregulation of epilepsy genes; potentially miR-324-null mice may also be affected by the dysregulation of genes annotated to other neurological conditions as well.

RNA sequencing and RT-qPCR validation revealed that two epilepsy-associated genes were identified to be differentially expressed in the hippocampus and neocortex of mice lacking *Mir324*; *Suox* and *Pnpo*. Dysregulation of human *SUOX* is causal of ISOD, a disorder which results in epilepsy-like seizures, and mutant human *PNPO* results in PPDE. By utilising 3'UTR-luciferase assays, *Suox* was additionally shown to be a direct target of miR-324-5p *in vitro*, as was *Cd300lf*, a gene indirectly associated with neurological function through the modulation of matrix metalloprotease expression and activity. The neurological phenotypes identified in

miR-324-null mice may therefore result from the altered expression of one or multiple of these genes. Further investigation into the downstream effects of *Mir324* removal may reveal novel pathways involved in ISOD and PPDE and therefore also may identify novel pharmaceutical targets for treating these conditions.

In summary, I have shown in this chapter that miR-324-null mice lack *Mir324* expression in the hippocampus and neocortex. This lack of *Mir324* results in increased seizure events *ex vivo* in addition to an increased rearing and altered gait phenotype *in vivo*, the former of which is often found in rodent models of epilepsy, bipolar disorder and schizophrenia. RNA-seq revealed that miR-324-null mice show decreased expression of *Pnpo* and increased expression of *Suox*, both of which would be predicted to result in neurological phenotypes. *Suox* and another gene, *Cd300lf*, which is also associated with neurological function, were both validated as direct miR-324 targets, and therefore the miR-324-null neurological phenotypes identified in this chapter may stem from the dysregulation of these targets.

Chapter 4 - miR-324-null mice display a high bone mass phenotype *in vivo*

4.1 Introduction

4.1.1 *miR-324 is associated with bone remodelling and cartilage maintenance*

miR-324 has previously been associated across several studies with musculoskeletal biology and in mice, both miR-324-5p and -3p are expressed at higher levels than almost every other tissue, the exception being the brain [109]. In humans, the abundance of miR-324-3p in serum shows a statistically significant positive correlation with bone mineral density (BMD), mineral apposition rate (MAR), bone formation rate (BFR) and mineralised bone surface. Additionally, a statistically significant negative correlation has been reported between miR-324-3p serum abundance and cortical porosity [316, 317]. These correlations suggest that increased levels of miR-324 may act to either enhance bone formation or repress bone resorption. However, when a separate study used the murine MSC-like cell line C3H10T1/2 cells to investigate whether transfection with additional miR-324-5p could enhance osteogenesis, a decrease in bone nodule formation and mineralisation was in fact observed [151]. The results of these studies combined suggest that potentially miR-324-5p and -3p regulate bone formation in opposing directionalities, although it is clear that an *in vivo* model is required in order to elucidate fully the role of miR-324 in mammalian bone formation.

miR-324 has additionally been the focus of several publications relating to cartilage maintenance. In a study investigating miRNAs differentially expressed in cartilage obtained from osteoarthritis (OA) patients relative to neck of femur fracture (NOF; the control group) patients, miR-324-5p was found to be significantly upregulated in OA tissue, suggesting a link between miR-324 and OA [151, 188]. This was hypothesised to be via the regulation of the Hedgehog (Hh) signalling pathway, which is essential to normal endochondral ossification, the process through which cartilage is replaced by bone [178-180]. Several key genes involved in the process are reported miR-324 targets; *SMO* and *GLI1* have been shown to be direct targets in humans, whereas *Gpc1* has been reported to be the murine miR-324 Hh target [151, 186, 187]. Dysregulation of these target genes, and therefore of the Hh signalling pathway overall, would be expected to lead to severe deformity *in vivo* [181, 184], and therefore again highlights the necessity to investigate the activity of miR-324 *in vivo*.

4.1.2 *The use of knockout mouse models to investigate bone diseases*

The human skeleton is a complex system, within which many different cell types cooperate or compete with one another to grow and maintain bone tissue throughout life. Due to these complexities, it is perhaps unsurprising that bone diseases comprise a wide spectrum, in terms

of severity, cause and age at which each disease manifests. The skeletons of other mammals such as rhesus monkeys and rats have been demonstrated to bear much similarity to the human skeleton, most notably in that the bone mass of each of these species decreases with age as it does in the human skeleton [415, 416]. However, this ageing-mediated bone loss has also been well-studied in the mouse *Mus musculus* [417-419], which is the most commonly used mammalian model organism for translational research. The use of mice therefore allows access to a far greater range of genetic tools than rhesus monkeys, such as the use of global and conditional knockout technologies.

Many important discoveries in relation to bone diseases have been identified in mouse models since the development of gene knockout technology. For example, *Tnfrsf11b* (osteoprotogerin; OPG)-null mice were found to develop early-onset osteoporosis, demonstrating that OPG is a regulator of osteoclastogenesis [420]. Mice lacking *Runx2* were found to show a complete lack of mature osteoblasts, with the *Runx2*-null mice dying immediately after birth due to lack of ossification in the ribs, thus preventing breathing [421]. This therefore proved not just that *Runx2* is essential for osteoblast lineage commitment, but that *Runx2* is essential for viability as well.

Mouse models also allow a greater understanding of cells which are ordinarily very difficult to investigate, such as the osteocyte. These are cells embedded within mineralised bone, which are thought to act in a regulatory fashion in order to assist in balancing bone resorption and formation, responding to chemical signals as well as mechanical stress [422]. Due to their location deep within the mineralised bone, isolation of these cells has proved challenging over the years and therefore understanding has remained limited. The use of mouse models has allowed conditional knockout of genes selectively in the osteocyte, most commonly through the use of the *Dmp1*-Cre driver [423-425]. This has allowed remarkable insight into the key roles osteocytes play in the skeleton, such as that osteocytes are essential sources of RANK-L, which is required by osteoclasts for differentiation and maturation [203, 426]. The use of knockout mouse models to study bone is therefore crucial in the elucidation of key processes involved in bone diseases.

A final essential importance of mouse models in the study of any chosen disease is that the vast majority of research required to elucidate disease mechanisms, and therefore eventually develop treatments for diseases, would be highly unethical in humans. The biological similarities of mice and humans allow such work to be undertaken in mice, therefore

advancing the research to a point where a clinical trial could be brought to human patients. Furthermore, the use of a model organism such as the mouse allows for tight control of the environment, such that any effect observed is likely to be from a biological cause, rather than an environmental one, as would be an issue if human patients were used.

4.1.3 *Bone formation and resorption*

Bone remodelling consists of two opposing processes, resorption and formation, which are tightly regulated to maintain bone mass whilst bone tissue is concomitantly being constantly turned over. Osteoclasts are multinucleated cells which are responsible for bone resorption. They are formed through the fusion of up to several hundred haematopoietic lineage-derived macrophages, upon simulation with M-CSF and RANK-L [197, 198], which is provided by osteoblasts, bone lining cells and/or osteocytes [199-205]. Once matured, osteoclasts can form a sealed pocket against the mineralised bone surface, into which is pumped protons and vesicles containing the proteolytic enzyme cathepsin K, allowing dissolution of the inorganic and organic bone components, respectively [196, 208, 210, 211]. Osteoclast life ultimately ends either in apoptosis or in cellular fission into several smaller multinucleate cells, known as osteomorphs. These cells hold the ability to fuse together with each other once again or fuse with mononucleated pre-osteoclasts in order to re-mature [216].

Osteoblasts are the cells which mediate the opposing process, bone formation. Unlike osteoclasts, osteoblasts are mononuclear cells and are derived from the mesenchymal lineage. Upon subsequent stimulation with Sox9, Runx2 and Osx, MSCs are directed into the osteochondroprogenitor lineage and onwards towards osteoblasts. Once matured, osteoblasts act in functional units rather than individually and secrete proteins required to form the bone matrix, which include alkaline phosphatase, a key enzyme in the bone formation process. Hydroxyapatite is also deposited, allowing calcium to be added into the skeleton [218-220]. Osteoblasts are able to signal to immature osteoclasts during this process with M-CSF and RANK-L, or the RANK-L decoy receptor OPG, thus helping to maintain a balance between bone resorption and formation [223, 224]. Osteoblasts either commit apoptosis at the end of life, enter a quiescent state and become a bone lining cell or embed themselves into the surrounding matrix and terminally differentiate into an osteocyte [225, 226]. These cells are just as crucial as osteoblasts and osteoclasts in regulating bone remodelling, although they do not directly act to resorb or form new bone. Instead, osteocytes sense mechanical or chemical signals and can secrete RANK-L and M-CSF in order to stimulate

osteoclastogenesis [201, 203, 205] or Sost (sclerostin) in order to repress osteoblast activity [230, 231].

4.1.4 *The use of micro-computed tomography and histomorphometry to analyse bone formation and resorption in vivo*

Even with the use of knockout mouse models to investigate bone diseases, research into the activity and communication of individual bone cell types would be incredibly difficult without the use of the technologies and methodologies that have become increasingly commonplace in the field in recent years. One of the key technologies used in the study of bone microstructure is micro-computed tomography (μCT), which allows high-resolution analyses of structures at a micron scale. The first μCT technologies were developed over 40 years ago, and the basic methodology remains similar to the present date; a sample is placed inside a chamber and subsequently rotated horizontally whilst an X-ray source and imaging array are used to image the sample at specific pre-set rotational intervals [427, 428]. Sequential transaxial tomographic reconstructions of the sample are produced by applying a tomographic reconstruction algorithm to the X-ray scans, and these can be appended on top of one another to generate a 3D model of the original sample [427]. The high resolution of this technology allows for in-depth analyses of the properties of both trabecular and cortical bone, in addition to the marrow space between the bone compartments. The utility of this technology is illustrated clearly by the increased usage of μCT in the bone research field; more than half of scientific publications relating to μCT in 2009 were focussed on bone [429].

Although μCT is of great benefit in imaging and analysing the eventual net result of bone cells, which is to say mineralised bone itself, it is of limited use in imaging these cells directly. Therefore, other methodologies must necessarily be used in combination with μCT to fully comprehend bone cell interactions and activities at a cellular level. For osteoclasts, *in vivo* imaging primarily utilises the osteoclast-selective marker tartrate-resistant acid phosphatase (TRAP), which is encoded by the *Acp5* gene in mice. Considering *Acp5* is expressed only at very low levels in surrounding cells, the expression of TRAP can be used to stain for mature osteoclasts in fixed tissue sections [430]. Subsequent analyses can therefore be undertaken to assess number and size of mature TRAP-expressing cells, thus resulting in a clear overview of how many osteoclasts survive to maturation *in vivo* in an individual sample.

Osteoblast imaging *in vivo* is more challenging than the imaging of osteoclasts, as these cells are mononucleated, far smaller than osteoclasts, and many of the characteristic genes

expressed by osteoblasts are also expressed in precursor cells to a certain degree. Therefore, rather than imaging osteoblasts directly *in vivo*, a methodology to assess the rate of bone formation, which is a direct result of osteoblast activity, is commonly used. For this, mice are injected twice with fluorochromes (generally calcein or alizarin red-S) prior to sacrifice, both of which intercalate with mineralised bone as it forms. Therefore, when the bones are fixed and sectioned, fluorescent imaging allows the identification of two bone formation lines, occurring as a result of calcein or alizarin red-S incorporated as bone was forming immediately after each injection [431]. The length of time between the injections and the physical distance between the calcein or alizarin red-S fluorochrome lines can therefore be used to calculate the rate of bone formation in terms of μm per day. Whilst this methodology is effective in assessing the rate of formation of mineralised bone, it does not assess the rate of formation of unmineralised bone, called the osteoid. This is an important distinction, as in diseases such as hypophosphatemic rickets, it is the amount of osteoid relative to the amount of mineralised bone that increases rather than a decrease in the overall amount of bone [247, 248]. For assessing the relative amount of osteoid therefore, a Goldner's Trichrome stain is utilised. This stain allows a sharp distinction between cartilage, which stains very pale green, osteoid, which stains red, and mineralised bone, which stains green [432, 433]. From this stain therefore, an accurate assessment of the amount of osteoid per bone can be elucidated in a sample *in vivo*. An additional benefit to this is than the nuclei of cells stain dark blue and the cytoplasm light grey, and therefore analyses in terms of population numbers of cells which are usually difficult to image, such as osteocytes, can also be obtained.

4.1.5 *Chapter aims*

1. Investigate and compare bone microstructure from miR-324-null and WT control mice.
2. Investigate bone formation rates of osteoblasts from miR-324-null and WT mice.
3. Assess differences between genotypes with regard to the other mesenchymal lineage cell type predominant in bone marrow; the adipocyte.
4. Compare the number and size of bone-resorbing cells, osteoclasts, in miR-324-null mice and WT controls.
5. Assess whether the number and density of osteocytes is altered between miR-324-null and WT mice.

6. Investigate whether any increase or decrease in cartilage damage can be observed in miR-324-null mice relative to WT controls.

4.2 Results

4.2.1 *miR-324-null mice display a high bone mass phenotype in addition to tibial bowing*

miR-324-5p has previously been associated with human osteoarthritis [151, 188] in addition to miR-324-3p serum levels correlating with bone mineral density (BMD), MAR, BFR and mineralised bone surface [316-318]. However, miR-324-related musculoskeletal phenotypes have until now remained unexplored *in vivo*. Therefore, we investigated how the bone microstructure of male miR-324-null mice differs from that of male wild-type mice (WTs), aged 5-, 7- and 14-months. Although miR-324-null mice lacked any obvious alterations to limb development or body size, they did display dramatically increased bone thickness, both in the femoral and tibial trabeculae and cortex. The femoral trabecular thickness of miR-324-null mice was increased by a mean average of more than 10% at 5-months relative to age-matched WT controls, and this difference increased to approximately 15% by the age of 14-months. Tibial trabecular thickness was increased to an even greater extent, initially by approximately 15% at 5-months and reaching upwards of a 20% increase by 14-months. Therefore, miR-324-null mice display an increased trabecular thickness phenotype in both hind leg bones which worsens with age (Figure 4.1). In addition to displaying trabecular thickness as a percentage of age-matched WT controls, unnormalised trabecular thickness is also plotted, in terms of µm rather than as a percentage of age-matched WTs. Here, trabecular thickness remains relatively constant in both WT leg bones with age, although a mild increase can be observed in the tibia. In the femur, the miR-324-null trabecular thickness also remains relatively constant with age, although again in the tibia an increase with age is observed (Figure 4.1).

In addition to the difference in trabecular thickness, the trabecular structural model index (SMI) is also increased in both femoral and tibial miR-324-null bone relative to WT controls (Figure 4.1). Despite post-hoc tests failing to identify any ages at which the SMI is statistically significantly altered, the overall effect of genotype is statistically significant in both the femur and tibia. This increased overall SMI suggests that the trabecular structure of miR-324-null mice is more rod-like in structure than WT controls and therefore theoretically possesses a less mechanically competent structure than is found in WT bone of the same age [434].

Notably, SMI increases with age in both genotypes, and therefore it appears that miR-324-null mice may display an accelerated ageing phenotype with regard to this metric.

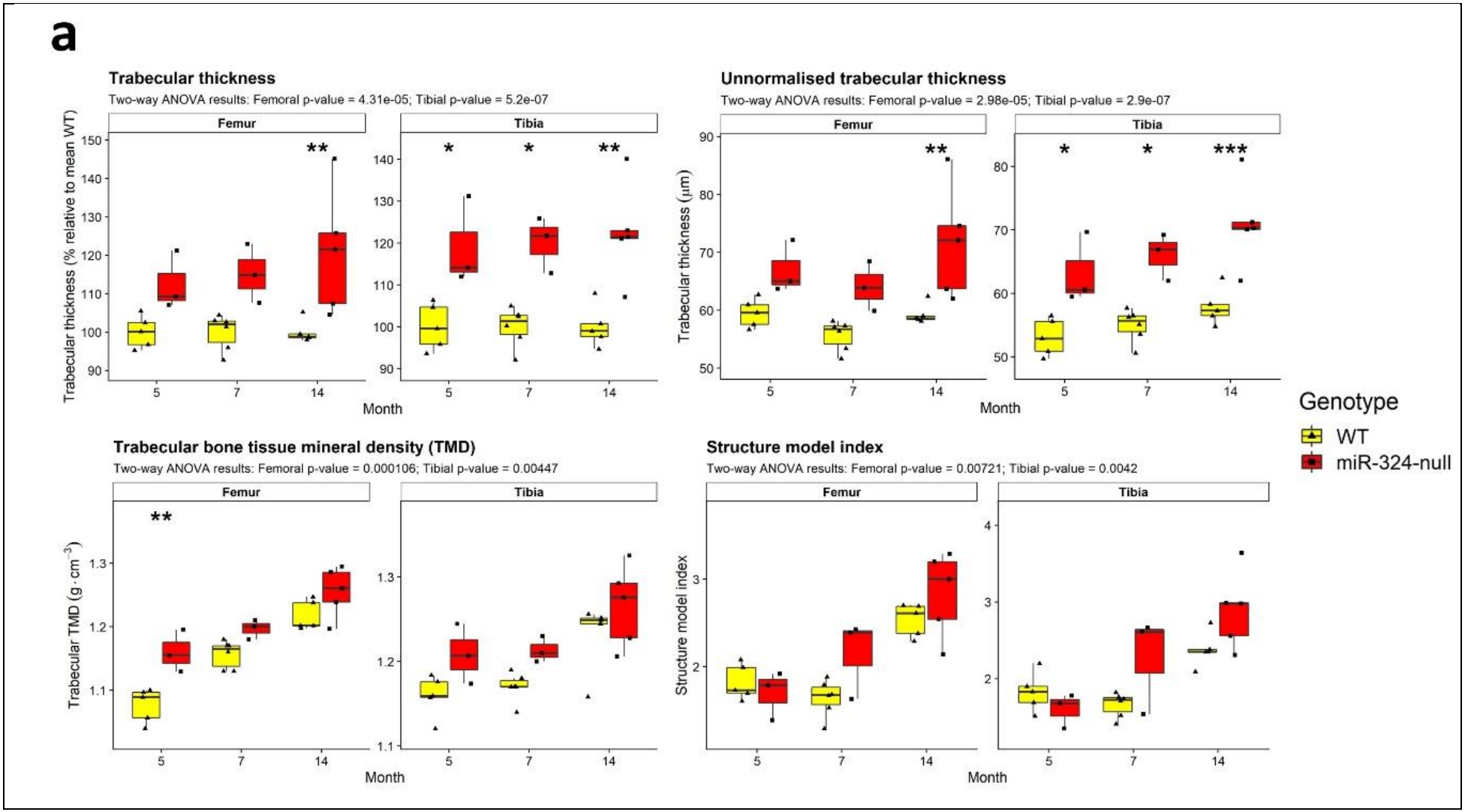
a
Trabecular thickness
Two-way ANOVA results: Femoral p-value = 4.31e-05; Tibial p-value = 5.2e-07
Femur
Tibia
Trabecular thickness (% relative to mean WT)
Month
Unnormalised trabecular thickness
Two-way ANOVA results: Femoral p-value = 2.98e-05; Tibial p-value = 2.9e-07
Trabecular thickness (μm)
Trabecular bone tissue mineral density (TMD)
Two-way ANOVA results: Femoral p-value = 0.000106; Tibial p-value = 0.00447
Trabecular TMD (g · cm⁻³)
Structure model index
Two-way ANOVA results: Femoral p-value = 0.00721; Tibial p-value = 0.0042
Structure model index
Genotype
WT
miR-324-null

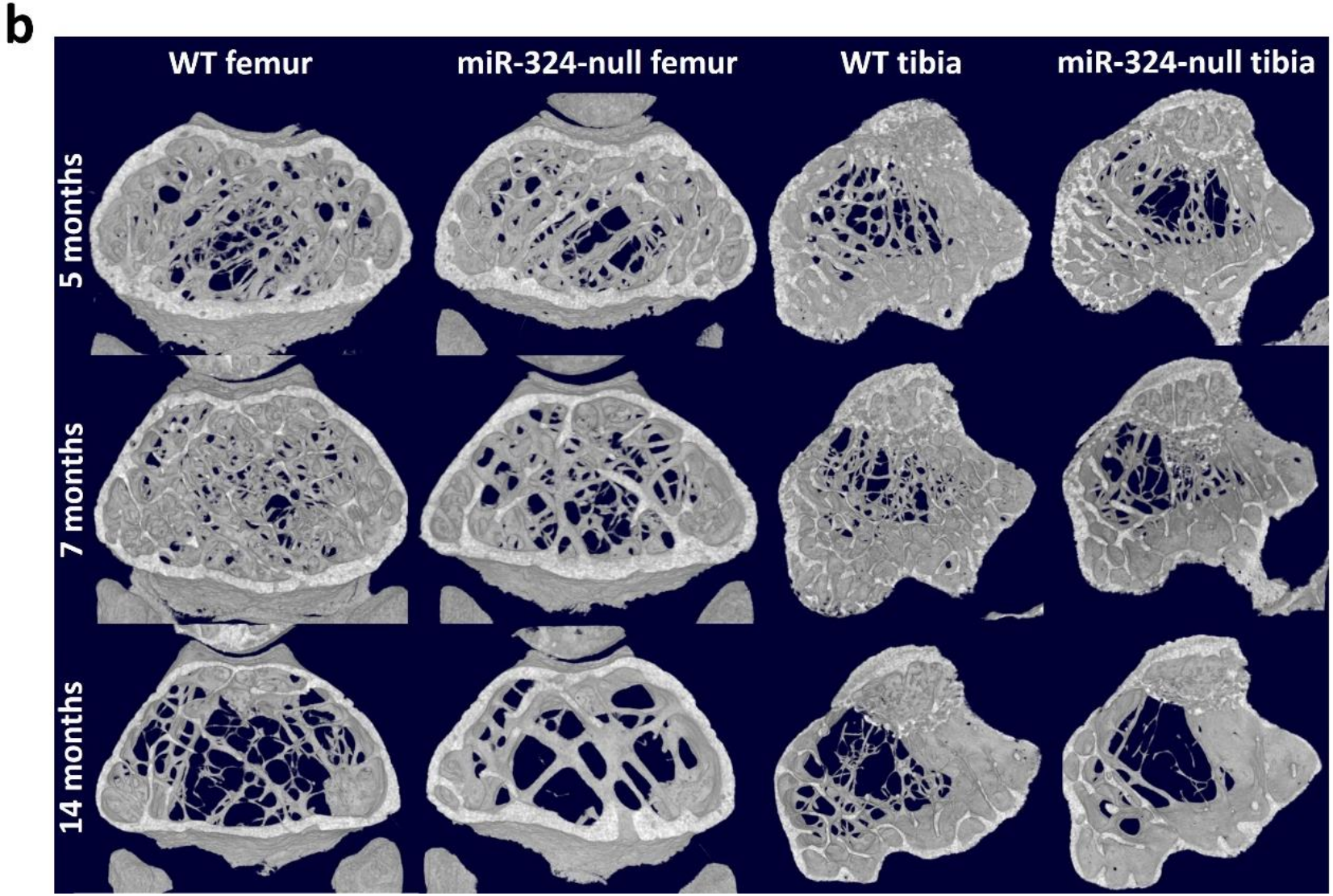
b
WT femur
miR-324-null femur
WT tibia
miR-324-null tibia
5 months
7 months
14 months

Figure 4.1 - miR-324-null mice aged display a high trabecular bone mass phenotype in addition to increased structure model index. (**a**) The trabecular thickness of both the femurs and tibiae of miR-324-null mice are significantly increased across the time points measured, as is the trabecular SMI and the bone tissue mineral density (TMD). In the femur, unnormalised trabecular thickness remains relatively constant with age in both miR-324-null and WT bone, whereas in the tibia, the trabecular thickness of both miR-324-null and WT bone appears to increase with age. Statistical significance overall across time points was assessed using two-way ANOVA and Tukey's HSD post-hoc tests were used to assess statistical significance at individual time points, for which *, ** and *** signify p-values ≤ 0.05, 0.01 and 0.001, respectively. (**b**) Representative trabecular femoral and tibial µCT reconstructions are shown for miR-324-null and WT mice aged 5-, 7- and 14-months. Slices on the transaxial plane are shown as a representation of cortical bone, taken from the midpoint of either the tibia or femur.

The hind leg bone cortical thickness of miR-324-null mice is also increased relative to WT controls, but unlike the trabecular phenotype, a worsening with age is not observed. The femoral cortical thickness of miR-324-null mice is fairly consistent relative to WT controls with ageing; femoral miR-324-null cortices remain approximately 10% thicker than WT cortices throughout life, perhaps with a slight reduction in the difference between genotypes by 14-months of age. miR-324-null tibial cortical thickness shows by far the greatest increase relative to WT cortical thickness at 5-months, with a mean increase in thickness of approximately 15%. However, this difference in thickness decreases by 7-months, to a mere 5% increase in miR-324-null tibial cortical thickness, and by 14-months the difference in tibial cortical thickness between genotypes is completely ablated (Figure 4.2). An interesting effect is observed when cortical thickness is plotted unnormalised with regard to age; in the femur, both in WT and miR-324-null cortices, the thickness increases from 5-months to 7-months, although a severe decrease in cortical thickness is subsequently observed at 14-months. In the tibial cortex, thickness is relatively constant in the WT samples with age, although miR-324-null cortical thickness decreased severely with age, until it reached WT levels by 14-months (Figure 4.2).

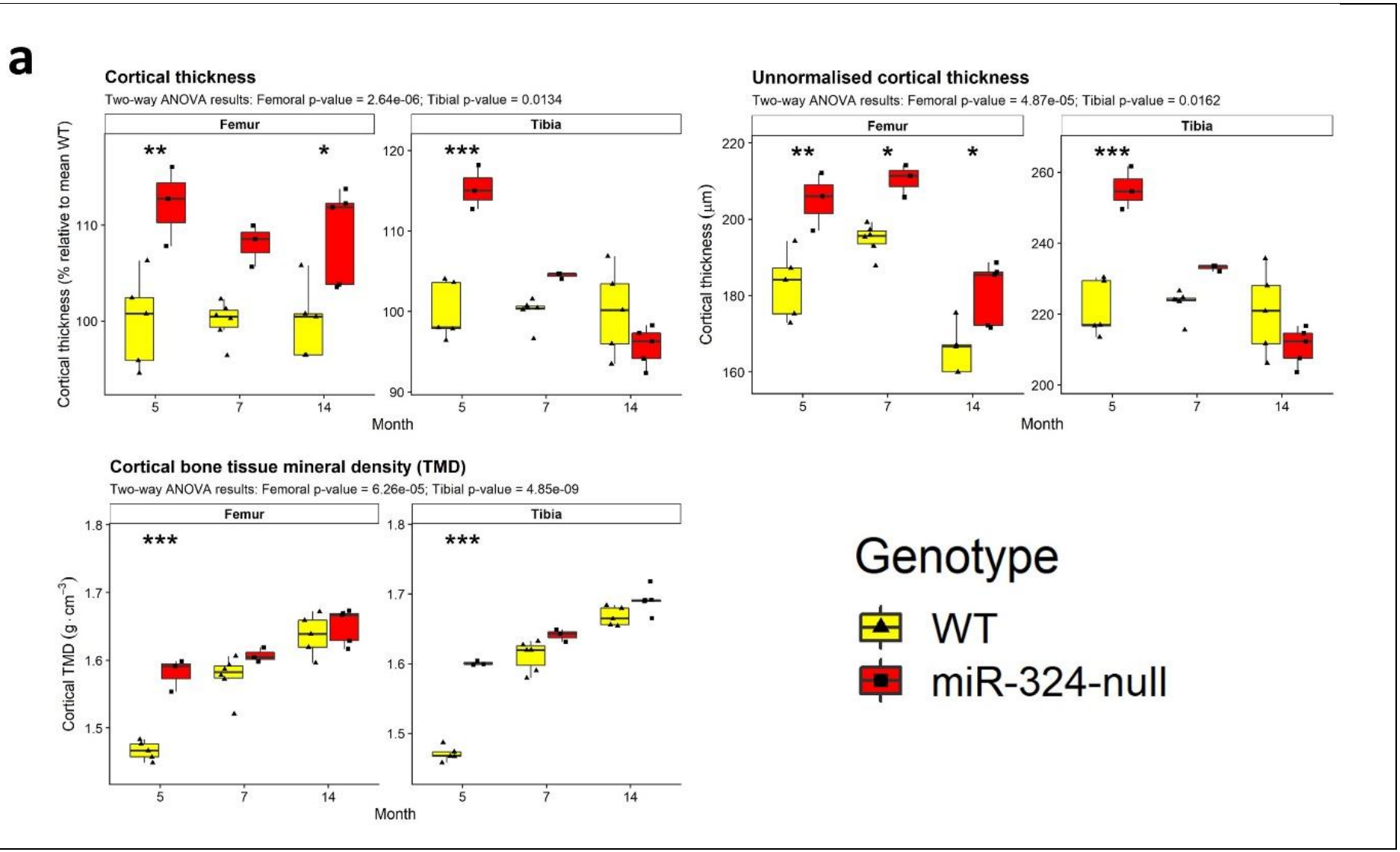
a
Cortical thickness
Two-way ANOVA results: Femoral p-value = 2.64e-06; Tibial p-value = 0.0134
Femur
Tibia
Cortical thickness (% relative to mean WT)
Month
Unnormalised cortical thickness
Two-way ANOVA results: Femoral p-value = 4.87e-05; Tibial p-value = 0.0162
Cortical thickness (µm)
Cortical bone tissue mineral density (TMD)
Two-way ANOVA results: Femoral p-value = 6.26e-05; Tibial p-value = 4.85e-09
Cortical TMD (g·cm⁻³)
Genotype
WT
miR-324-null

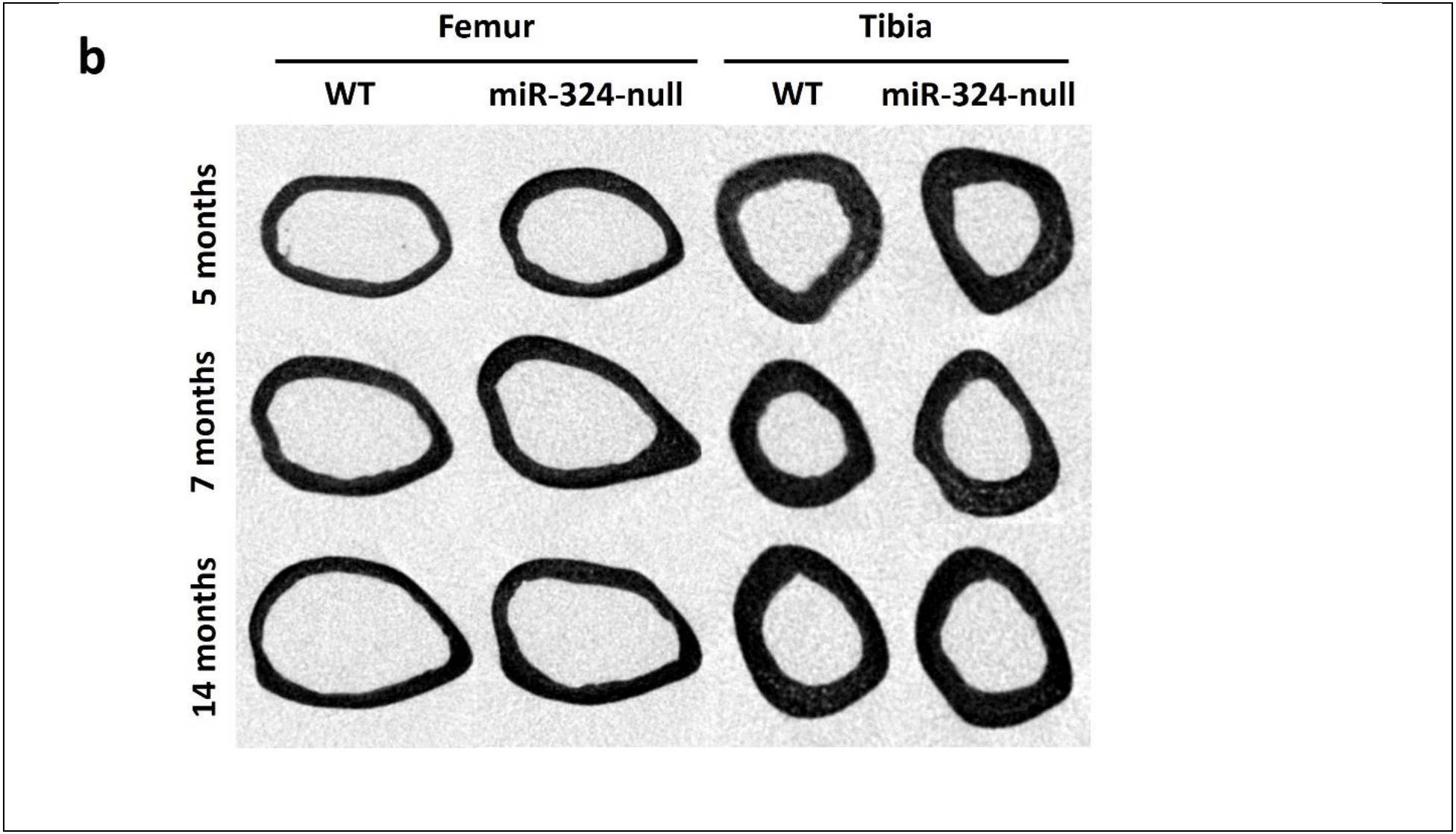
b
Femur
Tibia
WT
miR-324-null
WT
miR-324-null
5 months
7 months
14 months

Figure 4.2 - miR-324-null mice display a high cortical bone mass phenotype. (**a**) The thickness of both femoral and tibial miR-324-null cortices is significantly increased relative to WT age-matched controls, across the time points measured. The cortical bone TMD is also increased, most strikingly at 5-months. Unnormalised cortical thickness is also measured, revealing that although WT cortical thickness in the tibia remains relatively constant with age, miR-324-null cortical thickness dramatically decreases with age, such that by 14-months there appears to be no difference between the two genotypes. In the femur, the cortical thickness of both WT and miR-324-null mice increases slightly between 5- and 7-months, before decreasing sharply by 14-months. Unlike in the tibia, the femoral cortical thickness of miR-324-null mice remains higher than WT mice at all time points. Statistical significance overall across time points was assessed using two-way ANOVA and Tukey's HSD post-hoc tests were used to assess statistical significance at individual time points, for which *, ** and *** signify p-values ≤ 0.05, 0.01 and 0.001, respectively. (**b**) Slices on the transaxial plane are shown as a representation of cortical bone, taken from the midpoint of either the tibia or femur.

The bone tissue mineral density (TMD) of miR-324-null mice was increased relative to WT mice in both the femur and tibia. In both trabecular and cortical bone (Figures 4.1 and 4.2, respectively), this increase was most apparent at the 5-month time point, most strikingly in cortical bone, where an increase of greater than 5% in TMD was observed in miR-324-null bone. The difference between genotypes in regard to TMD appears to decrease with age, contrasting with the observed increase in trabecular thickness, and by the 14-month time point almost no difference is present between miR-324-null and WT TMD. Due to the observed increase in TMD, we also investigated whether any bowing could be observed in the tibiae of miR-324-null mice by measuring the distance between the fibula and tibia at the vertical tibial midpoint. A greater horizontal distance between the fibula and tibia at the tibial midpoint was observed, an increase of approximately 5%, suggesting that miR-324-null tibiae show increased bowing relative to WT controls (Figure 4.3). It should however be noted that this effect was not statistically significant at any one time point by way of post-hoc tests, and only achieves significance at a 5% threshold when a two-way ANOVA is utilised to assess the effect of genotype across all measured time points.

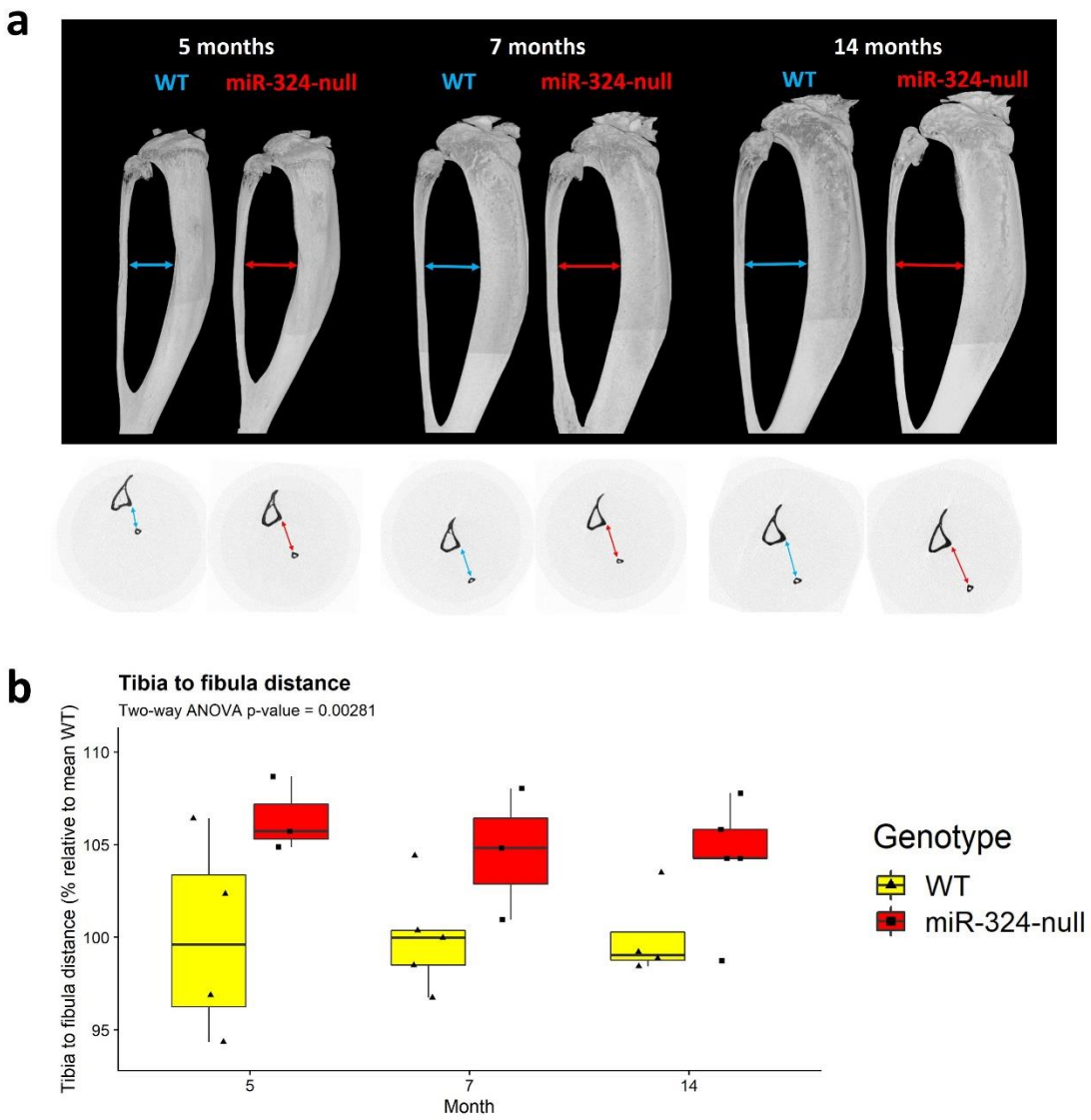

Figure 4.3 - miR-324-null mice display a tibial bowing phenotype. (**a**) Representative tibial µCT reconstructions are shown at each time point for miR-324-null or WT mice, illustrating the increased bowing observed in miR-324-null bones. The blue arrow at each age indicates the horizontal distance between the tibial midpoint and the fibula in WT mice, whereas the red arrow indicates the distance in miR-324-null mice, which is increased. Transaxial slices are also shown using the same colours. (**b**) The distance between the tibia and fibula at the tibial midpoint is severely increased in miR-324-null mice relative to WT controls. Statistical significance overall across time points was assessed using two-way ANOVA and Tukey's HSD post-hoc tests were used to assess statistical significance at individual time points, although no individual time point achieved statistical significance in post-hoc testing.

4.2.2 *Osteogenesis and adipogenesis are modulated in miR-324-null mice*

Considering the high bone mass phenotype observed in miR-324-null mice, we proceeded to investigate whether this could be explained by increased osteoblast-mediated bone formation. To assess whether the rate of bone formation differed between genotypes, miR-324-null and WT mice aged 14-months were injected with alizarin red-S and subsequently calcein, with a period of 6 days between the two injections. After the mice were sacrificed, visualisation of alizarin red-S and calcein in tibial sections revealed that miR-324-null mice show a significantly increased MAR, BFR and area of mineralising surface (Figure 4.4). In miR-324-null tibiae, the MAR shows a subtle increase of approximately 1% relative to WT controls, whilst the mineralising area is increased by approximately 40%. The BFR is also severely increased, by approximately 60%.

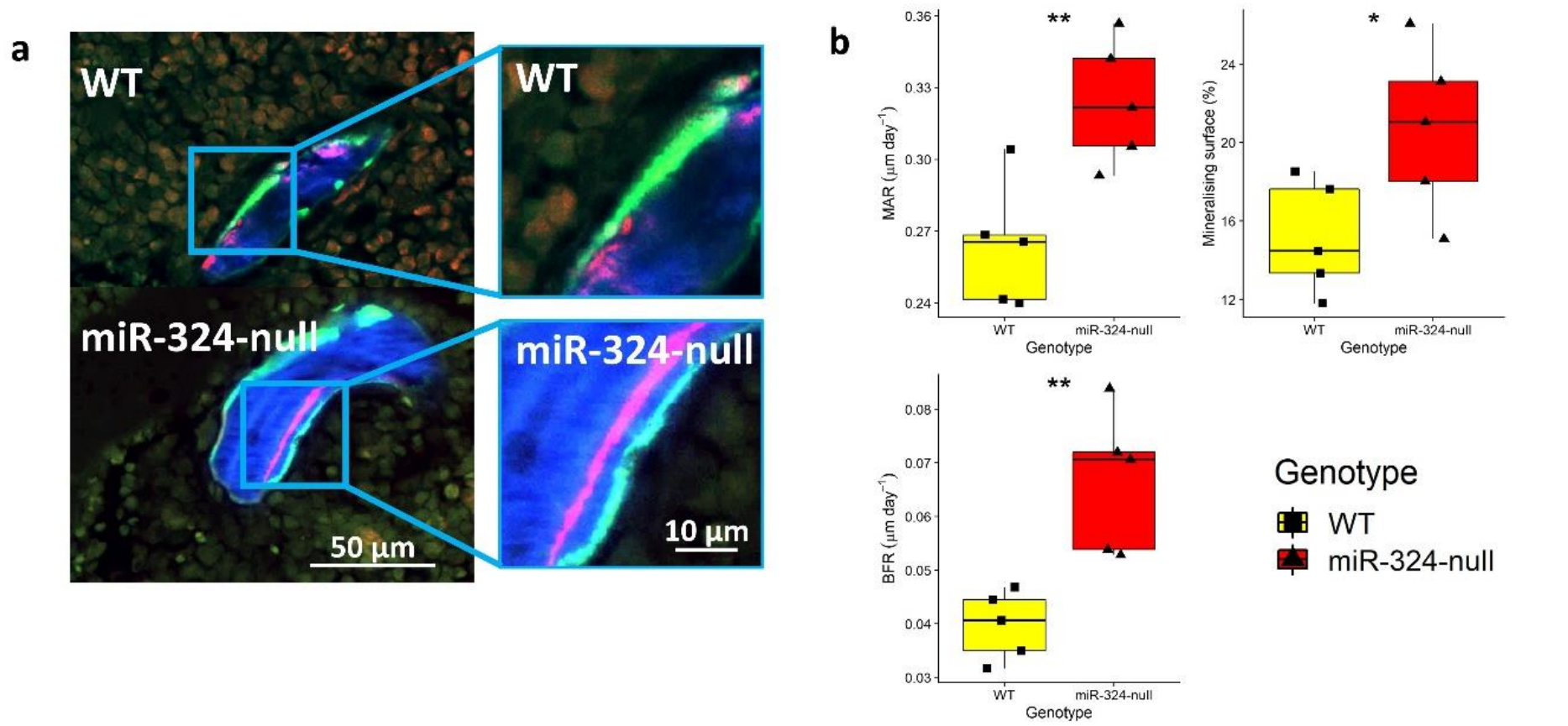

Figure 4.4 - miR-324-null mice display an increased rate of bone formation *in vivo*. (**a**) miR-324-null and WT mice aged 14-months were sacrificed following double-injection with alizarin red-S and calcein. Representative magnified images of the resulting double-labelled tibiae are shown. An increased distance between the corresponding calcium deposition lines was observed in the miR-324-null samples, indicating an increased amount

of bone being formed. (**b**) miR-324-null mice show a significant increase in MAR, BFR and mineralising surface area relative to WT controls. For each mouse, three slices were analysed and the mean of these was plotted as N = 1 per mouse. Student's two-tailed *t*-test was used to assess statistical significance between genotypes, where * and ** signify p-values ≤ 0.05 and 0.01, respectively.

The use of Goldner's Trichrome revealed that, in addition to an increased rate of bone formation, miR-324-null mice showed thickened osteoid (an increase of 8% relative to WT controls), which is the unmineralised component of bone (Figure 4.5). The miR-324-null tibial sections also displayed a clear reduction in lipid droplets, both in terms of number and mean area (Figure 4.6); approximately 9-fold fewer lipid droplets were present in miR-324-null tibiae than in WT controls, by number. In addition, the miR-324-null lipid droplets were a mean average of 65% the size of the WT lipid droplets. Combined, these results suggest that lack of *Mir324* in mice may result in the observed high bone mass phenotype at least in part through modulating the balance between osteogenesis and adipogenesis.

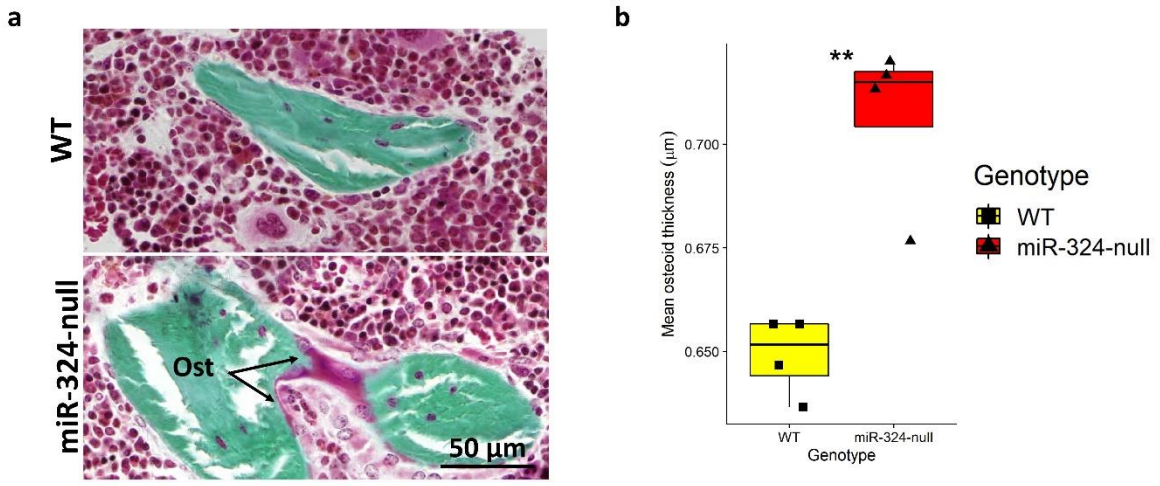

Figure 4.5 - miR-324-null mice display an increase in osteoid thickness. (**a**) Tibial sections from miR-324-null mice aged 14-months were stained with Goldner's Trichrome and the amount of osteoid was visualised. Representative images of WT and miR-324-null tibiae are shown, with mineralised bone stained green and osteoid stained pink, labelled as **Ost**. A clear increase in osteoid in miR-324-null samples can be observed. (**b**) Quantification of the mean osteoid thickness revealed that the osteoid in miR-324-null samples is significantly thickened relative to WT controls. For each mouse, three slices were analysed and the mean of these was plotted as N = 1 per mouse. Student's two-tailed *t*-test was used to assess statistical significance between genotypes, where ** signifies p-value ≤ 0.01.

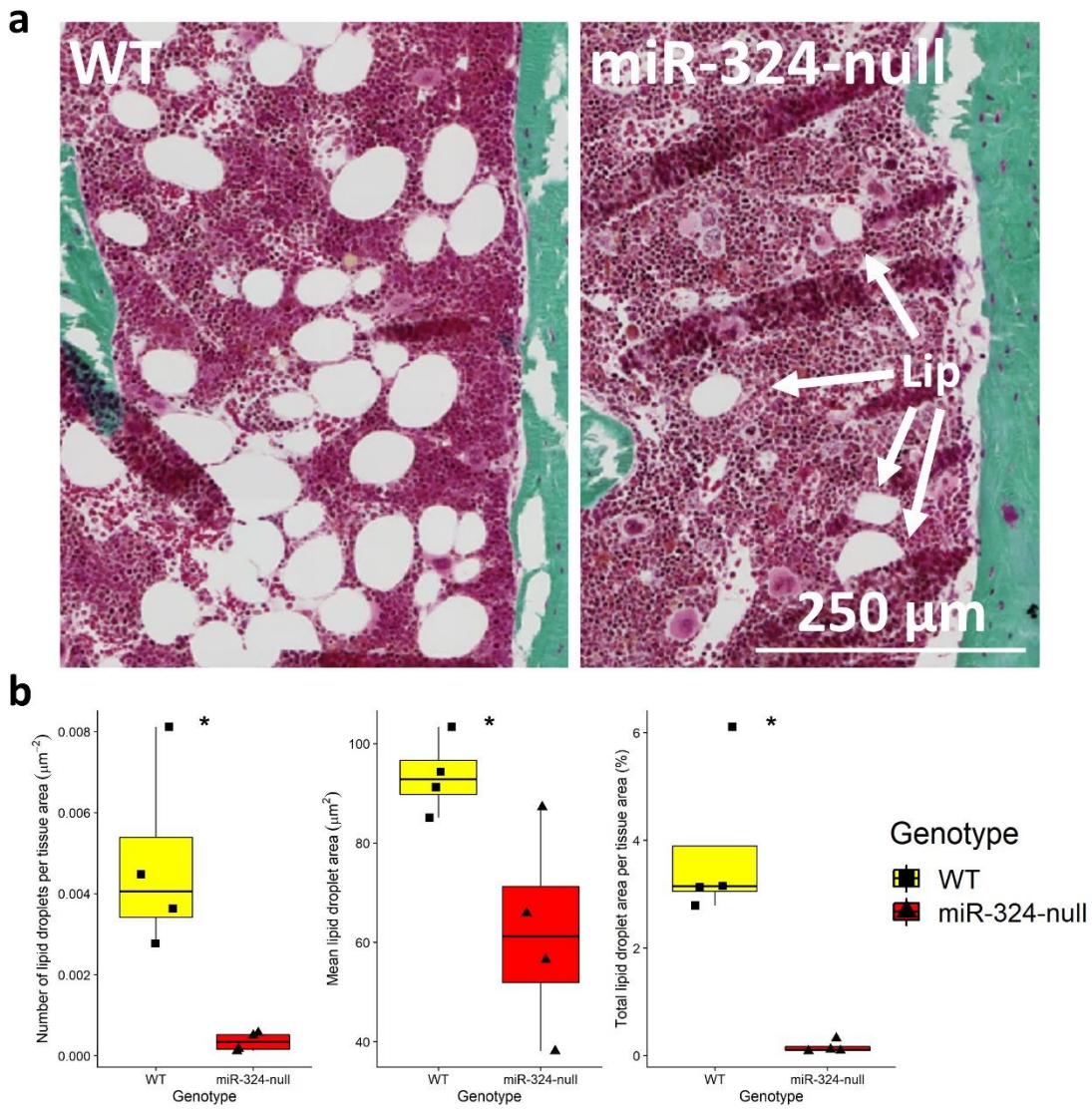

Figure 4.6 - miR-324-null mice display a severe decrease in lipid droplets. (**a**) Tibial sections from miR-324-null mice aged 14-months were stained with Goldner's Trichrome, revealing that miR-324-null mice show a severely reduced number of lipid droplets relative to WT controls, which appear as round areas lacking any staining. Representative tibial sections stained using Goldner's Trichrome illustrate this severe reduction in lipid droplets in miR-324-null samples. The few lipid droplets present in the miR-324-null representative section are labelled as **Lip**. (**b**) Quantification of lipid droplet number and area in miR-324-null and WT samples clearly illustrates the decreased number of lipid droplets in miR-324-null tibiae, in addition to a significantly reduced mean lipid droplet area and decreased lipid droplet area relative to tissue area analysed. For each mouse, three slices were analysed and the mean of these was plotted as N = 1 per mouse. Student's two-tailed *t*-test was used to assess statistical significance between genotypes, where * signifies p-values ≤ 0.05.

4.2.3 *miR-324-null mice are deficient in osteocytes and osteoclasts*

Despite the evident increase in osteoblast-mediated bone formation in miR-324-null samples relative to WT controls, it was also necessary to investigate the abundance of the other bone cell types, namely osteoclasts and osteocytes, as the activities of these cells may also be regulated by miR-324. Tibial sections stained with Goldner's Trichrome were utilised to measure the density of osteocytes within the trabecular bone of each genotype. Remarkably, there was a 40% decrease in osteocyte number per trabecular area in miR-324-null tibial sections relative to WT sections, suggesting that osteocytogenesis, the transition of osteoblasts into osteocytes, may also be affected by lack of *Mir324* (Figure 4.7).

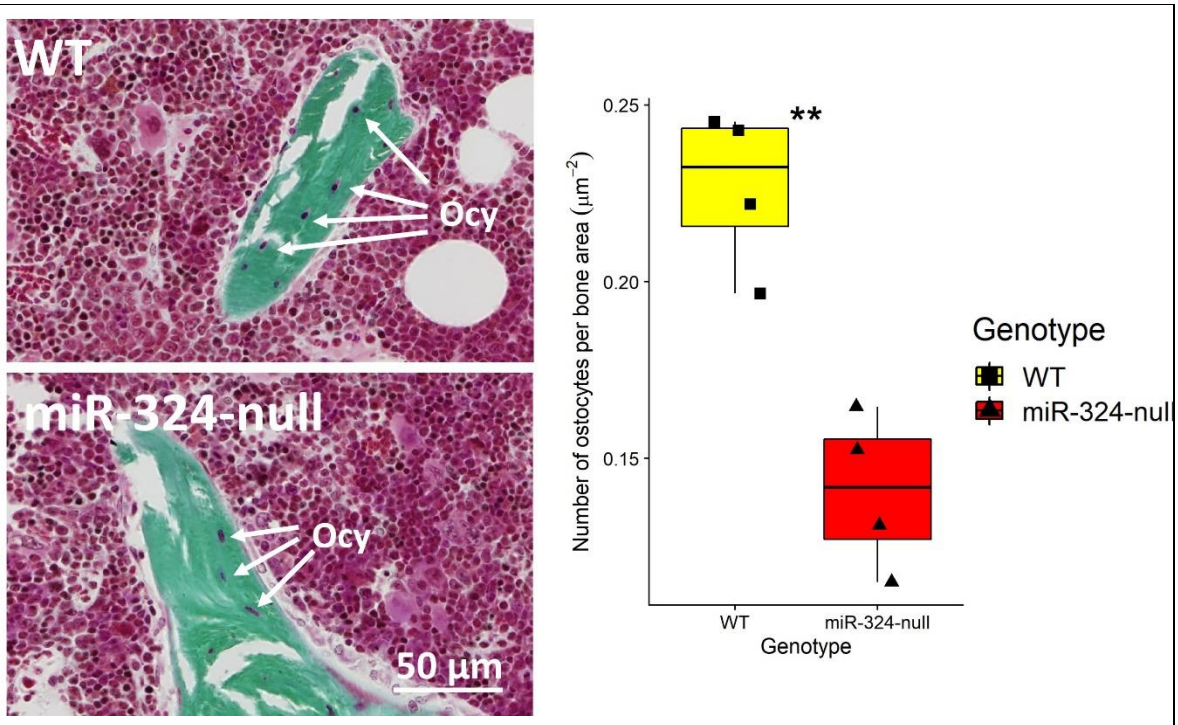

Figure 4.7 - miR-324-null mice display a reduction in osteocyte density. Tibial sections from miR-324-null mice aged 14-months were stained with Goldner's Trichrome and the density of osteocytes, which can be observed as darkly stained cells embedded within the mineralised trabecular bone, was found to be markedly decreased relative to that in WT bone. Examples of clear osteocytes are labelled as **Ocy**. For each mouse, three slices were analysed and the mean of these was plotted as N = 1 per mouse. Student's two-tailed *t*-test was used to assess statistical significance between genotypes, where ** signifies p-values ≤ 0.01.

In addition to a deficiency in osteocytes, a clear decrease in osteoclast number (N.Oc) was also observed, measured in tibial sections stained for TRAP, a key osteoclast marker, in miR-324-null samples relative to WT controls (Figure 4.8; decrease of approximately 50%). Mean osteoclast surface area per bone surface area (Oc.S.BS) was also lower in the miR-324-null samples, although this reduction was not statistically significant (p-value = 0.08). These results in tandem with the increased bone formation suggest that the high bone mass phenotype in miR-324-null mice may be due to decreased bone resorption as well as increased bone formation, in addition to a potential dysregulation of osteocytogenesis.

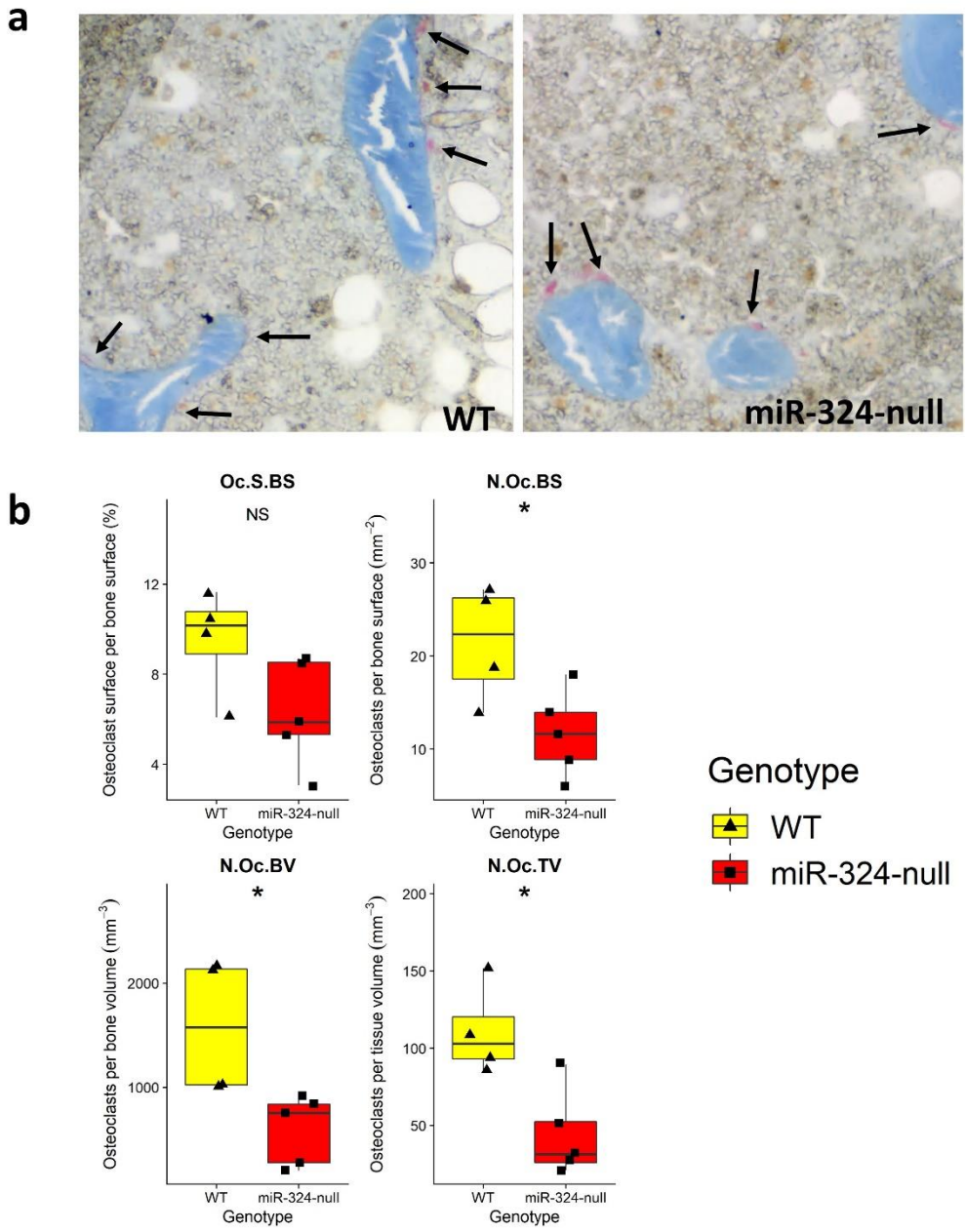

Figure 4.8 - miR-324-null mice display a deficiency in mature osteoclasts. (**a**) Tibial sections from miR-324-null mice aged 14-months were stained for TRAP-positive cells (stained pink; indicated with arrows) against a counter-stain of alcian blue. A decrease in osteoclast number was observed. (**b**) The number of TRAP-positive osteoclasts (N.Oc) is significantly decreased in miR-324-null tibiae upon quantification. Although the mean osteoclast surface area per bone surface area (Oc.S.BS) does not achieve statistical significance, there is a trend towards a decrease in this metric as well (p-value = 0.08). For both panels, Student's two-tailed *t*-test was used to assess statistical significance between genotypes, where * signify p-value ≤ 0.05.

4.2.4 *miR-324-null mice display increased cartilage damage*

Considering that miR-324-5p was identified as being significantly upregulated in end-stage OA patients relative to NOF controls [151, 188], we utilised the miR-324-null mice to investigate the relationship between miR-324 and cartilage damage. Mice aged 5-months underwent destabilisation of the medial meniscus (DMM) surgery [348], before being sacrificed and the left hind legs being fixed, decalcified, sectioned and finally stained using Safranin O, which stains cartilage red. Utilisation of the Osteoarthritis Society International (OARSI) scoring system [164] revealed that miR-324-null mice display a significant increase in cartilage damage when the damage scores for the medial femoral condyle (MFC) and medial tibial plateau (MTP) were summed, although individually neither the MFC nor the MTP score achieved statistical significance (Figure 4.9a). Due to this increased cartilage damage, I proceeded to investigate whether miR-324-null mice displayed increased damage spontaneously with age, without the use of DMM surgery. Therefore, 14-month old miR-324-null and WT mice were sacrificed and their hind legs also stained with Safranin O, revealing that miR-324-null mice indeed do display an increased cartilage damage phenotype spontaneously with age; although there was no significant increase in the MFC damage score, both the MTP and summed cartilage damage scores were significantly increased in miR-324-null mice relative to WT controls (Figure 4.9b).

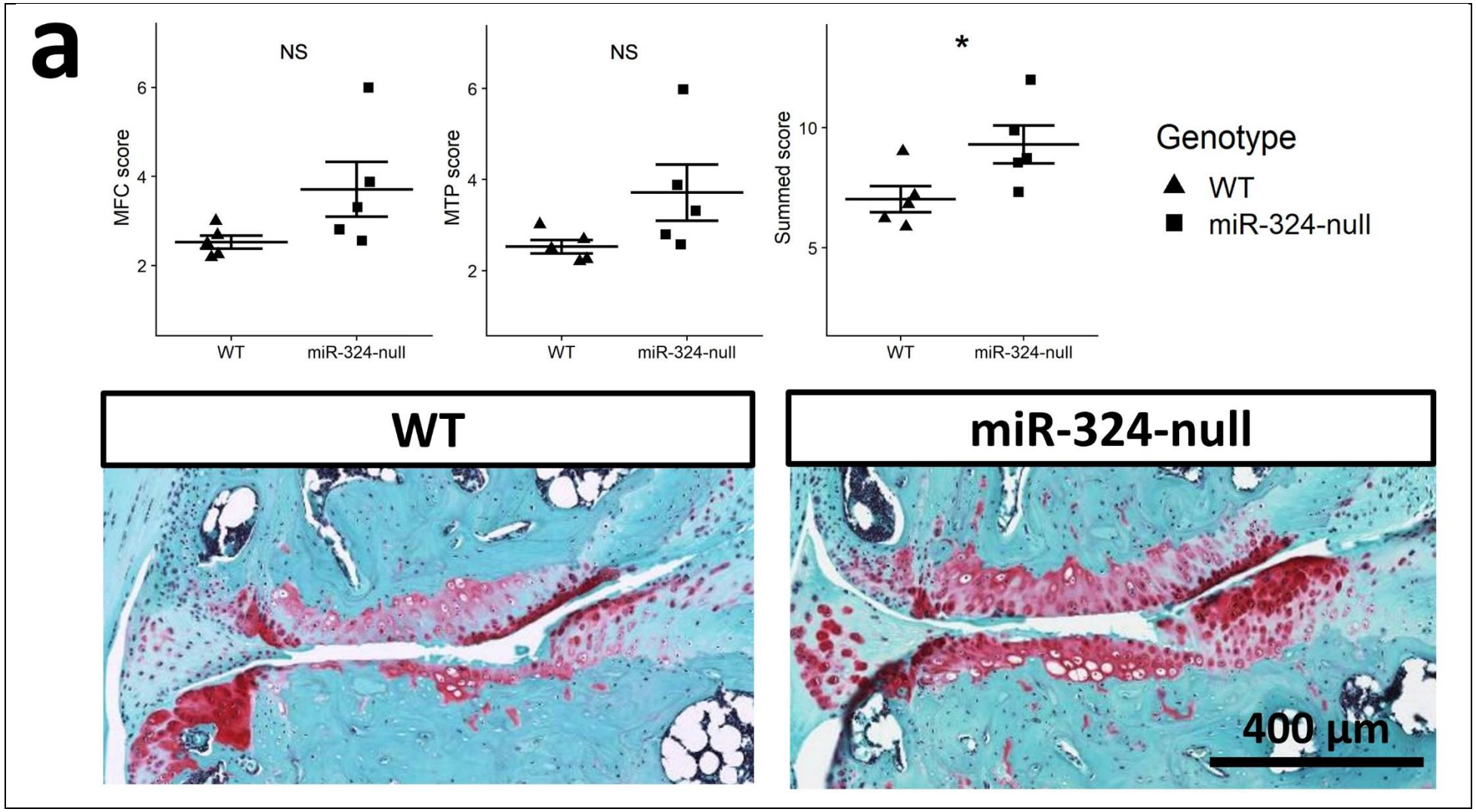
a
NS
NS
*
MFC score
MTP score
Summed score
WT
miR-324-null
Genotype
WT
miR-324-null
WT
miR-324-null
400 µm

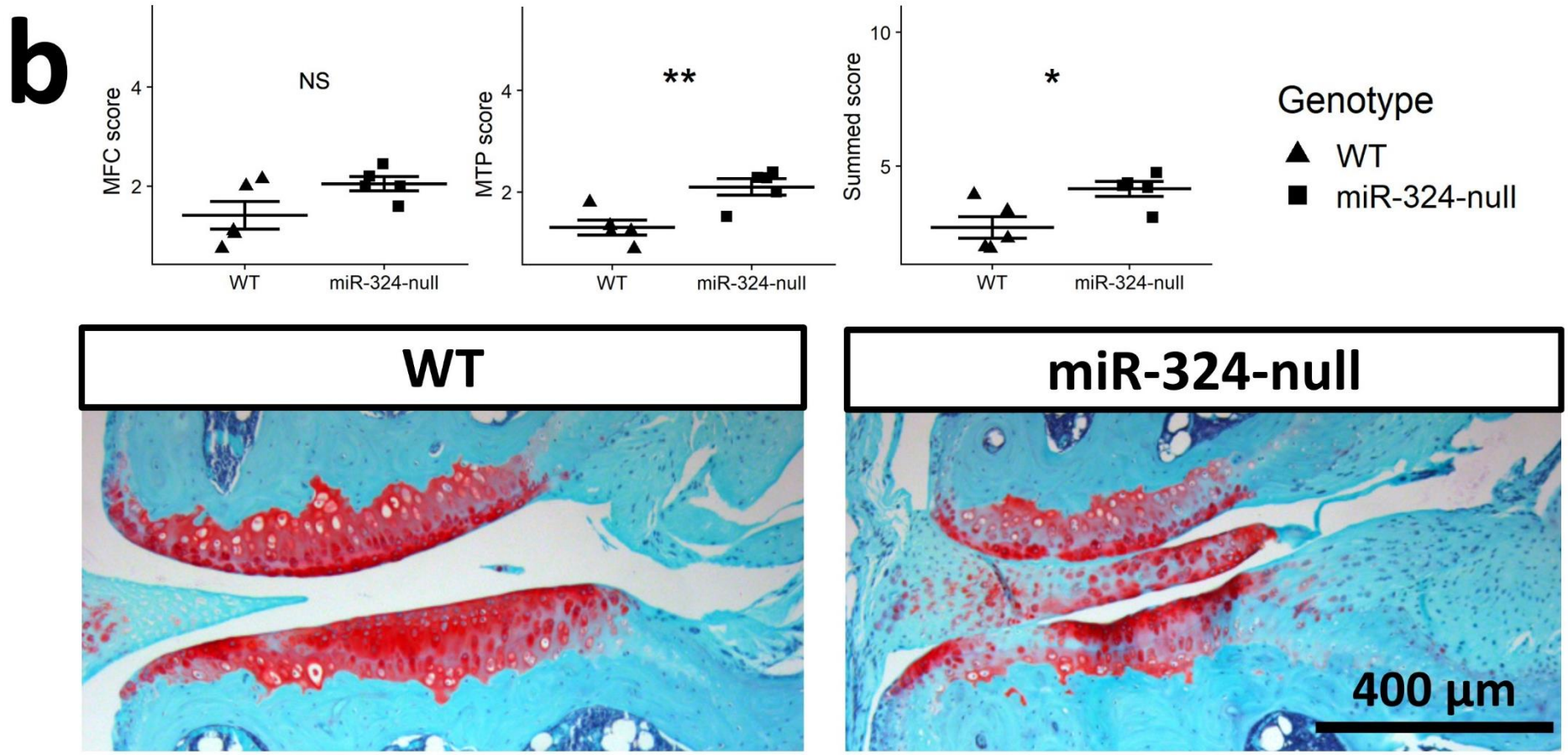

Figure 4.9 - miR-324-null mice display increased cartilage damage relative to WT controls. miR-324-null and WT mice were sacrificed and the left hind legs were fixed and decalcified, before being embedded in paraffin wax and sectioned. Sections were stained using Safranin O for cartilage, before being visualised and the damage scored using the OARSI histopathological scoring system [164]. (**a**) Prior to sacrifice, the younger cohort

underwent DMM surgery [348]. They were sacrificed 8 weeks after surgery, upon which OARSI histopathological scoring for cartilage damage revealed a mild significant increase in cartilage damage when the MFC and MTP damage scores were summed. The MFC and MTP damage scores also showed a trend towards increased damage individually, but this increase did not achieve statistical significance. Representative 6-month old sections stained with Safranin O are shown. (**b**) The 14-month cohort did not undergo DMM surgery prior to sacrifice, but still demonstrated an increase in cartilage damage, both in summed and the MTP damage score. Notably, the 14-month damage scores are far lower than those of 6-month old hind legs, as the older cohort did not undergo DMM surgery prior to sacrifice. Representative sections from the hind legs of 14-month old miR-324-null and WT mice are shown. For both panels, N = 1 per mouse and Student's two-tailed *t*-tests were used to assess statistical significance between genotypes, where ** and * signify p-values ≤ 0.01 and 0.05, respectively.

4.3 Discussion

4.3.1 *miR-324-null mice display a high bone mass phenotype which differs in magnitude between bone compartments and with age*

In femur and tibia and in both trabecular and cortical bone compartments, the bone thickness in miR-324-null mice is overall increased relative to WT controls. However, the magnitude of this effect differs at each time point tested in the cortex. Although in trabecular bone, thickness is increased at every time point by between 10 and 20% (Figure 4.1), the cortical thickness is most severely increased at 5-months, in both the femur and tibia (an increase of 10-15% relative to WT controls; Figure 4.2). The increase in femoral cortical thickness decreases only marginally at the 7-month and 14-month time points, whereas the increase in tibial cortex thickness reduces to an average increase of only 5% by 7-months, and by the 14-month time point no difference between WT and miR-324-null tibial cortical thickness can be observed. This suggests that whichever bone formation or resorption pathways the deletion of *Mir324* is affecting, these biological pathways likely differ in magnitude between both trabecular and cortical bone, and additionally between the femur and the tibia. A potential explanation for this is presented through the difference in bone formation between femoral and tibial cortical bone; in general in C57BL/6J mice, the average tibial cortical bone thickness has been found to be approximately 25% lower than femoral cortical thickness from the same cohort. Additionally, bone formation in the cortex is at high levels in young mice, aged only 6-weeks, but subsequently declines to minimal levels by 26-weeks [435]. The lower volume of cortical bone in the tibia would therefore present less opportunity for the miR-324-null high bone mass phenotype to develop early on, when bone formation is high, than in the femoral cortex, and subsequently increasingly less opportunity to form more bone as the animals age and the bone formation rate lessens. This decrease in bone formation rate with age also offers a potential explanation to the severe increase in TMD in 5-month old miR-324-null mice relative to WT controls, despite a subsequent far weaker difference between genotypes at 7- and 14-months; a severe increase in the already heightened bone formation rate at early time points results in initial increased mineral deposition. Subsequently however, this difference lessens as bone formation itself decreases with age, thus reducing the differences between genotypes.

Interestingly, a positive correlation has previously been identified between human miR-324 serum abundance and bone mineral density (BMD) [317]. As miR-324-null mice completely lack miR-324, the results shown here demonstrate a negative relationship between miR-324 levels and bone TMD. It is unclear how this discrepancy can be explained, as it seems unlikely that miR-324 would affect the same biological activities in both humans and mice, but with an opposite effect on those activities. One possible explanation is that the increased levels of miR-324 in circulating serum is in fact due to selective secretion of miR-324 out of tissues it plays a role in, such as osteoblasts, osteoclasts and osteocytes. This would therefore imply that in the aforementioned study, the resulting miR-324 levels in these cells would be decreased, as in the miR-324-null mice, and therefore the reported effect of miR-324 in that study would be the same as the observed effect in this project. However, without measurements within bone cells or other relevant tissues, it is impossible to know whether this hypothesis is correct.

The increase in TMD observed in miR-324-null mice (Figures 4.1 and 4.2) is interesting when considering that an increase in bowing was also observed, an effect usually associated with reduced TMD, commonly found in metabolic disorders such as rickets [436]. However, a potential explanation for this effect may be in the structural stability of the miR-324-null bone; in addition to heightened bone mass, an increased trabecular SMI was observed in miR-324-null mice, which was statistically significant across the entire time course using a two-way ANOVA, but not at any individual time point using post-hoc testing. This mild shift towards increased SMI implies a more rod-like trabecular structure in miR-324-null mice, interpreted as being less structurally stable [434]. It seems likely therefore that although miR-324-null mice form excess bone, this bone is not regulated well in relation to its overall structure, which could potentially explain the observed bowing phenotype. To confirm this it would be beneficial to test whether miR-324-null mice show this decreased resistance to bending through the use of a three-point bending test [437]. It is also worth considering that the tibial bowing phenotype could be a result of abnormal bone modelling in miR-324-null mice. Bone modelling is distinct to bone remodelling in that rather than requiring the coupled activity of osteoblastic bone formation with osteoclastic bone resorption, as occurs in bone remodelling, bone modelling shapes bones through the independent activity of these cells [438]. Considering that bone modelling has long been known to contribute to the expansion of the periosteum throughout life [439], it is possible that the increased bowing observed in miR-

324-null mice may be a result of bone remodelling-independent osteoblast activity at specific tibial sites. This possibility however requires further investigation to validate.

An additional point of interest with regard to the high bone mass phenotype of miR-324-null mice is that although the phenotype is severe, it is not osteopetrotic, which is where very little if any bone marrow remains, instead replaced with excess bone. Osteopetrosis is a disorder resulting primarily from lack of osteoclast activity, the cells which resorb bone and thus keep the osteoblast-mediated bone formation in balance [198, 266, 273]. It was therefore reasonable to assume that there is some osteoclast activity occurring in miR-324-null mice, as a large amount of marrow space is still present. Following on from this, the high bone mass phenotype observed in miR-324-null mice is likely the result of only a mild osteoclast defect, or a combination of this defect in tandem with an increase in osteoblast-mediated bone formation. It is worth noting that although the results in this section demonstrate that miR-324-null mice show increased leg bone thickness, no other bones were investigated. It would be beneficial in future studies to investigate whether other miR-324-null bones, in particular the vertebrae, demonstrate the same increase in thickness, considering that vertebral bone has a high fracture risk in patients affected by osteoporosis [440]. Therefore the translational potential of the high bone mass phenotype identified in this project would be improved in relation to potential osteoporosis treatment if the miR-324-null high bone mass phenotype is conserved between the leg bones and vertebrae.

4.3.2 *Bone, adipose and cartilage tissues are dysregulated in miR-324-null mice*

In miR-324-null tibiae, the BFR, MAR and mineralising surface area were all significantly increased relative to WT controls (Figure 4.4). This strongly suggests that even if miR-324-null mice harbour an osteoclast defect, they certainly show upregulated osteoblast activity as well. In relation to this upregulated osteoblast-mediated bone formation, this could result from three potential causes; an increase in activity of each individual osteoblast, an enhancement of osteoblast differentiation from the mesenchymal stromal cell (MSC) population, so increasing the number of osteoblasts, or both of the aforementioned possibilities in tandem. Although it cannot be ruled out at this stage that each individual miR-324-null osteoblast is forming more bone than each individual WT osteoblast, the severe decrease in lipid droplets observed in miR-324-null sections (Figure 4.6) lends itself to the hypothesis of an increased osteogenesis to adipogenesis ratio. In addition to alterations to these two processes, this potential mechanism would necessarily result in an upregulation of chondrogenesis as well,

due to an increased commitment of MSCs to the osteochondroprogenitor lineage. It is however difficult to find direct evidence of this in the literature. There are many studies in which factors have been shown to regulate the shift between adipogenesis and osteogenesis [441-443], but there is a surprising lack of studies in which adipogenesis, osteogenesis and chondrogenesis have been investigated as part of the same study. However, in the case of *Cbfb*, a gene encoding Core binding factor-β (CBFβ), adipogenesis, osteogenesis and chondrogenesis have all been investigated. CBFβ is an essential factor in the activation of target gene transcription by RUNX1, RUNX2 and RUNX3 [444-446]. Therefore, it is unsurprising that *Cbfb*-null mice display reduced osteogenesis, due to a lack of active Runx2, but in the context of MSC lineage commitment it is interesting to note that these animals also display increased adipogenesis and inhibited chondrocyte differentiation [447, 448]. In theory this supports a central regulation of osteogenic, adipogenic and chondrogenic lineages, although it is unclear whether the chondrogenic deficiency in *Cbfb*-null mice is a direct effect on at the lineage commitment stage or whether this is merely due to targeting of the chondrocyte differentiation pathway subsequent to lineage commitment. Similarly, in the case of *Sdc3*-null mice, which also showed a decrease in osteogenesis and an increase in adipogenesis, chondrocyte organisation and differentiation was defective, resulting in stunted long bone growth [346]. Again however, although this is suggestive of increased adipogenic commitment impairing commitment to both osteogenesis and chondrogenesis, it is not conclusive that the effect is direct. Assuming that any alteration to adipogenic lineage commitment would necessarily affect both chondrogenesis and osteogenesis as proposed however, then presumably *Mir324* deletion must affect the expression or activity of a key factor involved in the lineage commitment of MSCs, increasing the ratio of cells committing to the osteochondroprogenitor lineage rather than the adipogenic lineage (summarised in Figure 4.10). It is therefore confusing that miR-324-null mice appear to display a cartilage damage phenotype at both 5-months, utilising DMM surgery [348], and at 14-months of age (Figure 4.9). One possibility is that an increased number of MSCs in miR-324-null mice commit to the chondrogenesis lineage, but some other cartilage defect resulting from the deletion of *Mir324* overpowers this effect, therefore resulting in cartilage tissue which is subjected to increased damage through some unknown mechanism. The observed increase in cartilage damage does not offer any further insight into this hypothesis, but it is important to note that a previous study identified that miR-324 is important in the regulation of the Indian Hedgehog (Ihh) signalling pathway through the direct regulation of *Gpc1*, thereby downregulating the

pathway [151]. Ihh signalling is crucial in normal cartilage development, and in osteoarthritis (OA) it has been shown to be upregulated, leading to increased cartilage damage [189-192]. It is therefore plausible that regardless of the fact that an increased number of MSCs commit to the chondrogenesis lineage, eventual cartilage damage is inevitable due to the lack of the miR-324-mediated regulation of the Ihh signalling pathway. It is worth noting that the DMM model of OA induction is specifically a model of post-traumatic OA, rather than of spontaneous or age-associated OA. Alone therefore, the increase in cartilage damage does not necessarily indicate that any normal cartilage homeostatic or developmental processes are affected by deletion of *Mir324*. However, the fact that these results demonstrate that miR-324-null mice also display increased spontaneous cartilage damage with age suggests that a shared mechanism between these models is likely to be impaired by *Mir324* deletion, such as chondrocyte differentiation or function.

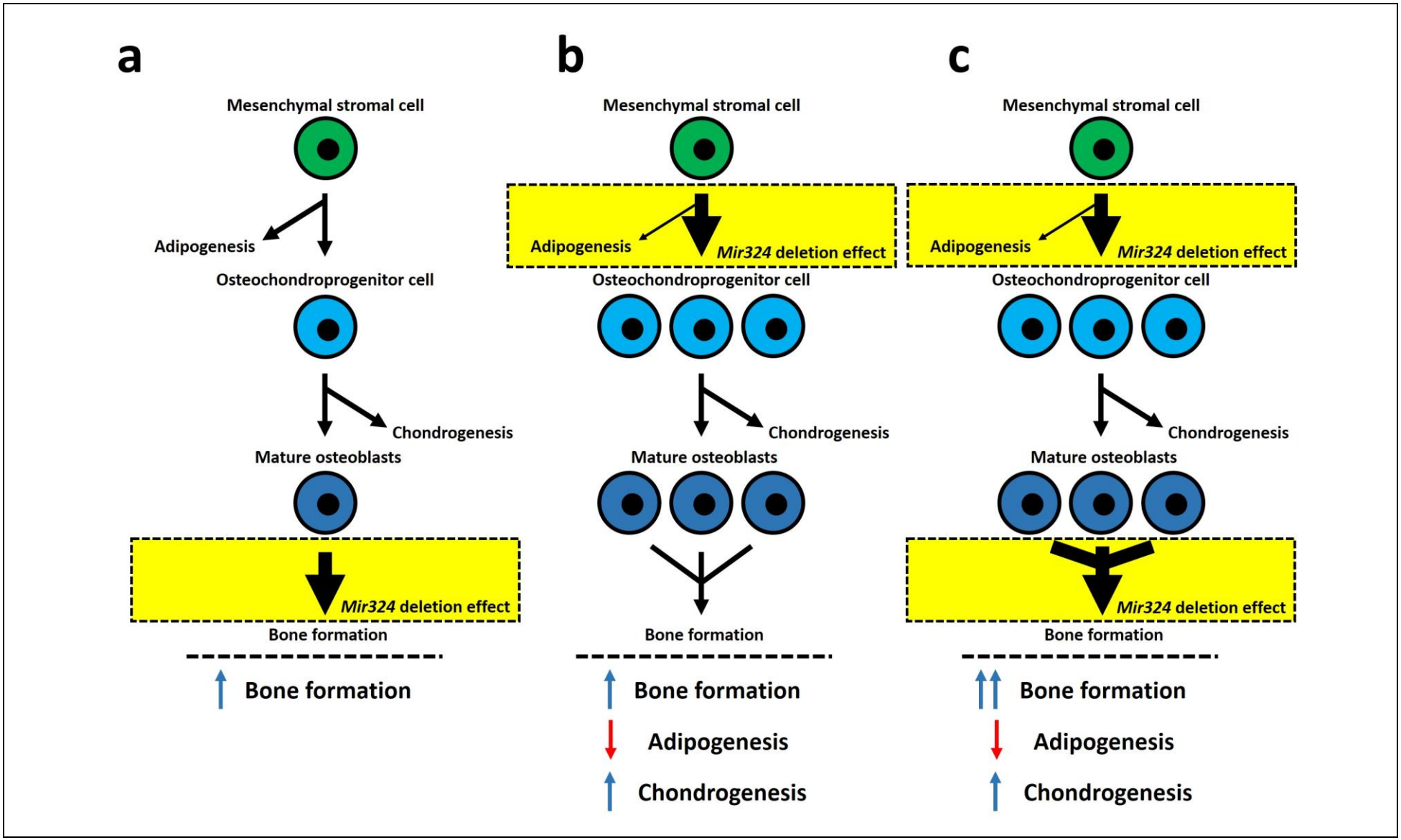
a
Mesenchymal stromal cell
Adipogenesis
Osteochondroprogenitor cell
Chondrogenesis
Mature osteoblasts
Mir324 deletion effect
Bone formation
Bone formation
b
Mesenchymal stromal cell
Adipogenesis
Mir324 deletion effect
Osteochondroprogenitor cell
Chondrogenesis
Mature osteoblasts
Bone formation
Bone formation
Adipogenesis
Chondrogenesis
c
Mesenchymal stromal cell
Adipogenesis
Mir324 deletion effect
Osteochondroprogenitor cell
Chondrogenesis
Mature osteoblasts
Mir324 deletion effect
Bone formation
Bone formation
Adipogenesis
Chondrogenesis

Figure 4.10 - The three possible modes of action of Mir324 deletion to result in increased osteoblast-mediated bone formation. The point in osteogenesis at which *Mir324* deletion is proposed to affect the downstream bone formation for each proposed mechanism is highlighted in yellow. (**a**) If *Mir324* deletion increased bone formation solely through upregulating osteoblast activity, there would not be expected to be any decline in adipogenesis, as a normal number of MSCs would differentiate down each of the adipogenic and osteochondroprogenitor lineages. (**b**) If the effect of *Mir324* deletion occurred at the MSC lineage commitment stage then adipogenesis would be expected to decrease in addition to an increase in both bone formation and chondrogenesis. (**c**) If *Mir324* deletion affected both of these potential sites then the net result would be expected to be very similar to that shown in panel **b**. The only difference would likely be that an even greater increase in bone formation, but not in chondrogenesis, would occur.

Considering the increase in bone mass in miR-324-null femurs and tibiae, it is interesting to note that miR-324-null mice do not display an overall difference in weight (data not shown) relative to age-matched WT controls. This was initially confusing considering their increased bone mass. However, perhaps the observed reduction in lipid content is sufficient to return the weight of miR-324-null mice back to that of WT controls; if this is true then a higher proportion of the miR-324-null mouse weight is due to bone and a lower proportion due to fat, relative to WT animals.

4.3.3 *Osteocytogenesis may be affected by lack of miR-324*

Osteocytes are cells of the mesenchymal lineage, terminally differentiated from osteoblasts as they become embedded in bone matrix. Following this differentiation, known as osteocytogenesis, osteocytes are essential mechanosensory cells as well as being key in the coordination of osteoblasts and osteoclasts for bone remodelling [203, 239, 242, 243]. In WT mice, they are by far the most populous cell in the bone environment; over 90% of bone cells are osteocytes [229]. However, in miR-324-null tibiae, the number of osteocytes per bone area was found to be decreased relative to WT controls (Figure 4.7). It is however unclear whether this is due to a defect in osteocytogenesis, or merely an artefact of increased osteoblast activity, thus resulting in more bone matrix being produced per individual transitioning osteoblast, therefore decreasing this metric through increasing the bone area rather than decrease of the osteocyte number itself. However, the implication of reduced adipocyte-produced lipid droplets in miR-324-null samples is that it is more likely that more osteoblasts are differentiating from MSCs, rather than an increase in individual osteoblast activity. If this is the case, then it is likely that in addition to increasing differentiation into osteoblasts, *Mir324* deletion reduces the differentiation of osteoblasts into osteocytes. It is of course entirely possible that both increased osteoblast differentiation and increased individual osteoblast activity are occurring, as previously mentioned, in which case further investigation into miR-324 activity in osteocytogenesis is required to identify whether this process is directly affected in miR-324-null mice.

4.3.4 *Osteoclastogenesis may be impaired in miR-324-null mice*

Through the use of TRAP staining, miR-324-null tibiae were shown to display a significantly decreased number of osteoclasts in addition to a mild decrease in osteoclast surface area, although the latter did not achieve statistical significance and so cannot be considered a confirmed effect of *Mir324* deletion (Figure 4.8). The fact that some miR-324-null osteoclasts

were able to successfully form and express *Acp5*, which encodes TRAP, demonstrates that initiation and completion of osteoclastogenesis is evidently possible in miR-324-null bone marrow macrophages (BMMs), the precursors from which osteoclasts form. However, the decrease in osteoclast number implies that some aspect of the osteoclastogenesis process may be impaired. A bottleneck event early in the differentiation process could potentially explain this effect; if *Mir324* deletion results in the deficiency of an important osteoclastogenic factor, then this could conceivably permit the fusion of far fewer BMMs, resulting both in a reduced eventual number of mature osteoclasts relative to WT samples and potentially also in reduced osteoclast size, assuming deficiency in this key factor slows the fusion even of osteoclasts which are able to pass this bottleneck (summarised in Figure 4.11). Regardless of the mechanism behind the decreased number of osteoclasts observed in miR-324-null mice, the fact that the population of mature osteoclasts in miR-324-null samples is reduced suggests that a reduction in bone resorption, in addition to the previously discussed increase in bone formation, is expected in miR-324-null mice relative to WTs.

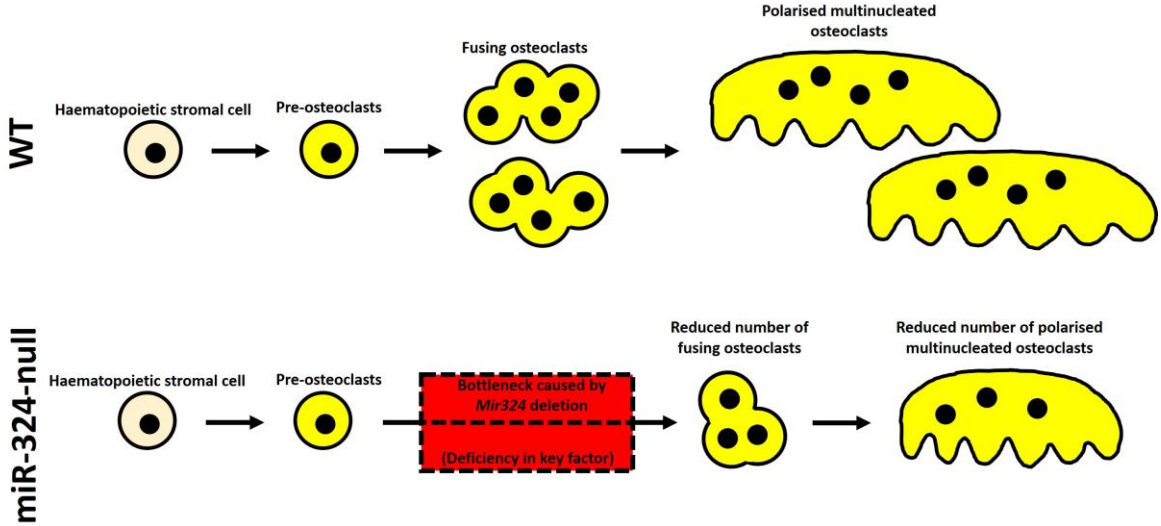

Figure 4.11 - A mechanism to explain how deletion of *Mir324* results in a reduced number of mature osteoclasts. If miR-324-null pre-osteoclasts, or a cell further upstream in the haematopoietic stromal cell (HSC) lineage, harbours a deficiency in a key factor involved in osteoclastogenesis then a bottleneck would be expected to form during the differentiation process, such that only a small number of fusing osteoclasts are able to progress further through the differentiation. This would result in an eventual reduced number of mature polarised osteoclasts relative to a WT cell population undergoing osteoclastogenesis in parallel. Additionally, assuming the deficiency results in slowed differentiation even in

osteoclasts that are permitted to mature, it would be reasonable to also assume that these miR-324-null osteoclasts would appear smaller relative to WT osteoclasts as well.

4.3.5 *Comparison of the in vivo miR-324-null bone phenotype to that of other mouse models*

miR-324-null mice display a striking increase in bone mass and decrease in adiposity *in vivo*, in addition to a mild increase in cartilage damage (Figures 4.1, 4.2, 4.6 and 4.9). This bears striking similarities to several other knockout mouse models. For example, knockout of *Smarca2*, a component of the SWI/SNF chromatin remodelling complex, also results in severely increased bone mass and decreased adiposity [449]. The decrease in adiposity observed in *Smarca2* is however markedly less striking than that observed in miR-324-null mice; an approximate 4-fold decrease in lipid droplet number is reported in *Smarca2*-null mice, whereas the decrease observed in miR-324-null mice is more than twice this in magnitude. It is not possible to directly compare the *Smarca2*-null and miR-324-null bone phenotypes, due to differences both in time points used and metrics compared. However, it is clear that *Smarca2*-null mice do not show the same severe increase in TMD as observed in young miR-324-null mice, therefore suggesting that the miR-324-null and *Smarca2*-null phenotypes are not caused by dysregulation of identical mechanisms.

Mice lacking *Cbfb*, an important partner of the Runx family of proteins for transcriptional activation of target genes [447], *Cxcl12*, an important factor in the regulation of homeostasis in the bone marrow environment [304], and *Sdc3*, a receptor involved in Wnt signalling [346], each display increased adipogenesis and decreased osteogenesis, the opposite phenotype as that observed in *Smarca2*-null and miR-324-null mice. In each of these, the increase in adiposity is striking, matching the miR-324-null phenotype in terms of magnitude, or, in the case of *Cbfb*-null mice, exceeding it. All three knockout models display decreased bone volume and additionally *Sdc3*-null and *Cxcl12*-null mice show decreased trabecular thickness and bone formation rate, relative to WT controls. *Sdc3*-null mice also display a phenotype of impaired chondrogenesis, and although the *Cxcl12*-null mice were not investigated for chondrogenesis specifically, other studies have suggested that *Cxcl12* may be beneficial to cartilage maintenance [450, 451], implying that *Cxcl12*-null mice may be expected to mimic the impaired chondrogenesis phenotype of the *Sdc3*-null mice. If this is true, then *Cxcl12*-null mice might be expected to display stunted limb growth as observed in the *Sdc3*-null mice, although this has not been reported in the publication [304]. The similar shift between adipogenesis

and osteogenesis shown here across several mouse models is as expected, considering the large number of publications documenting this lineage commitment shift. However, the fact that cartilage maintenance is impaired in miR-324-null mice where it would be expected to be enhanced from the hypothesis posed in Figure 4.10 suggests that either an additional distinct process is affecting cartilage maintenance in miR-324-null mice, where it is not in *Sdc3*-null mice, or that the shift between adipogenesis and chondrogenesis is not as direct as the switch between adipogenesis and osteogenesis.

4.4 Summary

I have shown that mice lacking *Mir324* display a high bone mass phenotype. Through the use of µCT I have shown that the thickness of both trabecular and cortical bone is significantly increased overall in miR-324-null mice, relative to WT controls. Although the average increase in trabecular thickness in miR-324-null mice remains relatively consistent both between time points (5-, 7- and 14-months) and leg bone (femur and tibia), the average increase in cortical thickness in the femur is marginally weaker in older mice, and the difference between miR-324-null and WT tibial cortical thickness is ablated entirely by 14-months of age. In addition to this increase in trabecular and cortical thickness, I have shown that the SMI and TMD of miR-324-null mice is significantly increased relative to WT controls. miR-324-null TMD is increased most strikingly in cortical bone, and in both bones at 5-months of age. Interestingly, despite this increase in TMD, tibial bowing was observed, an effect normally seen when a decrease in bone mineralisation occurs.

Through the use of alizarin red-S/calcein double-injections and *in vivo* histology, I have demonstrated that miR-324-null mice show an increased BFR, MAR, mineralising surface area and osteoid thickness, all indicative that osteoblast-mediated bone formation is upregulated in miR-324-null mice. Additionally, I showed that lipid droplet production, presumably as a result of adipogenesis, is severely inhibited in miR-324-null mice, suggesting that the increase in osteoblast activity may be due to an increase in MSC commitment to the osteochondroprogenitor lineage rather than to the adipogenic lineage. Furthermore, I have demonstrated that miR-324-null mice show a decreased osteocyte density, which may be due to inhibition of osteocytogenesis.

Through the use of DMM surgery and the OARSI histopathological staining system, I have demonstrated that miR-324-null mice display an increased cartilage damage phenotype. This was observed at 5-months, using DMM surgery, and additionally at 14-months, where it occurs spontaneously with age. Considering the observed miR-324-null increased bone formation and decreased adipogenesis phenotypes, I hypothesised that the cartilage defect likely does not occur through a decrease in chondrogenesis lineage commitment, as chondrocytes share the same precursor cell as osteoblasts. Instead, I suggested that lack of miR-324 may affect the Ihh signalling pathway, as previously reported in the literature [151], which would result in a similar phenotype of increased cartilage damage to that observed in the miR-324-null mice.

Finally, by staining for the protein product of the osteoclast-selective gene *Acp5*, encoding TRAP, I demonstrated that the number of mature osteoclasts was significantly reduced in miR-324-null tibiae, in addition to a trend towards decreased osteoclast surface area. I hypothesised that this lack of mature osteoclasts may be due to the deficiency of a key factor involved in osteoclastogenesis, creating a bottleneck in the differentiation process in miR-324-null mice.

In summary, I have demonstrated that miR-324-null mice display a high bone mass phenotype, which is likely to be the result of increased osteoblast activity in addition to a diminished osteoclast population. In the next chapter I will utilise *ex vivo* osteoclastogenesis and osteogenesis assays to investigate whether the *in vivo* miR-324-null phenotypes identified in this chapter can be recapitulated *ex vivo*, in addition to *in vitro* lineage commitment assays to investigate whether miR-324 really does play a role in MSC lineage commitment.

Chapter 5 - *Ex vivo* and *in vitro* investigation into the miR-324-null high bone mass phenotype

5.1 Introduction

5.1.1 *miR-324-null mice display a high bone mass phenotype*

In Chapter 4 I showed that miR-324-null mice showed a high bone mass phenotype. *In vivo*, miR-324-null mice displayed increased bone formation in addition to a deficiency in mature osteoclasts and a severe lack of lipid droplets, indicative of a decrease in adipogenesis. miR-324-null mice also displayed a decreased number of mature osteocytes per mineralised bone area. In this chapter, in order to identify the biological pathways modulated by deletion of *Mir324*, I will investigate osteogenesis, osteoclastogenesis and adipogenesis *ex vivo* and *in vitro*, utilising cells isolated from miR-324-null and WT mice in addition to an immortalised mesenchymal stromal cell (MSC)-like cell line, to test lineage commitment in the presence and absence of miR-324.

5.1.2 *Studying osteoclast differentiation and maturation ex vivo*

Osteoclasts undergo a striking change as they mature, from mononucleated macrophage-like precursor cells to huge multinucleate cells capable of bone resorption [196]. Although mature osteoclast number can be quantified in an *in vivo* sample, utilising tartrate-resistant acid phosphatase (TRAP)-staining on a fixed tissue section as discussed previously in section 4.1.4, this only reveals information about the end point of osteoclast differentiation and maturation. Therefore, to investigate the process of osteoclastogenesis as a whole, *ex vivo* or *in vitro* osteoclast differentiation experiments are required. *Ex vivo* osteoclastogenesis requires the isolation of haematopoietic stromal cells (HSCs) from bone marrow and subsequent stimulation with M-CSF in order to differentiate the HSCs into macrophages [346]. These can in turn act as the precursors for osteoclastogenesis, and further stimulation with M-CSF in combination with Receptor Activator of Nuclear Factor-kappa B ligand (RANK-L) is able to trigger the downstream signalling pathways. These result in the upregulation and activation of the transcription factor NFATc1, allowing transcription of key osteoclastogenesis genes, such as *Acp5*, *Ctsk* and *Mmp9* [452-454]. *Ex vivo* osteoclastogenesis assays therefore allow identification of gene expression changes over the entire process of osteoclastogenesis, in addition to between experimental groups.

5.1.3 *Studying osteoblast activity ex vivo*

Unlike osteoclasts, *in vivo* data utilising the calcein/alizarin red-S double-labelling method discussed previously in section 4.1.4 can reveal information regarding physical activity of the cell, in this case that of bone formation. However, it is very difficult to determine from this *in*

vivo evidence alone whether alterations in bone formation are solely due to osteoblasts or whether the effect is due to communication from other cell types within the system. In order to counter this, *ex vivo* osteogenesis experiments are commonly used, which enable the determination of bone formation rates under different conditions, such as gene perturbation or stimulation with different chemicals. The osteoblast precursors used for these assays are commonly obtained from two locations in mice; the calvariae, for obtaining osteoblasts from pups, or the leg bones, for obtaining osteoblasts from older animals [455, 456]. Although both of these methods result in mature osteoblasts which can actively produce and mineralise bone matrix [456], the bone formed by each is not identical; the bone matrix in calvariae is distinct to that found in long bone, as is the response to mechanical loading and morphology of calvarial osteoblasts relative to osteoblasts derived from long bone fragments [456-458]. However, for the purposes of osteogenesis assays, both calvarial- and long bone-derived osteoblasts are frequently utilised, although the two populations should not be treated as the same cell population. Stimulation of isolated osteoblasts with osteogenic media, which commonly includes β-glycerophosphate and L-ascorbic acid (which act as a phosphate source and enhance secretion of type I collagen, respectively [459]), encourages the deposition and mineralisation of bone matrix by the osteoblasts, and this mineralisation can be detected using an alizarin red-S stain, which binds to calcium. Therefore, in addition to being able to lyse the osteoblasts for RNA or protein, it is possible to also obtain a quantitative metric of how much bone-like mineralised matrix has been formed over the course of the assay.

5.1.4 *Studying adipogenic and osteogenic lineage commitment in mesenchymal stromal cells*

MSCs undergo a complex programme of lineage commitment in the bone marrow, which is dependent on several key transcription factors guiding them down one particular lineage in preference over another. Initially, Sox9 directs MSCs into the osteochondroprogenitor lineage, whereas high Pparg activity will instead result in commitment to the adipogenic lineage. At the osteochondroprogenitor stage, high abundance of Runx2 causes the cells to differentiate into pre-osteoblasts rather than chondrocytes, and subsequent abundance of Osx (Sp7/Osterix) consolidates this lineage choice [217, 218]. There is a high degree of plasticity between the osteogenic and adipogenic cell lineages and Pparg has been shown to be a direct suppressor of *Runx2* expression, so revealing direct competition for MSC lineage choice, rather than a simple decision based on relative transcription factor abundance [460-463]. This negative regulation of *Runx2* has been supported by a study attempting to stimulate

embryonic stem cells lacking *PPARG* to undergo adipogenesis, where no adipogenesis was observed and instead the cells underwent osteogenesis [464]. The complex interactions between adipogenic and osteogenic lineage commitment suggest therefore that the dysregulation of either *Runx2* or *Pparg* could have severe implications on the balance of osteogenesis and adipogenesis.

In a research context it is crucial to be able to model the plasticity between osteogenesis and adipogenesis and thus understand the interactions between the two processes. A recent discovery that the use of dexamethasone in osteogenic media stimulated adipogenesis and osteogenesis to occur simultaneously in cell populations paved the way for adipo-osteogenesis (AdiOst) co-differentiation assays [355]. By utilising the dexamethasone-containing osteogenic media with MSCs or MSC-like cell lines, an effective assessment of whether cells more frequently differentiate into one lineage rather than another upon treatment with a certain condition can be gauged.

5.1.5 *Chapter aims*

1. Investigate whether HSCs obtained from miR-324-null mice undergo osteoclastogenesis at an altered rate to HSCs obtained from WT mice.
2. Investigate whether miR-324-null murine osteoblasts form bone at an altered rate to that of WT murine osteoblasts.
3. Evaluate whether restoration of physiological levels of miR-324-5p and -3p can rescue any abnormal miR-324-null osteoblast phenotype.
4. Assess differential lineage commitment of an MSC-like cell line transfected with miR-324 mimics or inhibitors upon AdiOst co-differentiation conditions.

5.2 Results

5.2.1 *Ex vivo miR-324-null bone marrow macrophages display severely impaired osteoclastogenesis*

Considering that miR-324-null mice display a deficiency in mature osteoclasts *in vivo*, we proceeded to isolate hematopoietic stromal cells (HSCs) from miR-324-null and WT bone marrow and investigate whether miR-324-null HSCs displayed any inhibition of osteoclastogenesis *ex vivo*. HSCs of each genotype were stimulated first exclusively with M-CSF in order to produce M-CSF-dependent bone marrow macrophages (BMMs) and then

subsequently with M-CSF in addition to RANK-L to induce osteoclastogenesis. RNA was isolated from each genotype at both the BMM and osteoclast stages of differentiation and additionally cells were stained for TRAP following RANK-L stimulation in order to compare the number of mature osteoclasts formed (Figure 5.1).

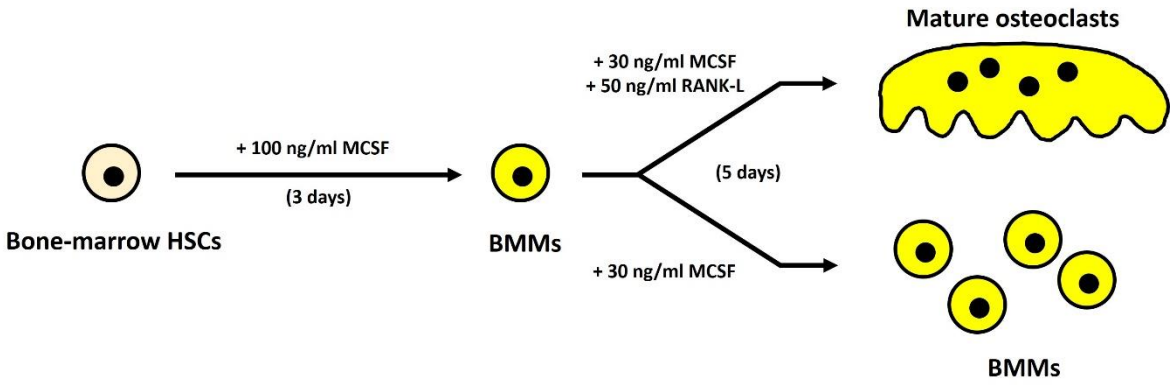

Figure 5.1 - Schematic of osteoclastogenesis experiments from HSCs isolated from murine bone marrow. All samples were initially stimulated for 3 days with 100 ng/ml M-CSF. Subsequently, half of samples were stimulated with 50 ng/ml RANK-L and 30 ng/ml M-CSF for 5 days before the experimental end point. These were treated as "osteoclast samples". The other half of samples were stimulated only with 30 ng/ml M-CSF for the same period of time, as an undifferentiated control population, and treated as "BMM samples".

Cells isolated from miR-324-null samples had significantly fewer mature osteoclasts after M-CSF and RANK-L stimulation in addition to a significant decrease in mean number of nuclei per osteoclast. Although there was no decrease in mean osteoclast area in miR-324-null samples relative to WT controls, there was a significant decrease in total osteoclast area (Figure 5.2).

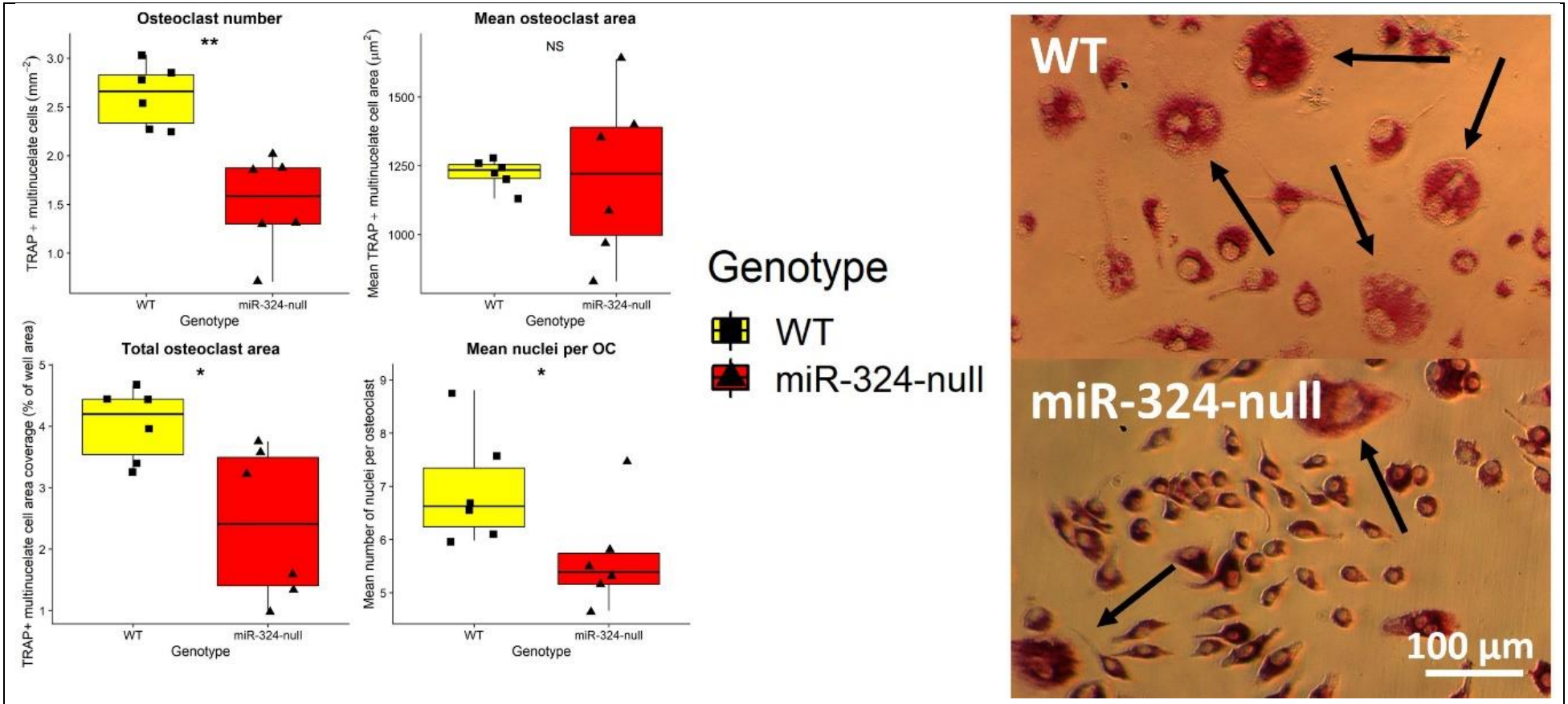

Figure 5.2 - miR-324-null BMMs display a severe defect in osteoclastogenesis. HSCs extracted from the bone marrow of miR-324-null and WT mice were stimulated with 100 ng/ml M-CSF for 3 days and subsequently with 30 ng/ml M-CSF and 50 ng/ml RANK-L for a further 5 days. miR-324-null samples showed a severe reduction in the number of mature osteoclasts and the mean number of nuclei per osteoclast relative to WT controls. No reduction in mean osteoclast area was observed, although a significant decrease in total osteoclast area was identified in miR-324-null samples.

Representative images of TRAP-stained osteoclasts from each genotype are shown. Black arrows indicate examples of mature osteoclasts in each genotype. Here, ** and * represent p-values ≤ 0.01 and 0.05, respectively, calculated using Student's two-tailed *t*-tests.

In order to identify the cause of this osteoclastogenic inhibition, RNA sequencing (RNA-seq) was undertaken in miR-324-null and WT BMMs and osteoclasts. At a transcriptomic level, miR-324-null osteoclasts were highly distinct from WT osteoclasts, segregating well by Principal Component Analysis (PCA), with almost 9000 genes being differentially expressed between genotypes. In fact, it seems likely that the underlying reason for the lack of osteoclastogenesis in miR-324-null samples is not due to a specific dysfunction during the osteoclastogenic process, but instead because of alterations in BMMs, or even prior to this, in HSCs; miR-324-null and WT BMMs also segregated remarkably well by PCA, with more than 7000 genes differentially expressed (adjusted p-value ≤ 0.05; Figures 5.3a and 5.3b). More than half of these dysregulated genes in BMMs were also dysregulated in osteoclasts; in fact, 3425 of the 4855 dysregulated in both cell types were dysregulated in the same directionality in both BMMs and osteoclasts, with a total of 1933 genes upregulated and 1492 genes downregulated in both cell types (Figures 5.3ci and 5.3cii).

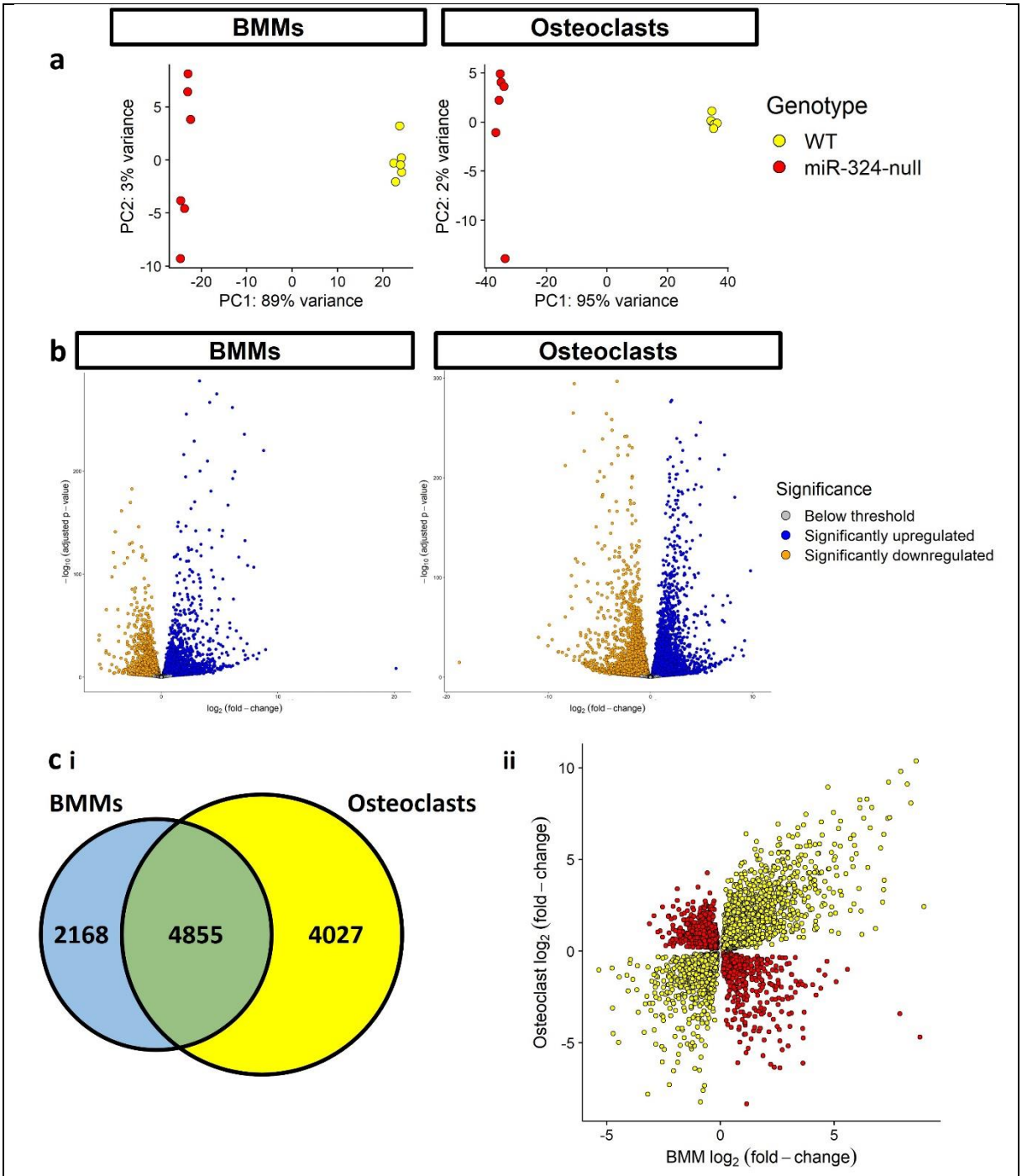

Figure 5.3 - miR-324-null BMMs and osteoclasts are highly distinct from WTs at a transcriptomic level. As shown in Figure 5.1, "BMMs" were stimulated only with M-CSF (100 ng/ml for 3 days and then 30 ng/ml for 5 days), whereas "osteoclasts" were stimulated initially with 100 ng/ml M-CSF for 3 days and then subsequently with 30 ng/ml M-CSF and 50 ng/ml of RANK-L for 5 days. Both cell types were differentiated from HSCs extracted from the bone marrow of miR-324-null or WT mice. (**a**) In both BMMs and osteoclasts, samples segregated well by genotype in principal component analysis. (**b**) Volcano plots illustrate the large array of genes dysregulated in miR-324-null BMMs and osteoclasts; over 7000 and

almost 9000 genes, respectively, were significantly dysregulated in miR-324-null samples relative to WT controls (adjusted p-value ≤ 0.05). Blue points represent genes significantly upregulated in miR-324-null samples, orange points represent genes significantly downregulated in miR-324-null samples and grey points indicate genes which did not achieve statistical significance (adjusted p-value ≥ 0.05). (**c**) Many genes are dysregulated in both miR-324-null BMMs and osteoclasts. (**i**) More than half of the genes dysregulated in miR-324-null BMMs are also dysregulated in miR-324-null osteoclasts. The total number of genes dysregulated in BMMs totals at 7023, whereas in osteoclasts the number comes to 8882 genes (34.1% and 43.2% of all genes tested, respectively). (**ii**) A scatter plot comparing the $\log_2$ fold-changes in BMMs and osteoclasts of genes dysregulated in both cell types. The majority of genes dysregulated in both cell types were dysregulated in the same directionality in both BMMs and osteoclasts; 1933 genes were upregulated and 1492 genes downregulated in both cell types. In this plot, yellow indicates genes with a shared directionality of regulation in both cell types, whereas red indicates genes which are dysregulated in both BMMs and osteoclasts, but not in the same directionality.

Genes annotated in the Disease Ontology (DO) [343] to "Arthritis" and to "Regulation of ERK1 and ERK2 cascade" in the gene ontology (GO) [465, 466] are enriched both in the BMM and osteoclast RNA-seq results (Figure 5.4a). Both arthritis and the ERK1/ERK2 cascade have clear relationships to osteoclast biology; much of the bone destruction observed in rheumatoid arthritis is due to increased osteoclast activity [467] and the ERK1/ERK2 cascade has been demonstrated to upregulate osteoclastogenesis [468]. Considering that genes annotated to these terms are dysregulated both at the BMM (prior to osteoclastogenesis) and the osteoclast (at the end point of osteoclastogenesis) stages, it is possible that these dysregulations could play a role in the osteoclastogenesis defect observed in miR-324-null cells. Interestingly, the expression of *Nfatc1*, the key osteoclastogenesis transcription factor, and *Tnfrsf11a*, the gene encoding the RANK receptor, were significantly decreased in both miR-324-null BMMs and osteoclasts (Figure 5.4b). *Tnfrsf11a* is annotated in the GO "Regulation of ERK1 and ERK2 cascade" term and both *Tnfrsf11a* and *Nfatc1* are annotated in the DO "Arthritis" term. Notably, the expression of both of these genes is essential for osteoclastogenesis [454, 469-471]. The osteoclast marker genes *Acp5*, which encodes TRAP, and *Mmp9*, which are both also annotated to the GO "Arthritis" term, were also both

significantly downregulated in miR-324-null osteoclasts. Curiously however both of these genes were upregulated in miR-324-null BMMs relative to WT controls (Figure 5.4b).

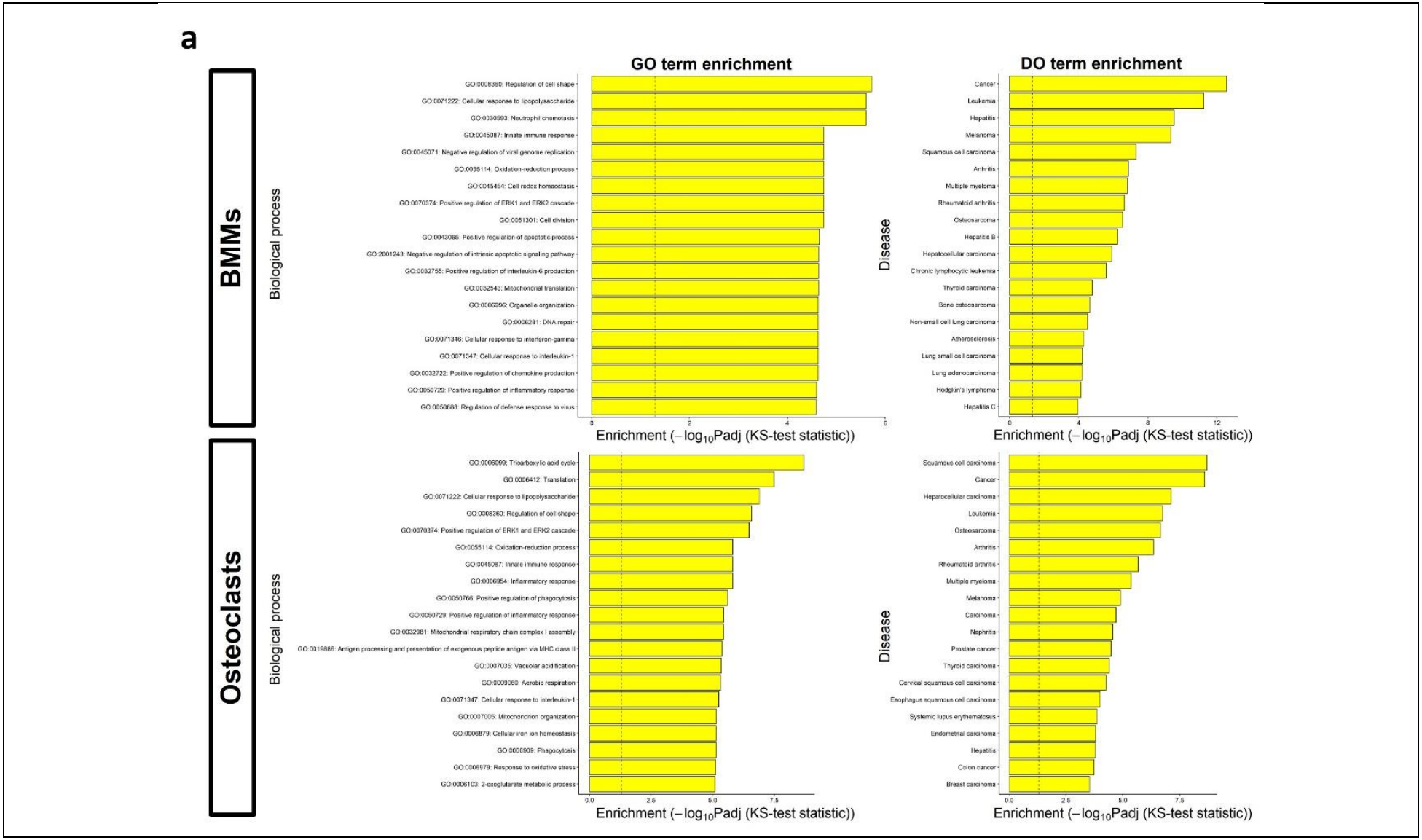
a
BMMs
Osteoclasts
Biological process
GO term enrichment
GO:0008360: Regulation of cell shape
GO:0071222: Cellular response to lipopolysaccharide
GO:0030593: Neutrophil chemotaxis
GO:0045087: Innate immune response
GO:0045071: Negative regulation of viral genome replication
GO:0055114: Oxidation-reduction process
GO:0045454: Cell redox homeostasis
GO:0070374: Positive regulation of ERK1 and ERK2 cascade
GO:0051301: Cell division
GO:0043065: Positive regulation of apoptotic process
GO:2001243: Negative regulation of intrinsic apoptotic signaling pathway
GO:0032755: Positive regulation of interleukin-6 production
GO:0032543: Mitochondrial translation
GO:0006996: Organelle organization
GO:0006281: DNA repair
GO:0071346: Cellular response to interferon-gamma
GO:0071347: Cellular response to interleukin-1
GO:0032722: Positive regulation of chemokine production
GO:0050729: Positive regulation of inflammatory response
GO:0050688: Regulation of defense response to virus
0
2
4
6
Enrichment (−log10Padj (KS-test statistic))
DO term enrichment
Disease
Cancer
Leukemia
Hepatitis
Melanoma
Squamous cell carcinoma
Arthritis
Multiple myeloma
Rheumatoid arthritis
Osteosarcoma
Hepatitis B
Hepatocellular carcinoma
Chronic lymphocytic leukemia
Thyroid carcinoma
Bone osteosarcoma
Non-small cell lung carcinoma
Atherosclerosis
Lung small cell carcinoma
Lung adenocarcinoma
Hodgkin's lymphoma
Hepatitis C
0
4
8
12
Enrichment (−log10Padj (KS-test statistic))
Biological process
GO:0006099: Tricarboxylic acid cycle
GO:0006412: Translation
GO:0071222: Cellular response to lipopolysaccharide
GO:0008360: Regulation of cell shape
GO:0070374: Positive regulation of ERK1 and ERK2 cascade
GO:0055114: Oxidation-reduction process
GO:0045087: Innate immune response
GO:0006954: Inflammatory response
GO:0050766: Positive regulation of phagocytosis
GO:0050729: Positive regulation of inflammatory response
GO:0032981: Mitochondrial respiratory chain complex I assembly
GO:0019886: Antigen processing and presentation of exogenous peptide antigen via MHC class II
GO:0007035: Vacuolar acidification
GO:0009060: Aerobic respiration
GO:0071347: Cellular response to interleukin-1
GO:0007005: Mitochondrion organization
GO:0006879: Cellular iron ion homeostasis
GO:0006909: Phagocytosis
GO:0006979: Response to oxidative stress
GO:0006103: 2-oxoglutarate metabolic process
0.0
2.5
5.0
7.5
Enrichment (−log10Padj (KS-test statistic))
Disease
Squamous cell carcinoma
Cancer
Hepatocellular carcinoma
Leukemia
Osteosarcoma
Arthritis
Rheumatoid arthritis
Multiple myeloma
Melanoma
Carcinoma
Nephritis
Prostate cancer
Thyroid carcinoma
Cervical squamous cell carcinoma
Esophagus squamous cell carcinoma
Systemic lupus erythematosus
Endometrial carcinoma
Hepatitis
Colon cancer
Breast carcinoma
0.0
2.5
5.0
7.5
Enrichment (−log10Padj (KS-test statistic))

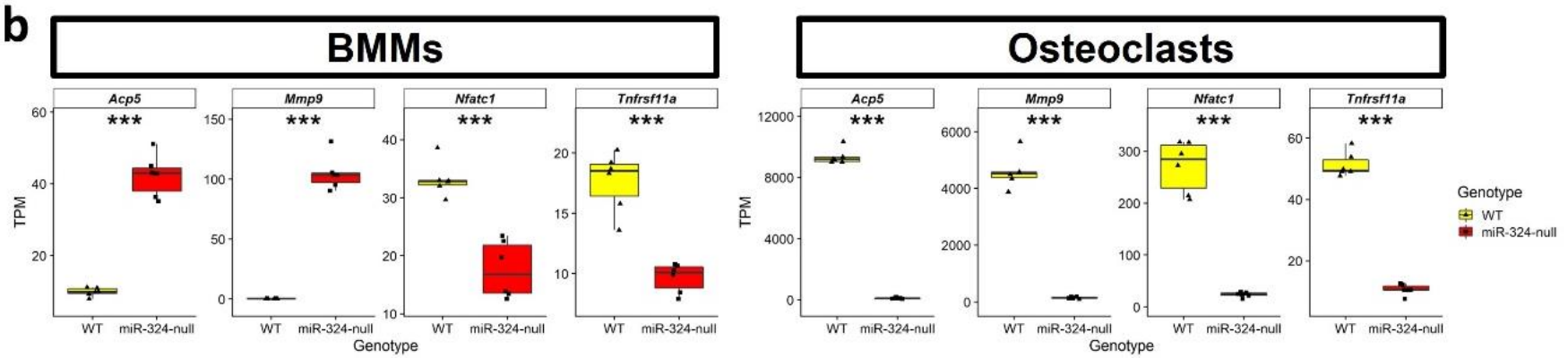

Figure 5.4 - Important osteoclastogenesis genes are dysregulated in miR-324-null BMMs and osteoclasts. (**a**) GO and DO enrichment of RNA-seq results revealed that genes annotated to the 'Positive regulation of ERK1 and ERK2 cascade' and genes annotated to 'Arthritis', respectively, were significantly enriched in both the BMM and osteoclast experiments. These have strong links to osteoclast biology in the literature [467, 468]. (**b**) Both miR-324-null BMMs and osteoclasts displayed a severe downregulation of the key osteoclastogenesis genes *Nfatc1* and *Tnfrsf11a*. *Tnfrsf11a* is annotated to the "Regulation of ERK1 and ERK2 cascade" GO term and both *Tnfrsf11a* and *Nfatc1* are annotated to the "Arthritis" DO term. *Acp5* and *Mmp9* were also severely downregulated in miR-324-null osteoclasts relative to WT controls, but interestingly were significantly upregulated in miR-324-null BMMs. Here, *** indicates adjusted p-values ≤ 0.001, computed as part of RNA-seq analysis.

5.2.2 *miR-324-null osteoblasts show increased bone formation*

In addition to a defect in mature osteoclasts *in vivo*, miR-324-null samples also displayed evidence of increased bone formation, relative to WT controls. Therefore, pre-osteoblasts were isolated from murine calvariae and, after being grown to confluency (14 days), were stimulated with osteogenic media in order to test whether this was also the case *ex vivo*. After 7 days of stimulation with osteogenic media, miR-324-null and WT osteoblasts were fixed and stained with alizarin red-S, as well as testing for alkaline phosphatase activity. In parallel, RNA was extracted from cells of the same genotypes. miR-324-null osteoblasts showed a statistically significant increase of approximately 5% in alizarin red-S intensity and an increase of approximately 30% in alkaline phosphatase activity (Figure 5.5a). Additionally, the expression of the key osteogenesis genes *Alpl*, *Col1a1*, *Col1a2* and *Runx2* was significantly upregulated in miR-324-null osteoblasts (Figure 5.5b).

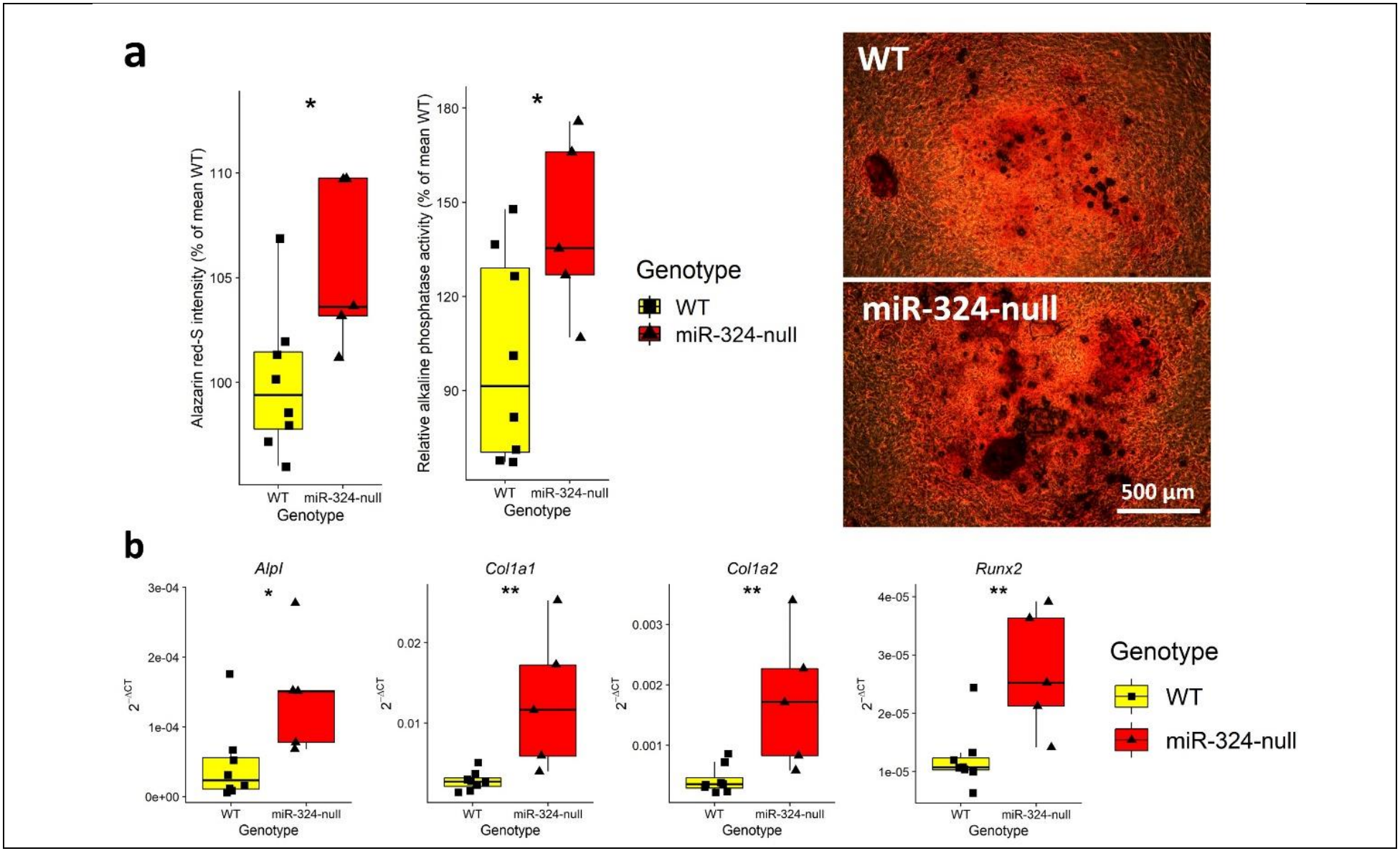
a
Alazarin red-S intensity (% of mean WT)
110
105
100
*
WT
miR-324-null
Genotype
Relative alkaline phosphatase activity (% of mean WT)
180
150
120
90
*
WT
miR-324-null
Genotype
Genotype
WT
miR-324-null
WT
miR-324-null
500 µm
b
Alpl
3e-04
2e-04
1e-04
0e+00
2^-ΔCT
*
WT
miR-324-null
Genotype
Col1a1
0.02
0.01
2^-ΔCT
**
WT
miR-324-null
Genotype
Col1a2
0.003
0.002
0.001
2^-ΔCT
**
WT
miR-324-null
Genotype
Runx2
4e-05
3e-05
2e-05
1e-05
2^-ΔCT
**
WT
miR-324-null
Genotype
Genotype
WT
miR-324-null

Figure 5.5 - miR-324-null calvarial osteoblasts display increased bone formation. (**a**) miR-324-null calvarial osteoblasts show increased osteogenesis relative to WT controls after 7 days of stimulation with osteogenic media. (**a**) Alizarin red-S staining intensity and alkaline phosphatase activity, two markers of bone formation, are significantly upregulated in miR-324-null calvarial osteoblasts stimulated with osteogenic medium, relative to WT controls. Representative images are shown of alizarin red-S stained bone nodules formed by osteoblasts obtained from the murine calvariae of each genotype, illustrating the increased number of bone nodules produced by miR-324-null cells. (**b**) miR-324-null calvarial osteoblasts show significantly increased expression of the key osteogenesis genes *Alpl*, *Col1a1*, *Col1a2* and *Runx2*, relative to WT calvarial osteoblasts, after 7 days of stimulation in osteogenic media. *18S* was utilised as the housekeeping gene to normalise against. For all panels, ** and * represent p-values ≤ 0.01 and 0.05, respectively, calculated using two-tailed Student's *t*-tests.

To confirm that these changes were due to the lack of miR-324, reintroduction of miR-324-5p and -3p to miR-324-null cells was required. First, the expression levels of miR-324-5p and -3p were determined in WT calvarial osteoblasts and a transfection titration using miR-324-5p and -3p mimics was undertaken in order to determine what final concentration of each mimic was required in order to restore miR-324-5p and -3p levels to those of WT controls. From this titration experiment, transfection with each miR-324 arm at 0.5 nM was determined to give near physiological levels (Figure 5.6a). Upon transfection with mimics the increased bone formation previously observed in miR-324-null osteoblasts was severely reduced, as evidenced by a decrease of more than 10% in alizarin red-S staining (Figure 5.6bi). Additionally, the expression of *Col1a2* and *Runx2* were significantly reduced upon mimic addition and whilst *Col1a1* displayed the same trend, the downregulation did not achieve statistical significance (p-value = 0.054). Interestingly, addition of the miR-324 mimics failed to reduce the expression of *Alpl*, implying that this miR-324-null-driven dysregulation cannot be reversed by transient reintroduction of miR-324-5p and -3p (Figure 5.6bi). Analysis of Runx2 protein levels using western blotting confirmed that the re-introduction of miR-324-5p and -3p at physiological levels also rescues Runx2 abundance to normal WT levels at a protein level (Figure 5.6bii).

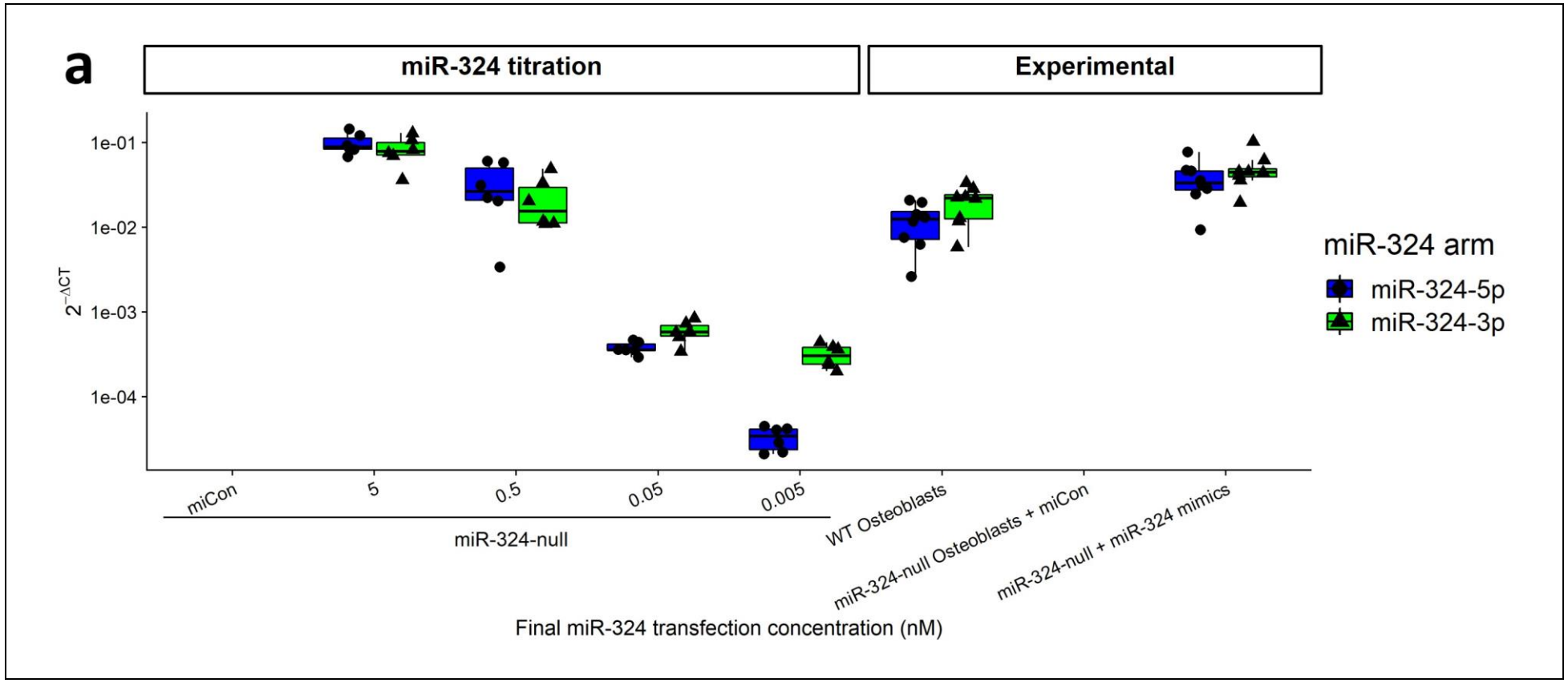
a
miR-324 titration
Experimental
1e-01
1e-02
1e-03
1e-04
$2^{-\Delta CT}$
miCon
5
0.5
0.05
0.005
WT Osteoblasts
miR-324-null Osteoblasts + miCon
miR-324-null + miR-324 mimics
miR-324-null
Final miR-324 transfection concentration (nM)
miR-324 arm
miR-324-5p
miR-324-3p

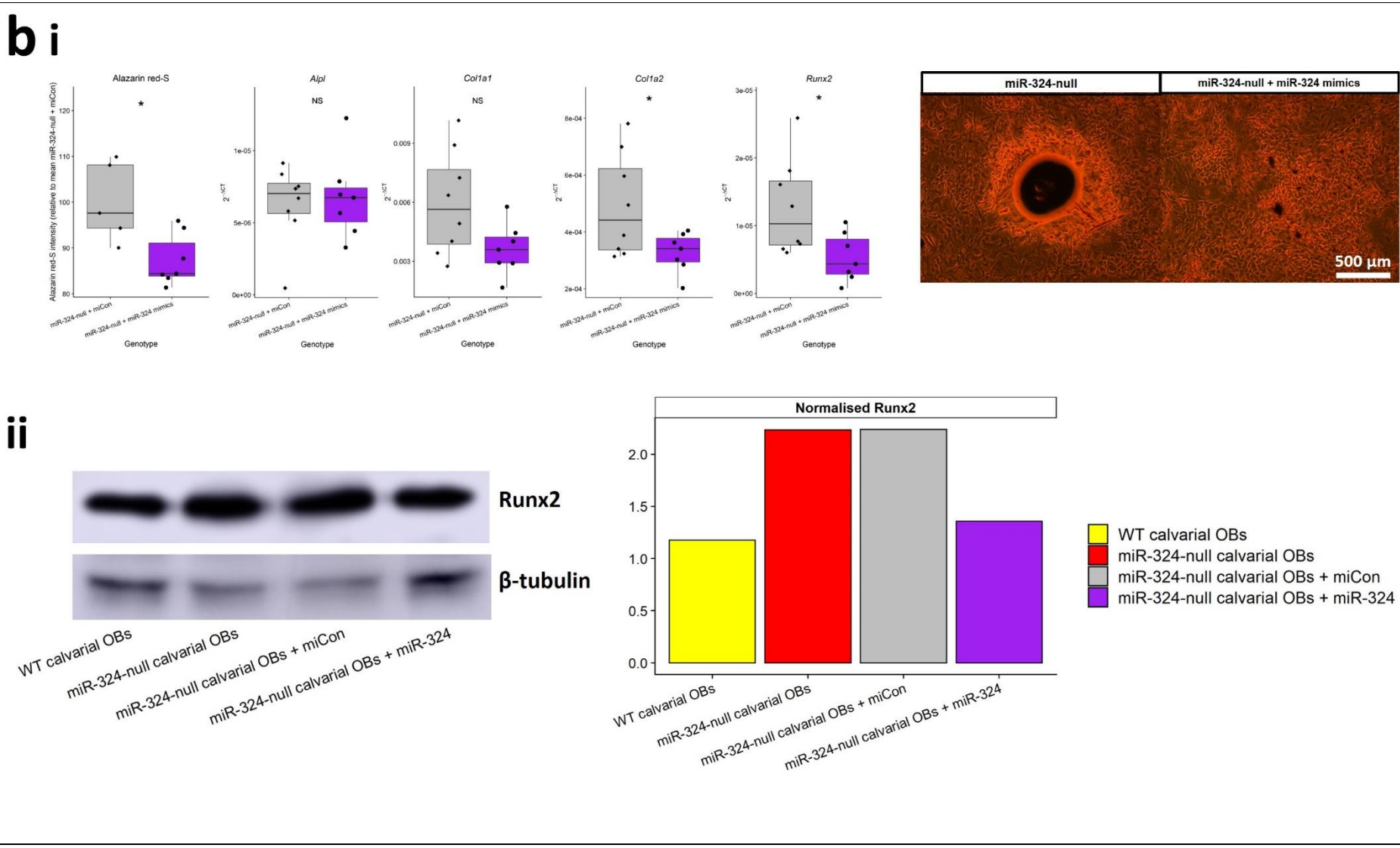
b i
Alazarin red-S
Alpl
Col1a1
Col1a2
Runx2
NS
*
Alazarin red-S intensity (relative to mean miR-324-null + miCon)
2^-dCT
miR-324-null + miCon
miR-324-null + miR-324 mimics
Genotype
miR-324-null
miR-324-null + miR-324 mimics
500 µm
ii
Runx2
β-tubulin
WT calvarial OBs
miR-324-null calvarial OBs
miR-324-null calvarial OBs + miCon
miR-324-null calvarial OBs + miR-324
Normalised Runx2
2.0
1.5
1.0
0.5
0.0

Figure 5.6 - The increased bone formation phenotype in miR-324-null osteoblasts can be reversed by the reintroduction of miR-324-5p and -3p mimics. (**a**) miR-324-null osteoblasts were transfected with 50 nM (final concentration) of miCon as a negative control, in addition to 4 test concentrations of each of miR-324-5p and -3p; 5 nM, 0.5 nM, 0.05 nM and 0.005 nM. WT osteoblasts were also included as a positive control. The optimum final transfection concentration to restore miR-324 to near physiological levels was identified as being 0.5 nM for each arm. (**b**)(**i**) Transfection with 0.5 nM of each of miR-324-5p and -3p at the same time decreased mean alizarin red-S stain intensity by more than 10%, relative to miR-324-null osteoblasts. Additionally, *Col1a2* and *Runx2* levels were significantly repressed by miR-324-5p and -3p reintroduction, quantified using RT-qPCR. *Col1a1* mean levels were also reduced, but this downregulation did not achieve statistical significance (p-value = 0.054). *Alpl* levels failed to be repressed by transfection with miR-324-5p and -3p mimics. *18S* was utilised as the housekeeping gene to normalise against. (**ii**) Western blotting of Runx2 and β-tubulin was undertaken in osteoblasts treated with the following conditions: WT, miR-324-null, miR-324-null + 50nM miCon and miR-324-null + 50nM miR-324 mimics. This demonstrated that transfection of miR-324-5p and -3p at near physiological levels in miR-324-null osteoblasts was able to rescue the excess levels of Runx2. Here, * represents p-value ≤ 0.05, calculated using two-tailed Student's *t*-tests.

In order to identify which genes were dysregulated by the lack of miR-324 in murine osteoblasts, and therefore which of these could cause the increased bone formation phenotype, RNA-seq was undertaken in osteoblasts isolated from hind leg bone chips obtained from individual miR-324-null and WT mice, following 16 days of stimulation with osteogenic media. The bone chip method was utilised in place of the calvarial method here in order to accurately assess biological variance, since in the calvarial isolation method samples are pooled by genotype in order to isolate sufficient cell numbers for experimental work.

The RNA-seq results revealed that over 3500 genes were significantly differentially expressed (adjusted p-value ≤ 0.05) between miR-324-null and WT osteoblasts, resulting in the samples segregating well by genotype using principal component analysis (Figures 5.7a and 5.7b). Marginally more of these were downregulated than were upregulated; 1596 genes were significantly upregulated, whereas 1909 genes were significantly downregulated in miR-324-null osteoblasts. As in the BMM and osteoclast RNA-seq analyses, DO enrichment analysis [343] identified "Arthritis" as an enriched term, but GO enrichment [465, 466] revealed that unexpected terms were enriched, such as "Translation and mitochondrial respiratory chain complex I assembly", implying that *Mir324* deletion may affect key cellular processes in osteoblasts (Figure 5.7c). RNA-seq analysis also revealed that important osteogenic genes such as *Col1a1* and *Runx2* were significantly upregulated in miR-324-null osteoblasts relative to WT controls, as was previously observed in the *ex vivo* calvarial osteoblast experiments. *Alpl* and *Col1a2* also displayed a trend towards upregulation in the miR-324-null samples, although neither of these dysregulations achieved statistical significance at a 5% threshold (adjusted p-values = 0.36 and 0.56, respectively; Figure 5.7d).

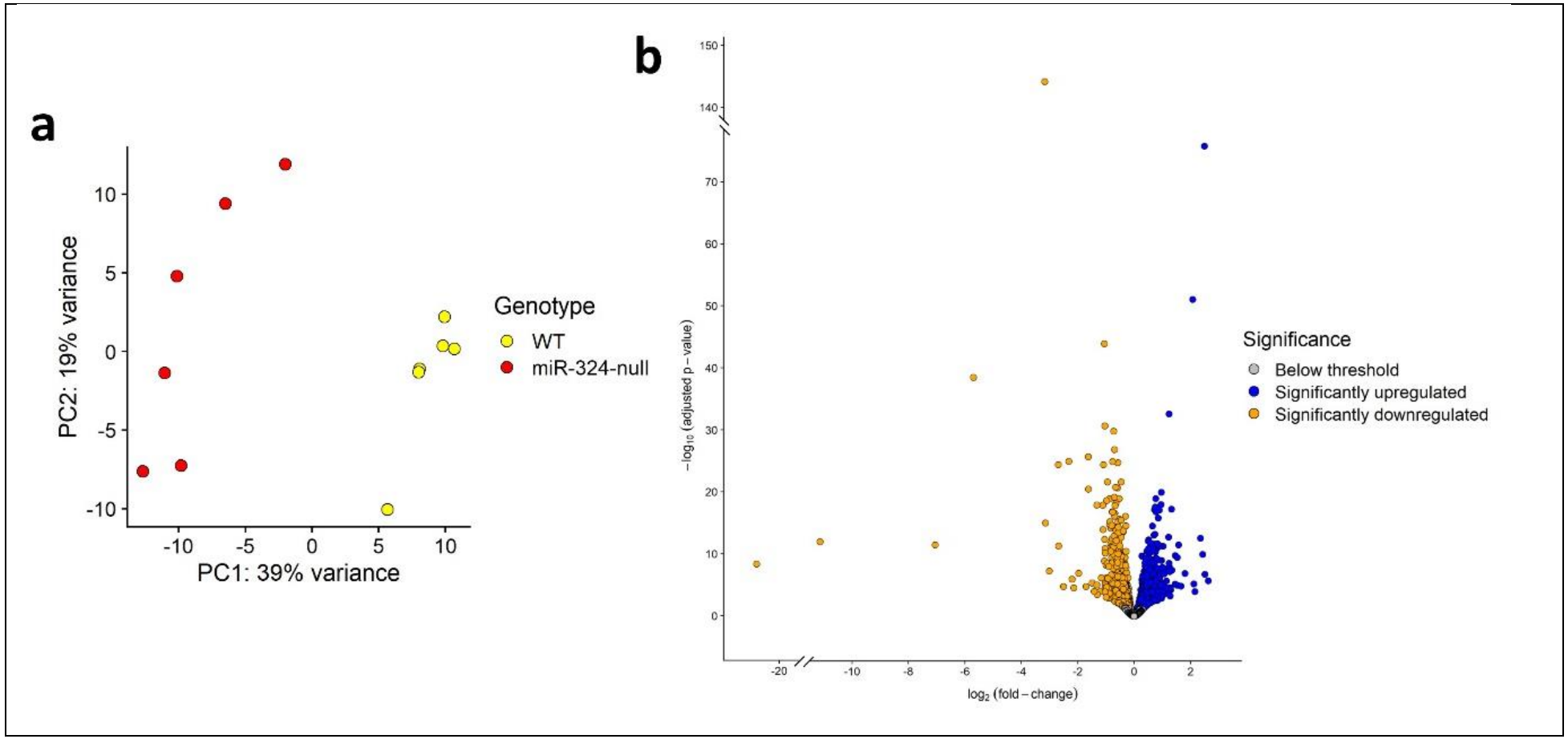
a
PC2: 19% variance
PC1: 39% variance
Genotype
WT
miR-324-null
b
−log10 (adjusted p − value)
log2 (fold − change)
Significance
Below threshold
Significantly upregulated
Significantly downregulated

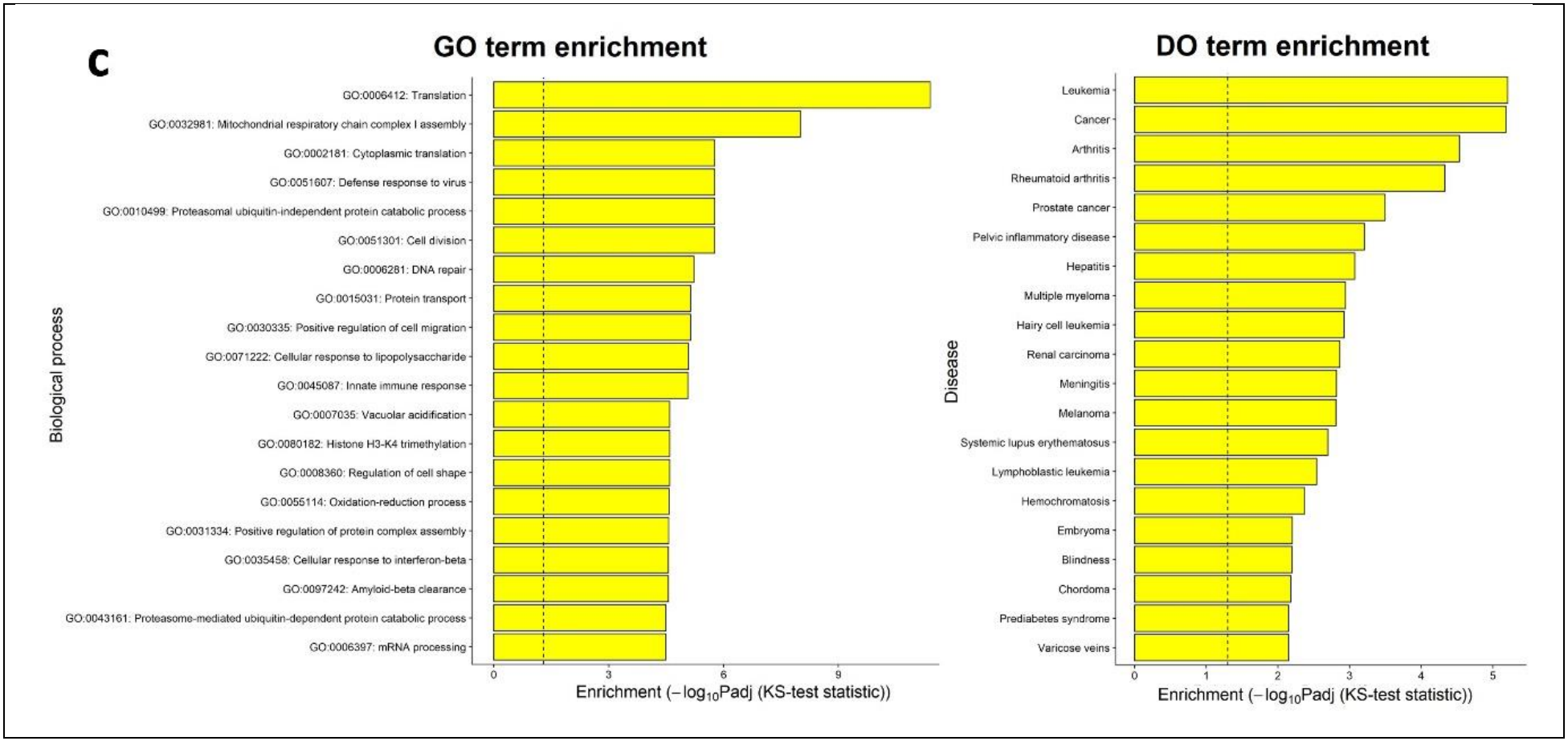
C
GO term enrichment
GO:0006412: Translation
GO:0032981: Mitochondrial respiratory chain complex I assembly
GO:0002181: Cytoplasmic translation
GO:0051607: Defense response to virus
GO:0010499: Proteasomal ubiquitin-independent protein catabolic process
GO:0051301: Cell division
GO:0006281: DNA repair
GO:0015031: Protein transport
GO:0030335: Positive regulation of cell migration
GO:0071222: Cellular response to lipopolysaccharide
GO:0045087: Innate immune response
GO:0007035: Vacuolar acidification
GO:0080182: Histone H3-K4 trimethylation
GO:0008360: Regulation of cell shape
GO:0055114: Oxidation-reduction process
GO:0031334: Positive regulation of protein complex assembly
GO:0035458: Cellular response to interferon-beta
GO:0097242: Amyloid-beta clearance
GO:0043161: Proteasome-mediated ubiquitin-dependent protein catabolic process
GO:0006397: mRNA processing
Biological process
0
3
6
9
Enrichment (−log10Padj (KS-test statistic))
DO term enrichment
Leukemia
Cancer
Arthritis
Rheumatoid arthritis
Prostate cancer
Pelvic inflammatory disease
Hepatitis
Multiple myeloma
Hairy cell leukemia
Renal carcinoma
Meningitis
Melanoma
Systemic lupus erythematosus
Lymphoblastic leukemia
Hemochromatosis
Embryoma
Blindness
Chordoma
Prediabetes syndrome
Varicose veins
Disease
0
1
2
3
4
5
Enrichment (−log10Padj (KS-test statistic))

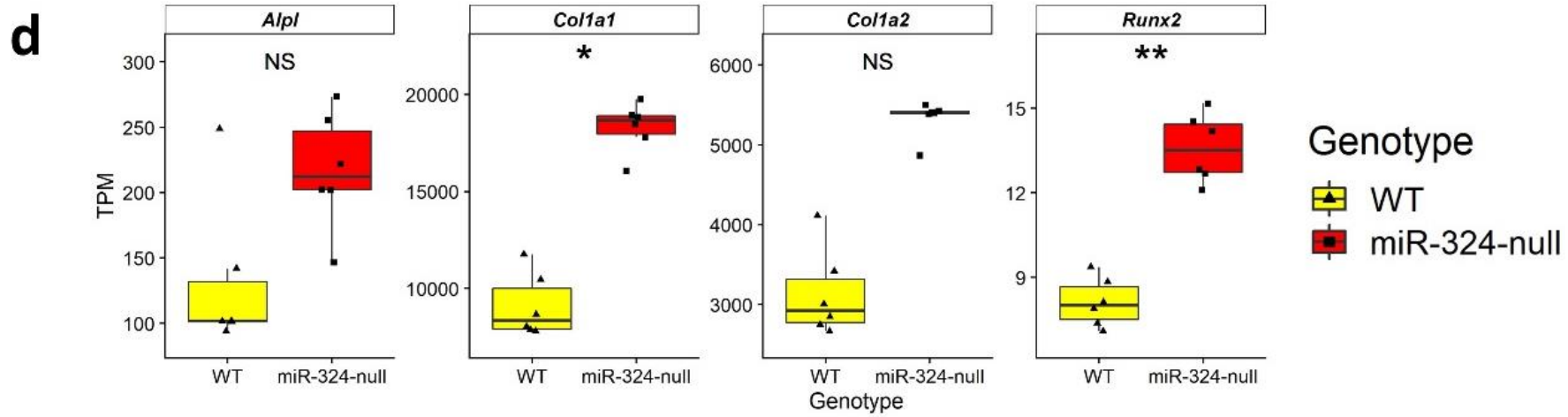

Figure 5.7 - miR-324-null osteoblasts are distinct from WT osteoblasts at a transcriptomic level using RNA-seq analysis. (**a**) miR-324-null osteoblasts segregate well from WT osteoblasts in principal component analysis. (**b**) A volcano plot illustrates that approximately 4000 genes were dysregulated in miR-324-null osteoblasts, relative to WT controls. Blue points represent genes significantly upregulated in miR-324-null samples, orange points represent genes significantly downregulated in miR-324-null samples and grey points indicate genes which did not achieve statistical significance (adjusted p-value ≤ 0.05). (**c**) Illustration of terms enriched in miR-324-null osteoblasts using GO and DO enrichment analysis. Notably, "Arthritis" is enriched in DO enrichment analysis again, as it was in the BMM and osteoclast RNA-seq results. (**d**) The key osteogenesis genes *Col1a1* and *Runx2* are significantly upregulated in miR-324-null osteoblasts, relative to WT controls. *Alpl* and *Col1a2* also show a strong trend towards upregulation, although these dysregulations did not achieve statistical significance at a 5% threshold (adjusted p-values = 0.36 and 0.56, respectively). Here, ** and * represent adjusted p-values ≤ 0.01 and 0.05, respectively, computed as part of RNA-seq analysis.

5.2.3 *miR-324-5p and miR-324-3p both regulate the balance between osteogenesis and adipogenesis in the differentiation of murine mesenchymal stromal cells*

Both *in vivo* and *ex vivo*, miR-324-null samples showed increased bone formation. Additionally, *in vivo*, miR-324-null mice showed an almost complete lack of lipid droplets (a reduction of 92.8%), implying a lack of adipogenesis. Therefore, we proceeded to investigate whether this shift from adipogenesis to osteogenesis could be replicated *in vitro* using the immortalised murine MSC-like cell line C3H10T1/2. Cells were transfected with either control, miR-324-5p or miR-324-3p miRNA mimics or hairpin inhibitors and subsequently stimulated with co-differentiation (AdiOst) media for 14 days in order to measure the shift between osteogenesis and adipogenesis under each condition [355]. By using this co-differentiation AdiOst media, alizarin red-S and oil red-O staining can be utilised to assess the relative levels of adipogenesis and osteogenesis in each sample, therefore allowing calculation of an AdiOst ratio (the ratio of oil red-O to alizarin red-S stain intensity for each replicate). Upon transfection of C3H10T1/2 cells with hairpin inhibitor (hp-) against either miR-324-5p or miR-324-3p, only hp-miR-324-5p significantly increased osteogenesis whilst inhibiting adipogenesis, relative to a negative control miRNA hairpin (hpCon). Similar findings were obtained for hp-miR-324-3p, although this did not significantly inhibit adipogenesis (p-value = 0.067). Transfection with each of the hairpin inhibitors resulted in significant decreases in the AdiOst ratio (Figures 5.8a and 5.8b). When either miR-324-5p or -3p mimics were added, alizarin red-S stain intensity was significantly decreased and oil red-O stain intensity was significantly increased, relative to a negative control miRNA mimic (miCon), together resulting in a significantly increased AdiOst ratio (Figures 5.8a and 5.8b).

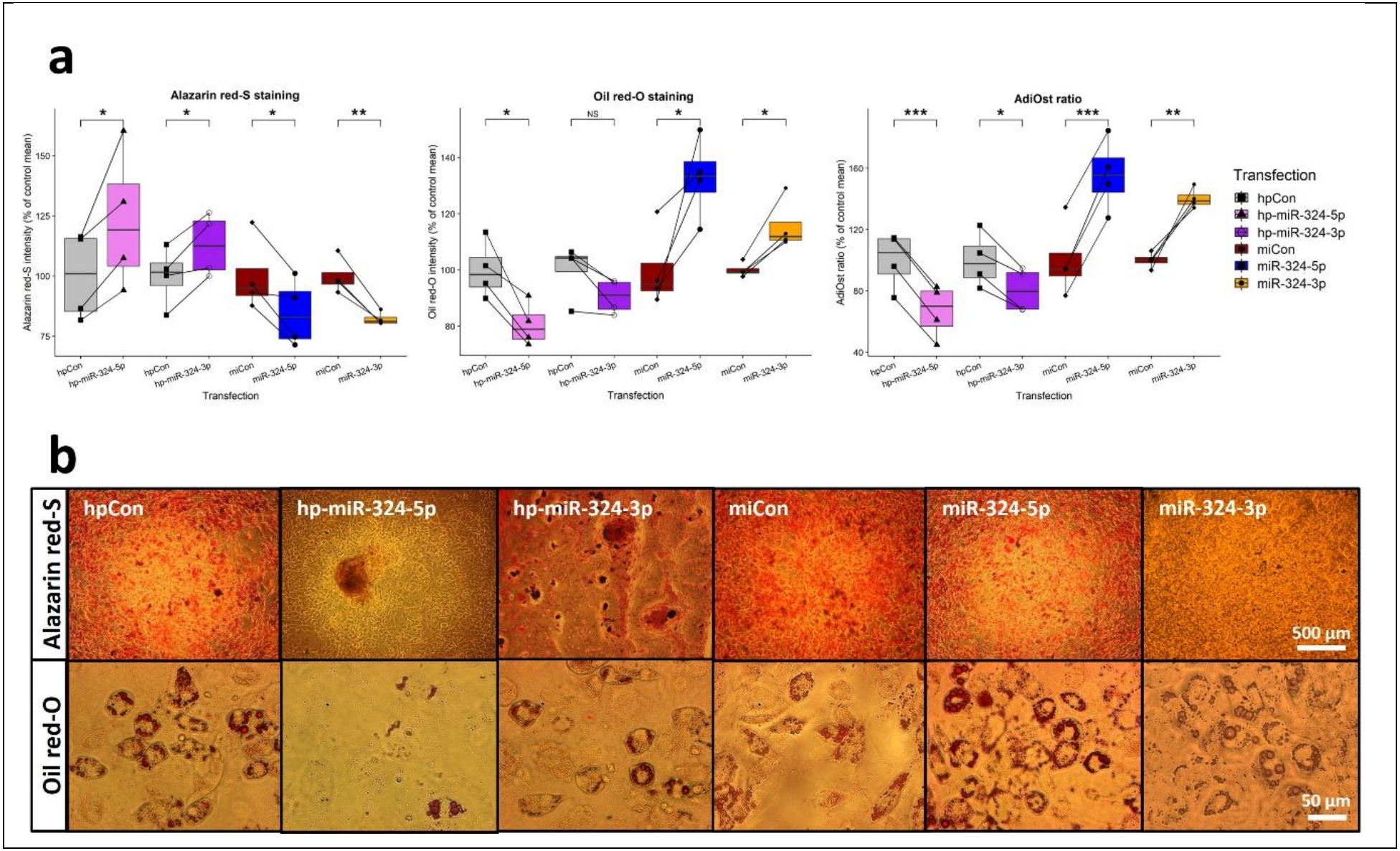
a
Alazarin red-S staining
Alazarin red-S intensity (% of control mean)
Oil red-O staining
Oil red-O intensity (% of control mean)
AdiOst ratio
AdiOst ratio (% of control mean)
NS
Transfection
hpCon
hp-miR-324-5p
hp-miR-324-3p
miCon
miR-324-5p
miR-324-3p
b
Alazarin red-S
Oil red-O
hpCon
hp-miR-324-5p
hp-miR-324-3p
miCon
miR-324-5p
miR-324-3p
500 μm
50 μm

Figure 5.8 - Overexpression or inhibition of miR-324-5p and -3p modulates the lineage commitment between adipogenesis and osteogenesis in C3H10T1/2 cells. C3H10T1/2 cells were transfected either with the negative control miRNA mimic (miCon), miR-324-5p mimic, miR-324-3p mimic, the negative control miRNA hairpin inhibitor (hpCon), miR-324-5p hairpin inhibitor (hp-miR-324-5p) or miR-324-3p hairpin inhibitor (hp-miR-324-3p; all at a final concentration of 50 nM). After 18 days, cells were fixed and stained with alizarin red-S and oil red-O, as indicators of the levels of osteogenesis and adipogenesis, respectively. (**a**) Both hp-miR-324-5p and -3p produced significant increases in alizarin red-S staining intensity, although hp-miR-324-3p failed to significantly reduce adipogenesis (p-value = 0.067). The AdiOst ratio was significantly reduced by transfection of each hairpin inhibitor. Overexpression of each of miR-324-5p and -3p resulted in significantly decreased alizarin red-S staining intensity, significantly increased oil red-O staining intensity and a significantly decreased AdiOst ratio. Here, ***, ** and * represent p-values ≤ 0.001, 0.01 and 0.05, respectively, calculated using Student's two-tailed paired *t*-tests. The means of 4 independent experiments were used to test statistical significance, with 3 technical replicates in each independent experiment. (**b**) Representative images of C3H10T1/2 cells plated in AdiOst co-differentiation media, transfected with either miCon, hp-miR-324-5p, hp-miR-324-3p, miR-324-5p or miR-324-3p, and stained either with alizarin red-S or oil red-O. Cells were imaged at 5X magnification for alizarin red-S stains and 40X magnification for oil red-O stains.

As predicted from the histological analysis, samples transfected with either hp-miR-324-5p or hp-miR-324-3p displayed significantly increased *Runx2* expression in addition to significantly decreased *Pparg* expression (Figure 5.9). In samples where the miR-324-5p mimic was added, the mean *Runx2* expression level trended towards a decrease, although this did not achieve statistical significance (p-value = 0.193), and *Pparg* expression was significantly increased. In samples transfected with the miR-324-3p mimic, *Runx2* expression was significantly downregulated and *Pparg* expression was significantly upregulated (Figure 5.9).

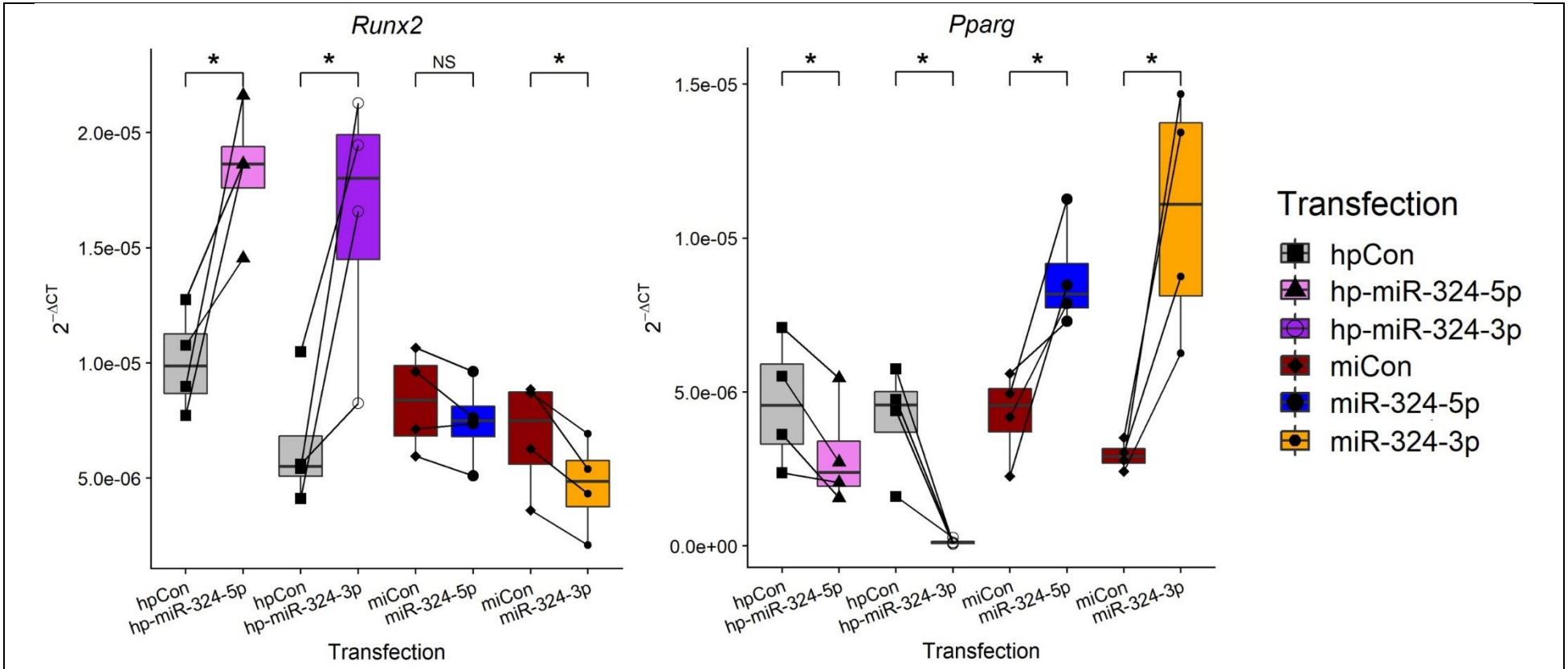

Figure 5.9 - Overexpression or inhibition of miR-324-5p and -3p modulates expression of the osteogenic and adipogenic transcription factors *Runx2* and *Pparg*. C3H10T1/2 cells were transfected either with the negative control miRNA mimic (miCon), miR-324-5p mimic, miR-324-3p mimic, the negative control miRNA hairpin inhibitor (hpCon), miR-324-5p hairpin inhibitor (hp-miR-324-5p) or miR-324-3p hairpin inhibitor (hp-miR-324-3p; all at a final concentration of 50 nM). After 18 days, cells were lysed and the expression of the key transcription factors *Runx2* (for osteogenesis) and *Pparg* (for adipogenesis) were measured by RT-qPCR, utilising *18S* as the housekeeping gene to normalise against. Inhibition of either miR-324-5p

or -3p significantly increased *Runx2* expression and decreased *Pparg* expression. Overexpression of miR-324-5p significantly upregulated *Pparg*, but failed to significantly downregulate *Runx2* expression (p-value = 0.193). Overexpression of miR-324-3p significantly reduced *Runx2* expression and upregulated *Pparg* expression. Here, * represents p-value ≤ 0.05, calculated using Student's two-tailed paired *t*-tests. The means of 4 independent experiments were used to test statistical significance, with 3 technical replicates in each independent experiment.

5.3 Discussion

5.3.1 *Osteoclastogenesis is severely impaired in miR-324-null mice*

The number of miR-324-null osteoclasts relative to WT controls is severely decreased, as is the number of nuclei per mature osteoclast (Figure 5.2), as was suspected based on the *in vivo* results of Chapter 4. However, what was not anticipated from the previous chapter was the sheer scale of dysregulation in miR-324-null osteoclasts generated *ex vivo* relative to WT controls; almost 9000 genes were significantly dysregulated in these cells using an adjusted p-value, which is over 40% of all genes tested (Figure 5.3). Considering the scale of this dysregulation, it is almost surprising that osteoclasts are able to form at all, but despite their transcriptomic background, a small number of mature multinucleate miR-324-null osteoclasts are still observed. The fact that osteoclastogenesis is able to proceed to apparent completion in a small number of cases implies that the process of osteoclastogenesis is only impaired in miR-324-null mice, rather than inhibited entirely. This supports the hypothesis posited in Chapter 4 of a bottleneck at some point during the osteoclastogenic process, presumably dependent on the availability of a key factor which is repressed by *Mir324* deletion. Although no specific methodology has been utilised to identify this factor, it is difficult to ignore the severe downregulation of *Nfatc1*, which encodes a key osteoclastogenic transcription factor and *Tnfrs11a*, which encodes RANK, in miR-324-null osteoclasts (Figure 5.4b). These genes are essential in the normal formation and maturation of osteoclasts, forming an amplification loop between one another to transcribe more *Tnfrs11a*, thus allowing the binding of more RANK-L, increased *Nfatc1* activation and subsequent further *Tnfrs11a* transcription, in addition to other key osteoclastogenic genes [452-454]. Downregulation of either *Nfatc1* or *Tnfrs11a* would therefore necessarily lead to a decrease in the expression of the other. Potentially one of these genes could encode the key factor required for the hypothesis proposed in Chapter 4, although if this is the case it is unclear how far downstream of *Mir324* deletion this effect is found; as both *Nfatc1* and *Tnfrs11a* are downregulated upon *Mir324* deletion, there cannot be a canonical direct targeting interaction between miR-324 and either of these genes. If either *Nfatc1* or *Tnfrs11a* encode this key factor then the impaired miR-324-null osteoclastogenesis phenotype is evidently caused at the BMM stage of differentiation in addition to during the osteoclastogenesis process, as even in miR-324-null BMMs are these two genes found to be severely downregulated. This would therefore suggest that the bottleneck proposed in Chapter 4 actually occurs at the very start of osteoclastogenesis. The lack of *Tnfrs11a* in particular would result in a severe lack of the receptor required to initiate

the osteoclastogenesis process. Presumably this would result in a similar phenotype as has been previously observed upon overexpression of other osteoclastogenesis inhibitors, such as *Irf8* and *Bcl6*; a severe decrease in the number of mature multinucleate osteoclasts and a resulting relative increase in the number of mononucleated precursors [472, 473]. Additionally, it is unclear how this downregulation of *Nfatc1* or *Tnfrs11a* would allow only some miR-324-null BMMs to undergo osteoclastogenesis, whilst inhibiting others, considering that both genotype and environment (the cell culture medium and conditions) are identical for all cells. It would therefore be highly beneficial to utilise single cell RNA-seq in future investigation of this phenotype to compare individual miR-324-null cells which have managed to fuse and mature with those which failed to undergo any fusion. It is worth noting that other genes essential for normal osteoclast activity, such as *Acp5* and *Mmp9*, are also severely downregulated in miR-324-null osteoclasts (Figure 5.4b), but these genes are not required to initiate the differentiation process, and so I believe it is more likely that downregulation of either *Nfatc1* and *Tnfrs11a* in BMMs is where the cause of the miR-324-null osteoclast deficiency lies.

Although miR-324-null mice are deficient in osteoclasts, which can be replicated *ex vivo*, the function of mature miR-324-null osteoclasts relative to WT controls has not been tested herein. This is an important point, as examples of modulated osteoclast function irrespective of altered osteoclast number have previously been reported [346]. In order to confirm whether this is the case with miR-324-null osteoclasts, it would be necessary to undertake resorption assays, as it is possible that despite the severe decrease in osteoclast number, pathways involved in bone resorption could be more active. In lieu of this evidence however, the most probable effect of the deficiency in miR-324-null osteoclasts is that miR-324-null mice will also display a corresponding decrease in bone resorption.

It is important to discuss that although the scale of modulation *Mir324* deletion has effected upon the osteoclast transcriptome is vast, there are caveats to the methodology utilised which could have amplified the observed effects. In order to assess osteoclastic differentiation *ex vivo* and thus obtain the RNA used to compare miR-324-null and WT osteoclasts, bone marrow was extracted and the cells within these extractions were stimulated with M-CSF. The concentration of this chemokine was tightly controlled, but the quality and number of viable cells extracted from the bone marrow could have varied greatly between samples and genotypes. For example, if the marrow extracted from miR-324-null bones contained a more

heterogeneous cell population, and thus fewer cells with the potential to differentiate along the osteoclastic lineage, then fewer mature osteoclasts would be observed following RANK-L stimulation in addition to reduced expression of key osteoclast genes, despite there theoretically being no barrier to miR-324-null osteoclastic differentiation. This possibility seems unlikely considering that no obvious difference in cell number between genotypes following stimulation with M-CSF was observed, but it is an important caveat to consider in the context of the results presented in this chapter.

5.3.2 *miR-324-null bone marrow macrophages are distinct from WT controls*

Although miR-324-null BMMs show marginally less dysregulation in terms of gene number relative to miR-324-null osteoclasts, over 34% of all genes tested were still found to be differentially expressed, of which more than half were also dysregulated in miR-324-null osteoclasts (Figure 5.3c). Therefore, many of the genes dysregulated in miR-324-null osteoclasts were likely dysregulated throughout the entire osteoclastogenesis process, suggesting that altered expression of these genes could be responsible for the osteoclast deficiency phenotype. It is unknown at present however whether the differentiation of HSCs into BMMs is the point at which the majority of this gene dysregulation occurs, or whether the dysregulation is present at even earlier stages in the haematopoietic lineage, such as in HSCs themselves. Regardless of this, *Nfatc1* and *Tnfrs11a* are significantly downregulated both at the BMM and osteoclast stages of differentiation, suggesting that these genes could at least in part be causal of the miR-324-null impaired osteoclastogenesis phenotype. Interestingly however, *Acp5*, a highly osteoclast-selective gene identified as being downregulated in miR-324-null osteoclasts, is actually severely upregulated in miR-324-null BMMs (Figure 5.4b). It is unclear exactly what the effect of premature *Acp5* upregulation would be in this context. Overexpression of human *ACP5* has been demonstrated to increase the proliferative and migratory abilities of various cancer cell lines [474-476], although no obvious increase in BMM proliferation was observed here. Despite osteoclast precursor migration and proliferation being essential components of osteoclastogenesis, this purported *Acp5*-mediated increase in proliferation is certainly insufficient to rescue the osteoclastogenesis defect *in vivo*, or else no such defect would be observed, and a clear decrease in osteoclast number in miR-324-null tibiae was demonstrated in Chapter 4. It is therefore unclear at present whether a premature increase in *Acp5* expression would have any effect on osteoclastogenesis.

Considering the large number of genes dysregulated in miR-324-null BMMs, it would be interesting to assess immunological functions of miR-324-null mice related to macrophage biology, such as phagocytosis and the production of cytokines. It would be highly surprising if there was no effect of *Mir324* deletion on the immune system, due to the fact that over 7000 genes were differentially expressed in miR-324-null BMMs relative to WT controls. It is additionally possible that the dysregulation is also present in HSCs and the observed dysregulation in miR-324-null BMMs is merely a reflection of this. If this is the case then many cells of the haematopoietic lineage could conceivably show abnormal activity due to miR-324-null-mediated gene dysregulation, as found in mice deficient in *Ikaros*, which encodes an important haematopoietic lineage-specific transcription factor [477]. Furthermore, the miR-324-null haematopoietic lineage dysregulation could be linked to the miR-324-null bone marrow fat deficiency. Although adipocytes are of the mesenchymal lineage, the bone marrow fat they produce has been shown to play an important role in HSC proliferation, through secretion of factors such as adiponectin and leptin [478-480]. Through this mechanism, adipocytes are purported to be supportive of the haematopoietic niche *in vivo* [481]. It is therefore plausible that the severe lack of bone marrow fat observed *in vivo* in miR-324-null mice (Chapter 4) may affect the expression of important haematopoietic genes at an early stage in the lineage. If this were the case then any dysregulation identified in miR-324-null cells of the HSC lineage could in fact be attributed to the effects of miR-324 in shifting the balance of commitment to adipogenesis and osteogenesis in the mesenchymal lineage.

5.3.3 *miR-324-null osteoblasts display increased bone formation, which can be rescued by transfection of miR-324 mimics*

Osteogenesis assays utilising osteoblasts obtained from miR-324-null and WT murine calvariae showed that *Mir324* deletion results in increased bone formation (Figure 5.5), as was expected from the *in vivo* data in Chapter 4. Additionally, by transfecting these cells with miR-324-5p and -3p mimics at physiological levels, the excess bone phenotype was corrected (Figure 5.6). This adds further weight to the evidence that the excess bone phenotype is not a consequence of deletion of the genomic loci proximal to the *Mir324* gene, but instead is due to lack of miR-324 activity.

An interesting result of identifying the final transfection concentrations of miR-324-5p and -3p to restore each to physiological levels was that at lower final concentrations (0.05 and 0.005 nM), the miR-324-3p mimic had a higher transfection efficiency than the miR-324-5p

mimic (Figure 5.6a). The reason behind this effect is unclear, especially considering that at higher final transfection concentrations (5 and 0.5 nM), both mimics showed similar transfection efficiencies. Potentially at lower concentrations, effects of reduced stability of miR-324-3p are observable relative to miR-324-5p, considering that the predicted optimal structure of miR-324-3p is marginally less stable than that of miR-324-5p (minimum free energies = -3.30 and -2.60 kcal/mol, respectively, according to RNAFold [482-484]), although whether this theoretical optimal structure is actually the structure adopted by the miR-324 mimics is unknown and would require further investigation.

The *ex vivo* increased bone formation phenotype supports one hypothesis suggested in Chapter 4; that miR-324 deficiency both increases commitment of mesenchymal-derived cells to the osteogenic lineage rather than adipogenesis and increases the bone formation activity of mature osteoblasts. Despite seeding at equal densities, miR-324-null osteoblasts still showed an increase in bone formation relative to WT controls (Figure 5.5), strongly suggesting that the increase in bone formation observed *in vivo* cannot merely be due to a shift in lineage commitment alone. If that were the case, then seeding at equal densities in this *ex vivo* experiment, when the cells were already committed to the osteoblast lineage, should result in no difference in the amount of bone formed. Equally however, the severe *in vivo* decrease in adipogenesis shown in Chapter 4 suggests that *Mir324* deletion also affects the shift between the adipogenic and osteochondroprogenitor lineages. The same phenotype of excess bone formation was observed in osteoblasts isolated from murine leg bones, and RNA sequencing of these osteoblasts revealed that over 3500 genes were differentially expressed in miR-324-null samples (Figure 5.7). Considering the scale of this dysregulation it is entirely plausible that deletion of *Mir324* really could affect multiple components of the bone formation pathway. miR-324 therefore may be a key regulator of the osteoblast differentiation and the bone formation pathway as a whole.

The GO [465, 466] term “Translation and mitochondrial respiratory chain complex I assembly” was significantly enriched in miR-324-null osteoblasts relative to WT controls, and therefore it is possible that *Mir324* deletion also affects energy metabolism processes. This is unlikely to be an effect through *Acadvl* dysregulation due to the original deletion of the *Mir324* locus, considering that in Chapter 3 I showed that protein levels of Acadvl and the other the proximal gene to *Mir324*, *Dvl2*, were unaltered in miR-324-null mice. However, this does not exclude the possibility that mitochondrial pathways are indirectly affected by *Mir324* deletion through

an as yet unidentified target. Mitochondrial dysfunction is known to severely alter the rate of fat metabolism [485, 486] and therefore an alteration in mitochondrial activity could also offer a potential alternative explanation to the lack of lipid droplets identified in miR-324-null tibial bone marrow in Chapter 4. Further experiments are required to determine whether mitochondrial activity really is affected by *Mir324* deletion, for which a useful preliminary investigation would be to utilise a Seahorse assay to measure mitochondrial respiration levels [487].

5.3.4 *Both miR-324-5p and miR-324-3p are able to modulate the lineage choice between adipogenesis and osteogenesis in vitro*

In order to confirm that miR-324 affected the lineage commitment of MSCs, I undertook a co-differentiation AdiOst experiment in murine C3H10T1/2 MSC-like cells [355]. Transfection with miR-324-5p, miR-324-3p, hp-miR-324-5p or hp-miR-324-3p all resulted in significant shifts in the ratio of adipogenesis to osteogenesis (AdiOst ratio); overexpression of both miR-324 arms resulted in increased adipogenesis relative to osteogenesis, whereas hp-miR-324-5p and hp-miR-324-3p resulted in decreased adipogenesis relative to osteogenesis, mimicking the miR-324-null *in vivo* phenotype (Figure 5.8). Therefore, in combination with the other results in this chapter, it seems likely that *Mir324* deletion affects multiple components of the osteoblast differentiation and bone formation pathway; these AdiOst results demonstrate that miR-324 can affect the lineage commitment of MSCs, whereas the other *ex vivo* experiments in this chapter demonstrate that lack of miR-324 can additionally likely increase mature osteoblast activity.

It is interesting that, at least in regard to the miR-324-mediated shift in MSC lineage commitment, both arms of miR-324 appear to produce the same result. There are two possibilities as to why this is, the simplest of which is that both miR-324-5p and -3p may target the same mRNAs and therefore through these affect the same pathway (summarised in Figure 5.10a). These targets would necessarily be key factors involved throughout the osteoblast differentiation and bone formation pathway, although it is difficult to explain the evolutionary impetus behind this, unless one miR-324 arm is insufficient on its own. Potentially this is not as unlikely as it initially seems in the case of miR-324; the -3p arm of miR-324 in particular is predicted by the TargetScan miRNA target prediction algorithm [5, 67] to target 5078 transcripts, which corresponds to almost 25% of all genes, and the -5p arm is also predicted to target 3143 transcripts, approximately 15% of all genes. Most importantly, 1304 genes are

predicted to be targeted by both miR-324-5p and -3p, meaning that more than 40% of all predicted miR-324-5p targets are also predicted to be targets of miR-324-3p, and over 25% of all miR-324-3p targets are also predicted -5p targets (Figure 5.10b). Of course this does not mean that all of these genes are real physiological targets of both or indeed either arm of miR-324 (discussed further in Chapter 6), but it does increase the likelihood of both arms targeting the same transcript. The second and more complicated possibility is that each arm of miR-324 targets different mRNAs, but these targets exert their effects on the same components of the bone formation pathway. Considering however that the magnitude of the effects of miR-324-5p and -3p, and their corresponding hairpin inhibitors, is approximately equal for each arm, this limits the feasibility of this idea, unless those targets cross-regulated one another. If that were the case then it would be expected that the dysregulation of one arm would produce identical effects to the dysregulation of the other arm, and indeed to the dysregulation of both at the same time (summarised in Figure 5.10c and d). If both targets were indeed part of a positive feedback loop, then it could be argued that miR-324 may act to block the excessive activity of this cycle; perhaps when the levels of one or both targets reaches a threshold then *Mir324* expression is upregulated in order to inhibit the feedback loop. A miRNA acting in this way is not unheard of; miR-200b has been shown to operate in a similar manner by downregulating *PRKCA*, the protein product of which forms a positive feedback loop with WNT5B resulting in increased cancer metastasis [488]. However, miR-200b did not target both members of the positive feedback loop, as may be the case with miR-324 here. If this is indeed the case, an explanation could be found in the fact that both miR-324-5p and -3p are detected at near identical levels, at least in the mesenchymal lineage. Perhaps each target requires an individual mature miRNA to repress it in order to effectively inhibit the feedback loop, such that both members of the positive feedback loop are downregulated together. The similar physiological levels of miR-324-5p and -3p may have resulted in miR-324 being an excellent evolutionary candidate for this, so that when miR-324 levels require increasing to inhibit the feedback loop both arms can be co-regulated from the same *Mir324* locus. Regardless of which of these potential explanations is correct, it is intriguing that both arms of a single miRNA exert precisely the same effect as one another on exactly the same pathway, and therefore at this stage it is unclear which, if either, arm of miR-324 is more important in the processes of bone formation and osteoblastic differentiation; neither arm appears to have a dominant effect relative to the other, potentially due to the proposed overlap between miR-324-5p and -3p targets.

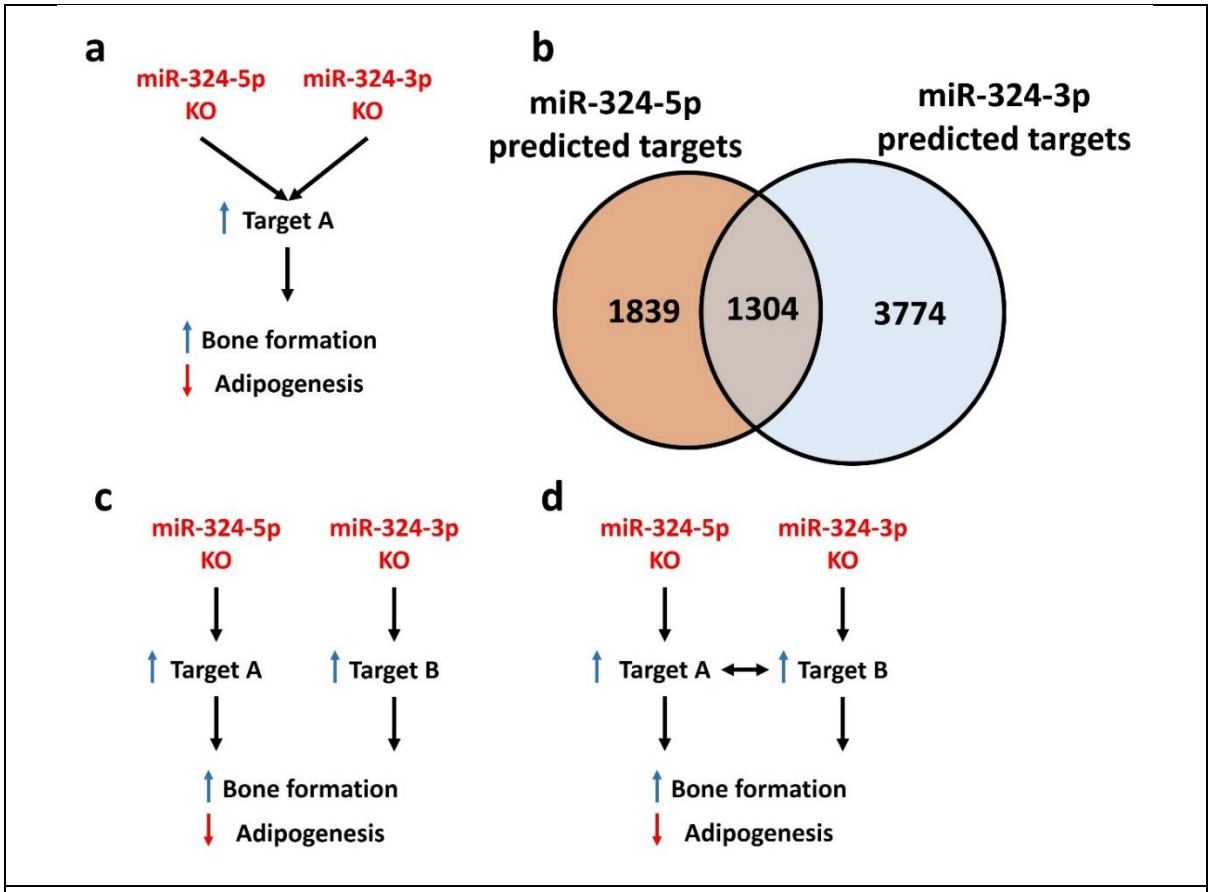

Figure 5.10 - The proposed mechanisms through which both miR-324-5p and miR-324-3p may regulate the same pathways. (**a**) If both miR-324-5p and -3p targeted the same mRNA, a key factor involved in adipogenesis and osteogenesis, it would be expected for both arms to produce the same effect on this pathway. However, it is unclear why this would be necessary evolutionarily. (**b**) A large proportion of miR-324 target genes predicted by the TargetScan algorithm [5, 67] are predicted to be targeted by both miR-324-5p and -3p, and thus regulation of the same target by both arms may be more likely than at first expected; over 40% of predicted miR-324-5p targets are also predicted targets of miR-324-3p, and more than 25% of miR-324-3p targets are also predicted -5p targets. (**c**) If each miR-324 arm targeted a distinct mRNA, but both targets exerted a similar effect on adipogenesis and osteogenesis, then both arms may be expected to exert the same downstream effect as one another. However, this would be unlikely to produce effects of identical magnitude, as is observed in the results here. (**d**) The final option through which miR-324-5p and -3p could regulate the same pathways is identical to panel **c**, except that here Target A and Target B also regulate one another. This would result in the modulation of expression of one miR-324 arm producing an identical response to that of the other, and probably also an identical result as would be found if the expression of both arms was modulated simultaneously.

5.4 Summary

In this chapter I have shown that miR-324-null BMMs display a severe impairment in osteoclastogenic differentiation *ex vivo*. Using RNA-seq I showed that over 40% of all genes tested were differentially expressed, most notable of which were the key osteoclastogenic genes *Nfatc1* and *Tnfrs11a*, which were robustly downregulated both in BMMs and osteoclasts. I hypothesised that the dysregulation of these genes may be the cause of the decreased number of mature osteoclasts observed in miR-324-null samples, although these cannot be direct targets of miR-324 themselves as miRNAs canonically repress their target mRNA transcripts. I also showed that BMMs are themselves already highly distinct between the genotypes assessed even before osteoclastogenic differentiation, with over 30% of genes differentially expressed. It is therefore likely that the dysfunction relating from *Mir324* deletion occurs upstream of osteoclastogenic differentiation, suggesting that miR-324-null mice may show potential defects in other cells of the haematopoietic lineage, in addition to the bone phenotypes identified in Chapter 4.

I have also demonstrated that *ex vivo* osteoblasts from both calvarial and leg bone origins show an increased bone formation phenotype in miR-324-null samples relative to WT controls. Calvarial osteoblasts were utilised to restore miR-324-5p and -3p to physiological levels in miR-324-null cells, demonstrating that this re-introduction was able to successfully rescue the phenotype. Osteoblasts isolated from murine hind leg bones were utilised for an RNA-seq experiment following osteogenesis, in which almost 20% of all genes tested were significantly differentially expressed in miR-324-null osteoblasts relative to WT controls. The fact that in these experiments osteoblasts still produced excess bone even when seeded at equal densities demonstrates that the activity of individual osteoblasts is increased, in addition to the suspected modulation of MSC lineage commitment suggested by the results in Chapter 4. Considering the vast array of genes dysregulated in miR-324-null osteoblasts, it is perhaps unsurprising that *Mir324* deletion should affect multiple components of the bone formation pathway, rather than merely at a single point.

Using *in vitro* co-differentiation adipo-osteogenesis assays, I have showed that overexpression of both miR-324-5p and -3p each resulted in a shift towards adipogenesis and away from osteogenesis, and inhibition of each of these arms produced a shift in the opposite direction. This therefore supports the hypothesis posited in Chapter 4, in which deletion of *Mir324* affects both MSC lineage commitment and activity of osteoblasts *per se*. However, the fact

that miR-324-5p and -3p both appear to exert the same effect, and of a similar magnitude, was unexpected. This led me to hypothesise that miR-324-5p and -3p are likely to either target the same bone formation-related mRNA as one another or each target separate mRNAs, but with these targets additionally regulating one another.

In summary, I have shown that *ex vivo* miR-324-null BMMs are impaired during the process of osteoclastogenesis and that miR-324-null osteoblasts show an increased bone formation phenotype even when plated at equivalent densities as WT controls. Additionally, RNA-seq revealed that osteoblasts, osteoclasts and BMMs each show huge numbers of dysregulated genes between genotypes. Finally, I showed that *in vitro* both arms of miR-324 are able to modulate the lineage commitment choice of MSCs between adipogenesis and osteogenesis and I hypothesised that the direct targets through which this phenotype is exerted may regulate one another, thus producing the same effect regardless of which arm of miR-324 is modulated in expression. In the next chapter I will utilise target prediction algorithms and *in vitro* validation assays to identify novel targets of miR-324 likely to be causal of the phenotypes identified in this chapter and Chapter 4.

Chapter 6 - Prediction and validation of novel miR-324 targets in bone cells

6.1 Introduction

6.1.1 *Gene repression by microRNAs*

miRNAs act as gene repressors, guiding the biological silencing machinery known as the RNA-induced silencing complex (RISC) towards a target RNA [1, 20, 21]. The miRNA is the RISC component which allows such specific binding to a target, through the complementarity of the miRNA seed sequence with a binding site usually located within the 3'UTR of an mRNA [5-7]. This binding allows the components of the RISC complex, primarily through the GW182 protein [49, 50, 56], to mediate repression of the target transcript by interacting with two key components essential for mRNA stability and translational potential; the 5' cap and the poly(A) tail. The 5' mRNA cap is targeted through the recruitment of the RNA helicase DDX6, which interacts with the RISC component GW182 through another key silencing factor called EDD [63-65]. The poly(A) tail is targeted by several components of the RISC complex; GW182 directly interacts with the poly(A) binding protein (PABP) to destabilise the circular mRNA structure, whilst also positioning the poly(A) tail spatially proximal to the CCR4-NOT and PAN2-PAN3 complexes, which together enact deadenylation of the mRNA [46, 57-59, 61, 62]. Decapping and deadenylation of mRNAs upon targeting by a RISC complex therefore act in tandem in order to undermine the stability of the mRNA and thus inhibit its translation [46-48].

6.1.2 *microRNA target prediction*

Prediction of which transcripts are targeted by each miRNA has long been a challenge in the field. Although it is clear that miRNA-transcript binding is primarily guided by complementarity of binding sites in the target 3'UTR to the miRNA seed sequence, it is also becoming increasingly evident that many other factors play a role. The most obvious of these factors is the cellular context in which the interaction could take place; for example, if a miRNA target is barely expressed in one tissue relative to the expression level of the miRNA then a miRNA-target interaction is intrinsically less likely to occur *in vivo* at the physiological levels of that tissue than it would be in a different tissue, in which the target transcript is expressed at a higher level. Likewise, if an isoform of the target transcript is preferentially transcribed in this tissue in which an alternative 3'UTR is used, containing fewer or no binding sites, then again minimal *in vivo* targeting is likely to occur [489]. Long noncoding RNAs (lncRNAs) and circular RNAs (circRNAs) may also play a role in mediating *in vivo* miRNA regulation; the concept of miRNA sponging has in recent years gained traction, whereby lncRNAs or circRNAs enriched

for binding sites complementary to a single miRNA (or group of miRNAs which regulate the same pathway) can be upregulated in order to sequester those miRNAs away from their real targets and thus upregulate the pathway previously held under miRNA-mediated repression [490-493].

Other than the physiological context, there are other influences on miRNA-target binding which do not correspond directly to the seed but are still sequence specific and important. The first of these is the complementarity of the mRNA and miRNA beyond the seed sequence, especially between the 13th and 16th nucleotides of the miRNA. Complementarity between this site and the target 3'UTR nucleotides 5' from the canonical binding site increases the ability of the RISC complex to induce silencing and can even compensate for mismatched base pairs at the canonical seed site [7, 67, 494-496]. A final factor is free energy, which is a measure of thermodynamic binding strength between the sequences of the miRNA and the target transcript; if a higher free energy is required to bind, then that interaction is less likely to take place. This also allows prediction of the secondary structures each mRNA is likely to adopt, and therefore can also hypothesise whether the putative miRNA binding site in the target transcript would likely be accessible to the RISC complex [497, 498]. It should also be noted that in addition to all of the complex factors involved in target prediction, some miRNAs are also capable of binding sites outside of the 3'UTR, therefore suggesting that by limiting the predictions exclusively to the 3'UTR, a wide array of miRNA-target interactions may be missed [499].

Target prediction algorithms aim to make use of many of these properties, the three most popular of which are TargetScan, DIANA Tools and miRanda. DIANA Tools and miRanda each take account of a larger number of features than TargetScan, such as free energy and site accessibility, in addition to conservation of the target-seed interaction and the seed match itself across a range of species [5, 7, 67, 500-502]. However, despite this, TargetScan is still widely used, at least in part due to its high sensitivity; although DIANA Tools and miRanda predict fewer targets than TargetScan, a higher percentage are confirmed to be genuine due to the increased specificity of these algorithms relative to TargetScan. However, TargetScan identifies a higher number of genuine targets as it predicts more target transcripts overall, thus also generating a greater number of false positive results due to reduced specificity [496, 503]. Between these algorithms therefore there is a trade-off between how few false positives

are permitted without increasing the rate of false negative interactions and thus losing predictive capability.

6.1.3 *Validation of microRNA-target interaction*

miRNA target prediction is an excellent tool in generating putative targets for a given miRNA, but at present the algorithms commonly used lack the accuracy to confidently predict an interaction without experimental validation. Therefore, high-throughput sequencing approaches are often used in combination with miRNA target predictions in order to filter predictions. The use of RNA sequencing (RNA-seq) of a cell population in which a miRNA has been deleted compared to a WT control cell population for example would allow identification of which genes were significantly upregulated in the knockout cells, though of course not all upregulated genes will be a direct targets. Therefore, putative miRNA targets, predicted by an algorithm such as TargetScan [5, 67], can be used to filter the RNA-seq to genes that are both significantly upregulated in the knockout cells and are predicted miRNA targets, thus generating a new set of putative target genes specific for the cell population or tissue from which the RNA-seq data was obtained. Other sequencing approaches can also be used, the majority of which focus on the purification (pull-down) of proteins within the RISC complex, such as Ago2, and crosslinking that protein with any bound RNA, followed by sequencing of the RNA. The most popular variant of this methodology is called High-throughput sequencing of RNAs isolated by crosslinking immunoprecipitation (HITS-CLIP) and was first described in 2009 [504].

Regardless of the methodology used to identify putative miRNA targets, these still require validation *in vitro*. Most commonly, luciferase reporter assays are used for this. Luciferase assays consist of a plasmid containing a luciferase reporter gene, downstream of which is cloned the 3'UTR of a gene suspected of being a miRNA target. A common luciferase assay variant is known as the dual luciferase assay, in which an additional luciferase reporter gene is utilised, commonly the luciferase isolated from the sea pen *Renilla* (Renilla), to normalise the results between different samples. This Renilla gene is either cloned within the same plasmid as the 3'UTR-regulated luciferase reporter or co-transfected at the same time, but in a separate plasmid [505]. Subsequent to transfection with the reporter constructs, cells are also transfected with either a mimic of the miRNA predicted to target the cloned 3'UTR or with a control miRNA mimic. After a fixed period, the cells can be lysed and the amount of luciferase activity relative to Renilla activity will reveal whether transfection of the miRNA is

able to repress the relative luciferase activity. It should be noted that this experiment is also not sufficient alone to prove that a gene is a direct miRNA target; as mentioned in section 6.1.2, secondary structure of the mRNA target transcript can have a large impact on whether that RNA is able to be bound by a complementary miRNA, even if the mRNA harbours one or multiple highly predicted binding sites. By artificially cloning a fragment of a putative target 3'UTR into a luciferase plasmid, it is highly likely that the secondary structure adopted by the luciferase plasmid-encoded mRNA will be distinct from the structure formed when the 3'UTR is complete and present as part of a longer mRNA transcript. Furthermore, by using a luciferase assay, the miRNA and the luciferase plasmid will be expressed at levels likely far higher than those at physiological conditions in the tissue of interest, and so all the assay can conclusively demonstrate is that a putative target RNA transcript can be directly targeted by a miRNA in a highly artificial environment. Hence a miRNA-target interaction in a specific tissue can only be confidently posited by combining the results of luciferase assays with evidence recorded in the correct physiological context, for example using RNA-seq or at the very least RT-qPCR in the tissue of interest. Target prediction algorithms, sequencing experiments in the tissue of interest and validation reporter assays are therefore all essential components of determining miRNA targets.

6.1.4 *Previously validated miR-324 targets*

miR-324 holds the potential to regulate a wide array of target genes; TargetScan predicts over 2000 genes for each of miR-324-5p and -3p, although some of these overlap and many of these are not conserved between mouse and human [5, 67]. Some of these predicted targets have previously been validated in published work, although these only comprise a small fraction of the overall number of putative miR-324 targets.

In the musculoskeletal system, miR-324 has previously been discussed in relation to both cartilage and bone. miR-324 has been shown to regulate genes involved in the Hedgehog (Hh) signalling pathway, a key component of bone and cartilage development and maintenance [180, 181], across multiple tissues. Interestingly however, this regulation is effected through different targets between humans and mice; in humans miR-324-5p was demonstrated to directly repress *SMO* and *GLI1*, whereas in mouse cells miR-324-5p targeted *Gpc1* [151, 186, 187]. Each of these target genes are essential components of the Hh signalling pathway, and therefore downregulation of any of these genes would severely impede Hh signalling. A limited amount of work has been undertaken relating to target prediction and validation for

miR-324 in bone, although the correlations between serum abundance of miR-324-3p and bone formation rate [316] suggest it likely affects bone remodelling pathways through at least one target gene. Additionally, miR-324 has recently been reported to be exported from osteoclasts in vesicles and through this mechanism act to induce osteoblast-mediated bone formation, through repression of the osteogenesis inhibitor *ARHGAP1* [319].

6.1.5 *Chapter aims*

1. Identify novel miR-324 targets in murine osteoblasts.
2. Identify novel miR-324 targets in murine bone marrow macrophages (BMMs) and osteoclasts.
3. Identify novel miR-324 targets in murine osteocytes.
4. Hypothesise how these targets may be causing the observed miR-324-null phenotypes in each tissue and test these hypotheses where possible *in vitro*.

6.2 Results

6.2.1 *Identification of putative miR-324 targets in osteoblasts*

miR-324-null mice display a striking high bone mass phenotype which is at least partly due to increased osteoblast-mediated bone formation. This increased osteogenesis manifests as a result of severe upregulation of key osteogenesis genes, which include *Col1a1*, *Alpl* and *Runx2*. However, in order to fully elucidate the pathway resulting from lack of miR-324 to this dysregulation and the downstream phenotype, direct targets of miR-324 in osteoblasts necessarily require identification.

In order to identify these targets, the RNA-seq dataset comparing miR-324-null and WT osteoblasts stimulated with osteogenic media (OGM), extracted from the hind leg bones of mice aged 5-months, was utilised. Within this dataset, more than 1,500 genes were statistically significantly upregulated (adjusted p-value ≤ 0.05) in miR-324-null osteoblasts relative to WT controls. Despite this wide-reaching dysregulation, utilisation of the Sylamer algorithm [506] did not reveal a noticeable enrichment in transcripts matching the seed sequence of miR-324-5p or -3p which were highly upregulated by the deletion of *Mir324* (Appendix Ca). In order to filter the more than 1500 upregulated genes, so as to identify putative target genes more likely to have an impact on osteogenesis and bone formation, the Disease Ontology (DO) was utilised [343], such that genes which were not annotated to a

bone- or metabolism-related disorder (Appendix B) were filtered out of the putative target gene subset. A χ^2 test demonstrated that there was not a significant association between the bone- or metabolism-associated genes and the genes predicted as miR-324 targets ($\chi^2 = 1.88$, p-value = 0.170). Subsequently, the TargetScan miRNA target prediction algorithm [5, 67] was utilised, resulting in a subset of 29 bone- or metabolism-associated genes which were upregulated in miR-324-null osteoblasts and predicted to be targets of either miR-324-5p or -3p (Figure 6.1a). Finally, the most promising targets to test in 3'UTR-luciferase assays were selected by setting thresholds for the TargetScan total context score and the $\log_2$ fold-change of < -0.25 and > 0.35, respectively. The total context score is representative of the likelihood of the predicted target being a real target bound by the miRNA, such that the more negative the total context score is, the more highly predicted the transcript is of being a target, as calculated by the TargetScan algorithm. This was utilised here as it combines several key prediction parameters into one score, such as the number of predicted binding sites, how complimentary each site is to the miRNA seed sequence and the thermodynamic stability of the miRNA-3'UTR duplex formed upon theoretical binding [507]. The thresholds for this and the $\log_2$ fold-change were chosen so as filter the putative targets down to only the most promising genes, as testing the entire subset in luciferase assays was likely to result in false positives. These thresholds resulted in a subset of 4 osteoblast putative miR-324 target genes; *Klf7*, *Cxcl12* (which encodes SDF-1), *Top1* and *Runx2* (Figure 6.1b). In order to test whether any of these genes were direct targets of miR-324, 3'UTR-luciferase constructs were designed. However, in the case of murine *Cxcl12* there are 3 discrete isoforms, *Cxcl12*-α, *Cxcl12*-β and *Cxcl12*-γ, of which none share an identical 3'UTR (Figure 6.1ci). All of the *Cxcl12* isoforms contain a minimum of 2 miR-324-5p or -3p binding sites, but no single 3'UTR isoform has exactly the same binding sites as any single other isoform. Additionally, each of the *Cxcl12* transcript variants is individually upregulated in miR-324-null osteoblasts, although the upregulation of *Cxcl12*-β and -γ is greater than *Cxcl12*-α, which is generally considered to be the canonical isoform (Figure 6.1cii) [508]. Therefore, in order to elucidate whether any single *Cxcl12* isoform was a direct target of miR-324, 3'UTR-luciferase constructs were made for each isoform, in addition to constructs for *Klf7*, *Top1* and *Runx2*. Dual luciferase assays with these constructs revealed that *Klf7, Top1*, *Cxcl12*-α and *Cxcl12*-β were not direct targets of miR-324. However the *Runx2* and Cxcl12-γ 3'UTRs displayed significant repression of the upstream luciferase gene when miR-324-5p (for *Runx2*) or miR-324-5p and -3p (for *Cxcl12*-γ) were added (Figure 6.1di). Considering that *Cxcl12*-γ shares several predicted miR-324 binding sites with

Cxcl12-β, but the *Cxcl12*-β 3'UTR-luciferase construct was not significantly repressed by either miR-324 arm, the real miR-324-5p and -3p binding sites in the *Cxcl12*-γ 3'UTR were presumed to be located in the part of the *Cxcl12*-γ 3'UTR which was not shared with *Cxcl12*-β. Therefore a 3'UTR-luciferase construct was also made containing only the part of the *Cxcl12* 3'UTR unique to *Cxcl12*-γ, referred to as "*Cxcl12*-γ (unique)". TargetScan did not predict this region to be a miR-324-3p target, but this construct replicated both the miR-324-5p and -3p-mediated repression of luciferase expression observed with the full *Cxcl12*-γ 3'UTR construct, suggesting that miR-324 binds the 3'UTR exclusively at this unique region (Figure 6.1di). Therefore miRmap, an alternative miRNA target prediction algorithm, was utilised to search for an additional predicted miR-324-3p binding site [351]. miRmap allows for limited G-U base pairing between the predicted binding site and the miRNA seed considering that this pairing shows comparable thermodynamic stability to canonical Watson-Crick pairing [350], and one such site was identified in the *Cxcl12*-γ (unique) 3'UTR. This was therefore taken to be the real miR-324-3p binding site. The miR-324-mediated repression of both *Runx2* and *Cxcl12*-γ (unique) was ablated when 2 nt in each miR-324 binding site were mutated, including the *Cxcl12*-γ (unique) binding site containing the predicted G-U base pairing with miR-324-3p (Figure 6.1dii; binding site locations and mutant sequences are shown in Table 2.2). *Cxcl12*-γ (unique) contained 3 predicted binding sites (2 miR-324-5p sites and 1 miR-324-3p site) and therefore all of these were mutated in the mutant 3'UTR-luciferase construct.

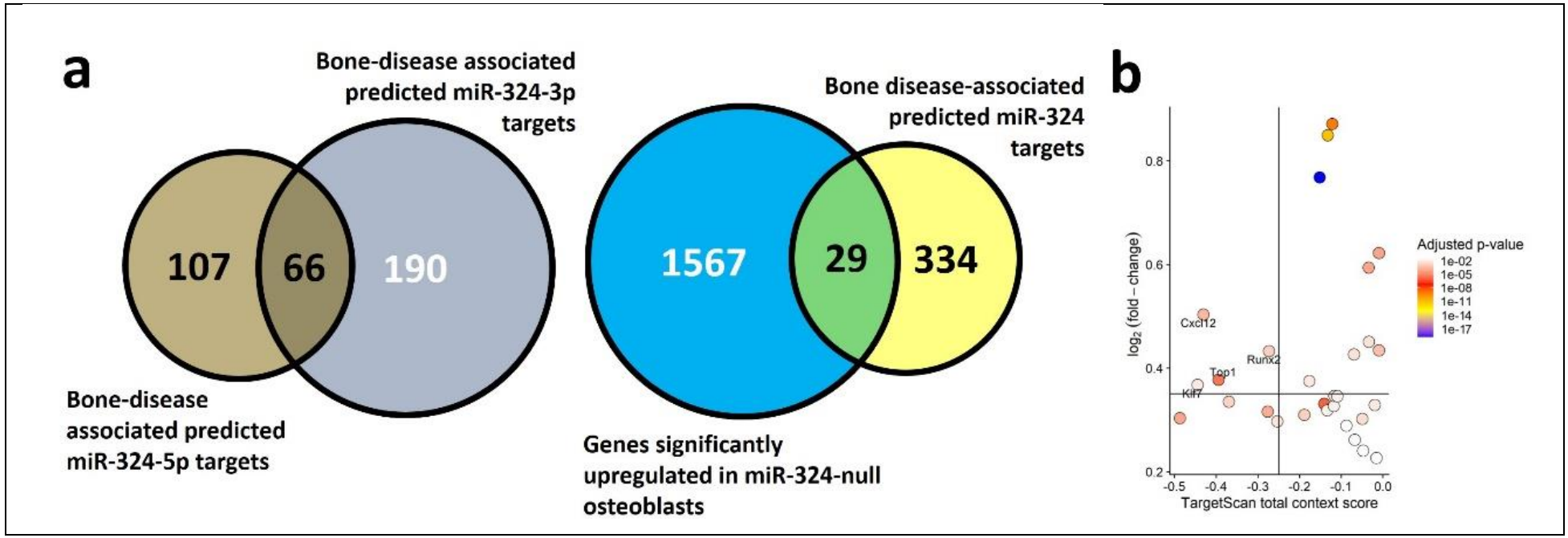
a
Bone-disease associated predicted miR-324-3p targets
107
66
190
Bone-disease associated predicted miR-324-5p targets
Bone disease-associated predicted miR-324 targets
1567
29
334
Genes significantly upregulated in miR-324-null osteoblasts
b
log2 (fold – change)
0.8
0.6
0.4
0.2
Cxcl12
Runx2
Top1
Kif7
-0.5
-0.4
-0.3
-0.2
-0.1
0.0
TargetScan total context score
Adjusted p-value
1e-02
1e-05
1e-08
1e-11
1e-14
1e-17

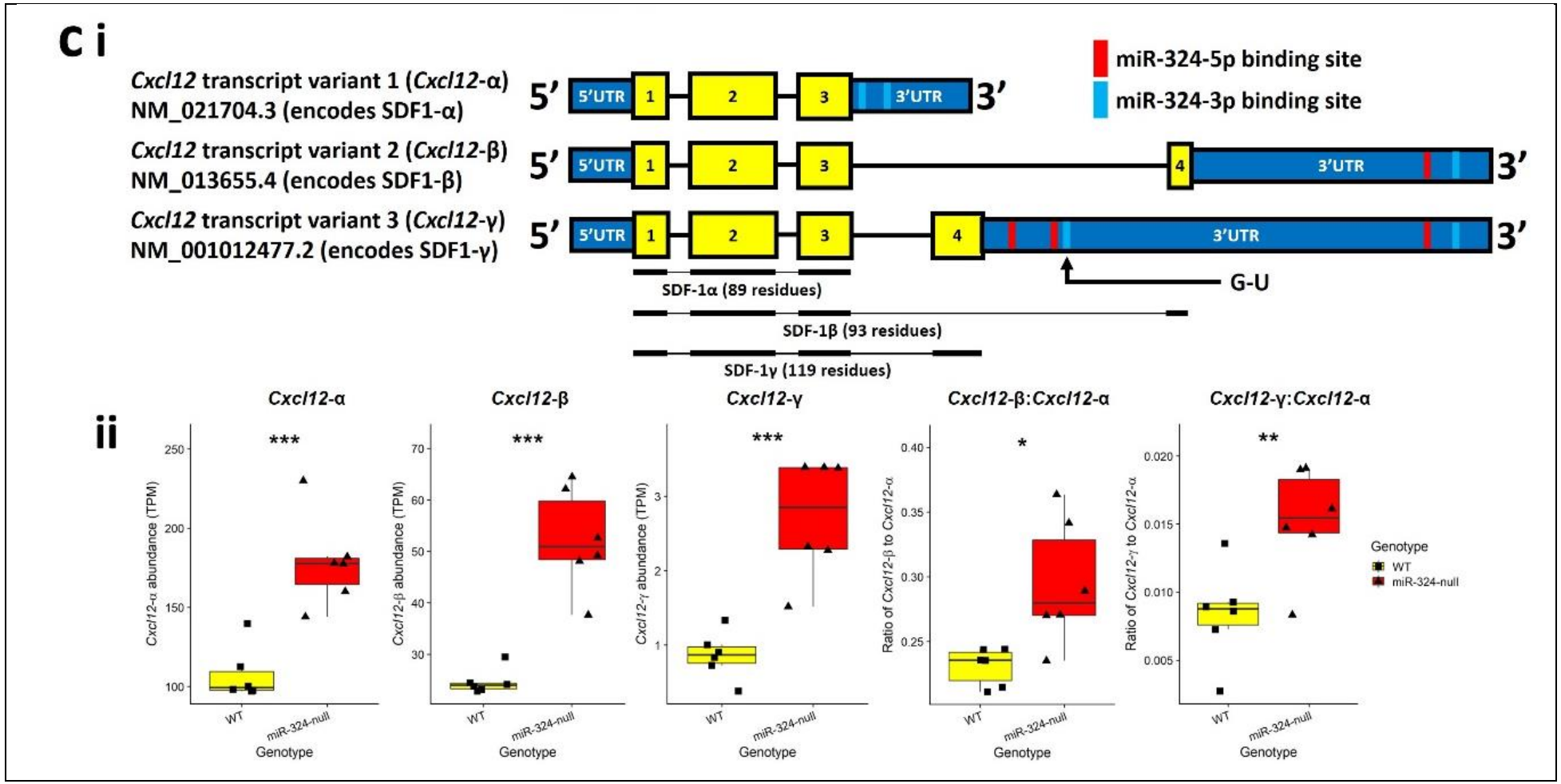
c i
Cxcl12 transcript variant 1 (Cxcl12-α)
NM_021704.3 (encodes SDF1-α)
Cxcl12 transcript variant 2 (Cxcl12-β)
NM_013655.4 (encodes SDF1-β)
Cxcl12 transcript variant 3 (Cxcl12-γ)
NM_001012477.2 (encodes SDF1-γ)
5'
3'
5'UTR
1
2
3
4
3'UTR
miR-324-5p binding site
miR-324-3p binding site
G-U
SDF-1α (89 residues)
SDF-1β (93 residues)
SDF-1γ (119 residues)
ii
Cxcl12-α
Cxcl12-β
Cxcl12-γ
Cxcl12-β:Cxcl12-α
Cxcl12-γ:Cxcl12-α
Cxcl12-α abundance (TPM)
Cxcl12-β abundance (TPM)
Cxcl12-γ abundance (TPM)
Ratio of Cxcl12-β to Cxcl12-α
Ratio of Cxcl12-γ to Cxcl12-α
***
*
**
WT
miR-324-null
Genotype

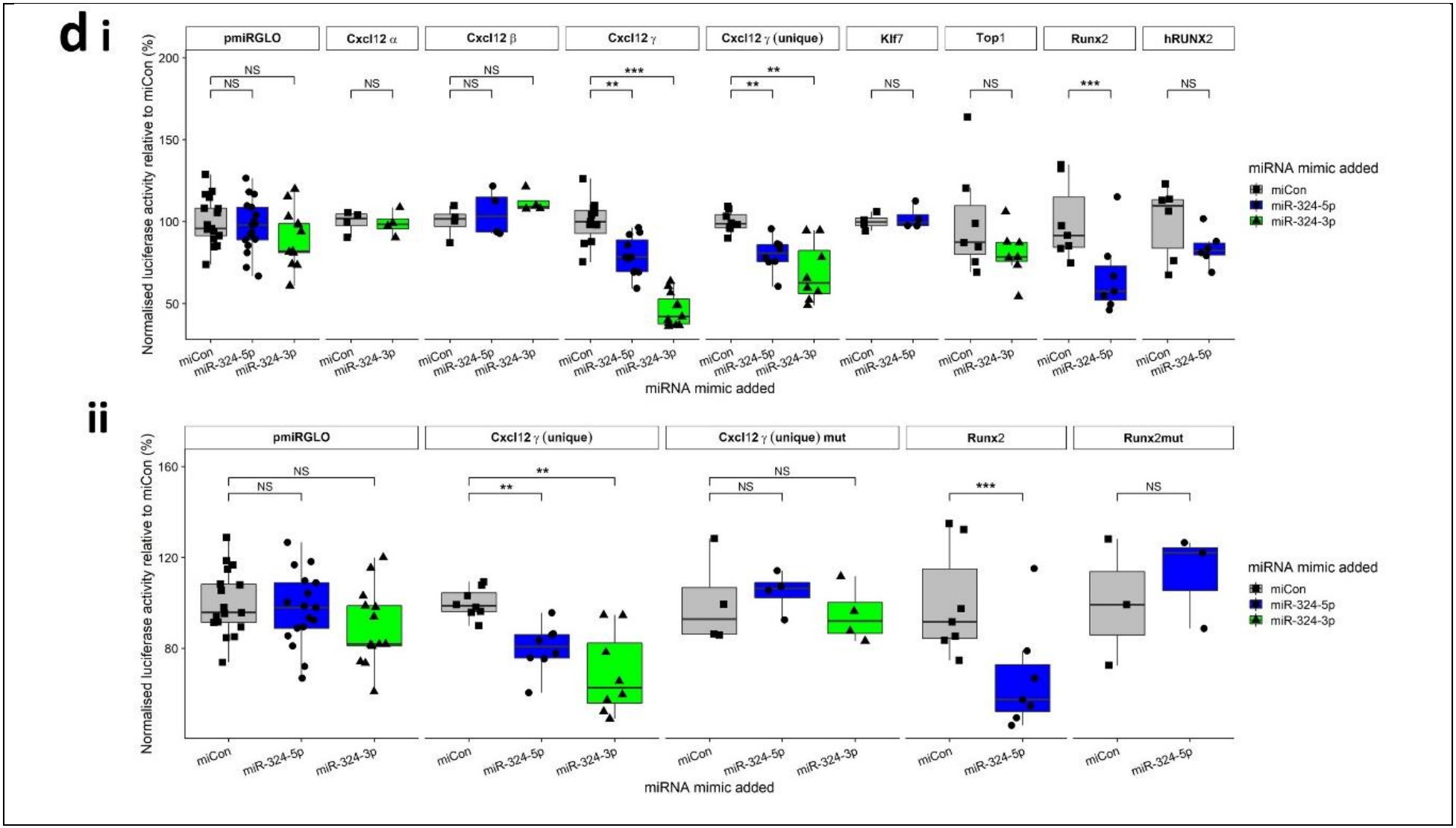
di
pmiRGLO
Cxcl12 α
Cxcl12 β
Cxcl12 γ
Cxcl12 γ (unique)
Klf7
Top1
Runx2
hRUNX2
Normalised luciferase activity relative to miCon (%)
200
150
100
50
NS
**
***
miCon
miR-324-5p
miR-324-3p
miRNA mimic added
ii
pmiRGLO
Cxcl12 γ (unique)
Cxcl12 γ (unique) mut
Runx2
Runx2mut
Normalised luciferase activity relative to miCon (%)
160
120
80
miRNA mimic added

Figure 6.1 - Identification and validation of novel osteoblast miR-324 target genes. (**a**) Of the predicted targets of miR-324 which were bone- or metabolism-associated, more genes were predicted to be targeted by miR-324-3p than -5p. More than 1,500 genes were upregulated in miR-324-null osteoblasts relative to WT controls, and of these 29 were associated with bone or lipid disorders in the DO [343] and were predicted targets of miR-324. (**b**) Thresholds were set for the TargetScan total context score and the $\log_2$ fold-change of < -0.25 and > 0.35, respectively, resulting in 4 osteoblast putative miR-324 target genes; *Klf7*, *Cxcl12*, *Top1* and *Runx2*. (**c**)(**i**) There are 3 distinct isoforms of *Cxcl12*, each of which possess distinct 3'UTRs and encode distinct proteins; *Cxcl12*-α, -β and -γ encode SDF-1α, -β and -γ, respectively. All isoforms possess the exons within *Cxcl12*-α, whereas -β and -γ each possess an additional unique exon. For each isoform, the locations of miR-324-5p and -3p binding sites are shown in red and blue, respectively. One of the predicted miR-324-3p binding sites in the *Cxcl12*-γ isoform would bind to miR-324-3p through a non-canonical G-U base pairing, and this site is indicated on the diagram. (**ii**) Each *Cxcl12* transcript variant is upregulated in miR-324-null osteoblasts, although the *Cxcl12*-β and -γ isoforms are upregulated to a greater degree than the -α isoform, in the osteoblast RNA-seq data. (**d**)(**i**) C3H10T1/2 murine cells were transfected with 3'UTR-pmiRGLO constructs and subsequently also with either a negative control miRNA mimic (miCon) or a mimic of miR-324-5p or miR-324-3p. Luciferase activity was measured after cells were incubated at 37°C and 5% CO_2 for 24 hours. Relative luciferase activity was calculated as a ratio of Renilla activity, an internal transfection control within pmiRGLO, and values were plotted as a percentage of mean miCon luciferase activity for each construct. *Runx2* and the *Cxcl12*-γ 3'UTRs resulted in a significant downregulation of luciferase activity when miR-324 mimics were added. Here, *Cxcl12*-γ (unique) excludes the part of the *Cxcl12*-γ 3'UTR shared with *Cxcl12*-β, whereas the 3'UTR marked *Cxcl12*-γ includes the shared and unique parts of the 3'UTR. For *hRUNX2*, the same protocol was undertaken, but using human Y201 cells in place of murine C3H10T/2 cells. (**ii**) When 2 nt in each miR-324 binding site was mutated, the ability of miR-324 to repress the luciferase gene upstream of each 3'UTR was ablated. For panel **d**, the means of at least 4 independent experiments were used to test statistical significance, which were calculated from ≥ 3 technical replicates in each independent experiment. A negative control plasmid (pmiRGLO) and negative control mimic (miCon) in addition

to a previously validated miR-324 target 3'UTR (as a positive control) was included for each independent experiment. For all panels, *, ** and *** signify p-values ≤ 0.05, 0.01 and 0.001, respectively, assessed using Student's two-tailed *t*-tests. For luciferase assays, paired *t*-tests were used.

Due to the successful use of C3H10T1/2 cells with miR-324-5p and -3p mimics to model adipogenesis and osteogenesis, we proceeded to utilise this model in order to overexpress *Runx2* and *Cxcl12* over the co-differentiation time-course and investigate whether we could mimic the effect of miR-324 inhibition. Therefore, a FLAG-tagged overexpression plasmid containing *Runx2* (pCMV-ENTRY-*Runx2*) and the recombinant Cxcl12-α protein (the product of the shared exons between the *Cxcl12* isoforms) were used. C3H10T1/2 cells were transfected with pCMV-ENTRY-*Runx2* (detection of FLAG-tagged Runx2 protein shown in Figure 6.2a) or stimulated with Cxcl12-α (50 ng/mL) under adipo-osteogenic (AdiOst) conditions. A significant increase in alizarin red-S staining intensity was observed upon overexpression of *Runx2*, but not by stimulation with Cxcl12-α (p-value = 0.051). Both treatments significantly decreased oil red-O staining intensity by a magnitude of approximately 10%, and additionally the overall ratio of adipogenesis to osteogenesis (AdiOst ratio) in terms of staining was significantly decreased by an average of 20% in both conditions (Figures 6.2b and 6.2c). As expected, overexpression of *Runx2* resulted in a dramatic increase in *Runx2* mRNA, but *Runx2* expression was also significantly increased by Cxcl12-α stimulation. *Pparg*, a key adipogenesis marker gene, was significantly downregulated by *Runx2* overexpression, and a trend towards decreased *Pparg* expression was observed in cells stimulated with Cxcl12-α (p-value = 0.088). Overexpression of *Runx2* also resulted in an increase in the expression of *Cxcl12*-α, but not -β or -γ, whereas treatment with the Cxcl12-α chemokine produced an upregulation of all three *Cxcl12* isoforms. In fact, *Cxcl12*-β and -γ expression was only detected in samples treated with Cxcl12-α (Figure 6.2d).

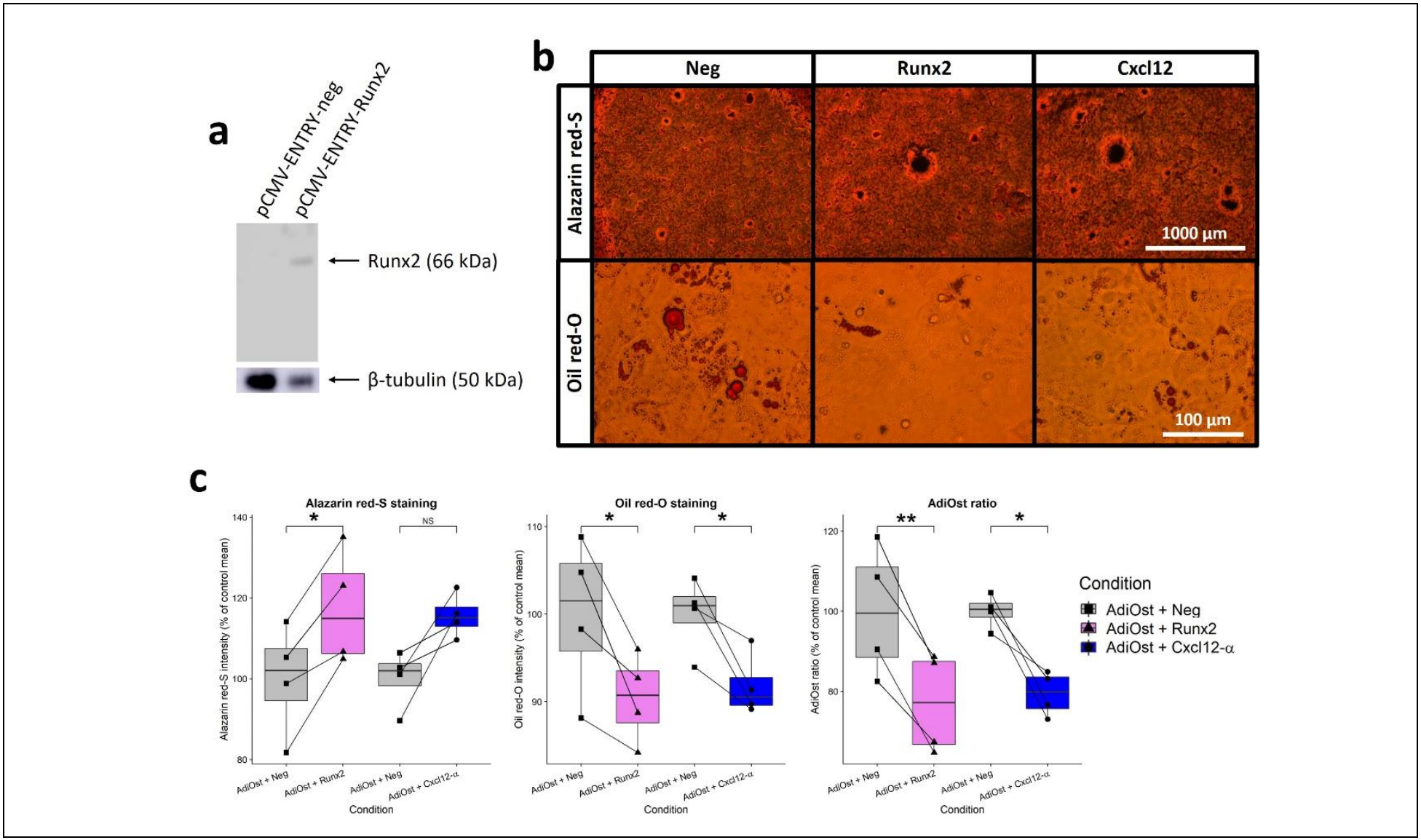
a
pCMV-ENTRY-neg
pCMV-ENTRY-Runx2
Runx2 (66 kDa)
β-tubulin (50 kDa)
b
Neg
Runx2
Cxcl12
Alazarin red-S
Oil red-O
1000 µm
100 µm
c
Alazarin red-S staining
Oil red-O staining
AdiOst ratio
Alazarin red-S intensity (% of control mean)
Oil red-O intensity (% of control mean)
AdiOst ratio (% of control mean)
NS
AdiOst + Neg
AdiOst + Runx2
AdiOst + Cxcl12-α
Condition

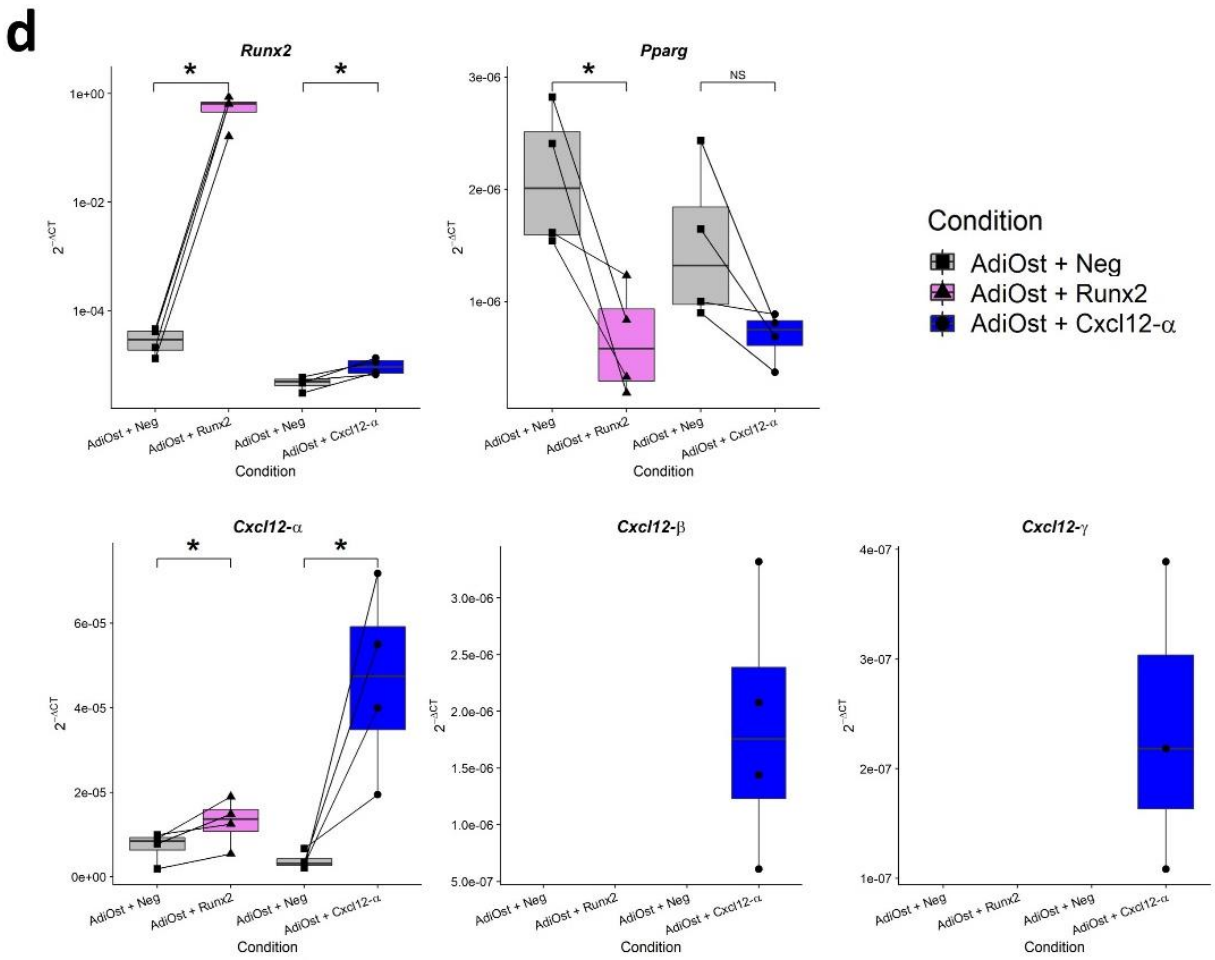

Figure 6.2 - Overexpression of miR-324 osteoblast target genes in C3H10T1/2 cells treated with co-differentiation adipo-osteogenic media for 18 days shifted cells towards the osteoblast lineage. (**a**) Runx2 protein can be detected using western blotting in protein lysate obtained from cells transfected with the *Runx2* FLAG-tagged overexpression plasmid, using an anti-FLAG antibody. No FLAG-tagged protein was detected in lysate

obtained from cells transfected with the negative control. An anti-β-tubulin antibody was utilised as the positive control to confirm that protein was present in all loaded samples. (**b**) Representative images of C3H10T1/2 cells undergoing AdiOst co-differentiation in each condition, stained with alizarin red-S or oil red-O. Cells were imaged at 5X magnification for alizarin red-S stains and 40X magnification for oil red-O stains. (**c**) Cells overexpressing *Runx2* displayed a significant increase in alizarin red-S staining intensity, a significant decrease in oil red-O staining intensity and a significant decrease in the AdiOst ratio. Cells stimulated with 50 ng/mL Cxcl12-α showed a trend towards increased alizarin red-S staining intensity (p-value = 0.051) and a significant decrease both in oil red-O staining intensity and in the AdiOst ratio. (**d**) RT-qPCR was utilised to demonstrate that overexpression of *Runx2* significantly upregulated *Cxcl12*-α and significantly downregulated *Pparg*. The mRNA level of *Runx2* was also significantly increased. Stimulation of cells with Cxcl12-α also significantly increased *Runx2* expression, in addition to trending towards decreased *Pparg* expression (p-value = 0.088). Additionally upregulation of all *Cxcl12* isoforms was observed, although statistical significance could not be calculated for *Cxcl12*-β and -γ as they were undetected in the absence of Cxcl12-α stimulation. *18S* was utilised as the housekeeping gene to normalise against for RT-qPCR. For all panels, ** and * represent p-values ≤ 0.01 and 0.05, respectively, calculated using Student's two-tailed paired *t*-tests. The means of 4 independent experiments were used to test statistical significance, which were each calculated from 3 technical replicates in each independent experiment.

Considering that overexpression of *Runx2* and stimulation with Cxcl12-α each resulted in a shift towards osteogenesis and away from adipogenesis in C3H10T1/2 cells, I proceeded to investigate whether each of these conditions, or a combination of the two, were sufficient to initiate spontaneous osteogenesis in the absence of AdiOst media over 18 days. Remarkably, *Runx2* overexpression, Cxcl12-α stimulation, and both conditions combined, resulted in a significant increase in alizarin red-S staining intensity relative to cells transfected solely with the control vector (pCMV-ENTRY-neg), though this staining was noticeably less intense than the equivalent control cultured in AdiOst media. Furthermore, cells transfected with *Runx2* and stimulated with Cxcl12-α at the same time showed a significantly increased alizarin red-S staining intensity relative to either condition individually (Figures 6.3a and 6.3b). Interestingly, a low level of spontaneous osteogenesis was detected even in cells transfected solely with pCMV-ENTRY-neg (Figure 6.3a), which suggests that stimulation with β-glycerophosphate and L-ascorbic acid is not required for initiation of osteogenic differentiation *in vitro*. Oil red-O staining intensity showed a mild downward trend for all conditions, but only cells treated with both Cxcl12-α and overexpressing *Runx2* displayed a statistically significant decrease in oil red-O staining intensity at a 5% threshold. However, no obvious lipid droplets were observed upon imaging in any condition, suggesting that any decrease in oil red-O staining intensity was likely to be very small in magnitude, even if adipogenesis was inhibited completely. The AdiOst ratio was significantly decreased in all conditions and, as with alizarin red-S staining intensity, cells overexpressing *Runx2* and stimulated with Cxcl12-α displayed a statistically significant decrease relative to either condition individually (Figures 6.3a and 6.3b). *Runx2* expression was increased and *Pparg* expression was significantly decreased in all conditions (Figure 6.3c).

Contrary to the findings when cells were cultured in AdiOst media (Figures 5.8 and 5.9), the expression of *Cxcl12*-α was significantly downregulated by *Runx2* overexpression and by *Runx2* overexpression combined with Cxcl12-α stimulation, and showed a trend towards decreased expression when stimulated solely with Cxcl12-α as well (p-value = 0.096). *Cxcl12*-β showed a mild decrease when *Runx2* was overexpressed, although this did not achieve statistical significance at a 5% threshold (p-value = 0.057), and *Cxcl12*-γ also showed no statistically significant changes, although a trend towards decreased expression was observed upon stimulation with Cxcl12-α and *Runx2* overexpression individually (p-values = 0.227 and 0.125, respectively). Interestingly however, a significant increase in *Cxcl12*-γ expression was observed upon overexpression of *Runx2* and stimulation with Cxcl12-α combined, relative to

each condition individually (Figure 6.3c). It is also of note that here, all isoforms of *Cxcl12* were detected in all conditions, whereas under AdiOst conditions neither *Cxcl12*-β nor -γ were detected in the absence of Cxcl12-α stimulation.

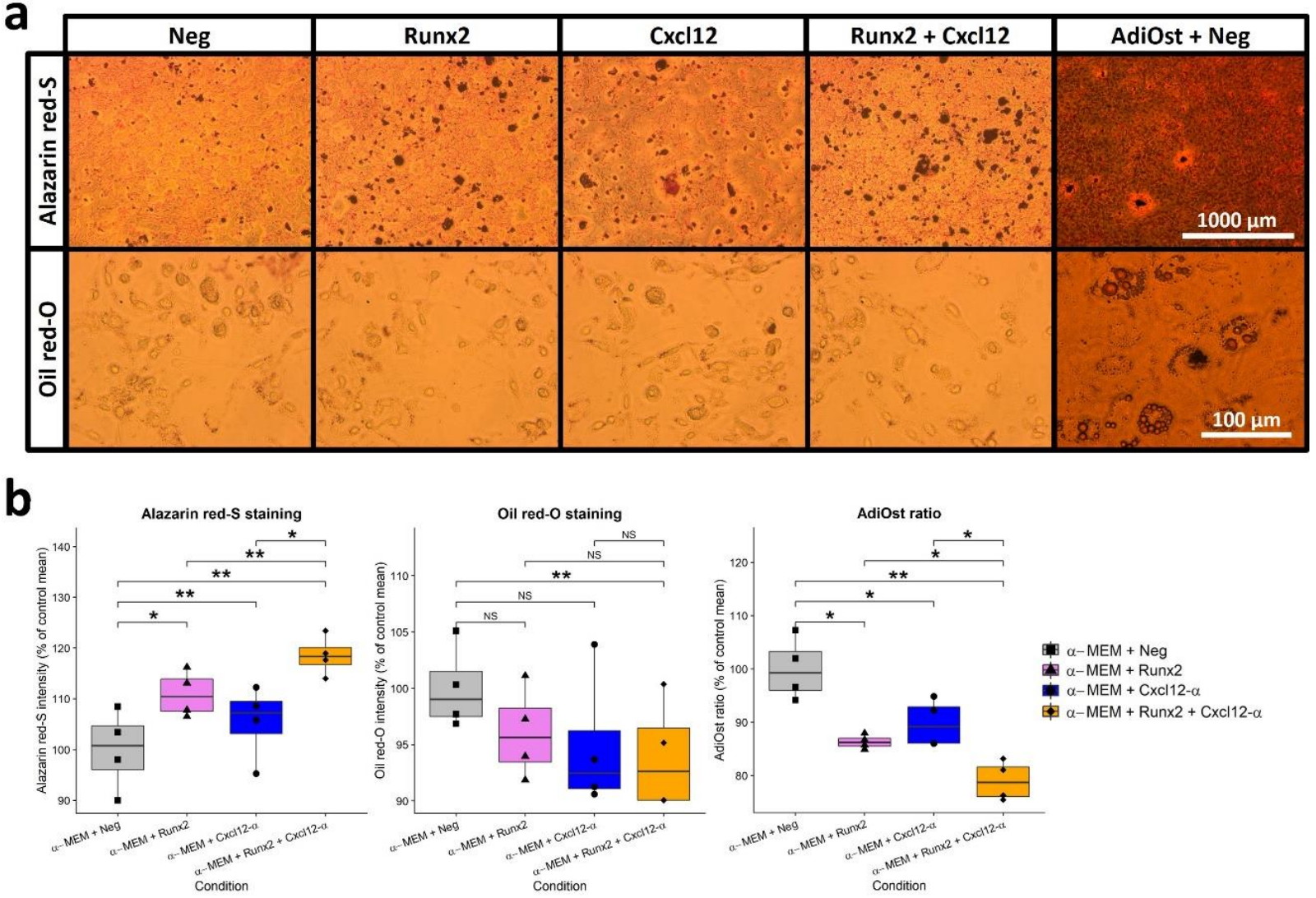
a
Neg
Runx2
Cxcl12
Runx2 + Cxcl12
AdiOst + Neg
Alazarin red-S
Oil red-O
1000 µm
100 µm
b
Alazarin red-S staining
Alazarin red-S intensity (% of control mean)
Oil red-O staining
Oil red-O intensity (% of control mean)
AdiOst ratio
AdiOst ratio (% of control mean)
NS
α−MEM + Neg
α−MEM + Runx2
α−MEM + Cxcl12-α
α−MEM + Runx2 + Cxcl12-α
Condition

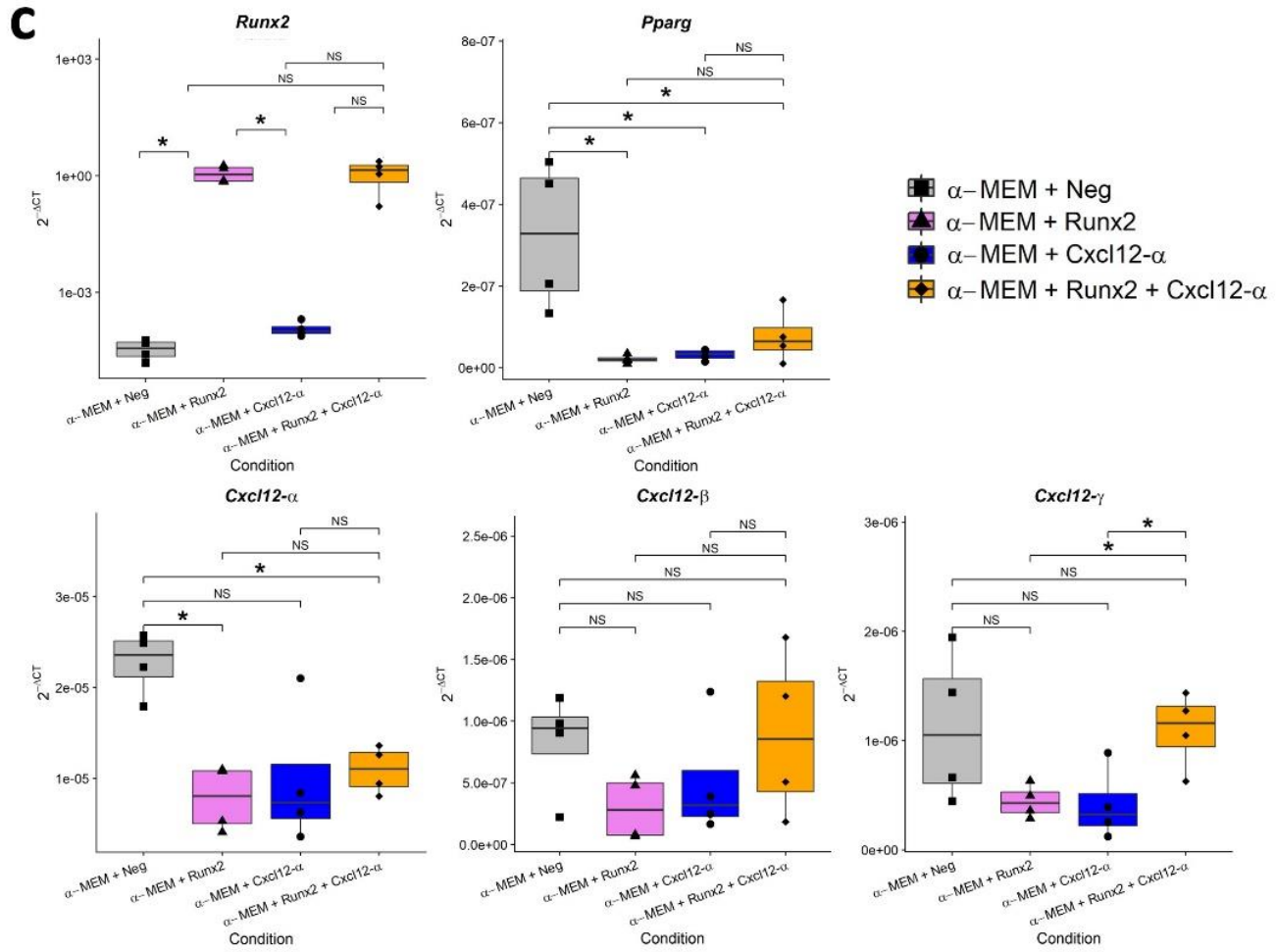

Figure 6.3 - Overexpression of miR-324 osteoblast target genes in C3H10T1/2 cells stimulated spontaneous osteogenesis. (**a**) Representative images of C3H10T1/2 cells are shown, where cells were plated in α-MEM in each condition and stained with alizarin red-S or oil red-O. Cells were imaged at 5X magnification for alizarin red-S stains and 40X magnification for oil red-O stains. A positive control was also included, where cells were

plated in co-differentiation AdiOst media to confirm that bone nodules and lipid droplets were being formed. (**b**) Cells either overexpressing *Runx2*, stimulated with Cxcl12-α or both each display significant increases in alizarin red-S staining intensity in the absence of AdiOst media. The effect of both overexpressing *Runx2* and stimulating with Cxcl12-α combined results in significantly increased alizarin red-S staining intensity relative to either condition individually. All three treatments show a trend towards decreased oil red-O staining, although only treatment with both conditions at the same time results in a significant decrease (p-values for *Runx2* overexpression and Cxcl12-α stimulation = 0.053 and 0.054, respectively). *Runx2* overexpression, Cxcl12-α stimulation and both combined all result in significant decreases to AdiOst ratio. Additionally, the effect of both conditions combined significantly reduces the AdiOst ratio relative to either condition individually. (**c**) RT-qPCR demonstrated that overexpression of *Runx2* and stimulation with Cxcl12-α each resulted in significantly increased *Runx2* expression. Both treatments combined also resulted in a strong upregulation of *Runx2*, although this did not achieve statistical significance at a 5% threshold (p-value = 0.064). *Pparg* expression was significantly downregulated by all treatments. *Cxcl12*-α expression was significantly decreased by overexpression of *Runx2* and both treatments combined. Stimulation with Cxcl12-α also produced a decrease in *Cxcl12*-α expression, although this did not achieve statistical significance (p-value = 0.096). Overexpression of *Runx2* produced a trend towards decreased *Cxcl12*-β and -γ expression (p-values = 0.057 and 0.125, respectively). Interestingly, both conditions combined produced a significant increase in *Cxcl12*-γ levels relative to either treatment individually. The *18S* housekeeping gene was utilised to normalise results. For all panels, ** and * represent p-values ≤ 0.01 and 0.05, respectively, calculated using Student's two-tailed paired *t*-tests. The means of 4 independent experiments were used to test statistical significance, with 3 technical replicates in each independent experiment.

6.2.2 *Identification, validation and in vitro overexpression of putative miR-324 targets in osteocytes*

Osteocytes are important regulatory cells in regulation of bone remodelling and mineral homeostasis [225, 233, 422]. Due to the observed alterations to bone microstructure and mineral density therefore, it was important to investigate whether miR-324-null mice show dysregulation of important genes in these cells in addition to osteoblasts and osteoclasts. Osteocytes are, by definition, embedded in mineralised bone and therefore the extraction and isolation of these cells poses a significant challenge. In order to investigate miR-324 target gene dysregulation, we merely required the isolation of osteocyte RNA rather than the cells themselves, therefore we utilised several sequential collagenase digestions followed by snap freezing of the digested bone in liquid nitrogen in order to extract pure osteocyte RNA [349].

In order to confirm the osteocyte purity of the cell population from which we isolated RNA, the expression of key osteoblast and osteocyte genes were measured; namely *Alpl*, *Bglap* (which encodes osteocalcin), *Csf1* (which encodes M-CSF, which is essential for osteoclastogenesis [198]), *Mepe*, *Phex*, *Runx2* and *Sost*. Considering that *Runx2* is expressed by osteocytes as well as osteoblasts and was comparable in expression between miR-324-null and WT osteocyte RNA samples, and that the osteocyte-selective genes *Mepe*, *Phex* and *Sost* were detected in samples from both genotypes, the purity of the miR-324-null osteocyte populations from which RNA was isolated was taken to be similar to that of the osteocyte population from which WT RNA was isolated. Interestingly all the osteocyte and osteoblast signature genes tested, with the exception of *Sost* and *Runx2*, were statistically significantly dysregulated; *Alpl* and *Bglap* were significantly upregulated in miR-324-null osteocytes, whereas *Csf1*, *Mepe* and *Phex* were all significantly downregulated. (Figure 6.4a).

Due to the poor quality of RNA extracted through this methodology (RNA integrity scores of between 1.4 and 3.1), an RT-qPCR screening pipeline was utilised in order to identify putative targets, rather than an RNA-seq approach (Figure 6.4b). RT-qPCR is a useful approach to use in a situation such as this one, where the RNA integrity is poor, in place of high-throughput sequencing, as far less of a transcript of interest is required to be intact in order to detect its expression; only the region including and between the two primer binding sites is required to be present in order for a transcript to be amplified and detected. Genes predicted to be miR-324-5p or -3p targets by the TargetScan algorithm [5, 67] were filtered by the osteocyte active transcriptome, a set of 1239 genes recently identified to be enriched in osteocytes relative to

other cell populations [216], resulting in 443 putative targets. This subset was subsequently filtered further by utilising RNA-seq datasets previously undertaken in various tissues in the miR-324-null mice, such that only putative targets found to be upregulated with an adjusted p-value ≤ 0.1 in previous RNA-seq experiments (hippocampus, neocortex (see Chapter 3) and rib chondrocytes (not shown)) remained in the putative target gene subset. Finally, the 5 genes predicted by TargetScan to be most likely to be miR-324-5p or -3p targets (using the total context score) which were not in the osteocyte active transcriptome, in addition to the 4 miR-324 target genes validated thus far in this project (*Cd300lf*, *Cxcl12*, *Runx2* and *Suox*), were added into the subset. This resulted in a final putative target subset of 30 genes to test the expression of between miR-324-null and WT osteocyte samples. OATargets [353] was utilised in order to annotate whether each of these genes was associated with body height, bone mineral density or osteoarthritis (OA) through genome-wide association studies (GWAS). Of the 30 putative target genes measured, only 4 displayed statistically significant upregulations in miR-324-null osteocytes relative to WT controls (p-value ≤ 0.05); *Cxcl12*, *Hoxa9*, *Samd5* and *Rgs5*. *Spon1* showed a p-value of 0.09 so was also included in the subset due to proximity to the 5% threshold (Figure 6.4c).

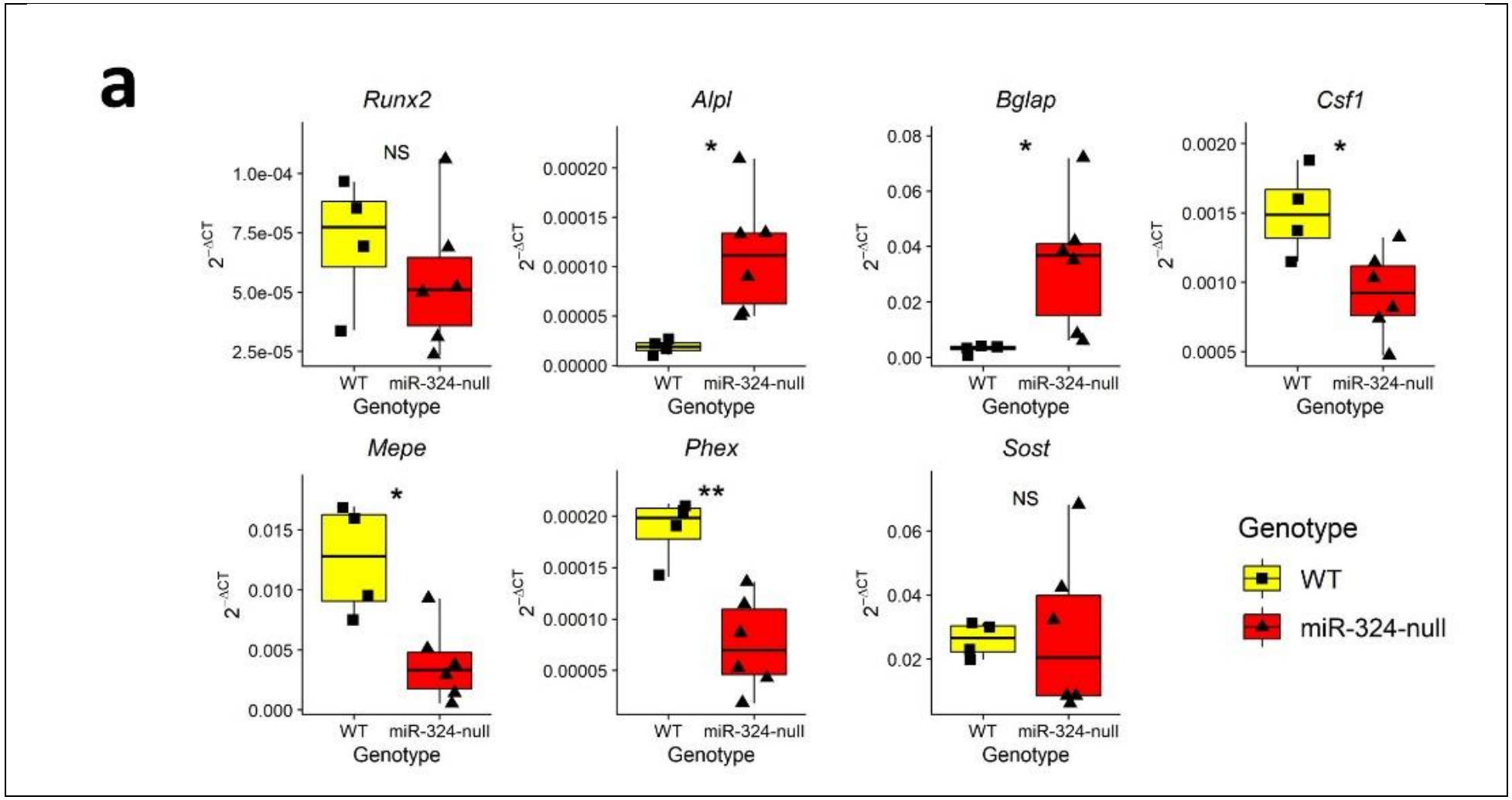
a
Runx2
NS
1.0e-04
7.5e-05
5.0e-05
2.5e-05
$2^{-\Delta CT}$
WT
miR-324-null
Genotype
Alpl
*
0.00020
0.00015
0.00010
0.00005
0.00000
Bglap
*
0.08
0.06
0.04
0.02
0.00
Csf1
*
0.0020
0.0015
0.0010
0.0005
Mepe
*
0.015
0.010
0.005
0.000
Phex
**
Sost
NS
Genotype
WT
miR-324-null

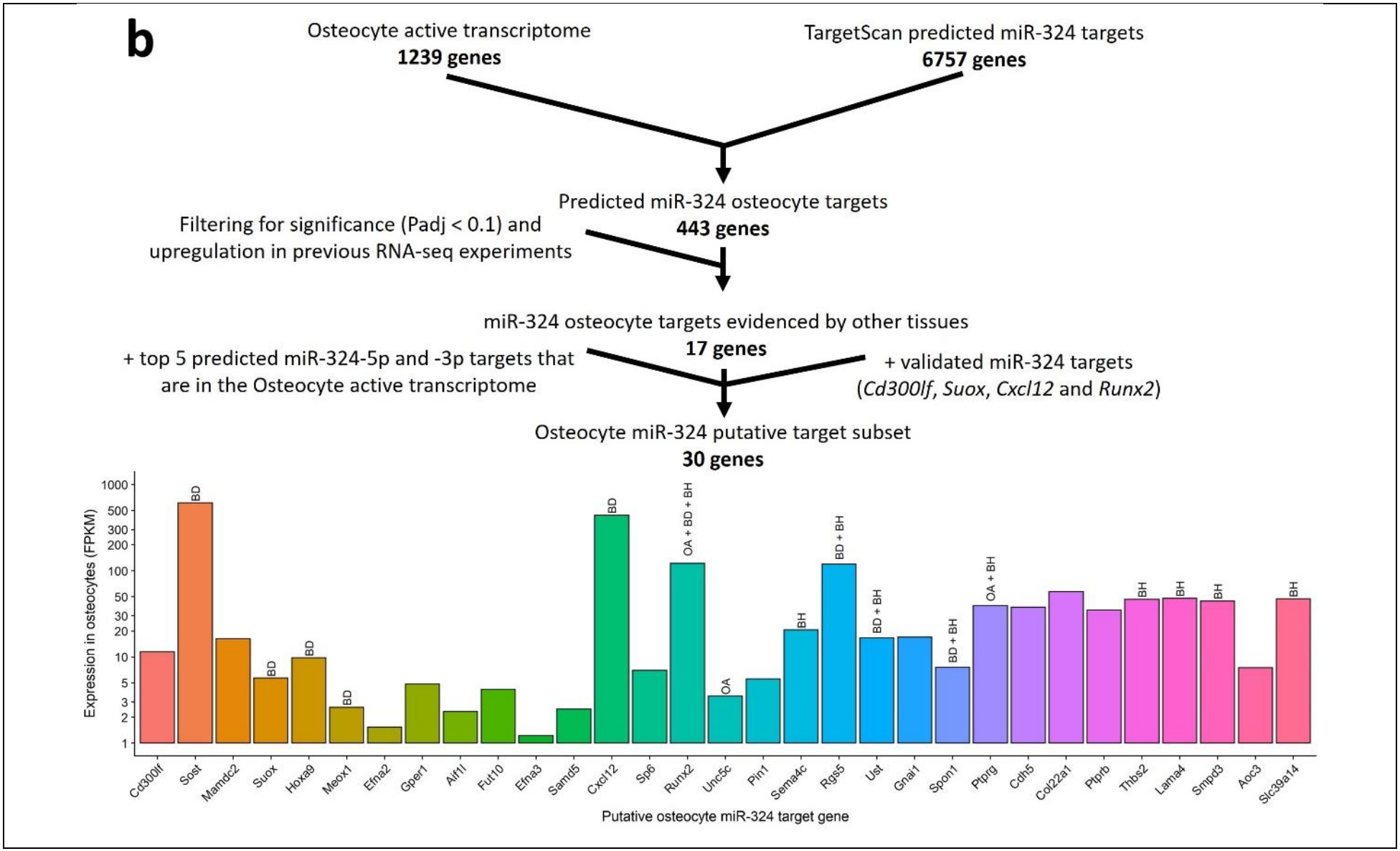
b
Osteocyte active transcriptome
1239 genes
TargetScan predicted miR-324 targets
6757 genes
Predicted miR-324 osteocyte targets
443 genes
Filtering for significance (Padj < 0.1) and
upregulation in previous RNA-seq experiments
miR-324 osteocyte targets evidenced by other tissues
17 genes
+ top 5 predicted miR-324-5p and -3p targets that
are in the Osteocyte active transcriptome
+ validated miR-324 targets
(Cd300lf, Suox, Cxcl12 and Runx2)
Osteocyte miR-324 putative target subset
30 genes
Expression in osteocytes (FPKM)
1000
500
300
200
100
50
30
20
10
5
3
2
1
BD
BD
BD
BD
BD
OA + BD + BH
OA
BH
BD + BH
BD + BH
BD + BH
OA + BH
BH
BH
BH
BH
Cd300lf
Sost
Mamdc2
Suox
Hoxa9
Meox1
Efna2
Gper1
Alf1l
Fut10
Efna3
Samd5
Cxcl12
Sp6
Runx2
Unc5c
Pin1
Sema4c
Rgs5
Ust
Gnai1
Spon1
Ptprg
Cdh5
Col22a1
Ptprb
Thbs2
Lama4
Smpd3
Aoc3
Slc39a14
Putative osteocyte miR-324 target gene

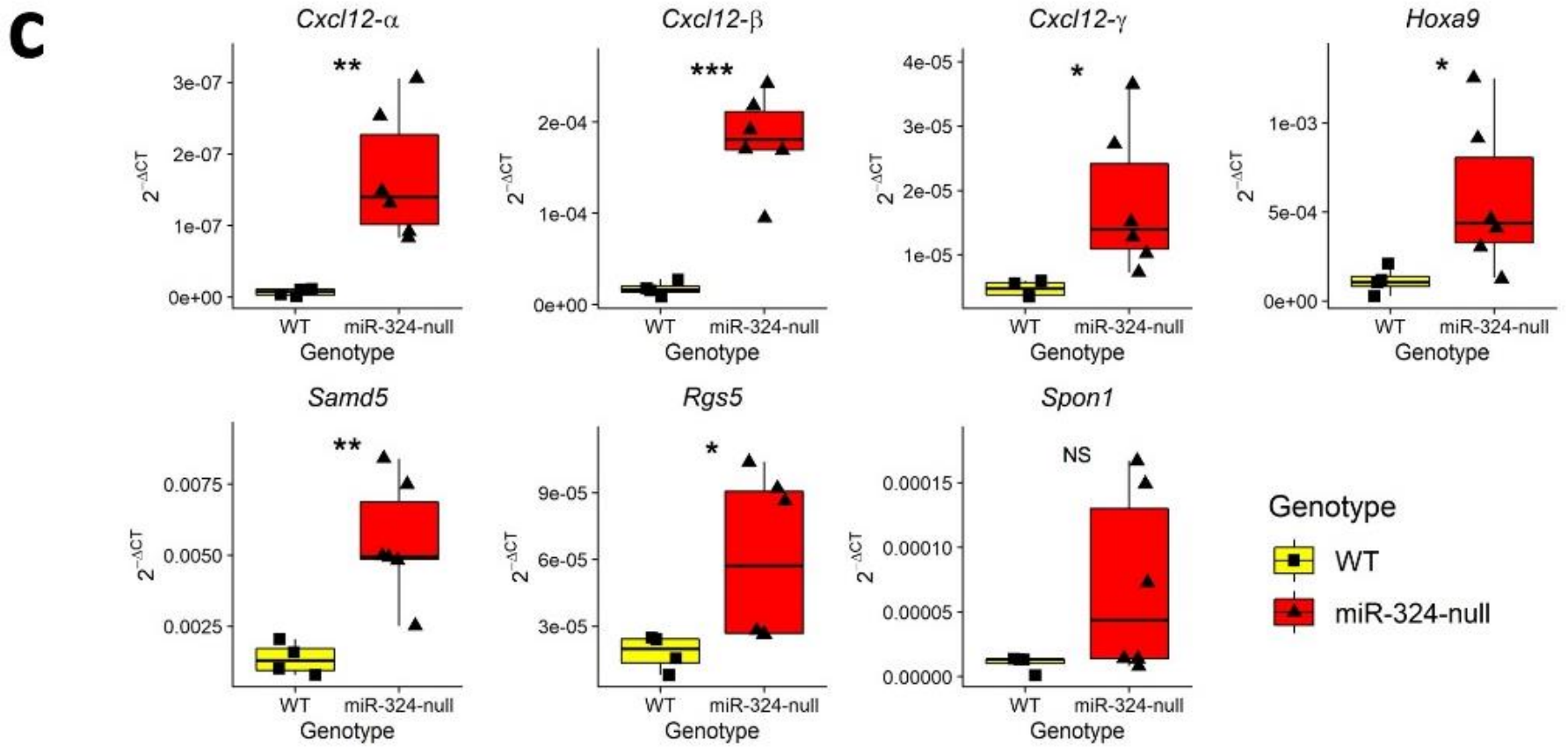

Figure 6.4 - Identification of novel miR-324 osteocyte target genes. (**a**) The osteocyte-selective genes *Mepe*, *Phex* and *Sost* were detected in both miR-324-null and WT osteocyte samples and *Runx2* remained unchanged in expression between genotypes, confirming that the cells from which the RNA was extracted were of similar osteocyte purity between genotypes. The important osteoblast and osteocyte genes *Alpl*, *Bglap*, *Csf1*, *Phex* and *Mepe* were dysregulated in miR-324-null osteocyte samples relative to WT controls. (**b**) Putative osteocyte target genes were identified by filtering

the osteocyte active transcriptome [216] by predicted target genes of miR-324 utilising the TargetScan algorithm [5, 67]. These genes were then filtered further for previous evidence of upregulation in miR-324-null datasets. Finally, the 5 most highly predicted miR-324-5p and -3p targets according to the TargetScan algorithm that were not in the osteocyte active transcriptome were added into the subset, as were the 4 miR-324 targets validated over the course of this project. OATargets [353] was utilised to identify any GWAS associations between these putative target genes and body height (labelled BH), bone mineral density (labelled BD) or osteoarthritis (OA). (**c**) Of the 30 putative target genes tested, 5 (in which the *Cxcl12* isoforms were treated as 1 gene, despite all 3 being upregulated) were statistically significantly upregulated or close to the 5% threshold (*Spon1* showed a p-value of 0.09) using RT-qPCR. The housekeeping gene *18S* was utilised to normalise results. For all panels, *, ** and *** signify p-values ≤ 0.05, 0.01 and 0.001, respectively, with statistical significance calculated using two-tailed Student's *t*-tests.

In order to validate whether *Hoxa9*, *Samd5* and *Rgs5* were directly regulated by miR-324, 3'UTR-luciferase assays were undertaken in C3H10T1/2 cells. These showed a mean reduction of luciferase activity of approximately 20% and 25% for *Samd5* and *Hoxa9*, respectively, whereas no change in luciferase activity was observed for the *Rgs5* and *Spon1* 3'UTRs (Figure 6.5ai). The miR-324-mediated repression of *Samd5* and *Hoxa9* was abolished upon 2 nt mutations of the predicted miR-324 binding sites in the 3'UTR of each gene (Figure 6.5aii; binding site locations and mutant sequences are shown in Table 2.2). It was not necessary to test *Cxcl12* in this specific subset of genes, as the interaction of *Cxcl12*-γ with miR-324-5p and -3p has already been demonstrated in section 6.2.1.

In order to assess what effect the overexpression of each of these genes would have on the expression of other osteocyte genes, *Samd5* and *Hoxa9* were overexpressed using the FLAG-tagged pCMV-ENTRY vector (western blotting of FLAG-tagged Hoxa9 and Samd5 protein shown in Figure 6.5bi) in MLO-Y4 cells, an osteocyte-like cell line [354]. As previously utilised to model *Cxcl12* upregulation in section 6.2.1, recombinant Cxcl12-α was used to stimulate the MLO-Y4 cells. Several genes considered essential in osteocytes (*Phex*, *Mepe* and *Sost*) in addition to the three *Cxcl12* isoforms were not expressed in MLO-Y4 cells at detectable levels and therefore the effect of miR-324 target upregulation on the expression of these genes remains unknown. However, *Alpl*, *Bglap* and *Csf1*, which were all significantly dysregulated in miR-324-null osteocytes *in vivo*, were expressed in MLO-Y4 cells. The overexpression of Hoxa9 in MLO-Y4 cells resulted in a significant upregulation of *Bglap* and downregulation of *Csf1* ($\log_2$ fold-changes of 0.93 and -0.61, respectively), modelling the dysregulation of these genes observed *in vivo* effectively. However, no change was observed in the expression of *Alpl* upon *Hoxa9* upregulation. Overexpression of *Samd5* also resulted in a significant downregulation of *Csf1* ($\log_2$ fold-change of -0.84), but failed to alter *Alpl* or *Bglap* expression (Figure 6.5bii). Stimulation with Cxcl12-α did not significantly alter *Csf1* expression, although a trend towards a decrease was observed ($\log_2$ fold-change of -0.68, p-value = 0.11; Figure 6.5biii). The dysregulation of *Hoxa9* and *Samd5* due to lack of miR-324 may therefore be the cause of *Bglap* and *Csf1*, but not *Alpl*, dysregulation in miR-324-null osteocytes.

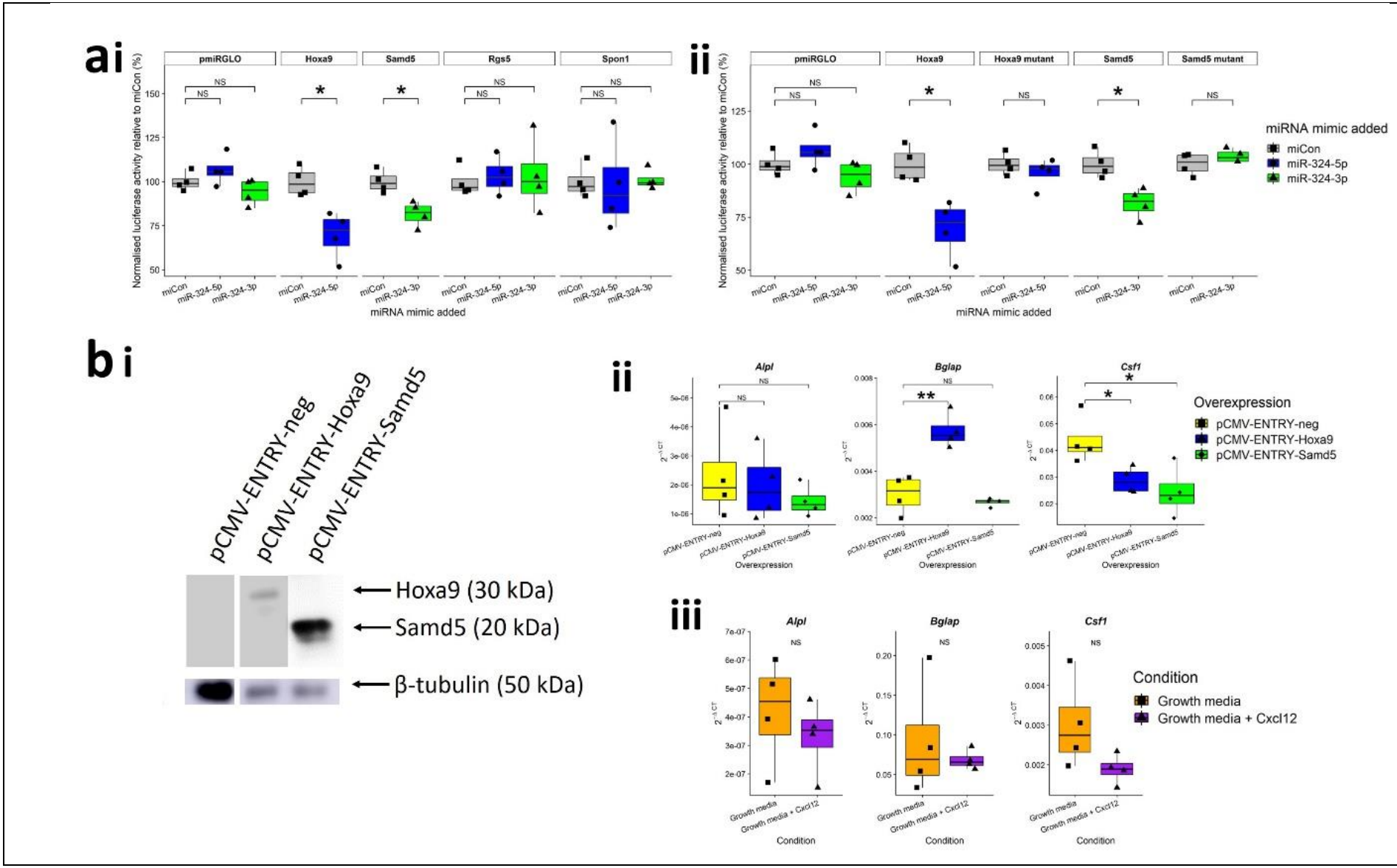
ai
pmiRGLO
Hoxa9
Samd5
Rgs5
Spon1
Normalised luciferase activity relative to miCon (%)
NS
*
miCon
miR-324-5p
miR-324-3p
miRNA mimic added
ii
pmiRGLO
Hoxa9
Hoxa9 mutant
Samd5
Samd5 mutant
Normalised luciferase activity relative to miCon (%)
miRNA mimic added
miRNA mimic added
miCon
miR-324-5p
miR-324-3p
bi
pCMV-ENTRY-neg
pCMV-ENTRY-Hoxa9
pCMV-ENTRY-Samd5
Hoxa9 (30 kDa)
Samd5 (20 kDa)
β-tubulin (50 kDa)
ii
Alpl
Bglap
Csf1
NS
*
**
Overexpression
pCMV-ENTRY-neg
pCMV-ENTRY-Hoxa9
pCMV-ENTRY-Samd5
iii
Alpl
Bglap
Csf1
NS
Condition
Growth media
Growth media + Cxcl12

Figure 6.5 - Validation of putative miR-324 osteocyte target genes. (**a**)(**i**) The putative miR-324 target genes which were upregulated in miR-324-null osteocytes relative to WT controls were assessed for direct interaction with miR-324-5p or -3p in 3'UTR-luciferase assays. C3H10T1/2 murine cells were transfected with 3'UTR-pmiRGLO constructs and subsequently also with either a negative control miRNA mimic (miCon) or a mimic of miR-324-5p or miR-324-3p. Luciferase activity was measured after cells were incubated at 37°C for 24 hours. Relative luciferase activity was calculated as a ratio of Renilla activity, an internal transfection control of pmiRGLO, and values were plotted as a percentage of mean miCon luciferase activity for each construct. The *Hoxa9* and *Samd5* 3'UTRs resulted in a significant downregulation of luciferase activity when miR-324-5p and -3p mimic were added, respectively. The *Cxcl12* 3'UTRs were not tested here as the interaction between *Cxcl12*-γ and miR-324 has already been confirmed (section 6.2.1). (**ii**) When 2 nt in each predicted binding site was mutated, the ability of miR-324 to repress the luciferase gene upstream of each 3'UTR was ablated. A negative control plasmid (pmiRGLO) and miCon in addition to a previously validated miR-324 target 3'UTR as a positive control was included for each independent experiment. (**b**) The coding regions of *Hoxa9* and *Samd5* were overexpressed using the FLAG-tagged pCMV-ENTRY overexpression vector and the Cxcl12-α chemokine was used to stimulate MLO-Y4 cells to investigate any effects due to increased abundance of Cxcl12 in the osteocyte model cell line MLO-Y4. (**i**) Hoxa9 and Samd5 protein can be detected using western blotting in protein lysate obtained from cells transfected with the *Hoxa9* and *Samd5* FLAG-tagged overexpression plasmids (respectively), using an anti-FLAG antibody. No FLAG-tagged protein was detected in lysate obtained from cells transfected with the negative control. An anti-β-tubulin antibody was utilised as the positive control to confirm that protein was present in all loaded samples. (**ii**) A significant upregulation of *Bglap* and a significant downregulation of *Csf1* was observed using RT-qPCR when *Hoxa9* was overexpressed. *Samd5* overexpression also resulted in a significant downregulation of *Csf1*, but no change to the expression of *Alpl* or *Bglap*. (**iii**) *Csf1* showed a mild decrease in expression using RT-qPCR upon *Cxcl12* stimulation, although this did not achieve statistical significance at a 5% threshold (p-value = 0.11). Additionally, no dysregulation of *Alpl* or *Bglap* was observed upon Cxcl12 stimulation. For panels **bi** and **bii**, the *18S* housekeeping gene was utilised to normalise results. For all panels, * and ** signify p-values ≤ 0.05

and 0.01, respectively, with statistical significance calculated using two-tailed Student's *t*-tests. For panel **a**, paired *t*-tests were used and the means of ≥ 4 independent experiments, each containing ≥ 3 technical replicates, were used to test statistical significance.

6.2.3 *Identification of putative miR-324 targets in BMMs*

In addition to the bone formation activity of osteoblasts, other bone cells could also be partly responsible for the miR-324-null high bone mass phenotype, such as the osteoclast. However, as discussed in Chapter 5, miR-324-null osteoclasts, derived *ex vivo* from BMMs, are immature in that they fail to differentiate successfully from BMM precursors and therefore almost 9000 genes are significantly dysregulated between miR-324-null and WT osteoclasts (adjusted p-value ≤ 0.05; Figure 5.3). Therefore, we attempted to identify targets in BMMs, which had not yet been stimulated with RANK-L and therefore had in theory not yet deviated hugely from the WT controls. However, there were still more than 7000 genes dysregulated between genotypes in these BMMs (approximately 4000 genes were significantly upregulated; adjusted p-value ≤ 0.05 and $\log_2$FC > 0). As was the case in section 6.2.1 for osteoblast target prediction, utilisation of the Sylamer algorithm [506] did not show an enrichment in transcripts matching the miR-324 seed sequences which were highly upregulated by the deletion of *Mir324* in each of the BMM and osteoclast RNA-seq data (Appendices Cb and Cc, respectively), likely due to the large number of dysregulated transcripts masking any signal derived from direct miR-324 target dysregulation. Because of this, the same target prediction pipeline as utilised for the prediction of osteoblast targets was used here. Of the 363 bone or lipid disease-associated putative miR-324 targets, 42 were significantly upregulated in miR-324-null BMMs relative to WT controls (Figure 6.6a) and of this subset, 9 genes passed the thresholds for the TargetScan total context score and the $\log_2$ fold-change (< -0.25 and > 0.35, respectively); *Ccne1*, *Pdgfa*, *Klf7*, *Icam1*, *Bcl2*, *Pin1*, *Ing1*, *Ptgs1* and *App* (Figure 6.6b). A 3'UTR luciferase reporter construct for each of these genes was generated and transfection with the predicted targeting miR-324 arm revealed that only *Pdgfa*, *Pin1*, *Ptgs1* and *App* were direct miR-324 targets (Figure 6.6ci). The human *PIN1* (*hPIN1*) 3'UTR was also cloned into the luciferase reporter plasmid and tested for direct interaction with human miR-324-5p, as the predicted binding site is conserved between human and mouse. Despite this conservation however, *hPIN1* was not a direct miR-324-5p target. Mutant 3'UTR constructs were constructed for each validated miR-324 target gene, in which 2 nt of each predicted binding site were mutated. The use of each of these mutant reporter plasmids in place of the WT reporter plasmids successfully ablated the miR-324-mediated repression of all the putative targets (Figure 6.6cii; binding site locations and mutant sequences are shown in Table 2.2). Therefore *Pdgfa*, *Ptgs1*, *App* and *Pin1*, but not *hPIN1*, are direct miR-324 target genes.

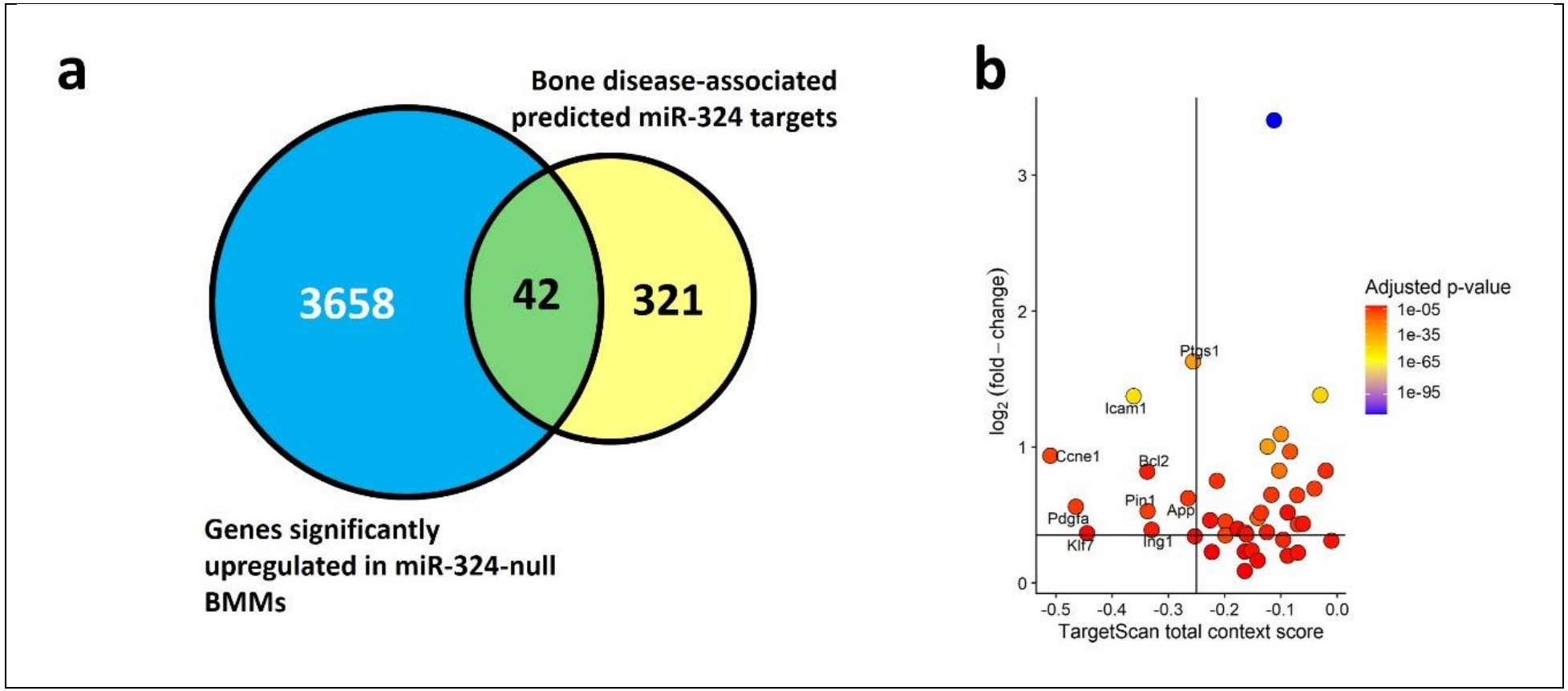
a
Bone disease-associated predicted miR-324 targets
3658
42
321
Genes significantly upregulated in miR-324-null BMMs
b
log2 (fold – change)
TargetScan total context score
Adjusted p-value
1e-05
1e-35
1e-65
1e-95
Ptgs1
Icam1
Ccne1
Bcl2
Pin1
App
Pdgfa
Klf7
Ing1

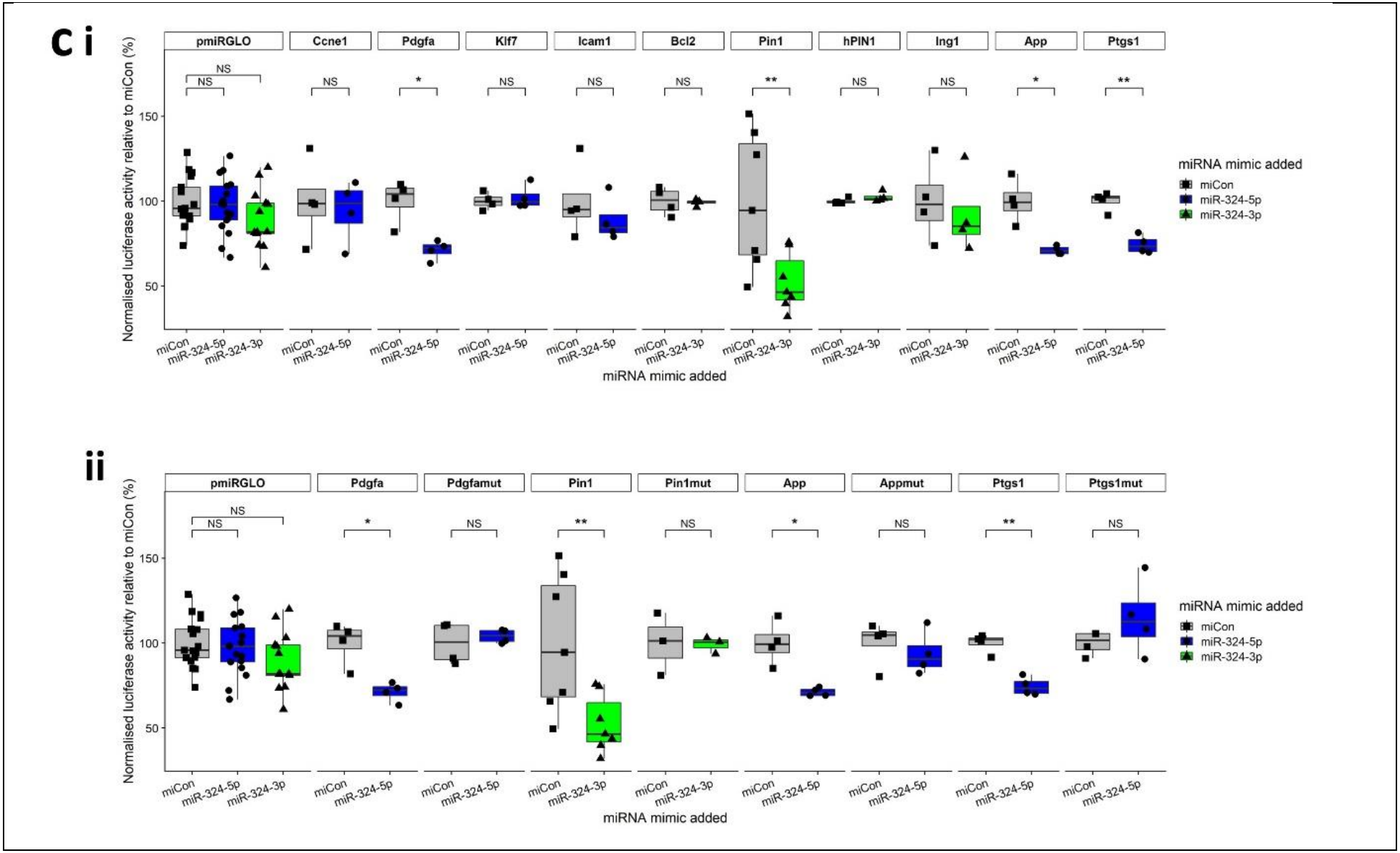
c i
pmiRGLO
Ccne1
Pdgfa
Klf7
Icam1
Bcl2
Pin1
hPIN1
Ing1
App
Ptgs1
NS
*
**
Normalised luciferase activity relative to miCon (%)
150
100
50
miCon
miR-324-5p
miR-324-3p
miRNA mimic added
ii
pmiRGLO
Pdgfa
Pdgfamut
Pin1
Pin1mut
App
Appmut
Ptgs1
Ptgs1mut
NS
*
**
Normalised luciferase activity relative to miCon (%)
150
100
50
miCon
miR-324-5p
miR-324-3p
miRNA mimic added

Figure 6.6 - Identification and validation of novel bone marrow macrophage miR-324 target genes. (**a**) 3700 genes were upregulated in miR-324-null BMMs relative to WT controls, and of these 42 were associated with bone or lipid disorders in the DO [343] and were predicted targets of miR-324. (**b**) Thresholds were set for the TargetScan total context score and the $\log_2$ fold-change of < -0.25 and > 0.35, respectively, resulting in 9 BMM putative miR-324 target genes; *Ccne1*, *Pdgfa*, *Klf7*, *Icam1*, *Bcl2*, *Pin1*, *Ing1*, *Ptgs1* and *App*. (**c**)(**i**) C3H10T1/2 murine cells were transfected with 3'UTR-pmiRGLO constructs and subsequently also with either miCon or a mimic of miR-324-5p or miR-324-3p. Luciferase activity was measured after cells were incubated at 37°C for 24 hours. Relative luciferase activity was calculated as a ratio of Renilla activity, an internal transfection control of pmiRGLO, and values were plotted as a percentage of mean miCon luciferase activity for each construct. The *Pdgfa*, *Pin1*, *Ptgs1* and *App* 3'UTRs resulted in a significant downregulation of luciferase activity when miR-324 mimics were added. Unlike the murine *Pin1* 3'UTR, the human *PIN1* (*hPIN1*) 3'UTR was not repressed by miR-324-5p mimic. For *hPIN1*, the same protocol was undertaken, but using human Y201 cells in place of murine C3H10T/2 cells. (**ii**) When 2 nt in each miR-324 binding site was mutated, the ability of miR-324 to repress the luciferase gene upstream of each 3'UTR was completely ablated. For panel **c**, the means of at least 4 independent experiments were used to test statistical significance. The negative control plasmid pmiRGLO and miCon in addition to a previously validated miR-324 target 3'UTR as a positive control was included for each independent experiment. For all panels, * and ** signify p-values ≤ 0.05 and 0.01, respectively, assessed using Student's two-tailed paired *t*-tests.

6.3 Discussion

6.3.1 *The important osteoblast genes Cxcl12 and Runx2 are in vitro targets of miR-324*

As discussed in Chapter 5, miR-324-null osteoblasts are highly distinct at a transcriptomic level from WT osteoblasts. Target prediction analysis was therefore utilised in order to identify predicted target genes of miR-324 that were significantly upregulated in miR-324-null osteoblasts in the RNA-seq experiment, annotated to a bone- or metabolism-related disorder in the DO [343] and were predicted by the TargetScan algorithm [5, 67] to bind at least one miR-324 arm. Of these resulting genes, only two were validated *in vitro* as direct miR-324 targets; *Runx2* and *Cxcl12*-γ (*Cxcl12*-α and -β, the other *Cxcl12* isoforms, were also predicted as targets but did not validate *in vitro*). *Runx2* shows an evident link to bone formation, as it is the master transcription factor which regulates osteogenesis and downstream bone formation [217, 218], but *Cxcl12* (also known as *Sdf1*) is not as well documented in this context. The three isoforms of *Cxcl12* encode three chemokine isoforms; Cxcl12-α, -β and -γ, each of which contain the full Cxcl12-α peptide sequence and thus combined with the predominant expression of *Cxcl12*-α over the other isoforms, Cxcl12-α is regarded as the canonical chemokine isoform. Comparatively, *Cxcl12*-γ is the isoform with the lowest expression level, and therefore it is unclear how relevant the dysregulation of this isoform is to the overall miR-324-null phenotype [508]. The Cxcl12 chemokine has been shown to bind one of two receptors, Cxcr4 or Ackr3 (CXCR4 and CXCR7 in humans), and this binding induces migration of progenitor cells in the bone marrow [509, 510]. The Cxcl12-α and -β chemokines are purported to bind the receptors with similar affinity, whereas the additional exon of Cxcl12-γ has been reported to increase binding affinity, resulting in longer-lasting Cxcl12-receptor interactions than would theoretically be found for the Cxcl12-α and -β chemokines [511, 512]. Two conditional knockout mouse models of *Cxcl12*, driven by *Prx1*-Cre and *Osx*-Cre (which are markers of developmental limb mesenchymal cells and pre-osteoblasts, respectively), have previously revealed phenotypes relating to the lineage commitment choice between adipogenesis and osteogenesis; both of these conditional *Cxcl12*-null mice have dramatically increased bone marrow adipose content relative to heterozygous control animals in addition to significantly increased adipogenesis marker gene expression (significantly upregulated *Pparg* in the *Prx1*-Cre mice and significantly upregulated *Adipoq* in both the *Prx1*-Cre and *Osx*-Cre Cxcl12-null conditional mouse models) and decreased osteogenesis marker gene expression (significantly downregulated *Runx2* in the *Prx1*-Cre mice and significantly downregulated *Alp* in the *Osx*-Cre mice) [304]. It is of note that this phenotype is precisely the

opposite of the *in vivo* phenotypes of miR-324-null mice, in which *Cxcl12* is upregulated. Furthermore, rat *Runx2* and *Cxcl12* have previously been reported to also be the targets of a different miRNA, miR-137-3p, and inhibition of this miRNA has been demonstrated to increase osteogenesis [301]. Although these studies strongly suggest that *Cxcl12*, in addition to *Runx2*, can modulate osteogenesis, and likely also adipogenesis, it additionally raises the possibility that *Cxcl12* may regulate *Runx2* itself, albeit not necessarily directly. Therefore, further *in vitro* assays are required in order to investigate this possibility and additionally to confirm whether *Runx2* or *Cxcl12* upregulation individually is sufficient to produce the observed increased osteogenesis and decreased adipogenesis phenotype *in vivo*.

6.3.2 *Cxcl12 and Runx2 interact in vitro and modulate osteogenesis and adipogenesis*

In order to confirm the effects of increased *Cxcl12* and *Runx2* levels on adipogenesis and osteogenesis, co-differentiation AdiOst media was utilised [355], allowing murine C3H10T1/2 MSC-like cells to commit to either the adipogenesis or osteogenesis lineages. Remarkably, both stimulation with Cxcl12-α and *Runx2* overexpression upregulated osteogenesis markers and downregulated adipogenesis markers, as well as decreasing the AdiOst ratio, measured using oil red-O and alizarin red-S staining intensities for lipid droplets and mineralised bone nodules, respectively. Furthermore, Cxcl12-α stimulation upregulated its own expression as well as that of the other two *Cxcl12* isoforms and *Runx2* expression. This Cxcl12-α-mediated regulation of all *Cxcl12* isoforms offers a potential explanation to why all isoforms were upregulated in the osteoblast RNA-seq experiment despite only *Cxcl12*-γ validating as a miR-324 target; under AdiOst conditions, *Cxcl12* is able to upregulate itself, although the mechanism of this auto-amplification is unclear. *Runx2* may play a role in this, as *Runx2* overexpression was able to upregulate *Cxcl12*-α, although it had no effect *Cxcl12*-β or -γ. This raises an intriguing paradox, in that if stimulation with Cxcl12-α is able to upregulate *Runx2* and the other *Cxcl12* isoforms and additionally *Runx2* is able to upregulate *Cxcl12*-α, then why does the latter not also result in upregulation of the other *Cxcl12* isoforms, through *Cxcl12*-α upregulation? It is likely therefore that the interaction between *Runx2* and *Cxcl12* is not direct, and it is the effect of one or multiple interaction partners which dictate precisely how this regulation operates.

6.3.3 *Cxcl12 and Runx2 stimulate spontaneous osteogenesis in vitro*

In order to dissect the interaction between *Cxcl12* and *Runx2* in osteogenesis and adipogenesis, I investigated whether high levels of either of these miR-324 target genes, or

both combined as would be found in miR-324-null mice, were able to stimulate osteogenesis to occur spontaneously, in the absence of AdiOst media. Remarkably, both *Runx2* overexpression, Cxcl12-α stimulation, and the two conditions combined were all able to stimulate spontaneous osteogenesis, as measured by an increase in both alizarin red-S staining intensity and *Runx2* expression. In regard to the alizarin red-S staining intensity, the effect of each individual condition appeared to be synergistic; *Runx2* overexpression and Cxcl12-α stimulation combined produced an increase in alizarin red-S staining intensity of similar magnitude as the summed magnitude of each individual condition. Furthermore, all conditions showed at least a trend towards decreased adipogenesis, measured through decreased *Pparg* expression and oil red-O staining intensity. Although minimal lipid droplet staining was observed, the decrease in these markers suggests that a basal level was occurring in the controls and high levels of the two miR-324 osteoblast target genes were able to shift this adipogenic cell population into the osteogenic lineage. It is interesting to note that even in the control conditions a low level of spontaneous osteogenesis was visible in C3H10T1/2 cells. This is surprising and, combined with the detection of a low level of lipid production through oil red-O staining, suggests that stimulation with AdiOst media merely amplifies the co-differentiation, rather than triggering its initiation.

Despite the fact that the downstream phenotype of cells overexpressing *Runx2* or stimulated with Cxcl12-α is the same in cells lacking AdiOst media as it is in cells in AdiOst conditions (upregulated osteogenesis at the expense of adipogenesis), the upstream mechanism resulting in this phenotype appears to be distinct in relation to *Cxcl12* (summarised in Figure 6.7a). It is difficult to explain the distinct responses upon Cxcl12-α stimulation, as it appears that some factor either within the AdiOst media, or only expressed when cells are plated into AdiOst media, entirely modifies the response to the Cxcl12-α chemokine. This could occur for example via an additional Cxcl12-α receptor expressed only in AdiOst media, to which the Cxcl12-α chemokine binds preferentially. One receptor could therefore stimulate one response in α-MEM (a negative feedback loop), whilst the additional receptor could stimulate a distinct response upon Cxcl12-α stimulation in AdiOst conditions (a positive feedback loop; summarised in Figure 6.7b). Of course this would not necessarily have to be a receptor; it is also possible that some factor further downstream of Cxcl12-α-receptor binding may be altered between conditions, but this receptor hypothesis is the most simplistic. Perhaps therefore, it is important for *Cxcl12* to be maintained at low levels before adipogenic or

osteogenic differentiation, but then during the differentiation its expression requires amplification. If this is the case however, then it is curious that at the end point of the AdiOst experiments, *Cxcl12*-β and -γ were undetected whereas in α-MEM these isoforms were detected at reasonable levels. This therefore would suggest that *Cxcl12* expression may be lower following AdiOst stimulation than before stimulation, and indeed this effect has previously been observed in the literature upon osteogenic differentiation [513]. Therefore perhaps increased *Cxcl12* expression is only required at the very start of differentiation, at the point of lineage commitment, and then is downregulated again by the experimental end point. Further investigation into the behaviour of the *Cxcl12* isoforms during osteogenesis and adipogenesis is required in order to test this hypothesis.

Regardless of the precise role of Cxcl12-α in this co-differentiation, it seems clear that upregulation of *Runx2* is the key result; in every condition tested, upregulation of *Runx2* and downregulation of *Pparg* were observed, leading to decreased adipogenesis and increased osteogenesis. It therefore seems likely that although *Cxcl12* plays a role in the resulting phenotype in miR-324-null mice, that role is in the upregulation of *Runx2*, an effect which is amplified by the fact that *Runx2* itself is also a direct miR-324 target gene. Other *Runx2*-targeting miRNAs, such as miR-135a-5p, miR-137-3p, miR-155 and miR-23a-5p, have previously also demonstrated the resulting modulation in bone formation [300-303], and therefore it can be stated with confidence that *Runx2* upregulation is the causal effector of the miR-324-null increased bone formation phenotype. In AdiOst conditions, an additional positive feedback loop forms, whereby upregulation of *Cxcl12* due to lack of miR-324 and increased *Runx2* expression leads to further upregulation of both itself and of *Runx2*.

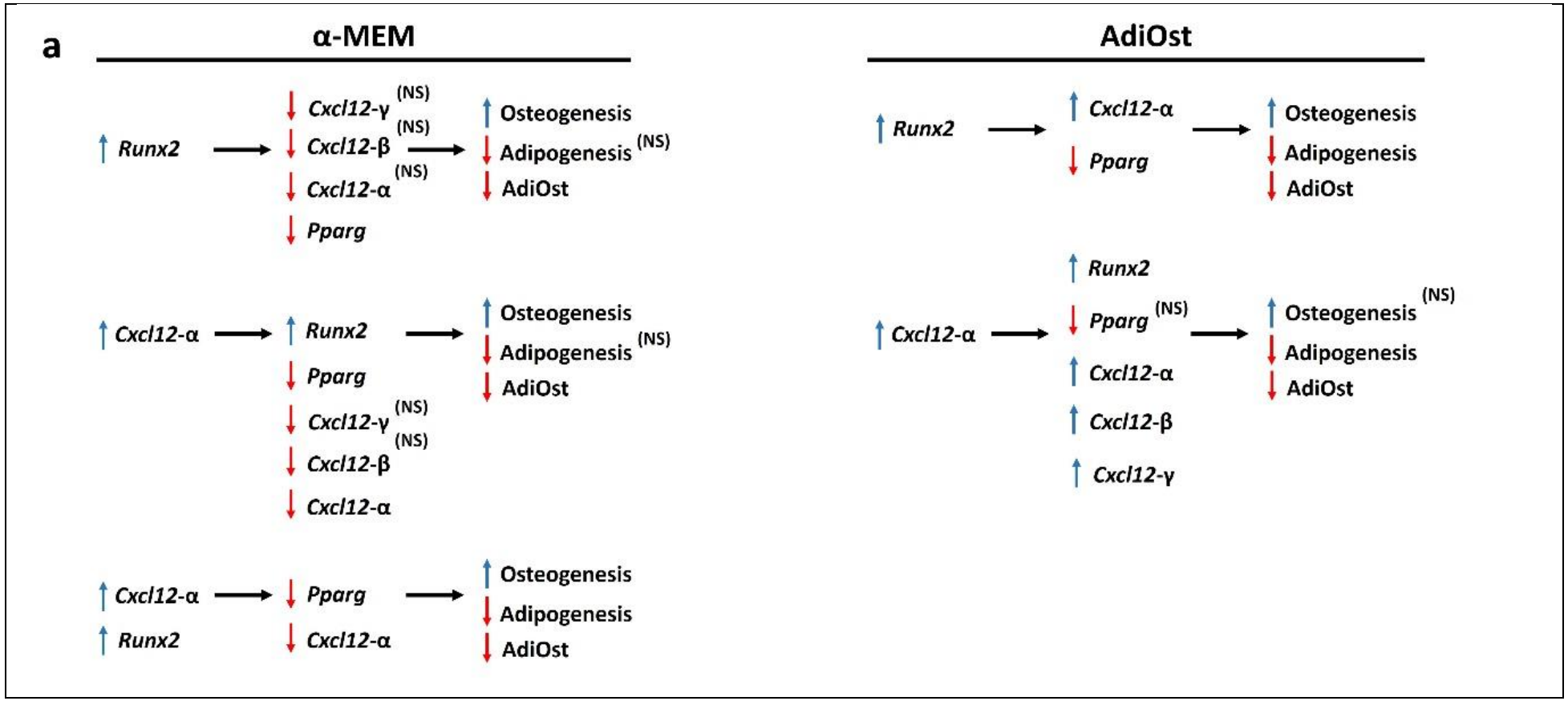
a
α-MEM
↑ Runx2
↓ Cxcl12-γ (NS)
↓ Cxcl12-β (NS)
↓ Cxcl12-α (NS)
↓ Pparg
↑ Osteogenesis
↓ Adipogenesis (NS)
↓ AdiOst
↑ Cxcl12-α
↑ Runx2
↓ Pparg
↓ Cxcl12-γ (NS)
↓ Cxcl12-β (NS)
↓ Cxcl12-α
↑ Osteogenesis
↓ Adipogenesis (NS)
↓ AdiOst
↑ Cxcl12-α
↑ Runx2
↓ Pparg
↓ Cxcl12-α
↑ Osteogenesis
↓ Adipogenesis
↓ AdiOst
AdiOst
↑ Runx2
↑ Cxcl12-α
↓ Pparg
↑ Osteogenesis
↓ Adipogenesis
↓ AdiOst
↑ Cxcl12-α
↑ Runx2
↓ Pparg (NS)
↑ Cxcl12-α
↑ Cxcl12-β
↑ Cxcl12-γ
↑ Osteogenesis (NS)
↓ Adipogenesis
↓ AdiOst

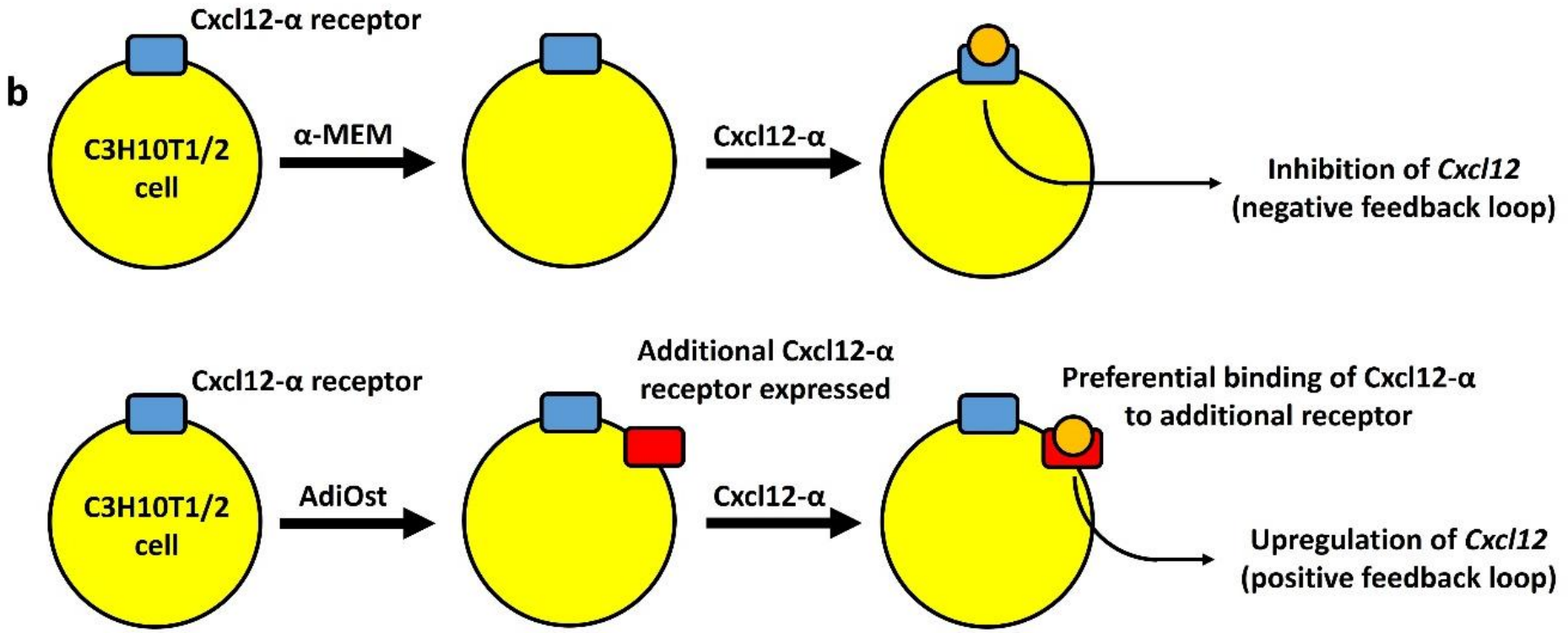

Figure 6.7 - The effect of overexpressing Runx2 or stimulating with Cxcl12-α in C3H10T1/2 cells under AdiOst and non-AdiOst conditions. (a) Although all conditions result in a downstream increase in osteogenesis and decrease in adipogenesis, the apparent mechanism of this in relation to the miR-324 target genes, *Runx2* and *Cxcl12*, appears to be distinct between α-MEM and AdiOst conditions. In α-MEM, overexpression of *Runx2* downregulated all *Cxcl12* isoforms in addition to *Pparg*, whereas in AdiOst conditions *Runx2* overexpression actually increased *Cxcl12*-α expression and yet still downregulated *Pparg*. Stimulation of C3H10T1/2 cells with Cxcl12-α in α-MEM resulted in upregulation of *Runx2* and downregulation of *Pparg* and *Cxcl12*-α. In AdiOst conditions however Cxcl12-α stimulation increased the expression of all *Cxcl12* variants, in addition to decreased

Pparg and increased *Runx2* expression. Simultaneous overexpression of *Runx2* and stimulation with Cxcl12-α in non-AdiOst conditions resulted in decreased *Pparg* and *Cxcl12*-α expression, but no change in expression in the other *Cxcl12* isoforms. Each of these scenarios resulted in increased osteogenesis and reduced adipogenesis (measured using alizarin red-S and oil red-O staining intensities, respectively). Results which did not achieve statistical significance at a 5% threshold but still showed a strong trend are marked with **(NS)**. Statistical analysis of the effect of Cxcl12-α stimulation on the expression of *Cxcl12*-β and -γ could not be calculated, as neither *Cxcl12*-β nor -γ were detected in the control condition. All other results shown achieved statistical significance. (**b**) A potential explanation for the discrepancies between α-MEM and AdiOst conditions is illustrated, in which the AdiOst media allows expression of an additional Cxcl12-α receptor, to which Cxcl12-α binds preferentially. If the binding to the original receptor produces a negative feedback loop, whereas the preferential AdiOst-expressed receptor produces a positive feedback loop then this could account for the differences between conditions.

6.3.4 *miR-324 regulates osteocyte genes involved in osteocytogenesis and osteoclastogenesis*

In order to identify novel miR-324 target genes in osteocytes, a key cell in the regulation of bone remodelling and bone mineral density (BMD), I isolated RNA from miR-324-null and WT osteocytes and utilised the TargetScan algorithm [5, 67] to predict putative miR-324 targets which were also identified within the osteocyte active transcriptome, a set of genes identified as defining the osteocyte transcriptomic landscape [352]. This analysis identified 30 putative miR-324 osteocyte target genes, of which 16 were found to show statistically significant associations with either osteoarthritis, bone mineral density or body height, using OATargets [353]. Although associations with these terms were not required in this experimental target identification pipeline, it is striking that more than half of the 30 predicted targets were associated with at least one of these terms, enforcing the essential nature of many of the genes within the osteocyte transcriptomic landscape in regard to skeletal biology.

Following RT-qPCR and 3'UTR-luciferase assay validation, 3 target genes were identified from the initial 30 putative targets; *Hoxa9*, *Samd5* and *Cxcl12*-γ (3'UTR-luciferase assay validation for *Cxcl12*-γ was already undertaken as it was previously validated as an osteoblast target). *Hoxa9* and *Samd5* were overexpressed in MLO-Y4 cells, a model osteocyte cell line [354], and stimulation with the Cxcl12-α chemokine was utilised to mimic high *Cxcl12* levels, allowing investigation into what the effect of dysregulation of these target genes may be to osteocyte biology. Overexpression of both *Hoxa9* and *Samd5* downregulated *Csf1*, a crucial gene not only in the identification of mature osteocytes, but additionally in osteoclastogenesis. *Csf1* encodes M-CSF and is crucial in the differentiation and maturation of mature osteoclasts from BMMs [198]. Osteocytes are an important source of the M-CSF required for the osteoclastogenesis process [205] and therefore, considering that both *Hoxa9* and *Samd5* result in *Csf1* downregulation and that *Csf1* is indeed repressed in miR-324-null osteocytes, it is reasonable to suggest that the dysregulation of *Hoxa9* and *Samd5* is causal of this effect. Additionally, deficiency in osteocyte *Csf1* is a likely contributing factor to the osteoclastogenesis deficiency observed *in vivo* in miR-324-null mice. However, it is certainly not the only cause of impaired osteoclastogenesis, as *ex vivo* osteoclastogenesis was also inhibited, in which M-CSF and RANK-L were added directly to cells.

In addition to the regulation of *Csf1*, *Hoxa9* overexpression also results in an upregulation of *Bglap*, the gene encoding osteocalcin, relative to negative controls. Notably, *Bglap* is a late osteoblast and early osteocyte marker gene [514], suggesting that this upregulation of *Bglap*

by *Hoxa9* is likely to affect osteocytes at an early stage, probably during the process of osteocytogenesis. In osteoblasts, *Bglap* upregulation is suggestive of increased bone formation and mineralisation, but it is unclear from the literature what effect this would produce in osteocytes. However, regardless of the precise phenotypic effect of increased *Bglap* expression, it seems plausible that the combination of this with downregulation of *Csf1* results in immature osteocytes. miR-324-null osteocytes presumably therefore terminate their differentiation from osteoblasts prior to the upregulation of *Csf1*. However, the fact that overexpression of *Samd5* represses *Csf1* without upregulating *Bglap* suggests that the negative regulation of *Csf1* in miR-324-null osteocytes does not require the upregulation of *Bglap*. It would be useful to overexpress *Bglap* and inhibit *Csf1* in MLO-Y4 cells in future experiments to confirm the precise order of regulation of these genes.

In addition to *Csf1* and *Bglap*, several other key osteocyte genes were found to be dysregulated in miR-324-null osteocytes; namely *Phex*, *Mepe* and *Alpl*. Both *Mepe* and *Phex* were severely downregulated in samples lacking miR-324, supporting the hypothesis that miR-324-null osteocytes are immature. The increased expression of *Alpl* in miR-324-null osteocytes also supports this hypothesis; although osteoblasts express *Alpl* at relatively high levels, the expression level in mature osteocytes is dramatically lowered [354]. This immaturity hypothesis does not in itself explain why less osteocytes are observed in miR-324-null mice *in vivo*, although it is plausible that the slowed and dysfunctional maturation could result in a proportion of the cells committing to apoptosis during osteocytogenesis. There is however currently no evidence to support this. Although the MLO-Y4 osteocyte model cell line, which was generated from the long bone matrix-embedded cells of transgenic mice expressing the SV40 large T-antigen oncogene under the control of a *Bglap* promoter [354], has been used to investigate osteocyte biology in recent years [205, 515-518], these cells unfortunately do not express *Phex*, *Mepe* or *Alpl* at detectable levels. It is therefore unknown how the overexpression of *Hoxa9* and *Samd5* or stimulation with Cxcl12-α affects the expression of *Phex*, *Mepe* and *Alpl*, if at all.

Interestingly, Cxcl12-α stimulation did not produce any statistically significant dysregulation of tested genes in MLO-Y4 cells. This could suggest that the important function of *Cxcl12* regulation by miR-324 is upstream of osteocytes in the osteoblast lineage and that in fact the dysregulation of *Cxcl12* in miR-324-null osteocytes is merely still the dysregulation observed at the osteoblast stage; after all, the osteocyte results in this chapter suggest that miR-324-

null osteocytes are immature. It is therefore plausible that regulation of miR-324 osteoblast target genes may still be in effect in miR-324 osteocytes. It is curious however if this is the case that *Runx2*, hypothesised as being the most important miR-324 osteoblast target gene responsible for the increased bone mass phenotype, is not dysregulated in miR-324-null osteocytes.

In order to elucidate whether the effects identified *in vitro* in MLO-Y4 cells on *Bglap* and *Csf1* expression are replicated in *ex vivo* osteocytes, in addition to investigating the effects on *Phex*, *Mepe* and *Alpl*, it would be beneficial to overexpress the miR-324 osteocyte target genes in WT osteocytes *ex vivo*. Considering the lack of detectable *Phex*, *Mepe* and *Alpl* expression in MLO-Y4 cells, this is likely the only method to investigate the dysregulation of these genes. However, isolating and culturing osteocytes is a challenging process, and few viable cells remain following the standard protocol of sequential collagenase digestions of long bone [349]. Therefore the isolation of viable cells through this method will likely require a high degree of optimisation.

6.3.5 *Important osteoclastogenesis genes are direct targets of miR-324 in vitro*

In Chapter 5, I demonstrated that osteoclastogenesis was impaired *ex vivo* in miR-324-null mice and that vast numbers of genes were differentially expressed both in miR-324-null BMMs and miR-324-null osteoclasts. In this chapter I identified novel target genes of miR-324 which were annotated to a bone- or metabolism-related disorder (Appendix B) in the Disease Ontology [343], were predicted targets of miR-324-5p or -3p using the TargetScan algorithm [5, 67] and were significantly upregulated in the miR-324-null BMM RNA-seq. The BMM RNA-seq results were utilised rather than the osteoclast experiment because the osteoclast RNA-seq generated too many putative target genes to test using luciferase assays. Additionally, considering that most miR-324-null BMMs failed to differentiate into osteoclasts, the gene dysregulation responsible for this was likely to already be present in BMMs prior to osteoclastogenesis. Of the 9 genes which were predicted by this methodology, 4 were validated using 3'UTR-luciferase assays; *Pdgfa*, *Pin1*, *App* and *Ptgs1*. The only member of these validated targets not directly linked to osteoclastogenesis in the literature is *Ptgs1* [519-522]; in the osteoblast lineage, *Ptgs1* inhibition has been shown to enhance osteogenesis [523], which would suggest if anything that *Ptgs1* overexpression would repress osteogenesis. However, in miR-324-null mice, *Ptgs1* expression is unchanged in osteoblasts; it is upregulated

significantly only in BMMs and osteoclasts, but it is unclear what the effect of this dysregulation would be upon osteoclastogenesis.

Pdgfa encodes Platelet-derived growth factor A (PDGF-A), a protein which can form a homodimer with itself (PDGF-AA) or alternatively can dimerise with the protein product of *Pdgfb*, resulting in a PDGF-AB heterodimer. The relative expression of *Pdgfa* and *Pdgfb* to one another, and therefore the resulting ratios of dimerised protein products, is thought to be crucial in terms of the activity of these proteins in key developmental pathways [524, 525]. *Pdgfa* and *Pdgfb* have shown to be upregulated temporally at distinct stages of the osteoclastogenesis process, with *Pdgfa* peaking in expression within the first 36 hours of the process, whereas *Pdgfb* peaks later, at approximately 60 hours, with protein levels following similar (but delayed) kinetics [522]. In miR-324-null osteoclasts and BMMs, *Pdgfa* is highly upregulated, due to being a direct miR-324-5p target, thus suggesting that increased levels of PDGF-AA and PDGF-AB would be expected, although this has not been tested experimentally. It is unclear whether these dimerised products reflect the progression of the osteoclastogenic process or whether they play some role in regulating it themselves. If the ratio of PDGF-AA and -AB to PDGF-BB is a determinant of osteoclastogenesis then upregulation of *Pdgfa* as observed in miR-324-null samples would certainly be expected to inhibit osteoclastogenesis at an early stage. Even if this ratio is not directly involved in regulation of osteoclastogenesis, the upregulation of *Pdgfa* and therefore also of PDGF-AA and -AB certainly fits the miR-324-null phenotype of an early inhibition in osteoclastogenesis.

App, the gene encoding the amyloid precursor protein, is not traditionally considered to be important in peripheral tissues such as the skeleton, and is largely investigated in relation to brain tissues, due to its strong relationship with Alzheimer's Disease (AD) [113]. However, AD patients commonly have reduced bone mass and higher risk of fractures than healthy individuals [526, 527], and therefore discussion in the literature over recent years has suggested that *App* may play a role in the skeleton as well as in the brain. Mice carrying the Swedish mutant *App* allele (App_{Swe}), a mutation which increases abnormal cleavage of *App* as is observed in AD patients [528], display increased osteoclast-mediated bone resorption and decreased osteoblast-mediated bone formation, producing an osteoporotic phenotype [519, 520]. The authors also demonstrated that in this mouse model, the effect on osteoclast activity is not consistent throughout life; older mutant App_{Swe} mice actually display decreased osteoclast activity, despite younger animals showing the increased osteoclast resorption

which presumably results in the osteoporotic *App*$_{Swe}$ phenotype [519]. Of course, the *App*$_{Swe}$ mutation cannot be considered the same as a complete lack of function mutation or a knockout mouse model of *App*, but the fact that young *App*$_{Swe}$ mutant mice display increased osteoclast activity, whereas miR-324-null mice with increased *App* expression show decreased osteoclast activity, the polar opposite effect, raises the possibility that *App* may be causal in this effect, although this requires experimental validation to confirm. In regard to bone mass, miR-324-null mice do not show the biphasic age-dependent effects observed in *App*$_{Swe}$ mice; in fact the miR-324-null bone mass continues to increase with age. Considering this, it is possible that the heightened *App* levels in miR-324-null mice actually only play a role in the increased bone mass phenotype at young ages, at the same time points as when the *App*$_{Swe}$ mutation has an effect, and it is other dysregulated genes which continue to affect bone mass through osteoclastogenesis at later time points.

Pin1 has been related to abnormal skeletal development. The *Pin1* gene encodes a Peptidyl-prolyl isomerase, a class of enzymes which modify and stabilise proteins through isomerisation of the phosphorylated serine/threonine-proline motif [529, 530], and therefore it is conceivable that through the modification of important proteins to skeletal development, *Pin1* could regulate important skeletal pathways. An obvious indication that this is actually the case is that *Pin1*-null mice show severe loss of bone with age compared to controls [531, 532], and therefore either osteoblast-mediated bone formation, osteoclast-mediated bone resorption or both is likely modulated in these animals. Investigation into the osteoblast activity of *Pin1*-null mice revealed that *Pin1* does indeed affect osteoblast activity; *Pin1* was demonstrated to be required for the stabilisation of *Runx2* during osteogenesis, resulting in reduced osteoblast activity in *Pin1*-null mice [533]. Additionally, a separate study showed that *Pin1* was not just key for the stability of *Runx2*; through associating with SMAD5, Pin1 mediates the expression of many key bone formation genes, such that *Pin1*-null mice show a severe defect in osteoblast-mediated bone formation. Interestingly, Shen *et al.* (2013) categorically identified no differences between *Pin1*-null and WT osteoclasts, both in terms of osteoclast size and in the expression of the key osteoclast genes *Tnfrsf11a*, *Acp5* and *Ctsk* [531]. Contradicting these findings, Islam *et al*. (2014), showed that *Pin1*-null mice displayed severely enhanced osteoclastogenic fusion; *Pin1* was shown to repress *Dcstamp*, a gene which is essential for osteoclastogenic fusion, although the biochemical mechanism behind this is not well understood [196, 207]. Therefore, in *Pin1*-null osteoclasts, *Dcstamp* expression is

severely upregulated, resulting in osteoclasts far larger than those differentiated from WT BMMs, with a far greater number of nuclei [521]. It is possible that this discrepancy is due to the former authors choosing not to investigate nuclei count or osteoclast size, and instead focusing solely on number, although it is difficult to account for the magnitude of alteration to osteoclast size reported by Islam *et al*. (2014) not being noticed during experimentation by Shen and colleagues (2013). Assuming that *Pin1* really does regulate osteoclast fusion through *Dcstamp*, it seems likely that this is a main driver of osteoclastogenesis inhibition in miR-324-null mice. In support of this, miR-324-null mice show a striking downregulation in *Dcstamp* expression both in BMMs and in osteoclasts (log_2 fold-changes of -2.25 and -7.29, respectively), likely producing the severe reduction in osteoclast fusion observed relative to WTs. In regard to the discussion of *Pin1* depletion increasing osteoblast activity, in miR-324-null osteoblasts, *Pin1* is actually significantly downregulated (log_2 fold-change of -0.25; adjusted p-value = 0.013) and therefore in miR-324-null osteoblasts this may be increasing osteoblast activity, as in *Pin1*-null mice. However, it is difficult to explain why *Pin1* is not targeted by miR-324 in osteoblasts despite being a direct target in the BMM lineage. It is possible that *Pin1* actually is a target, but that some other direct miR-324-null-mediated dysregulation is stronger than the direct regulation on *Pin1*, and this overpowers the direct targeting of *Pin1*. In this case, *Pin1* therefore would be a physiological target of miR-324 in WT osteoblast cells, despite not showing an increase in expression in the RNA-seq experiment. Alternatively it may be the case that in osteoblasts there are mRNA transcripts which are stronger miR-324 targets than *Pin1*, and that these transcripts are simply not expressed in the BMM lineage. In either case, it seems likely that the strongest effect of *Pin1* upregulation in miR-324-null bone remodelling is the repression of osteoclast fusion, which is likely the upstream cause of the severe reduction in *Dcstamp* and osteoclast fusion.

In order to confirm that the upregulation of *Pdgfa*, *App* and *Pin1* do impair osteoclastogenesis, it would be useful to overexpress each of these genes in WT BMMs and in the precursor to these, HSCs, and subsequently undertake osteoclastogenesis assays. This would prove which of these targets is resulting in the impaired osteoclastogenesis phenotype observed in miR-324-null mice, or at least which of these genes produces the most severe effect. Additionally, this would demonstrate whether upregulation of these targets at the HSC stage of the haematopoietic lineage is able to mimic the observed *ex vivo* miR-324-null BMM and osteoclast dysregulation.

6.4 Summary

In this chapter I have identified novel targets of miR-324 in three cell types; osteoblasts, BMMs and osteocytes. For all of these I have validated putative target genes using 3'UTR-luciferase assays and mutated the predicted miR-324 binding sites to confirm that the regulation is direct at those binding sites.

Target prediction in osteoblasts and subsequent validation using 3'UTR-luciferase assays revealed two novel direct targets of miR-324; *Runx2* and *Cxcl12*-γ. Despite all three isoforms of *Cxcl12* being upregulated in miR-324-null osteoblasts, only *Cxcl12*-γ was validated as a direct target, both of miR-324-5p and -3p. This therefore raised the potential that the miR-324-mediated upregulation of *Cxcl12*-γ may result in dysregulation of the other isoforms as well. The use of adipo-osteogenesis co-differentiation assays and Cxcl12-α stimulation showed that this was indeed the case; when stimulated with Cxcl12-α chemokine, C3H10T1/2 cells showed an upregulation in *Cxcl12*-α, -β and -γ. Cxcl12-α stimulation also upregulated the other direct miR-324 target, *Runx2*, under these conditions and additionally *Runx2* upregulated the expression of *Cxcl12*-α, although not *Cxcl12*-β or -γ. Both of these conditions resulted in upregulated osteogenesis and decreased adipogenesis, recapitulating the *in vivo* miR-324-null phenotypes observed in Chapter 4 and 5. Remarkably, both *Runx2* overexpression and Cxcl12-α stimulation also resulted in spontaneous osteogenesis when in normal primary cell growth media (unsupplemented with osteogenic or adipogenic factors), and the effect resulting from Cxcl12-α stimulation looked to be due to the downstream increase in *Runx2* expression. This therefore suggests that *Runx2* is the effector of the miR-324-null phenotype rather than *Cxcl12*, which is perhaps unsurprising considering that *Runx2* is widely considered the master transcription factor in osteogenesis [217, 218].

Four novel miR-324 target genes were identified and validated in BMMs; *Pdgfa*, *Pin1*, *App* and *Ptgs1*. miR-324-null BMMs show a strong inhibition in the capacity to undergo osteoclastogenesis relative to WT controls. Strikingly, 3 of the 4 miR-324 BMM target genes have been previously discussed in the literature in relation to osteoclastogenesis. *App* is widely thought of as only having importance in brain tissues, but in fact mice carrying the App_{Swe} mutant *App* allele show an osteoporotic phenotype due to increased osteoclast activity [519, 520]. Therefore it is entirely conceivable that upregulation of *App*, as is found in miR-324-null BMMs, would have the opposite effect, which is to say an inhibition of

osteoclastogenesis. *Pdgfa* has also been linked to osteoclastogenesis, in that its expression over the course of the differentiation is severely repressed, after an early peak [522]. The fact that *Pdgfa* is dysregulated above these levels in miR-324-null BMMs and osteoclasts indicates defects in the osteoclastogenesis process, even if it does not necessarily imply that *Pdgfa* upregulation is directly causal of the impairment observed in miR-324-null mice. Finally, *Pin1* has been implicated as a repressor of *Dcstamp*, a key gene in osteoclast fusion; *Pin1*-null mice display a severe upregulation of *Dcstamp*, resulting in larger osteoclasts, each containing a higher number of nuclei, than WT samples, resulting from the fusion of a greater number of cells [521]. It is therefore likely that the increased *Pin1* expression levels observed in miR-324-null BMMs directly results in decreased *Dcstamp* expression, confirmed by RNA-seq, which in turn reduces osteoclast fusion, contributing to the osteoclast deficiency observed in miR-324-null mice.

Osteocytes are cells essential to the normal regulation of bone remodelling and are differentiated from osteoblasts embedded in their own bone matrix, a process known as osteocytogenesis [225, 226]. In this chapter, I showed that key osteocyte and osteoblast genes are dysregulated in osteocytes obtained from the leg bones of miR-324-null mice; *Alpl* and *Bglap* are significantly upregulated and *Csf1*, *Mepe* and *Phex* are significantly downregulated in miR-324-null osteocytes. From these expression changes, I concluded that miR-324-null osteocytes appear to display an immature phenotype, where the osteocyte marker genes, *Mepe* and *Phex*, are dramatically reduced in expression, whereas the genes also expressed by osteoblasts, *Alpl* and *Bglap*, are upregulated. *Csf1* is also downregulated in miR-324-null osteocytes and considering that osteocytes are an important source of the *Csf1* protein product, M-CSF, in order to stimulate osteoclastogenesis, I suggested that this deficiency in miR-324-null osteocytes may contribute to the osteoclast deficiency observed in miR-324-null samples. I subsequently utilised the TargetScan miRNA target prediction algorithm [5, 67] in addition to the osteocyte active transcriptome, a set of genes recently identified as being enriched in osteocytes [216], to identify miR-324 targets potentially important to osteocyte biology. Following 3'UTR-luciferase assay validation, *Hoxa9* and *Samd5* were identified as direct miR-324 target genes, in addition to *Cxcl12*-γ, which had already been identified as an osteoblast target. By utilising MLO-Y4 cells [354], I showed that overexpression of each of *Hoxa9* and *Samd5* was sufficient to induce part of the gene dysregulation observed in miR-324-null osteocytes; *Samd5* overexpression repressed *Csf1* and *Hoxa9* overexpression both

downregulated *Csf1* expression and upregulated *Bglap* expression. Stimulation with the Cxcl12-α chemokine did not affect the expression of any tested osteocyte genes in MLO-Y4 cells. However, it may be involved in the regulation of *Phex* or *Mepe*, which were not expressed at detectable levels in MLO-Y4 cells. Alternatively, considering the immature osteocyte phenotype observed in miR-324-null mice, it is conceivable that *Cxcl12*-γ really is just an osteoblast target, but the inability of miR-324-null osteocytes to complete osteocytogenesis results in the osteoblastic regulation of *Cxcl12*-γ still being in place in these cells, but not in WT controls.

In summary, I have shown that miR-324 directly targets key genes in osteoblasts, osteocytes and in osteoclastogenesis. The dysregulation of these targets in miR-324-null mice results in excessive osteogenesis and impaired adipogenesis (due to severe upregulation of the master osteogenic transcription factor *Runx2*), osteoclastogenesis and likely osteocytogenesis as well. miR-324 therefore modulates the expression of multiple targets in all three key cells involved in bone remodelling, osteoblasts, osteocytes and osteoclasts, which each may interact with other targets, thus producing a complex regulatory system. Each bone cell also exerts regulatory activity on the other bone cells, thus meaning that although miR-324 in general only modulates its target transcripts by a modest degree, the cumulative dysregulation produced upon its deletion is severe.

Chapter 7 - General discussion

7.1 Summary of results

microRNAs (miRNAs) are short RNA molecules which do not encode proteins, but instead are incorporated into RNA-induced silencing complexes (RISCs), which is guided by the miRNA to target messenger RNA (mRNA) species, inducing destabilisation and translational inhibition [1-3, 20, 21]. It has been estimated that more than 60% of all protein-coding human mRNAs are regulated by at least one miRNA through this mechanism [7]. miR-324 is a miRNA predicted to target a large number of genes [5, 67] and has previously been evidenced in the literature to play a role in the brain [111, 112], cartilage [151, 187, 188] and bone [151, 316-319]. I therefore utilised the miR-324-null mice, which harbour a 133 bp global knockout at the *Mir324* locus, in order to investigate whether there was any function of miR-324 in cartilage, bone or brain tissue *in vivo*.

With regard to miR-324 in brain tissue, I showed in Chapter 3 that miR-324-null mice displayed a hippocampal hyperexcitability phenotype *ex vivo*, consisting of an increased frequency of interictal discharges (IIDs) and abnormal spikes in the local field potential (LFP), both of which are indicative of epileptic seizures. I therefore concluded that the hippocampal networks which regulate normal oscillatory activity may be impaired in miR-324-null mice. I also showed that, although no evidence of convulsive seizure activity was observed in miR-324-null mice, a decreased mean step length and increased number of maximum rears per minute was observed *in vivo* utilising the MouseTrapp behavioural testing system [334], the latter of which is frequently observed in murine models of epilepsy [367-369]. Additionally, I showed through RNA sequencing (RNA-seq) in the murine hippocampus and neocortex that the gene causal of a specific form of epilepsy known as pyridoxal phosphate-dependent epilepsy (PPDE), *Pnpo* [377, 378], was significantly downregulated in the miR-324-null hippocampus relative to WT hippocampi. Furthermore, I showed that two predicted miR-324-5p targets according to TargetScan [5, 67] were both significantly upregulated in miR-324-null hippocampal and neocortical samples; *Suox*, the gene causal of isolated sulfite oxidase deficiency (ISOD) [381], and *Cd300lf*, which is involved in the regulation of immune response to infection and may play a role in maintenance of the blood-brain barrier [385-387]. I subsequently demonstrated that both of these genes were direct targets of miR-324-5p, through the utilisation of 3'UTR-luciferase assays. I therefore suggested that the *ex vivo* hippocampal hyperexcitability and *in vivo* abnormal behaviour phenotypes observed in miR-324-null mice may be downstream consequences of the dysregulation of these two target genes.

In Chapter 4, I showed that miR-324-null mice displayed differences in terms of cartilage damage. Through the use of the Osteoarthritis Society International (OARSI) histopathological scoring system [164], I demonstrated that miR-324-null mice aged 5-months showed a significant increase in knee cartilage damage relative to WT controls, following destabilisation of the medial meniscus (DMM) surgery. Furthermore, I showed that miR-324-null mice aged 14-months spontaneously showed a significant increase in cartilage damage relative to WT controls. I concluded from the observed increased cartilage damage phenotype that a dysregulation of the Indian Hedgehog (Ihh) signalling pathway was likely responsible, considering that miR-324-5p has been previously demonstrated to regulate the important Ihh gene *Gpc1* [151], and increased Ihh activity has been shown to result in an increased cartilage damage phenotype [189-192].

miR-324-null mice also display a severe high bone mass phenotype, most strikingly consisting of increased trabecular and cortical thickness and a high bone tissue mineral density (TMD; Chapter 4). Despite this increase in thickness however, miR-324-null bone is not necessarily more structurally stable, considering that the structure model index (SMI) is increased in miR-324-null mice [434]. This hypothesis is supported by the fact that miR-324-null mice also show increased tibial bowing, usually observed when bones are weaker. Utilisation of alizarin red-S/calcein green double-injections demonstrated that miR-324-null mice showed an increased bone formation rate (BFR), due to either increased osteoblast-mediated bone formation activity, an increased number of osteoblasts, or both. A severe lack in lipid droplets was also identified in miR-324-null tibiae relative to WT controls, supporting the increased osteoblast number hypothesis; perhaps an increased number of mesenchymal stromal cells (MSCs) were committing to the osteochondroprogenitor lineage in miR-324-null bone marrow, resulting in more osteoblasts and fewer adipocytes. Interestingly however, I showed that the osteocyte density in miR-324-null tibial bone is reduced relative to WT controls. This suggested some defect in osteocytogenesis, considering that an increase in osteoblasts would be expected to result in an increase in osteocytogenesis, in addition to the other potential osteoblast fates, thus theoretically resulting in an enlarged osteocyte population. I also demonstrated that miR-324-null mice display significantly fewer mature osteoclasts, through the use of Tartrate-resistant acid phosphatase (TRAP)-staining, which would be presumed to result in increased bone mass, as would the increased osteoblast-mediated bone formation.

In order to investigate whether these *in vivo* bone phenotypes could also be observed *ex vivo*, haematopoietic stromal cells (HSCs) and osteoblasts were isolated and cultured from miR-324-null and WT hind leg bone marrow and bone fragments, respectively (Chapter 5). By stimulating the HSCs with RANK-L and M-CSF, I demonstrated that miR-324-null cells were severely impaired in terms of osteoclastogenesis; the number of mature multinucleate osteoclasts in miR-324-null samples was severely reduced relative to WT controls. Furthermore, RNA-seq experiments comparing miR-324-null and WT osteoclasts and bone marrow macrophages (BMMs; a negative control stimulated with M-CSF but not RANK-L) revealed that over 30% of all genes tested were significantly dysregulated in both miR-324-null BMMs and osteoclasts (adjusted p-value ≤ 0.05). I therefore concluded that miR-324-null may show potential defects in other cells of the haematopoietic lineage in addition to the high bone mass bone phenotype identified in Chapter 4. By utilising data from the BMM RNA-seq and filtering it using the TargetScan algorithm [5, 67], I showed that *Pdgfa*, *Pin1*, *Ptgs1* and *App* were upregulated in miR-324-null samples and by utilising 3'UTR-luciferase assays I showed they were direct targets of miR-324.

By stimulating osteoblasts with osteogenic media, I demonstrated that approximately 20% of all genes tested were significantly dysregulated by *Mir324* deletion in osteoblasts, including upregulation of the master osteogenesis transcription factor *Runx2* and osteogenesis marker genes such as *Col1a1* (Chapter 5). By utilising the TargetScan algorithm [5, 67], I also showed that *Runx2* was a direct target of miR-324, as was another gene, *Cxcl12*, which encodes a chemokine implicated in both osteogenesis and adipogenesis [304]. Osteoblasts isolated from murine calvariae also revealed that an increased amount of mineralised bone matrix was produced by miR-324-null osteoblasts relative to WT controls, and that transfection of miR-324-5p and -3p mimics to restore physiological levels was able to rescue this excess mineralised bone phenotype. From this I concluded that regardless of whether more osteoblasts are present in miR-324-null mice, they are more active in terms of bone formation. However, I showed using miR-324 mimics and hairpin inhibitors that in the murine C3H10T1/2 MSC-like cell line, under adipo-osteogenic (AdiOst) co-differentiation conditions [355], reduced miR-324 levels resulted in increased commitment to the osteogenic lineage at the expense of adipogenesis, whereas increased miR-324 levels resulted in decreased osteogenesis, but increased adipogenic lipid production. miR-324 therefore affects both commitment to the osteoblast lineage and osteoblastic bone formation activity.

In order to further investigate the reduced osteocyte density phenotype I identified in Chapter 4, I isolated osteocyte RNA from the hind leg bones of miR-324-null and WT mice (Chapter 6). Notably, miR-324-null osteocytes displayed dysregulation of several osteoblast and osteocyte marker genes; *Alpl* and *Bglap* were significantly upregulated in miR-324-null osteocytes, whereas *Csf1*, *Mepe* and *Phex* were all significantly downregulated. I utilised the osteocyte active transcriptome [352] and the TargetScan algorithm [5, 67] to identify a subset of putative osteocyte targets to test using RT-qPCR, from which I used 3'UTR-luciferase assays to demonstrate that *Hoxa9*, *Samd5* and *Cxcl12* were direct miR-324 osteocyte target genes. Furthermore, I showed that *Hoxa9* and *Samd5* overexpression in the osteocyte model cell line MLO-Y4 [354] resulted in a similar dysregulation of *Bglap* and *Csf1* as was observed in miR-324-null osteocytes. I therefore concluded that the dysregulation of these marker genes in miR-324-null osteocytes was likely to be due to upregulation of *Hoxa9* and *Samd5*, and this may be causal of the reduced osteocyte density phenotype observed in Chapter 4, through inhibition of osteocytogenesis.

In this chapter, I will discuss important topics explored throughout this project. I will explore questions which remain unanswered, and I will highlight where I believe further work is required in regard to miR-324.

7.2 miR-324-null mice may harbour dysfunctional mitochondria

My data show that miR-324-null mice display increased hippocampal hyperexcitability *ex vivo* and increased rearing *in vivo*, a phenotype which is also related to increased excitability and seizure events [367-369]. I demonstrated that *Suox* and *Cd300lf* were direct targets of miR-324 in the hippocampus and neocortex, and suggested that the hyperexcitability phenotype may be a direct result of the dysregulation of these genes; mutations in *Suox* are causal of ISOD [381] and *Cd300lf* may play a role in maintaining the blood-brain barrier [385-387]. However, these are unlikely to be the only targets regulated by miR-324 in hippocampal and neocortical tissue and therefore it is possible that neither are responsible for the observed miR-324-null phenotypes. An alternative possibility is that the hyperexcitability is a result of dysregulated mitochondrial activity, considering that in both humans and rodents mitochondrial dysfunction has been demonstrated to be causal of hyperexcitability [534-536]. Mitochondrial biology does indeed appear to be dysregulated in miR-324-null bone cells; in the RNA-seq of BMMs, "Mitochondrial translation" was significantly enriched using Gene Ontology (GO) analysis and in both osteoblasts and osteoclasts, "Mitochondrial respiratory

chain complex I assembly" was significantly enriched. *Mir324* is encoded from a locus antisense to an intron of *Acadvl*, an important mitochondrial gene which catalyses the metabolism of very long-chain fatty acids [537, 538]. However, I showed that in terms of protein, deletion of *Mir324* affected neither Acadvl nor Dvl2, which is also encoded proximal to the *Mir324* locus, using hippocampal tissue protein lysate. This does not mean that miR-324 does not regulate mitochondrial biology, however, and there may be other direct targets which affect mitochondrial activity. Interestingly, despite the expected effect of mitochondrial dysregulation in the brain closely mirroring the hyperexcitability observed in miR-324-null mice, the effect in the bone does not. In fact, mitochondrial dysfunction would be expected to produce a low bone mass phenotype, similar in many ways to osteoporosis. Mice conditionally lacking *Htra2*, which encodes a mitochondrial serine protease purported to regulate the misfolding of mitochondrial proteins [539], in all non-neuronal tissues lose an increasing amount of bone with age [540]. Similarly, mice containing a mutant *Polg* gene, which encodes the only mitochondrial polymerase [541], in which the proof-reading domain is defective, display increased bone resorption and decreased bone formation *ex vivo*, with a low bone mass phenotype *in vivo* [542]. My data show that miR-324-null mice display a high bone mass phenotype in addition to reduced fat, quite the opposite of osteoporosis. There are therefore two potential explanations for these results, the first of which is that there is no mitochondrial dysfunction in miR-324-null bone cells; GO enrichment analyses undertaken on the hippocampal and neocortical RNA-seq experiments(shown in Appendix D) show no enrichment of mitochondrial GO terms, unlike enrichment analyses undertaken for the bone RNA-seq experiments. If there actually is no effect of *Mir324* deletion on mitochondrial biology then then this would explain why miR-324-null mice display a high bone mass phenotype, rather than the osteoporotic *Htra2*-null and *Polg*-null phenotypes. Alternatively, the second explanation is there is some level of mitochondrial dysfunction in miR-324-null mice, but in the skeleton the direct impact of upregulated bone formation and downregulated bone resorption, through dysregulation of miR-324 target genes, is sufficient to overcome this. Perhaps in the hippocampus and neocortex, there are no miR-324 direct targets which act with enough strength when dysregulated to overcome the effect of even a mild mitochondrial dysfunction. Further investigation of this is essential, for example by assessing mitochondrial function and respiration between cells of each genotype, using Oroboros or Seahorse assays, in order to conclusively demonstrate the origins of the hyperexcitability phenotype [487, 543].

7.3 Impaired osteoclastogenesis is likely one of many haematopoietic lineage activities affected by lack of *Mir324*

In this project I showed that miR-324-null mice present with an osteoclast deficiency *in vivo* and severely impaired osteoclastogenesis *ex vivo*. Furthermore, I demonstrated that over 40% of all genes tested were significantly dysregulated in miR-324-null osteoclasts (adjusted p-value ≤ 0.05) and more than half of these were also dysregulated in BMMs, for which almost 35% of all genes tested were significantly dysregulated. This illustrates clearly that the dysregulation observed in miR-324-null osteoclasts is not solely present during the process of osteoclastogenesis; many of the dysregulated genes are also present in BMMs, which are the precursor cells to osteoclasts, raising the question of how deep into the haematopoietic lineage does this dysregulation originate? The fact that such a large number of genes are dysregulated in miR-324-null BMMs indeed raises the possibility that the precursor cells of BMMs, HSCs themselves, may also display miR-324-null-mediated dysregulation. Therefore, it is reasonable to assume that all cells of the haematopoietic lineage would show dysregulation due to lack of *Mir324*. Conditional lack of *Dicer* in HSCs, utilising the *Mx*-Cre driver to delete *Dicer* when mice were injected with the immunostimulant Polyinosinic:polycytidylic acid [544], demonstrated that miRNA regulation of the haematopoietic lineage is essential to normal HSC differentiation and activity [545]. Although miR-324 is a single miRNA, compared to the theoretical near-complete ablation of all mature miRNAs upon deletion of *Dicer* [546, 547], it may play important regulatory roles in the haematopoietic lineage, as is the case with several other murine miRNAs. For example, miR-125a overexpression results in an upregulation of HSC number and a downregulation of HSC apoptosis *in vivo* [545] and the ectopic expression of either miR-29a or miR-125b results in an increased HSC proliferation rate and eventual development of acute myeloid leukaemia [548, 549]. In order to test whether miR-324 produces similar effects to these miRNAs, it would be highly beneficial to undertake an RNA-seq experiment between miR-324-null and WT HSCs to understand whether the high level of dysregulation observed in BMMs and osteoclasts is really also present at the HSC stage. Additionally, it would be useful to investigate other haematopoietic-derived biological activities, such as the immune response, in which HSC-derived cells such as neutrophils and phagocytes play important roles [550, 551], and erythropoiesis, through which red blood cells are produced [552]. The quantities or behaviours of these cells in miR-324-null and WT mice could be measured initially from tissue biopsies, so as to elucidate which of these should be further investigated *in vivo*.

An additional consideration in relation to the haematopoietic dysregulation observed in miR-324-null mice is that this dysregulation may not be a direct effect of *Mir324* deletion on the haematopoietic lineage at all. The adipocyte-derived lipids found in bone marrow have been demonstrated to have a supportive role in HSC proliferation, despite adipocytes being derived from the mesenchymal lineage [481]. This effect would likely be driven by adipocyte-secreted factors such as adiponectin and leptin, both of which promote HSC proliferation [478-480]. This decreased proliferation would likely affect the expression of important genes for haematopoietic differentiation due to an altered local environment, in terms of a decreased HSC population. It is therefore possible that the dysregulation observed in miR-324-null osteoclasts and BMMs, in addition to the disruption I have hypothesised to occur in other haematopoietic lineage-related biological processes in miR-324-null mice, could merely be as a result of the lack of fat in miR-324-null bone marrow; the dysregulation would therefore act as a memory of an incorrect niche from an early stage of differentiation. My data demonstrated that the lack of lipid droplets in miR-324-null mice was due to a decrease in adipogenesis, which in turn was primarily due to upregulation of the miR-324-5p target gene *Runx2* (summarised in Figure 7.1). Therefore, if lack of fat is the reason for the observed miR-324-null haematopoietic dysregulation then miR-324-null mice demonstrate direct regulation of the haematopoietic lineage due to dysregulation of a mesenchymal target gene. However, a key limitation to this theory is that I have only investigated lipid droplets in miR-324-null mice at the 14-month time point at present. It therefore remains unknown whether the decreased lipid droplet phenotype holds true in younger mice too, as this purported mechanism necessitates.

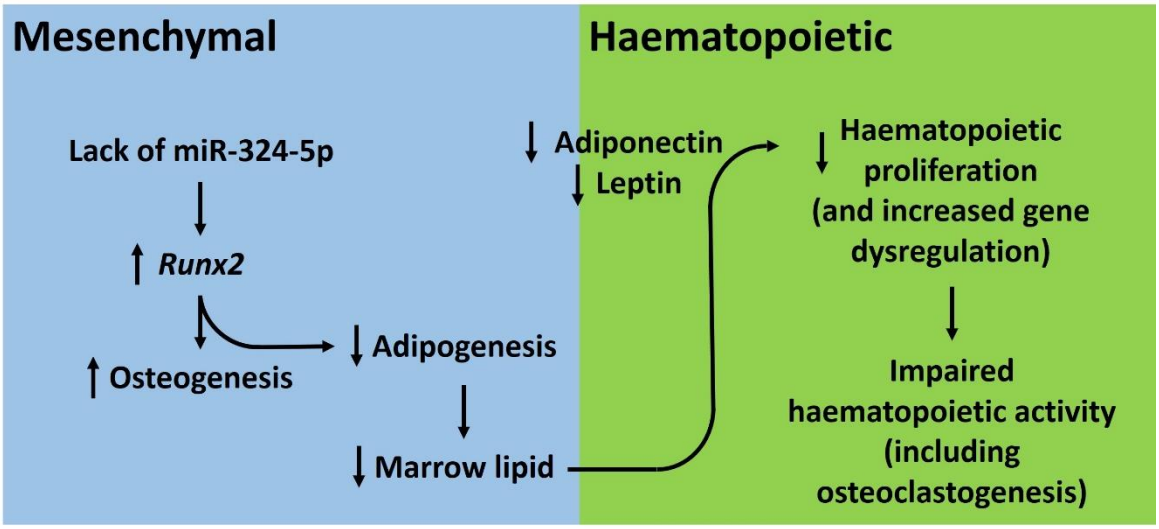

Figure 7.1 - Reduced adipogenesis in bone marrow MSCs may contribute to the impaired osteoclastogenesis phenotype of miR-324-null BMMs. My data demonstrated that deletion of *Mir324* upregulated the direct miR-324-5p target gene *Runx2*. This led to increased osteogenesis and reduced adipogenesis in the mesenchymal lineage, resulting in the reduced levels of bone marrow lipid observed in miR-324-null tibiae *in vivo*. It has been proposed in the literature that reduced adipocyte-derived adiponectin and leptin in the bone marrow results in decreased proliferation of HSCs [478-480], which would influence haematopoietic differentiation through reduction of the local HSC population number. Therefore, it is possible that the gene dysregulation and impaired osteoclastogenesis observed in miR-324-null mice is due to an altered niche at the HSC level, ultimately caused by an upregulation of *Runx2* in the mesenchymal lineage.

7.4 The excess bone formation phenotype in miR-324-null mice is effected through *Runx2* rather than *Cxcl12*

I showed that miR-324-null osteoblasts form more bone than WT controls, both *in vivo* and *ex vivo*. By utilising target prediction and 3'UTR-luciferase assays I subsequently demonstrated that *Cxcl12* and *Runx2* are both direct targets of miR-324. When *Runx2* was overexpressed or cells were stimulated with Cxcl12-α, bone formation was increased. However, Cxcl12-α stimulation always upregulated *Runx2*, which is presumably how *Cxcl12* can produce this effect on bone formation. Therefore, Runx2 appears to be the effector in this pathway. This positive regulation of *Runx2* by Cxcl12 has been observed previously in the literature, although not discussed to a great extent; mice conditionally lacking *Cxcl12* in developmental limb mesenchymal cells, under the *Prx1*-Cre driver, resulted in significantly reduced *Runx2*

expression in addition to reduced bone mass and increased marrow adiposity [304], essentially the opposite phenotype to that of miR-324-null mice, in which *Cxcl12* is upregulated. As would be expected of a regulatory gene rather than the actual effector gene, these limb mesenchymal-specific *Cxcl12*-null mice are viable, unlike many *Runx2* knockout mice; in global *Runx2*-null mice, ossification of the rib bones is unable to occur due to a lack of mature osteoblasts, resulting in death immediately after birth from an inability to breathe [421]. Conditional *Runx2* knockout mice under either the *Prx1*-Cre or *Col1a1*-Cre driver present with the identical perinatal lethality to global *Runx2*-null mice [553, 554]. Comparison of the conditional *Runx2* and *Cxcl12* knockout models therefore supports the proposed role of *Runx2* as the effector of the miR-324-null increased bone formation phenotype whilst *Cxcl12* is a modulator of it through regulation of *Runx2*; whilst *Cxcl12* is not required for differentiation and maturation of osteoblasts, despite being a potentially important regulatory component of the network, *Runx2* is essential for functional osteoblast-mediated bone formation, hence mice lacking *Runx2* completely lack osteoblasts, whereas mice lacking *Cxcl12* merely present with a bone formation deficiency. The precise effect of *Cxcl12* in bone formation and other mesenchymal lineage pathways is not as well defined as it is for *Runx2*, but presumably it binds the same receptors as it does in the haematopoietic lineage, Cxcr4 and Ackr3 (CXCR4 and CXCR7 in humans), through which it induces the migration of bone marrow progenitor cells [509, 510]. More investigation is therefore required to understand how the increased expression of *Cxcl12* in the mesenchymal lineage, presumably resulting in increased Cxcl12-receptor binding, results in a downstream upregulation of *Runx2* in miR-324-null mice.

7.5 The relationship between miR-324 and osteocytes

This project identified a decreased number of osteocytes per bone area in miR-324-null mice and that *Alpl*, *Bglap*, *Csf1*, *Mepe* and *Phex* were all significantly dysregulated in miR-324-null osteocytes relative to WT controls. Additionally, I identified that *Cxcl12*-γ, *Hoxa9* and *Samd5* were all direct miR-324 osteocyte targets and that in the MLO-Y4 osteocyte model cell line [555], overexpression of *Hoxa9* and *Samd5* replicated the dysregulation of *Bglap* and *Csf1* observed in miR-324-null osteocytes. Stimulation with Cxcl12-α however did not significantly dysregulate any genes which were dysregulated in miR-324-null osteocytes *in vivo*. From this I therefore concluded that the upregulation of *Hoxa9* and *Samd5* was sufficient to produce some of the dysregulation observed in miR-324-null osteocytes, but did not explain the

upregulation of *Alpl*. The cause of the *in vivo* dysregulation of *Mepe* and *Phex* is also currently unknown, and is impossible to discern from the MLO-Y4 cell line, considering that these cells do not express either of these genes at detectable levels using RT-qPCR, which is the most important limitation about this line of experiments. It will therefore be essential in future work to isolate and culture osteocytes from miR-324-null and WT mice, such that the effect of overexpressing *Hoxa9*, *Samd5* and *Cxcl12* on *Mepe* and *Phex* can be elucidated. Furthermore, this will allow the use of a high-throughput RNA-seq approach to identify further dysregulation and novel miR-324 targets in osteocytes, as this was not possible using the RNA of osteocytes extracted directly from bone herein. This is an important experiment to undertake, as the utilisation of an RT-qPCR screen as was used in this project is likely to have missed many targets which were not annotated to the osteocyte active transcriptome, or discarded due to other filters applied.

Due to the limitation of MLO-Y4 cells in regard to osteocyte gene expression, this cell line also cannot be definitively relied upon to mimic *in vivo* osteocyte biology. The most notable limitation in regard to this is the fact that MLO-Y4 cells are immortalised during the process of osteocyte differentiation and therefore the process of osteocytogenesis as a whole cannot be investigated using these cells. Nonetheless, the dysregulation observed upon *Hoxa9* and *Samd5* overexpression is suggestive of an immature osteocyte, which could explain why miR-324-null tibiae showed a reduced osteocyte density. In order to understand these changes more completely, a model of osteocytogenesis is required. Ideally, this would be undertaken using osteoblasts isolated from miR-324-null and WT bones, and subsequently stimulating these cells to initiate osteocytogenesis. However, this process is not understood well enough to allow for *ex vivo* stimulation as can be undertaken for osteogenesis and osteoclastogenesis, and factors to promote this differentiation in similar ways to RANK-L (for osteoclastogenesis) and β-glycerophosphate and L-ascorbic acid (for osteogenesis) remain elusive at present [225, 556]. Therefore an *in vitro* murine cell model such as the MLO-A5 cell line [557] is still the best alternative, despite being developed over two decades ago. MLO-A5 cells are immortalised at a pre-osteocyte but post-osteoblast stage of differentiation, at the point where an osteoblast has become embedded in osteoid but has not yet mineralised the matrix surrounding it. These cells therefore are likely the most representative model of the point at which osteocytogenesis begins, and so are the best cells to use in order to test the effects of miR-324 target overexpression at the point of commitment to osteocytes.

7.6 miR-324-null mice display wide-reaching skeletal dysregulation

Despite the fact that the bone-related experiments I have undertaken in this project have generally focused on only one component of the skeletal system at a time, it is important to appreciate that the skeletal system is not segregated in such a fashion *in vivo*. Therefore, in order to gauge an overview of the abnormal activity in miR-324-null skeletal system as a whole, it is essential to compile the results from each section together into a complete model, shown in Figure 7.2. This model allows testable predictions to be made, enabling future work to fully elucidate how the abnormal activity or gene expression identified in BMMs, osteoclasts, osteoblasts and osteocytes affects the overall high bone mass phenotype in miR-324-null mice.

Whilst it is not uncommon for a miRNA to affect a component of skeletal biology, the scale of the dysregulation throughout the skeletal system upon *Mir324* deletion is surprising, especially considering that miR-324-null mice are viable, born at expected Mendelian ratios and survive with normal longevity. In most bone-related miRNAs, it is unusual for more than one component of bone remodelling to be altered. For example, miR-185-null mice display an upregulation of the miR-185 direct target gene *Bgn*, encoding the skeletal proteoglycan biglycan [296, 297]. Bgn is an enhancer of *Bmp2*, one of the most important bone morphogenetic proteins (BMPs) in the bone formation process, and therefore this dysregulation results in an upregulation of osteoblast-mediated bone formation [298]. However, there is no evidence that deletion of *Mir185* has any concurrent effect on osteoclast activity or formation [296]. miR-21-null mice display increased bone volume, bone mineral density and trabecular thickness in addition to a reduction in osteoclast activity, purported to occur through dysregulation of *Pdcd4*, an inhibitor of osteoclastogenesis [558, 559]. Despite miR-21 overexpression previously having been demonstrated to also increase osteogenesis *in vitro* through regulation of the negative regulator of osteogenesis *Spry1* [560], this effect was not observed *in vivo*, and therefore again this miRNA acts only on one component of bone remodelling *in vivo*. Unlike miR-21, miR-324 produces similar effects *in vivo* as *in vitro* or *ex vivo*; the increased commitment to osteogenesis in preference to adipogenesis was observed both *in vivo* and *in vitro* by utilising C3H10T1/2 cells. Additionally, the dysregulation of *Csf1* and *Bglap* observed in miR-324-null osteocytes was successfully modelled in MLO-Y4 cells by the overexpression of the miR-324 target genes *Hoxa9* and *Samd5*. miR-324-null cells of the haematopoietic lineage also displayed the same impaired osteoclastogenesis phenotype *ex*

vivo as was observed *in vivo* in tibial sections stained for TRAP. Therefore, it can be confidently stated that osteoblasts, osteocytes and osteoclasts all display abnormalities in miR-324-null mice relative to WTs.

It is likely that the unusual magnitude of skeletal dysregulation observed in miR-324 mice is largely a result of the uncoupling of bone resorption to bone formation; in WT animals, osteoblasts and other cells of the mesenchymal lineage communicate with osteoclast precursors through the secretion of factors such as RANK-L and M-CSF, thereby upregulating bone resorption when bone formation is increased [199-205]. Similarly, a high level of osteoclast-mediated bone resorption releases TGF-β1 and IGF-1 from the bone matrix, which act to recruit mesenchymal precursors to the resorption area and induce osteogenesis in order to effect increased bone formation [561, 562]. My data show that miR-324-null osteocytes express lower levels of *Csf1* than WT controls, thus limiting the osteocyte-driven coupling of mesenchymal-derived bone cells to osteoclasts. It is also possible that the osteoclast-driven component of the coupling is also impaired; miR-324-null osteoclasts express significantly higher levels of both *Tgfb1* and *Igf1* than WT osteoclasts (log_2 fold-changes = 0.47 and 2.73, respectively; adjusted p-values = 6.14×10^{-3} and 1.13×10^{-187}, respectively), although this was not discussed in earlier sections. This increase in both factors is likely sufficient to overcome the necessity of osteoclasts to resorb bone in order to regulate osteogenesis; despite the immaturity of miR-324-null osteoclasts, they are constitutively expressing and presumably secreting high levels of *Tgfb1* and *Igf1*, hence such a striking increase in osteoblast-mediated bone formation despite osteoclastogenesis remaining so low (Figure 7.3). Of course, this requires further investigation to determine whether the excessive osteoclastic expression of *Tgfb1* and *Igf1* actually translates into higher secreted levels of TGF-β1 and IGF-1, for example using western blotting for these proteins or staining bone sections and investigating whether TRAP-positive miR-324-null osteoclasts co-localise with areas of high TGF-β1 and IGF-1 in the bone marrow environment. However, the high levels of the genes encoding these proteins is at the very least suggestive that this may be the uncoupling mechanism in the miR-324-null skeletal system. There was not sufficient time to assess the levels of TGF-β1 and IGF-1 during this project, but it would be beneficial to investigate this in future studies.

It is notable that in the literature, a positive correlation has previously been identified between human miR-324-3p serum abundance and BMD [317], whereas here I showed that mice lacking *Mir324* displayed an increased TMD. A potential explanation for this discrepancy

is that the increase in miR-324-3p levels in serum is a result of selective secretion of miR-324 from cells such as osteoblasts, such that the levels of miR-324 in osteoblasts is actually decreased, although the levels in serum are increased. Additionally, miR-324-3p levels were previously demonstrated to be decreased in patients with osteoporotic fractures [318]. In this project, I showed that miR-324-null mice display increased bone formation, which would be expected to result in a lower fracture risk. This correlation could be explained similarly to the correlation between serum abundance and BMD, but there is an additional alternative explanation for fracture risk; in addition to a high bone mass, I showed that miR-324-null mice also display an increased trabecular structure model index (SMI), which is interpreted as a less structurally stable rod-like trabecular structure [434]. Potentially therefore, miR-324-null bones may be more likely to fracture, despite being higher in mass, a hypothesis supported by the fact that increased bowing is observed in miR-324-null mice. A three-point bending would conclusively demonstrate whether miR-324-null mice do indeed show a decreased resistance to bending [437].

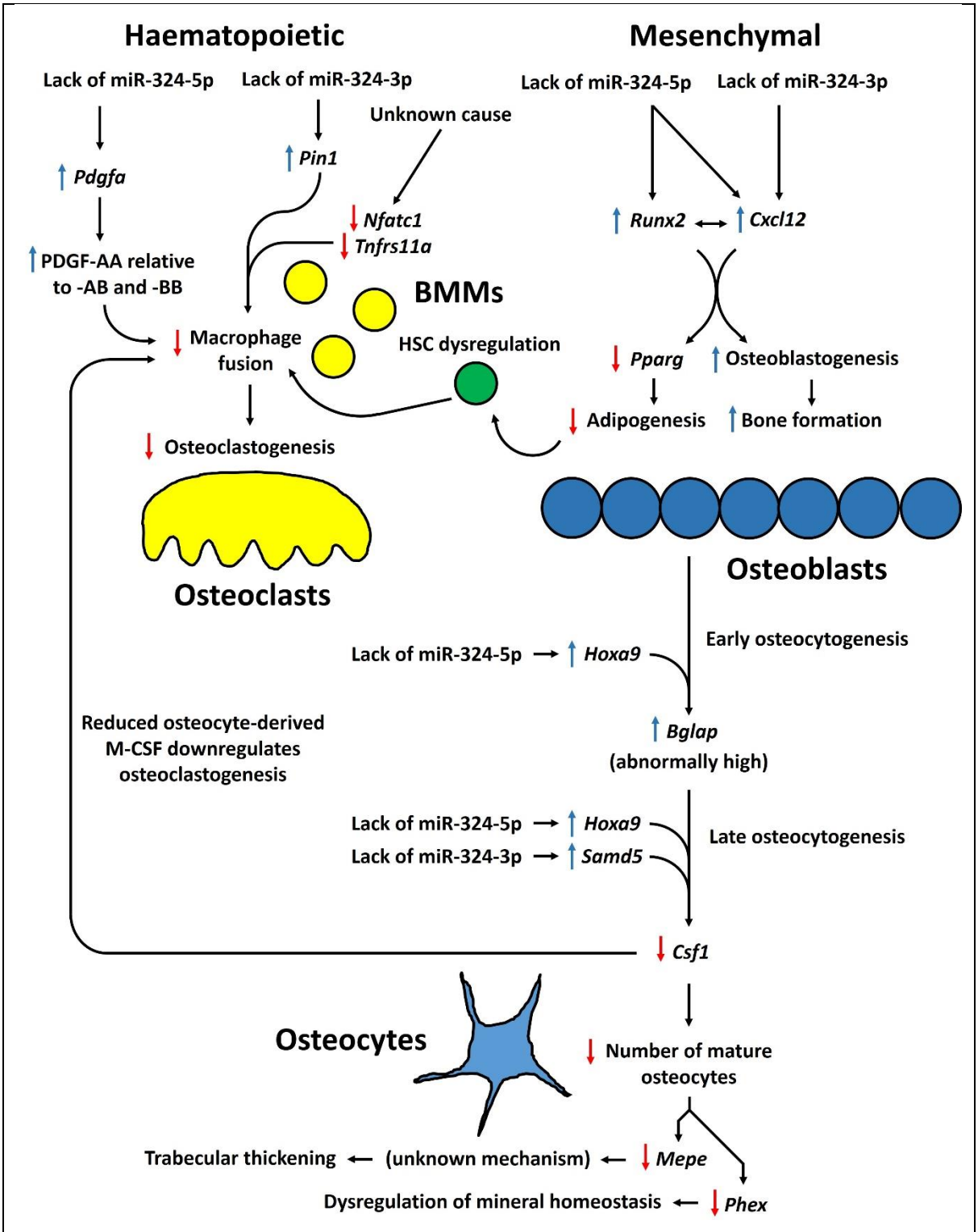

Figure 7.2 - Proposed model of the skeletal system in miR-324-null mice. In the mesenchymal lineage, dysregulation of the miR-324 target genes *Cxcl12* and *Runx2* results in increased osteogenesis and reduced adipogenesis, the latter of which has been suggested to negatively impact the haematopoietic stromal cell niche in the literature [478-481]. Of the mature osteoblast population, some differentiate into osteocytes, although this process is likely stunted in miR-324-null mice due to the dysregulation of the direct miR-

324 target genes *Hoxa9* and *Samd5*, which cause upregulated *Bglap* levels and downregulated *Csf1* levels, ultimately leading to a decreased number of mature osteocytes, as observed in miR-324-null mice *in vivo*. These immature miR-324-null osteocytes express reduced levels of the osteocyte marker genes *Mepe* and *Phex*, which have been shown to result in trabecular thickening and dysregulated mineral homeostasis, respectively [255, 256, 563, 564]. In the haematopoietic lineage, *Mir324* deletion results in dysregulation of the direct target genes *Pin1* and *Pdgfa*, both of which have been purported to negatively affect osteoclastogenesis [521, 522, 532]. *Nfatc1* and *Tnfrs11a* are both downregulated in miR-324-null BMMs and osteoclasts, but it is unclear whether this is a cause of target gene dysregulation or some other mechanism; it cannot be a result of the failure of osteoclasts to fuse as these genes are downregulated prior to the initiation of osteoclastogenesis. The HSC dysregulation resulting from reduced adipogenesis and reduced levels of osteocyte-derived M-CSF may also result in inhibition of osteoclastogenesis.

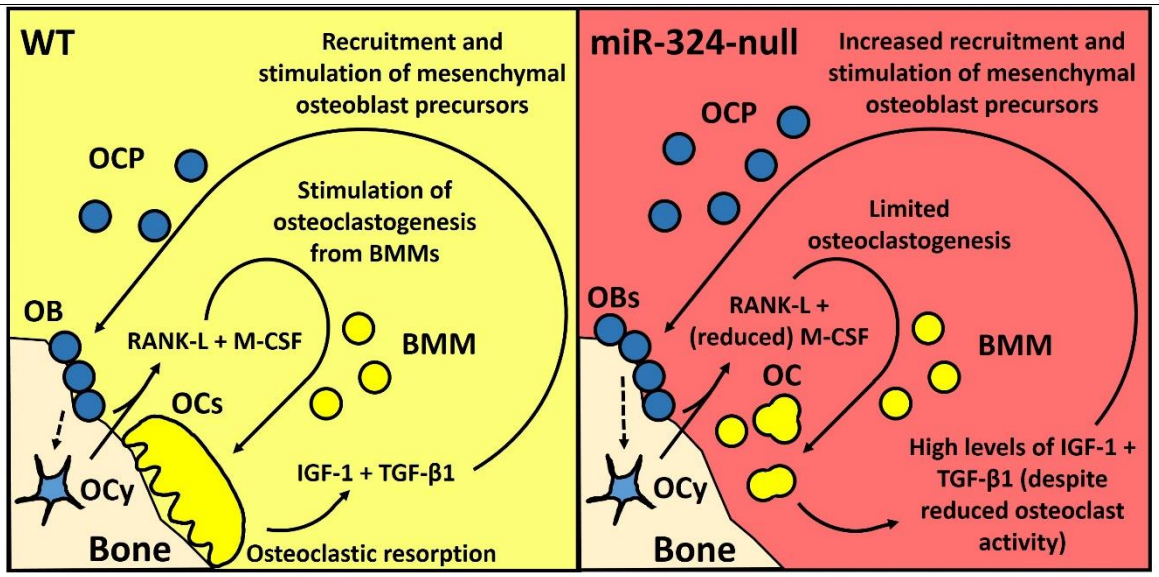

Figure 7.3 - miR-324-null osteoclasts and osteoblasts are uncoupled from one another. In WT bone, upon osteoclast (OC)-mediated resorption of bone, IGF-1 and TGF-β1 are released, stimulating the differentiation of mesenchymal-derived osteochondroprogenitor (OCP) cells into osteoblasts (OBs), some of which ultimately differentiate into osteocytes (OCys). OBs and OCys secrete RANK-L and M-CSF upon bone formation in order to stimulate osteoclastogenesis from bone marrow macrophages (BMMs) and therefore result in additional bone resorption. In this way, bone resorption and bone formation are coupled in WT bone. However, in miR-324-null bone, few osteoclasts are formed from BMM precursors. Despite this however, the immature RANK-L-stimulated cells actually express increased levels of *Tgfb1* and *Igf1*, which stimulates increased osteogenesis from OCPs, therefore resulting in increased bone resorption. However, miR-324-null osteocytes express lower levels of *Csf1* than WT osteocytes, likely contributing to the reduced osteoclastogenesis in spite of increased osteogenesis. This results in an uncoupling of osteoblast and osteoclast activity and their differentiation from precursor cells. This figure does not illustrate the lack of osteocytes which was observed in miR-324-null tibial bone *in vivo*, but this may be the cause of the decreased *Csf1* expression levels.

7.7 Similarities between miR-324-null and *Sost*-null mice

miR-324-null mice display increased bone tissue mineral density (TMD), bone mass and bone formation rate (BFR), phenotypes which display striking similarities to those of *Sost*-null mice. *Sost* encodes sclerostin, an osteocyte-derived negative regulator of osteoblasts through repression of the Wnt signalling pathway [230, 231]. *Sost*-null mice also display a high bone

mass, BFR and bone mineral density (BMD), but unlike miR-324-null mice show no alterations to osteoclast maturation or resorbing activity [565]. Furthermore, *Sost*-null mice display an increased bone strength, whereas although this remains untested in miR-324-null mice, this is a phenotype unlikely to be shared; despite the high bone mass, miR-324-null tibiae show bowing, an effect likely to be due to weaker trabecular structure. miR-324-null osteocytes additionally display no change to *Sost* expression *in vivo*, suggesting that any similarities between the *Sost*-null and miR-324-null mice are unlikely to originate from a shared causal factor. This does not however mean that lack of miR-324 does not alter the Wnt signalling pathway, which is the pathway through the increased bone mass in *Sost*-null mice is effected; despite the fact that no conclusive data in this project has shown a regulatory effect of miR-324 on Wnt signalling, it seems unlikely that such severe osteoblast-driven phenotypes as those observed in miR-324-null mice bypass Wnt signalling entirely.

7.8 Chondrogenesis and cartilage damage in miR-324-null mice

In addition to the skeletal phenotypes, my data have also shown that miR-324-null mice display increased cartilage damage relative to WT controls, both spontaneously with age and at a younger time point following DMM surgery. This appears in conflict with the fact that lack of *Mir324* results in an increased number of MSCs committing to the osteochondroprogenitor lineage, which would be expected to result in an increased number of mature chondrocytes and a theoretical increase in cartilage volume. Therefore, it seems likely that miR-324 plays multiple roles in cartilage biology; in contrast to the increased osteochondroprogenitor lineage commitment and therefore early increase in mature chondrocytes, miR-324-null cartilage may harbour some other defect later in development, resulting in the observed miR-324-null increased cartilage damage phenotype. This effect may occur through the Indian Hedgehog (Ihh) signalling pathway, which miR-324-5p has previously shown to be involved in, through the regulation of the important Ihh gene *Gpc1* (in humans, miR-324-5p instead targets *GLI1* and *SMO*) [151, 186, 187]. In osteoarthritis (OA), the Ihh signalling pathway, which ordinarily is important in cartilage development, is reactivated, through which cartilage damage has been demonstrated to occur [189-192]. The presumed dysregulation of *Gpc1* in miR-324-null chondrocytes would result in an upregulation of Ihh activity, in theory leading to the observed increase in cartilage damage. This would suggest that in spite of the increased number of MSCs committing to the chondrogenesis lineage, the eventual upregulation of Ihh signalling and resulting cartilage damage is inevitable in miR-324-null mice. There is however

currently no evidence for this mechanism in the miR-324-null mice beyond the increased cartilage damage phenotype. Therefore, in order to confirm this hypothesis, it would be beneficial to extract RNA from miR-324-null and WT cartilage and test whether *Gpc1* and other Ihh genes are upregulated in miR-324-null samples, as would be expected in this mechanism.

7.9 Conservation of miR-324 regulation between murine and human biology

miR-324-null mice display hippocampal hyperexcitability and dysregulated bone remodelling, but the relevance of these abnormalities to translational research depends primarily on the conservation of the affected mechanisms. The murine hippocampus, for example, is thought to be broadly homologous to the human hippocampus, both in structure and function across lifespan [566, 567]. Similarly, rodent models are thought to be effective models of epilepsy; no single epilepsy model is representative of the broad range of diseases encompassed by the term “epilepsy”, as is the case with many other such wide-spanning terms, such as for example cancer [568], but for most forms of human epilepsy there is a murine epilepsy homologue [569, 570]. Therefore, it is widely presumed that the majority of hippocampal- and epilepsy-focused research is broadly translatable to human biology. However, a major difficulty in assessing the translatability of my data relating to these fields of study is that the binding sites of the two direct hippocampal and neocortical targets of miR-324 I identified, *Suox* and *Cd300lf*, are not conserved in their human homologues and nor do either possess additional novel binding sites in humans [5, 67]. Considering the conservation of miR-324-5p and -3p between human and mouse, this suggests that these genes are unlikely to be human miR-324 targets. However, the levels of both miR-324-5p and -3p are higher in brain tissue than in any other tissue in humans as well as mouse [109, 110] and therefore it is highly unlikely that miR-324 has no regulatory activity in the human brain. More likely is that miR-324 undertakes similar regulatory activity, albeit through the regulation of different targets. The result of miR-324 dysregulation may ultimately be the same in humans as it is in mice, although this is mere speculation; for example, *Pnpo*, the causal gene of PPDE, which is highly conserved between humans and mice [377, 378], may be indirectly regulated by miR-324 in human hippocampal tissue just as in the murine hippocampus, but this would necessarily be through direct targets which were not identified by my work in miR-324-null hippocampal tissue. Evidently, further work on human tissue is required before similarities between the human and murine hippocampal activity of miR-324 can be assessed.

The serum and expression level of miR-324 has been previously discussed in relation to human bone and cartilage phenotypes in the literature [151, 188, 316-318]. Therefore, it is likely that the effects of miR-324 on bone identified in my data are at least partially conserved between the mouse and human bone remodelling systems. Of the miR-324 targets I validated in osteoblasts and BMMs, only two possessed binding sites conserved in their human homologues; *Runx2* (osteoblast target) and *Pin1* (BMM target). Human (h) *RUNX2* and *hPIN1* were tested for direct miR-324 binding using 3'UTR-luciferase assays, but neither of these validated *in vitro* as direct targets through this method. It is unclear why this should be the case but may be due to the context of the conserved seed sequence in relation to the rest of the 3'UTR, which may not be as highly conserved. Alternatively, it is possible that the secondary structures adopted by the 3'UTR-luciferase plasmid-expressed transcripts may not be representative of the real secondary structure adopted by each mRNA transcript *in vivo*. As a result of this this abnormal folding the ability of miR-324-containing RISC to access and bind the seed sequence may be prevented, therefore producing a false negative result. Assuming however that the luciferase assays are valid representations of the interactions between miR-324 and its putative target genes, *hRUNX2* and *hPIN1* are not direct miR-324 target genes in humans. Any miR-324-mediated regulation of bone remodelling would therefore necessarily operate through alternative, human-specific target transcripts. This differential human and mouse target selection has been noted previously in relation to the Hedgehog (Hh) signalling pathway; in humans, miR-324 downregulates the key Hh genes *SMO* and *GLI1*, whereas in the mouse Hh signalling pathway, miR-324 targets *Gpc1* instead of the murine homologues of *Smo* or *Gli1* [151, 186, 187]. The end result of this regulation is the same *in vitro* for both species, despite the alternative target selection; downregulation of the Hh signalling pathway. Further investigation is required to identify whether miR-324 indeed does regulate bone remodelling in humans through similar pathways as regulated in mice. The use of miR-324 inhibitors and mimics in human MSC-derived osteoblasts and HSC-derived BMMs and osteoclasts would allow *in vitro* osteogenesis and osteoclastogenesis assays to be undertaken, therefore demonstrating whether human bone formation or resorption is also modulated by miR-324.

My data also demonstrated that key osteocyte genes are dysregulated in miR-324-null osteocytes relative to WT controls. Of the three direct osteocyte miR-324 targets identified, two resulted in similar dysregulation in osteocytes when they were overexpressed in the MLO-

Y4 model osteocyte cell line (*Hoxa9* and *Samd5*). The predicted binding sites of both of these genes are perfectly conserved in the human homologues of each gene and it is therefore likely, although currently untested, that *Hoxa9* and *Samd5* are also human osteocyte targets of miR-324. As discussed in section 7.5, osteocytes and the process through which they differentiate from osteoblasts are not well understood, meaning that osteocytes cannot easily be generated from MSCs through stimulation with known chemicals. However, the human $SaOS_2$ cell line has the capacity to adopt an osteocyte-like phenotype upon culture in 3D collagen gels [571], therefore offering a suitable model in which to test whether miR-324 targeting of *hHOXA9* and *hSAMD5* can be replicated in human osteocytes. The $SaOS_2$ cell line also has the benefit of expressing *SOST*, *PHEX* and *MEPE*, unlike the MLO-Y4 model cell line utilised in this project, and therefore will allow a greater understanding of the regulation of these key osteocyte genes by miR-324 *in vitro*.

Ultimately, the use of a pre-clinical animal model such as the mouse is to identify novel mechanisms which may be potentially exploitable in the treatment of human disease. My data has demonstrated that the activity of miR-324 is worth exploring further in the field of epileptic diseases and in hippocampal biology in general. The most translatable component of this project is however the demonstration that *Mir324* ablation produces a high bone mass phenotype through the modulation of osteoblast, osteoclast and osteocyte activity. There is therefore potential from this project to develop treatments for prevalent diseases of low bone mass, such as osteoporosis [264, 265], through the inhibition of miR-324, upregulating osteoblast-mediated bone formation and reducing osteoclast-mediated bone resorption. Much further work is required to achieve this goal, but the data in this project forms the foundations from which the proposed translational research can be developed.

7.10 Strengths and limitations

In this project I have aimed to undertake a body of work as comprehensive as possible in the time permitted. However, there are some areas of the project which should be highlighted as requiring further investigation in future work. For example, the data presented in Chapter 3 focuses on the hippocampal hyperexcitability observed *ex vivo* in miR-324-null mice and the identification of potentially causal genes. Although comparisons in this data are always age- and sex-matched, not all time points and both sexes were investigated for every experiment. This will be an important component of this work to complete in future investigation, considering that neuronal activity in the CA3 hippocampal region, where electrophysiological

recordings were taken, varies greatly with age [406, 407] and additionally the incidence of different epilepsies varies greatly between sexes [408-411].

The data presented in this project relating to bone and cartilage (Chapters 4-6) also lacks completion in regard to sex and age; although multiple time points were studied in the *in vivo* work, hind leg bone-derived osteoblasts, HSCs and osteocytes were isolated only from the bones of miR-324-null and WT mice aged 14-months, and only male mice were used throughout this entire component of the project. Calvarial osteoblasts were also however isolated from mouse pups and showed the same phenotype and gene dysregulation as the osteoblasts from older animals. Therefore, combined with the *in vivo* data, there is strong evidence that the high bone mass phenotype is a result of the same dysregulation throughout life, at least regarding osteoblasts.

The fact that my data has investigated activity of bone cells both *in vivo* and *ex vivo* is a major strength of the work. This has permitted me to confidently conclude that lack of *Mir324* results in an upregulation of osteoblast-mediated bone formation and a downregulation of osteoclast-mediated bone resorption, by demonstrating that osteoblasts and osteoclasts show broadly the same effect when isolated in culture as they do when in their native murine environment. I can therefore be confident that the dysregulation and altered activities observed in these cells are real, rather than merely being artefacts of either *in vivo* sectioning or *ex vivo* culture. Similarly, another strength of this project is that the miR-324-null mice utilised here are global knockout animals, allowing investigation of miR-324 modulation *in vivo* for the first time. Several studies have investigated miR-324 activity *in vitro* [151, 187], and one has even utilised miR-324 expression modulators in an animal model [112], but none to my knowledge have to date made and investigated miR-324 in a global knockout or overexpressor mouse. The global knockout of *Mir324* in the miR-324-null mice therefore means that the work undertaken here was also more ethical than if, for example, *Mir324* was conditionally knocked out separately in the hippocampal neurons and in each individual bone cell; this would necessitate the sacrifice of large numbers of animals from each of these groups, whereas the use of a global knockout model allowed distinct tissues to be obtained from the same animals, thus minimising the number of animals required.

The transfection of miR-324 mimics at physiological levels in miR-324-null osteoblasts (Chapter 5) is a great strength of this project, as it clearly demonstrates that it is the lack of miR-324 itself, rather than a disruption of proximal genes, that is resulting at least in the

osteoblast-mediated high bone formation phenotype. The western blotting of Acadvl and Dvl2 using miR-324-null and WT hippocampal protein lysate (Chapter 3) goes some way to confirming that lack of miR-324 is also responsible for the observed hippocampal phenotype, by demonstrating that these proximal genes are unaltered in expression by *Mir324* deletion. It would be highly beneficial to utilise both of these experiments in other investigated cells in future work, such as osteocytes, osteoclasts and BMMs, in order to confirm that the miR-324-null phenotypes observed in these cells too are indeed due to lack of miR-324 and not due to disruption of *Acadvl* or *Dvl2*. Furthermore, utilising the miR-324-null mice as a background upon which to conditionally re-express *Mir324* in relevant cells, such as BMMs, osteoblasts, osteoclasts and hippocampal and neocortical neuronal populations, would conclusively demonstrate whether the observed phenotypes are really a result of *Mir324* deletion in each of these specific cell populations.

Some components of this project relating to the mesenchymal lineage still require further investigation in order to be confident of the effects I have purported *Mir324* deletion to result in. I showed *in vitro* in Chapters 5 and 6 that miR-324 and its target genes could modulate the balance between osteogenesis and adipogenesis in C3H10T1/2 cells. However, the best way to confirm this would be to undertake this co-differentiation experiment in MSCs isolated from miR-324-null and WT mice. This is therefore a key experiment to undertake in order to confirm that the effects observed *in vitro* using miR-324 inhibitors are also observed *ex vivo* in cells lacking the *Mir324* locus. Further work is also required in relation to the cartilage damage phenotype observed in miR-324-null mice (Chapter 4). Whilst it remains unclear whether this is due to any direct effect of *Mir324* ablation in chondrocytes or merely a cause of the miR-324-null high bone mass phenotype, it would be beneficial to explore this further. The best method through which to investigate this phenotype *ex vivo* would be using a chondrogenesis assay, which again requires miR-324-null and WT MSCs. This would therefore demonstrate conclusively whether there is any disruption to chondrocyte formation in miR-324-null mice.

It is important to note that although BMMs and osteoblasts were cultured *ex vivo*, to demonstrate these cells showed the same effects in culture as *in vivo*, osteocytes were instead isolated from bone tissue and the RNA directly extracted (Chapter 6). There is therefore a risk that this RNA may be contaminated with the material of other cells present in the bone environment, such as osteoblasts, although gene expression analysis of key osteoblast and osteocyte genes suggests that this is not the case. However, due to the method used to extract

osteocyte RNA, the quality was very poor, meaning that the RNA-seq-based approach used for identification of important dysregulated genes and novel miR-324 targets in BMMs, osteoblasts and osteoclasts could not be undertaken in osteocytes. An alternative *in silico* approach was therefore used in order to identify a panel of putative osteocyte target genes, combining the osteocyte active transcriptome [352] with the TargetScan algorithm [5, 67] and results of previous RNA-seq experiments. This approach allowed a RT-qPCR screen to identify novel target genes, validated subsequently using 3'UTR-luciferase assay, but it is likely that through this method important miR-324 target genes would have been missed, most likely due to lack of evidence of miR-324 regulation from previous RNA-seq experiments or understudied genes not being annotated to the osteocyte active transcriptome. Therefore, in future work attempts should be made to isolate osteocytes and culture them *ex vivo*, therefore allowing for a more high-throughput method in identifying novel miR-324 targets which are potentially causal of the miR-324-null osteocyte dysregulation. Alternatively, a cell model such as the OmGFP66 cell line could be utilised; OmGFP66 is a cell line which forms bone matrix upon osteogenic stimulation and subsequently upregulates key osteocyte genes [572]. The publication of this model suggests that it would be a sufficient osteocyte model to use for a repeat of this experiment, but it remains preferable to develop a methodology to extract high-quality RNA from murine osteocytes, in order to avoid any results produced by the cell line which are unrepresentative of true *in vivo* osteocytes.

For the identification of novel miR-324 target genes in all brain and bone tissues, the TargetScan algorithm [5, 67] was utilised to generate the initial list of miR-324 target genes. Although TargetScan is widely used to predict miRNA target genes due to a higher sensitivity than other commonly used algorithms, it does not identify every target (as discussed in Chapter 6). This point is proven by the fact that the *Cxcl12*-γ miR-324-3p target site showed one of the strongest effects of all 3'UTR-luciferase validated targets, despite not actually being predicted by TargetScan; instead the site was identified using a different algorithm, miRmap, which allows for limited G-U base pairing due to its comparable stability to the standard Watson-Crick pairs [350, 351]. It is entirely possible that TargetScan missed other miR-324 targets through this and other similar preferences. Furthermore it is likely that the use of the DO [343] in bone cells to limit target prediction to genes annotated to bone- or adipocyte-related terms also resulted in the excision of key target genes from the final validation subset. Therefore, the miR-324 target genes identified in each tissue in this project should not be

viewed as a comprehensive list of miR-324 targets, but instead as target genes most likely to be causal of the identified phenotypes, based on the evidence available at the time. Furthermore, as discussed in section 7.9, the ultimate goal of primary research involving model organisms, such as the miR-324-null mice used here, is to identify or characterise biological pathways and mechanisms that are exploitable in the treatment of human disease. Considering that the *Mir324* gene and many 3'UTRs across the genome are not perfectly conserved between human and mouse, miR-324 targets are likely to differ between species; for each of miR-324-5p and -3p, TargetScan predicts over 2000 putative target genes in the mouse, but many of these are not also predicted targets in humans [5, 67]. Therefore, future research should aim to investigate how conserved these targets really are, as this will indicate how relevant the biological activity of miR-324 observed in the miR-324-null mice is in directing future research into related human disease.

7.11 Summary and future directions

In this project I have shown that miR-324 plays important regulatory roles in neuronal networks of the hippocampus and in the musculoskeletal system. By utilising miR-324-null mice, I have demonstrated that murine hippocampal tissue lacking *Mir324* shows hyperexcitability *ex vivo*, which may be a result of the dysregulation of *Suox* and *Cd300lf*, direct miR-324-5p targets, and *Pnpo* downstream of these target genes.

miR-324-null mice also displayed an increase in bone mass, in addition to a mild increase in cartilage damage. *In vivo*, a decreased number of adipocyte-derived lipid droplets and osteoclasts, the cells which resorb bone, and an increase in the activity of osteoblasts, the cells which form new bone, was observed in miR-324-null mice. These effects were replicated *ex vivo*, and RNA-seq revealed that miR-324-null mice show a high level of gene dysregulation in osteoblasts and in the haematopoietic lineage, from which osteoclasts derive. This may originate from the decrease in bone marrow fat observed *in vivo*, which has been reported to affect the haematopoietic niche at an early stage in differentiation, or alternatively may be due to dysregulation of the direct miR-324 target genes *App*, *Pdgfa*, *Pin1* and *Ptgs1*, which were identified in this project.

In vitro assays in an MSC-like cell line demonstrated that miR-324 is an important driver of MSC commitment to the adipogenesis lineage, and lack of miR-324 results in increased osteogenic commitment, in addition to an increase in mature osteoblast activity, which was identified *ex vivo*. These effects were demonstrated to be due to direct dysregulation of the

novel miR-324 target genes *Runx2* and *Cxcl12*. Both of these genes have been implicated in similar bone phenotypes in the literature and each upregulates the other during osteogenesis in a positive feedback loop, although I have concluded from my data that Runx2 is the transcriptional effector of this phenotype.

I have demonstrated that miR-324-null osteocytes also show dysregulation of key genes, and through the utilisation of an *in silico* target prediction pipeline and *in vitro* 3'UTR-luciferase assays, I showed that *Cxcl12*, *Hoxa9* and *Samd5* were direct miR-324 osteocyte targets. Furthermore, overexpression of *Hoxa9* and *Samd5* in an osteocyte model cell line was able to replicate some of the *in vivo* osteocyte dysregulation.

This project would benefit from further work in several key areas in order to consolidate the data presented here. Future studies should confirm that *Suox* and *Cd300lf*, the genes identified as targets of miR-324 in the hippocampus and neocortex, are also regulated at a protein level, through the use of Western blotting and *in situ* hybridisation. Comparison of the phenotypes observed in *Suox*- and *Cd300lf*-overexpressor mice with miR-324-null mice would also determine whether dysregulation of these targets really is causal of the hippocampal excitability phenotype demonstrated in this body of work. In regard to the increased cartilage damage phenotype of miR-324-null mice, it would be beneficial to undertake *in situ* hybridisation of *Gpc1*, the miR-324 target previously identified in the literature [151], in cartilage to assess whether it is a target in the *in vivo* miR-324-null mouse models and thus assess whether *Gpc1* dysregulation could partially explain the cartilage phenotype. This would also demonstrate whether miR-324 does affect the Ihh pathway *in vivo*, as was previously reported *in vitro* [151]. Another key experiment to undertake in future work would be to measure the levels of TGF-β1 and IGF-1, to assess whether the constitutive expression of these in miR-324-null osteoclasts could be causal of the uncoupling from osteoblasts, and additionally to measure key circulating markers in miR-324-null and WT serum and thus assess whether HSC-derived cells other than osteoclasts and BMMs are affected by deletion of *Mir324*, as I hypothesised. Finally, it would be beneficial to utilise a three-point bending test [437] to demonstrate whether the bowing identified in miR-324-null tibiae really is indicative of a weaker trabecular structure, or whether this apparent bowing may instead be the result of bone modelling.

To conclude, this project has demonstrated that miR-324 is an important regulatory miRNA in neuronal and musculoskeletal biology. The identification of the miR-324-null hippocampal

hyperexcitability and high bone mass phenotypes has posited miR-324 as a novel pharmaceutical target, of for example a specific miRNA inhibitor such as an antagomir, which regulates epilepsy and bone diseases. Of these, the latter certainly holds the most potential; the inhibition of miR-324 offers promise for the treatment of diseases such as osteoporosis, in which bone resorption dominates new bone formation. A deeper understanding of the regulatory role of miR-324 in the musculoskeletal system as a whole is required prior to development of such a treatment, and therefore this should form the basis of future research.

Chapter 8 - Appendices

Appendix A. Primers and Universal Probe Library probes

Gene	Forward primer	Reverse primer	UPL probe	Amplicon length (nt)
18S	(Predesigned TaqMan assay used; catalogue number 4333760T)			
Acbd4	GCTGGCAGAGAGCTGACC	CCAACTCCTGTGGGCCTAT	7	91
Alpk1	AGAGGACAAGAGTGAGGACCAG	CGAAGGGCCACTTCATTTC	16	95
Alpl	CTTCGCTCTCCGAGATGGTG	CCCTCATGATGTCCGTGGTC	31	109
Bglap	GGTAGTGAACAGACTCCGGC	TTAAGCTCACACTGCTCCCG	26	87
Cd300lf	TTGGAGGATGGTGAGGAGAC	TCCAGAGACTGTGCCTGCT	49	66
Col1a1	CAGCGTAGCCTACATGGACC	CGATGACTGTCTTGCCCCAA	68	167
Col1a2	GGACACAGTGGTATGGATGGA	TTGACCTGGAGTTCCATTCTC	64	96
Csf1	TTGGATTCTTCTGTGGGGCG	GATAGTCCTGTGTGCCCAGC	24	110
Cxcl12-α	AACTGTGCCCTTCAGATTGT	CTACTGGAAAGTCCTTTGGG	80	100
Cxcl12-β	TGCCCTTCAGATTGTTGCAC	GCCCTTCCCTAACACTGACT	80	188
Cxcl12-γ	TGCCCTTCAGATTGTTGCAC	TTTTCCTTTTCTGGGCAGCC	80	191
Gad1	ATACAACCTTTGGCTGCATGT	TTCCGGGACATGAGCAGT	27	60
Gm10282	ACCAGAGACCTGTTGGAACC	GCAAAGTCCCCATCACTCAG	48	68
Gria1	CCAATTTCCCCAACAATATCC	AAAGCTGTCGCTGATGTTCA	38	149
Hoxa9	ACCACCCCTACGTGCATC	GCTGGGTTGTTTTTCTCTATCAA	70	78
Mepe	TCTGTTGGACTGCTCCTCTTC	GAATGCTGTCTTGATTGCCGC	68	88
Mir324-3p (human)	(Predesigned TaqMan assay used; catalogue number 4427975, assay 002161)			
Mir324-3p (mouse)	(Predesigned TaqMan assay used; catalogue number 4427975, assay 002509)			
Mir324-5p	(Predesigned TaqMan assay used; catalogue number 4427975, assay 000539)			
Ndufa2	GAATGCTCGGAGGTGCAG	CTTTGCCGCTTAGCACATT	21	127
Phex	GCCAGAATGCATAGAAGCCG	CAGCCATCACAAGCAAACCG	74	96
Pnpo	GGCCGAGAACTACTTCCATTC	GTTCCTCATTTTTCTTTCTCAGGT	71	113
Pparg	CTGTTTTATGCTGTTATGGGTGA	GCTGATTCCGAAGTTGGTGG	14	153
Rgs5	GCCAGCCAAAATGTGTAAGG	TGACAAGGTCAACAGCAGAGTC	25	122
Runx2	TCCCTGAACTCTGCACCAAG	GTGGTGGAGTGGATGGATGG	60	152
Samd5	GCCAGATATGCAGCTATATTGTCA	AGTTCATGGGGACCTTGCT	69	60
Scn5a	GGATGAGGAGAACAGCCTTG	CACAACTTGGGATTCCTGCT	69	67
Sost	(Predesigned TaqMan assay used; catalogue number 4331182, assay Mm00470479_m1)			
Sp6	GCAGCATCCTGCCTGTTC	GTCAAGGGTACCTCAGATGGA	10	149
Spon1	CCTCAGTGTCCCCTGTCCT	TGATCCACTCCGACATGGTA	11	101
Suox	GCCTCTGACCCTTATGCTGA	GGCGCTGGCTATTAATCCT	42	64
U6	(Predesigned TaqMan assay used; catalogue number 001973)			

Appendix B. Disease Ontology terms used to filter putative miR-324 targets

DO term	Number of genes annotated to term
Achondroplasia	1
Arthritis	546
Bilirubin metabolic disorder	1
Bone cancer	3
Bone giant cell tumor	13
Bone inflammation disease	3
Bone lymphoma	1
Bone marrow cancer	16
Bone marrow disease	2
Bone osteosarcoma	46
Chondrocalcinosis	2
Chondrosarcoma	62
Clear cell chondrosarcoma	1
Disease of metabolism	8
Extraskeletal myxoid chondrosarcoma	3
Fibrosarcoma of bone	3
Hypophosphatasia	1
Idiopathic juvenile osteoporosis	2
Inherited metabolic disorder	1
Iron metabolism disease	1
Juvenile rheumatoid arthritis	3
Mesenchymal chondrosarcoma	2
Metabolic syndrome X	20
Mitochondrial metabolism disease	11
Myxoid chondrosarcoma	3
Osteoarthritis	183
Osteochondritis dissecans	15
Osteochondrodysplasia	5
Osteogenesis imperfecta	6
Osteomalacia	7
Osteomyelitis	15
Osteonecrosis	26
Osteopetrosis	13
Osteopoikilosis	1
Osteoporosis	90
Osteosarcoma	214
Osteosclerosis	6
Paget's disease of bone	14
Pediatric osteosarcoma	1
Primary hypertrophic osteoarthropathy	1
Psoriatic arthritis	6
Reactive arthritis	15
Renal osteodystrophy	2
Rheumatoid arthritis	512

Rickets	8

Appendix C. Sylamer enrichment plots of miR-324-5p and -3p in osteoblasts, bone marrow macrophages and osteoclasts

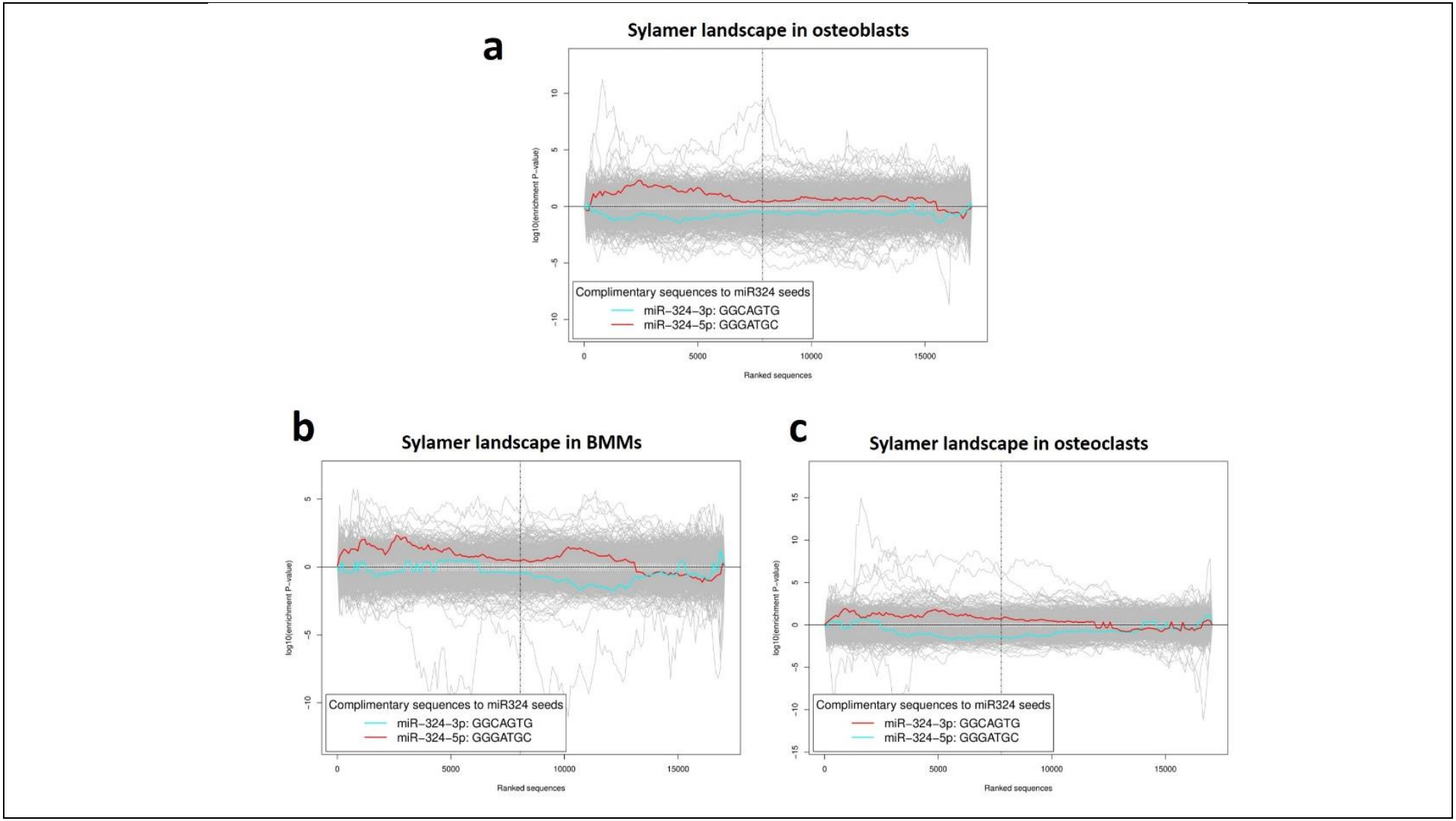

Appendix C - Utilisation of the Sylamer algorithm [506] **did not reveal a noticeable enrichment in transcripts matching the seed sequence of miR-324-5p or -3p which were highly upregulated by the deletion of *Mir324*.** The x-axes represent sorted transcript lists from those with the most positive fold-changes to the left and those with the most negative fold-change to the right. The y-axes represent enrichment of seeds of length 7. The dashed vertical line represents the point in the ranked transcript list at which the fold-change is equal to 0. Seed sequences corresponding to the microRNA deleted in the RNA sequencing experiment would be expected to peak on the left-hand side of the graph, and decline further to the right, as these seeds should be frequently identified in transcripts that are targets of the microRNA. On each panel, the enrichment profile for the miR-324-5p seed sequence is shown in red and that for miR-324-3p in turquoise. In the osteoblast (**a**), bone marrow macrophage (BMM; **b**) and osteoclast (**c**) RNA sequencing experiments, no clear signal can be observed for the miR-324-3p seed. A peak on the left and a decline towards the right can be observed for miR-324-5p, although this does not reach above the noise of the enrichment profiles for other microRNA seed sequences.

Appendix D. Gene Ontology enrichment in brain RNA-seq experiments

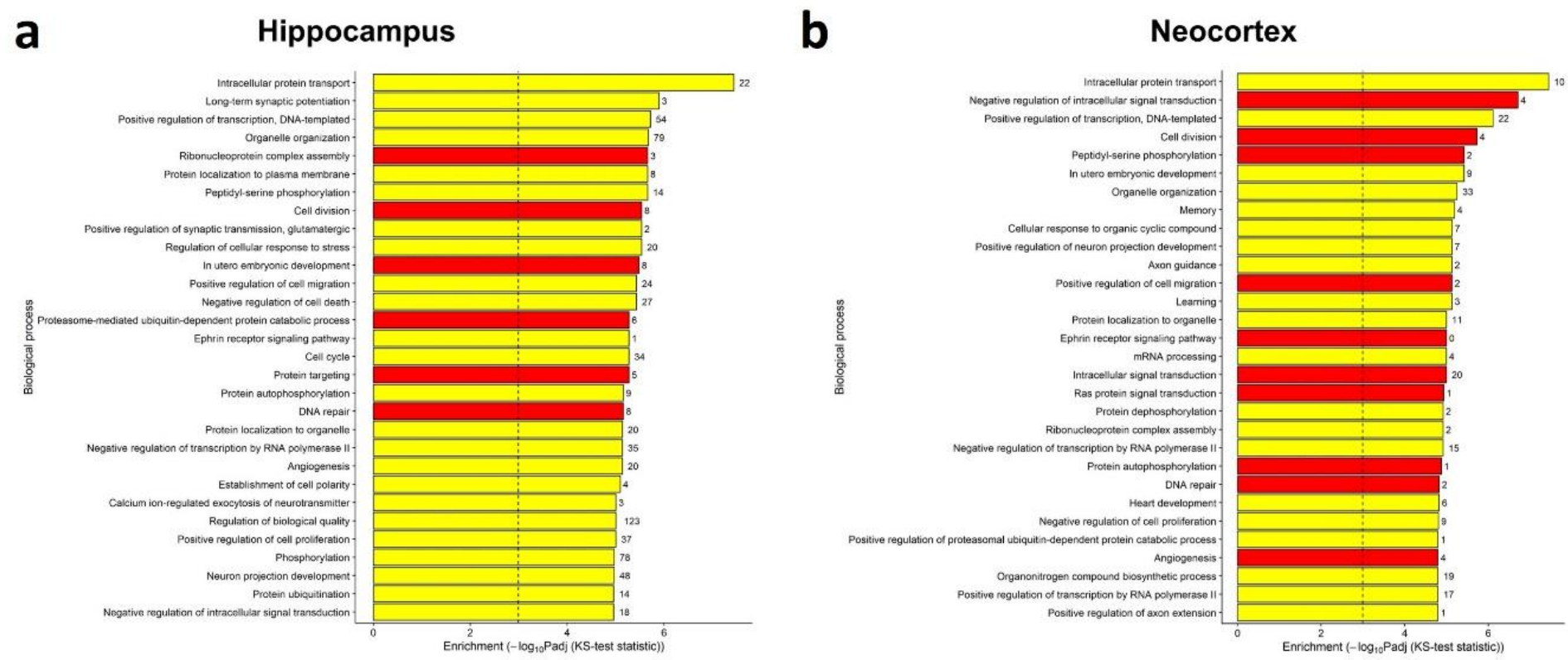

Appendix D - Gene Ontology enrichment in brain RNA sequencing experiments. In both plots (corresponding to hippocampal (**a**) and neocortical (**b**) RNA sequencing experiments), the most highly over-enriched and under-enriched (shown in yellow and red, respectively) terms are shown. The significance of each Disease Ontology term was established using a Kolmogorov-Smirnov test, and the dotted line on each plot shows where the cut-off for significance at a 5% level is found.

Chapter 9 - Bibliography

1. Bartel, D.P., *MicroRNAs: genomics, biogenesis, mechanism, and function.* Cell, 2004. **116**(2): p. 281-297.
2. Cai, Y., et al., *A Brief Review on the Mechanisms of miRNA Regulation.* Genomics Proteomics Bioinformatics, 2009. **7**(4): p. 147-154.
3. Cloonan, N., *Re-thinking miRNA-mRNA interactions: intertwining issues confound target discovery.* Bioessays, 2015. **37**(4): p. 379-388.
4. Hausser, J., et al., *Analysis of CDS-located miRNA target sites suggests that they can effectively inhibit translation.* Genome Res, 2013. **23**(4): p. 604-15.
5. Lewis, B.P., C.B. Burge, and D.P. Bartel, *Conserved seed pairing, often flanked by adenosines, indicates that thousands of human genes are microRNA targets.* Cell, 2005. **120**(1): p. 15-20.
6. Lewis, B.P., et al., *Prediction of mammalian microRNA targets.* Cell, 2003. **115**(7): p. 787-798.
7. Friedman, R.C., et al., *Most mammalian mRNAs are conserved targets of microRNAs.* Genome Res, 2009. **19**(1): p. 92-105.
8. Axtell, M.J. and D.P. Bartel, *Antiquity of microRNAs and their targets in land plants.* Plant Cell, 2005. **17**(6): p. 1658-73.
9. Cuperus, J.T., N. Fahlgren, and J.C. Carrington, *Evolution and functional diversification of MIRNA genes.* Plant Cell, 2011. **23**(2): p. 431-42.
10. Lee, C.T., T. Risom, and W.M. Strauss, *Evolutionary conservation of microRNA regulatory circuits: an examination of microRNA gene complexity and conserved microRNA-target interactions through metazoan phylogeny.* DNA Cell Biol, 2007. **26**(4): p. 209-18.
11. Ivey, K.N. and D. Srivastava, *microRNAs as Developmental Regulators.* Cold Spring Harb. Perspect. Biol., 2015. **7**(7): p. a008144.
12. Liu, C.J., *MicroRNAs in skeletogenesis.* Front Biosci (Landmark Ed), 2009. **14**: p. 2757-64.
13. Rajman, M. and G. Schratt, *MicroRNAs in neural development: from master regulators to fine-tuners.* Development, 2017. **144**(13): p. 2310-2322.
14. Ramirez-Moya, J. and P. Santisteban, *miRNA-Directed Regulation of the Main Signaling Pathways in Thyroid Cancer.* Front Endocrinol (Lausanne), 2019. **10**: p. 430.
15. Rizzuti, M., et al., *MicroRNA expression analysis identifies a subset of downregulated miRNAs in ALS motor neuron progenitors.* Sci. Rep., 2018. **8**(1): p. 10105.
16. Wang, Z., *MicroRNA: A matter of life or death.* World J. Biol. Chem., 2010. **1**(4): p. 41-54.
17. de Rie, D., et al., *An integrated expression atlas of miRNAs and their promoters in human and mouse.* Nat Biotechnol, 2017. **35**(9): p. 872-878.
18. Kim, V.N., J. Han, and M.C. Siomi, *Biogenesis of small RNAs in animals.* Nat Rev Mol Cell Biol, 2009. **10**(2): p. 126-39.
19. Kim, Y.K. and V.N. Kim, *Processing of intronic microRNAs.* EMBO J, 2007. **26**(3): p. 775-83.
20. Filipowicz, W., et al., *Post-transcriptional gene silencing by siRNAs and miRNAs.* Curr. Opin. Struct. Biol., 2005. **15**(3): p. 331-341.
21. Winter, J., et al., *Many roads to maturity: microRNA biogenesis pathways and their regulation.* Nat. Cell Biol., 2009. **11**(3): p. 228-234.
22. Schwarz, D.S., et al., *Asymmetry in the assembly of the RNAi enzyme complex.* Cell, 2003. **115**(2): p. 199-208.
23. Frank, F., N. Sonenberg, and B. Nagar, *Structural basis for 5'-nucleotide base-specific recognition of guide RNA by human AGO2.* Nature, 2010. **465**(7299): p. 818-22.
24. Grigelioniene, G., et al., *Gain-of-function mutation of microRNA-140 in human skeletal dysplasia.* Nat Med, 2019. **25**(4): p. 583-590.
25. Young, C.J., et al., *Reversing the miRNA -5p/-3p stoichiometry reveals physiological roles and targets of miR-140 miRNAs.* RNA, 2022.
26. Chatterjee, S., et al., *Target-mediated protection of endogenous microRNAs in C. elegans.* Dev Cell, 2011. **20**(3): p. 388-96.
27. Tsai, K.W., et al., *Arm Selection Preference of MicroRNA-193a Varies in Breast Cancer.* Sci Rep, 2016. **6**: p. 28176.

28. Ameres, S.L., et al., *Target RNA-directed trimming and tailing of small silencing RNAs.* Science, 2010. **328**(5985): p. 1534-9.
29. de la Mata, M., et al., *Potent degradation of neuronal miRNAs induced by highly complementary targets.* EMBO Rep, 2015. **16**(4): p. 500-11.
30. Fuchs Wightman, F., et al., *Target RNAs Strike Back on MicroRNAs.* Front Genet, 2018. **9**: p. 435.
31. Kleaveland, B., et al., *A Network of Noncoding Regulatory RNAs Acts in the Mammalian Brain.* Cell, 2018. **174**(2): p. 350-362 e17.
32. Sheu-Gruttadauria, J., et al., *Structural Basis for Target-Directed MicroRNA Degradation.* Mol Cell, 2019. **75**(6): p. 1243-1255 e7.
33. Yang, A., et al., *AGO-bound mature miRNAs are oligouridylated by TUTs and subsequently degraded by DIS3L2.* Nat Commun, 2020. **11**(1): p. 2765.
34. Cordova-Rivas, S., et al., *5p and 3p Strands of miR-34 Family Members Have Differential Effects in Cell Proliferation, Migration, and Invasion in Cervical Cancer Cells.* Int J Mol Sci, 2019. **20**(3).
35. Feng, H., et al., *MiR-34b-3p represses cell proliferation, cell cycle progression and cell apoptosis in non-small-cell lung cancer (NSCLC) by targeting CDK4.* J Cell Mol Med, 2019. **23**(8): p. 5282-5291.
36. Medley, J.C., G. Panzade, and A.Y. Zinovyeva, *microRNA strand selection: Unwinding the rules.* Wiley Interdiscip Rev RNA, 2021. **12**(3): p. e1627.
37. Berezikov, E., et al., *Mammalian mirtron genes.* Mol. Cell, 2007. **28**(2): p. 328-336.
38. Curtis, H.J., C.R. Sibley, and M.J.A. Wood, *Mirtrons, an emerging class of atypical miRNA.* Wiley Interdiscip. Rev. RNA, 2012. **3**(5): p. 617-632.
39. Schamberger, A., B. Sarkadi, and T.I. Orban, *Human mirtrons can express functional microRNAs simultaneously from both arms in a flanking exon-independent manner.* RNA Biol., 2012. **9**(9): p. 1177-1185.
40. Da Fonseca, B.H.R., D.S. Domingues, and A.R. Paschoal, *mirtronDB: a mirtron knowledge base.* Bioinformatics, 2019. **35**(19): p. 3873-3874.
41. Alles, J., et al., *An estimate of the total number of true human miRNAs.* Nucleic Acids Res, 2019. **47**(7): p. 3353-3364.
42. Ruby, J.G., C.H. Jan, and D.P. Bartel, *Intronic microRNA precursors that bypass Drosha processing.* Nature, 2007. **448**(7149): p. 83-6.
43. Sibley, C.R., et al., *The biogenesis and characterization of mammalian microRNAs of mirtron origin.* Nucleic Acids Res, 2012. **40**(1): p. 438-48.
44. Lim, L.P. and C.B. Burge, *A computational analysis of sequence features involved in recognition of short introns.* Proc Natl Acad Sci U S A, 2001. **98**(20): p. 11193-8.
45. Yandell, M., et al., *Large-scale trends in the evolution of gene structures within 11 animal genomes.* PLoS Comput Biol, 2006. **2**(3): p. e15.
46. Fabian, M.R. and N. Sonenberg, *The mechanics of miRNA-mediated gene silencing: a look under the hood of miRISC.* Nat Struct Mol Biol, 2012. **19**(6): p. 586-93.
47. Maroney, P.A., et al., *Evidence that microRNAs are associated with translating messenger RNAs in human cells.* Nat Struct Mol Biol, 2006. **13**(12): p. 1102-7.
48. Wu, L., J. Fan, and J.G. Belasco, *MicroRNAs direct rapid deadenylation of mRNA.* Proc Natl Acad Sci U S A, 2006. **103**(11): p. 4034-9.
49. Liu, J., et al., *A role for the P-body component GW182 in microRNA function.* Nat Cell Biol, 2005. **7**(12): p. 1261-6.
50. Rehwinkel, J., et al., *A crucial role for GW182 and the DCP1:DCP2 decapping complex in miRNA-mediated gene silencing.* RNA, 2005. **11**(11): p. 1640-7.
51. Mitchell, P. and D. Tollervey, *mRNA stability in eukaryotes.* Curr Opin Genet Dev, 2000. **10**(2): p. 193-8.
52. Newbury, S.F., *Control of mRNA stability in eukaryotes.* Biochem Soc Trans, 2006. **34**(Pt 1): p. 30-4.
53. Jackson, R.J. and N. Standart, *Do the poly(A) tail and 3' untranslated region control mRNA translation?* Cell, 1990. **62**(1): p. 15-24.

54. Rissland, O.S., *The organization and regulation of mRNA-protein complexes.* Wiley Interdiscip Rev RNA, 2017. **8**(1).
55. Sachs, A., *The role of poly(A) in the translation and stability of mRNA.* Curr Opin Cell Biol, 1990. **2**(6): p. 1092-8.
56. Huntzinger, E., et al., *The interactions of GW182 proteins with PABP and deadenylases are required for both translational repression and degradation of miRNA targets.* Nucleic Acids Res, 2013. **41**(2): p. 978-94.
57. Braun, J.E., et al., *GW182 proteins directly recruit cytoplasmic deadenylase complexes to miRNA targets.* Mol Cell, 2011. **44**(1): p. 120-33.
58. Piao, X., et al., *CCR4-NOT deadenylates mRNA associated with RNA-induced silencing complexes in human cells.* Mol Cell Biol, 2010. **30**(6): p. 1486-94.
59. Fukao, A. and T. Fujiwara, *The coupled and uncoupled mechanisms by which trans-acting factors regulate mRNA stability and translation.* J Biochem, 2017. **161**(4): p. 309-314.
60. Kahvejian, A., G. Roy, and N. Sonenberg, *The mRNA closed-loop model: the function of PABP and PABP-interacting proteins in mRNA translation.* Cold Spring Harb Symp Quant Biol, 2001. **66**: p. 293-300.
61. Zekri, L., et al., *The silencing domain of GW182 interacts with PABPC1 to promote translational repression and degradation of microRNA targets and is required for target release.* Mol Cell Biol, 2009. **29**(23): p. 6220-31.
62. Fabian, M.R., et al., *Mammalian miRNA RISC recruits CAF1 and PABP to affect PABP-dependent deadenylation.* Mol Cell, 2009. **35**(6): p. 868-80.
63. Chu, C.Y. and T.M. Rana, *Translation repression in human cells by microRNA-induced gene silencing requires RCK/p54.* PLoS Biol, 2006. **4**(7): p. e210.
64. Coller, J. and R. Parker, *General translational repression by activators of mRNA decapping.* Cell, 2005. **122**(6): p. 875-86.
65. Rouya, C., et al., *Human DDX6 effects miRNA-mediated gene silencing via direct binding to CNOT1.* RNA, 2014. **20**(9): p. 1398-409.
66. Cunningham, F., et al., *Ensembl 2019.* Nucleic Acids Res, 2019. **47**(D1): p. D745-D751.
67. Grimson, A., et al., *MicroRNA targeting specificity in mammals: determinants beyond seed pairing.* Mol Cell, 2007. **27**(1): p. 91-105.
68. Zerbino, D.R., et al., *Ensembl 2018.* Nucleic Acids Res., 2018. **46**(D1): p. D754-D761.
69. Kozomara, A. and S. Griffiths-Jones, *miRBase: integrating microRNA annotation and deep-sequencing data.* Nucleic Acids Res, 2011. **39**(Database issue): p. D152-7.
70. Burgess, N., E.A. Maguire, and J. O'Keefe, *The human hippocampus and spatial and episodic memory.* Neuron, 2002. **35**(4): p. 625-41.
71. Chang, Q. and P.E. Gold, *Switching memory systems during learning: changes in patterns of brain acetylcholine release in the hippocampus and striatum in rats.* J Neurosci, 2003. **23**(7): p. 3001-5.
72. Williams, G., et al., *The hypothalamus and the control of energy homeostasis: different circuits, different purposes.* Physiol Behav, 2001. **74**(4-5): p. 683-701.
73. Williams, G., J.A. Harrold, and D.J. Cutler, *The hypothalamus and the regulation of energy homeostasis: lifting the lid on a black box.* Proc Nutr Soc, 2000. **59**(3): p. 385-96.
74. Battaglia, F.P., et al., *The hippocampus: hub of brain network communication for memory.* Trends Cogn Sci, 2011. **15**(7): p. 310-8.
75. Sirota, A., et al., *Communication between neocortex and hippocampus during sleep in rodents.* Proc Natl Acad Sci U S A, 2003. **100**(4): p. 2065-9.
76. Witter, M.P., et al., *Cortico-hippocampal communication by way of parallel parahippocampal-subicular pathways.* Hippocampus, 2000. **10**(4): p. 398-410.
77. Kuss, A.W. and W. Chen, *MicroRNAs in brain function and disease.* Curr Neurol Neurosci Rep, 2008. **8**(3): p. 190-7.
78. Prodromidou, K. and R. Matsas, *Species-Specific miRNAs in Human Brain Development and Disease.* Front Cell Neurosci, 2019. **13**: p. 559.

79. Callaghan, B., et al., *Remission and relapse in a drug-resistant epilepsy population followed prospectively.* Epilepsia, 2011. **52**(3): p. 619-26.
80. Camfield, P. and C. Camfield, *Incidence, prevalence and aetiology of seizures and epilepsy in children.* Epileptic Disord, 2015. **17**(2): p. 117-23.
81. Fiest, K.M., et al., *Prevalence and incidence of epilepsy: A systematic review and meta-analysis of international studies.* Neurology, 2017. **88**(3): p. 296-303.
82. Hauser, W.A., J.F. Annegers, and L.T. Kurland, *Incidence of epilepsy and unprovoked seizures in Rochester, Minnesota: 1935-1984.* Epilepsia, 1993. **34**(3): p. 453-68.
83. Fisher, R.S., et al., *Epileptic seizures and epilepsy: definitions proposed by the International League Against Epilepsy (ILAE) and the International Bureau for Epilepsy (IBE).* Epilepsia, 2005. **46**(4): p. 470-2.
84. Beghi, E., *The Epidemiology of Epilepsy.* Neuroepidemiology, 2020. **54**(2): p. 185-191.
85. Holmes, G.L. and Y. Ben-Ari, *The neurobiology and consequences of epilepsy in the developing brain.* Pediatr Res, 2001. **49**(3): p. 320-5.
86. Bell, G.S., et al., *Suicide in people with epilepsy: how great is the risk?* Epilepsia, 2009. **50**(8): p. 1933-42.
87. Gaitatzis, A. and J.W. Sander, *The mortality of epilepsy revisited.* Epileptic Disord, 2004. **6**(1): p. 3-13.
88. Gaitatzis, A., et al., *Life expectancy in people with newly diagnosed epilepsy.* Brain, 2004. **127**(Pt 11): p. 2427-32.
89. Lhatoo, S.D., et al., *Mortality in epilepsy in the first 11 to 14 years after diagnosis: multivariate analysis of a long-term, prospective, population-based cohort.* Ann Neurol, 2001. **49**(3): p. 336-44.
90. Sander, J.W., *The epidemiology of epilepsy revisited.* Curr Opin Neurol, 2003. **16**(2): p. 165-70.
91. Kwan, P. and M.J. Brodie, *Early identification of refractory epilepsy.* N Engl J Med, 2000. **342**(5): p. 314-9.
92. Annegers, J.F., W.A. Hauser, and L.R. Elveback, *Remission of seizures and relapse in patients with epilepsy.* Epilepsia, 1979. **20**(6): p. 729-37.
93. Sillanpaa, M. and D. Schmidt, *Natural history of treated childhood-onset epilepsy: prospective, long-term population-based study.* Brain, 2006. **129**(Pt 3): p. 617-24.
94. Duncan, J.S., et al., *Adult epilepsy.* Lancet, 2006. **367**(9516): p. 1087-1100.
95. Simeone, T.A., S.D. Donevan, and J.M. Rho, *Molecular biology and ontogeny of gamma-aminobutyric acid (GABA) receptors in the mammalian central nervous system.* J Child Neurol, 2003. **18**(1): p. 39-48; discussion 49.
96. Ambrosio, A.F., et al., *Mechanisms of action of carbamazepine and its derivatives, oxcarbazepine, BIA 2-093, and BIA 2-024.* Neurochem Res, 2002. **27**(1-2): p. 121-30.
97. Mengel, H., *Tiagabine.* Epilepsia, 1994. **35 Suppl 5**: p. S81-4.
98. Benarroch, E.E., *GABAB receptors: structure, functions, and clinical implications.* Neurology, 2012. **78**(8): p. 578-84.
99. Goetz, T., et al., *GABA(A) receptors: structure and function in the basal ganglia.* Prog Brain Res, 2007. **160**: p. 21-41.
100. Cuellar, T.L., et al., *Dicer loss in striatal neurons produces behavioral and neuroanatomical phenotypes in the absence of neurodegeneration.* Proc Natl Acad Sci U S A, 2008. **105**(14): p. 5614-9.
101. Davis, T.H., et al., *Conditional loss of Dicer disrupts cellular and tissue morphogenesis in the cortex and hippocampus.* J Neurosci, 2008. **28**(17): p. 4322-30.
102. Kim, J., et al., *A MicroRNA feedback circuit in midbrain dopamine neurons.* Science, 2007. **317**(5842): p. 1220-4.
103. Schaefer, A., et al., *Cerebellar neurodegeneration in the absence of microRNAs.* J Exp Med, 2007. **204**(7): p. 1553-8.
104. Coolen, M., S. Katz, and L. Bally-Cuif, *miR-9: a versatile regulator of neurogenesis.* Front Cell Neurosci, 2013. **7**: p. 220.

105. Radhakrishnan, B. and A. Alwin Prem Anand, *Role of miRNA-9 in Brain Development.* J Exp Neurosci, 2016. **10**: p. 101-120.
106. Shibata, M., et al., *MicroRNA-9 regulates neurogenesis in mouse telencephalon by targeting multiple transcription factors.* J Neurosci, 2011. **31**(9): p. 3407-22.
107. Hu, K., et al., *Expression profile of microRNAs in rat hippocampus following lithium-pilocarpine-induced status epilepticus.* Neurosci Lett, 2011. **488**(3): p. 252-7.
108. Sano, T., et al., *MicroRNA-34a upregulation during seizure-induced neuronal death.* Cell Death Dis, 2012. **3**: p. e287.
109. Keller, A., et al., *miRNATissueAtlas2: an update to the human miRNA tissue atlas.* Nucleic Acids Res, 2022. **50**(D1): p. D211-D221.
110. Ludwig, N., et al., *Distribution of miRNA expression across human tissues.* Nucleic Acids Res, 2016. **44**(8): p. 3865-77.
111. Gross, C., et al., *MicroRNA-Mediated Downregulation of the Potassium Channel Kv4.2 Contributes to Seizure Onset.* Cell Rep, 2016. **17**(1): p. 37-45.
112. Tiwari, D., et al., *MicroRNA inhibition upregulates hippocampal A-type potassium current and reduces seizure frequency in a mouse model of epilepsy.* Neurobiol. Dis., 2019. **130**: p. 104508.
113. O'Brien, R.J. and P.C. Wong, *Amyloid precursor protein processing and Alzheimer's disease.* Annu Rev Neurosci, 2011. **34**: p. 185-204.
114. Selkoe, D.J. and J. Hardy, *The amyloid hypothesis of Alzheimer's disease at 25 years.* EMBO Mol. Med., 2016. **8**(6): p. 595-608.
115. Bernard, C., et al., *Acquired dendritic channelopathy in temporal lobe epilepsy.* Science, 2004. **305**(5683): p. 532-5.
116. Chen, X., et al., *Deletion of Kv4.2 gene eliminates dendritic A-type K+ current and enhances induction of long-term potentiation in hippocampal CA1 pyramidal neurons.* J. Neurosci., 2006. **26**(47): p. 12143-12151.
117. Lin, M.A., S.C. Cannon, and D.M. Papazian, *Kv4.2 autism and epilepsy mutation enhances inactivation of closed channels but impairs access to inactivated state after opening.* Proc Natl Acad Sci U S A, 2018. **115**(15): p. E3559-E3568.
118. Akkiraju, H. and A. Nohe, *Role of Chondrocytes in Cartilage Formation, Progression of Osteoarthritis and Cartilage Regeneration.* J Dev Biol, 2015. **3**(4): p. 177-192.
119. Heinegard, D. and T. Saxne, *The role of the cartilage matrix in osteoarthritis.* Nat Rev Rheumatol, 2011. **7**(1): p. 50-6.
120. Ballock, R.T. and R.J. O'Keefe, *The biology of the growth plate.* J Bone Joint Surg Am, 2003. **85**(4): p. 715-26.
121. Agirdil, Y., *The growth plate: a physiologic overview.* EFORT Open Rev, 2020. **5**(8): p. 498-507.
122. Samsa, W.E., X. Zhou, and G. Zhou, *Signaling pathways regulating cartilage growth plate formation and activity.* Semin Cell Dev Biol, 2017. **62**: p. 3-15.
123. Dong, Y., et al., *Wnt-mediated regulation of chondrocyte maturation: modulation by TGF-beta.* J Cell Biochem, 2005. **95**(5): p. 1057-68.
124. Komori, T., *Regulation of skeletal development by the Runx family of transcription factors.* J Cell Biochem, 2005. **95**(3): p. 445-53.
125. Bi, W., et al., *Sox9 is required for cartilage formation.* Nat Genet, 1999. **22**(1): p. 85-9.
126. Minina, E., et al., *BMP and Ihh/PTHrP signaling interact to coordinate chondrocyte proliferation and differentiation.* Development, 2001. **128**(22): p. 4523-34.
127. Yang, L., et al., *Hypertrophic chondrocytes can become osteoblasts and osteocytes in endochondral bone formation.* Proc Natl Acad Sci U S A, 2014. **111**(33): p. 12097-102.
128. Sun, M.M. and F. Beier, *Chondrocyte hypertrophy in skeletal development, growth, and disease.* Birth Defects Res C Embryo Today, 2014. **102**(1): p. 74-82.
129. Emons, J., et al., *Mechanisms of growth plate maturation and epiphyseal fusion.* Horm Res Paediatr, 2011. **75**(6): p. 383-91.
130. GBD Disease and Injury Incidence and Prevalence Collaborators, *Global, regional, and national incidence, prevalence, and years lived with disability for 354 diseases and injuries for 195*

countries and territories, 1990-2017: a systematic analysis for the Global Burden of Disease Study 2017. Lancet, 2018. **392**(10159): p. 1789-1858.
131. Arden, N. and M.C. Nevitt, *Osteoarthritis: epidemiology.* Best Pract Res Clin Rheumatol, 2006. **20**(1): p. 3-25.
132. Sandell, L.J., *Etiology of osteoarthritis: genetics and synovial joint development.* Nat Rev Rheumatol, 2012. **8**(2): p. 77-89.
133. Spector, T.D. and A.J. MacGregor, *Risk factors for osteoarthritis: genetics.* Osteoarthritis Cartilage, 2004. **12 Suppl A**: p. S39-44.
134. Makarczyk, M.J., et al., *Current Models for Development of Disease-Modifying Osteoarthritis Drugs.* Tissue Eng Part C Methods, 2021. **27**(2): p. 124-138.
135. Arthritis Care. *OA Nation 2012 report*. 2012 [cited 2021 03/09/2021]; Available from: https://issuu.com/arthritiscare/docs/oa_nation_2012_report.
136. Goldring, M.B. and S.R. Goldring, *Articular cartilage and subchondral bone in the pathogenesis of osteoarthritis.* Ann N Y Acad Sci, 2010. **1192**: p. 230-7.
137. Guilak, F., et al., *Osteoarthritis as a disease of the cartilage pericellular matrix.* Matrix Biol, 2018. **71-72**: p. 40-50.
138. Krishnan, Y. and A.J. Grodzinsky, *Cartilage diseases.* Matrix Biol, 2018. **71-72**: p. 51-69.
139. Rose, B.J. and D.L. Kooyman, *A Tale of Two Joints: The Role of Matrix Metalloproteases in Cartilage Biology.* Dis Markers, 2016. **2016**: p. 4895050.
140. Troeberg, L. and H. Nagase, *Proteases involved in cartilage matrix degradation in osteoarthritis.* Biochim Biophys Acta, 2012. **1824**(1): p. 133-45.
141. Burr, D.B. and M.A. Gallant, *Bone remodelling in osteoarthritis.* Nat Rev Rheumatol, 2012. **8**(11): p. 665-73.
142. Yuan, X.L., et al., *Bone-cartilage interface crosstalk in osteoarthritis: potential pathways and future therapeutic strategies.* Osteoarthritis Cartilage, 2014. **22**(8): p. 1077-89.
143. Little, C.B., et al., *Matrix metalloproteinase 13-deficient mice are resistant to osteoarthritic cartilage erosion but not chondrocyte hypertrophy or osteophyte development.* Arthritis Rheum, 2009. **60**(12): p. 3723-33.
144. Mattick, J.S. and I.V. Makunin, *Non-coding RNA.* Hum Mol Genet, 2006. **15 Spec No 1**: p. R17-29.
145. Ali, S.A., et al., *Sequencing identifies a distinct signature of circulating microRNAs in early radiographic knee osteoarthritis.* Osteoarthritis Cartilage, 2020. **28**(11): p. 1471-1481.
146. Beyer, C., et al., *Signature of circulating microRNAs in osteoarthritis.* Ann Rheum Dis, 2015. **74**(3): p. e18.
147. Miyaki, S. and H. Asahara, *Macro view of microRNA function in osteoarthritis.* Nat Rev Rheumatol, 2012. **8**(9): p. 543-52.
148. Nugent, M., *MicroRNAs: exploring new horizons in osteoarthritis.* Osteoarthritis Cartilage, 2016. **24**(4): p. 573-80.
149. Peffers, M.J., et al., *SnoRNA signatures in cartilage ageing and osteoarthritis.* Sci Rep, 2020. **10**(1): p. 10641.
150. Steinbusch, M.M., et al., *Serum snoRNAs as biomarkers for joint ageing and post traumatic osteoarthritis.* Sci Rep, 2017. **7**: p. 43558.
151. Woods, S., et al., *miR-324-5p is up regulated in end-stage osteoarthritis and regulates Indian Hedgehog signalling by differing mechanisms in human and mouse.* Matrix Biol., 2019. **77**: p. 87-100.
152. Xing, D., et al., *Identification of long noncoding RNA associated with osteoarthritis in humans.* Orthop Surg, 2014. **6**(4): p. 288-93.
153. Zhang, C., et al., *Upregulation of lncRNA HOTAIR contributes to IL-1beta-induced MMP overexpression and chondrocytes apoptosis in temporomandibular joint osteoarthritis.* Gene, 2016. **586**(2): p. 248-53.
154. Matta, C., et al., *Transcriptome-based screening of ion channels and transporters in a migratory chondroprogenitor cell line isolated from late-stage osteoarthritic cartilage.* J Cell Physiol, 2021. **236**(11): p. 7421-7439.

155. Fernandez-Moreno, M., et al., *Genetics in osteoarthritis.* Curr Genomics, 2008. **9**(8): p. 542-7.
156. Reynard, L.N. and M.J. Barter, *Osteoarthritis year in review 2019: genetics, genomics and epigenetics.* Osteoarthritis Cartilage, 2020. **28**(3): p. 275-284.
157. Felson, D.T., *The course of osteoarthritis and factors that affect it.* Rheum Dis Clin North Am, 1993. **19**(3): p. 607-15.
158. Karsdal, M.A., et al., *Osteoarthritis--a case for personalized health care?* Osteoarthritis Cartilage, 2014. **22**(1): p. 7-16.
159. McCoy, A.M., *Animal Models of Osteoarthritis: Comparisons and Key Considerations.* Vet Pathol, 2015. **52**(5): p. 803-18.
160. Malfait, A.M. and C.B. Little, *On the predictive utility of animal models of osteoarthritis.* Arthritis Res Ther, 2015. **17**: p. 225.
161. Wendler, A. and M. Wehling, *The translatability of animal models for clinical development: biomarkers and disease models.* Curr Opin Pharmacol, 2010. **10**(5): p. 601-6.
162. Lampropoulou-Adamidou, K., et al., *Useful animal models for the research of osteoarthritis.* Eur J Orthop Surg Traumatol, 2014. **24**(3): p. 263-71.
163. Glasson, S.S., T.J. Blanchet, and E.A. Morris, *The surgical destabilization of the medial meniscus (DMM) model of osteoarthritis in the 129/SvEv mouse.* Osteoarthritis Cartilage, 2007. **15**(9): p. 1061-9.
164. Glasson, S.S., et al., *The OARSI histopathology initiative - recommendations for histological assessments of osteoarthritis in the mouse.* Osteoarthritis Cartilage, 2010. **18 Suppl 3**: p. S17-23.
165. Simon, W.H., *Scale effects in animal joints. I. Articular cartilage thickness and compressive stress.* Arthritis Rheum, 1970. **13**(3): p. 244-56.
166. Kobayashi, T., et al., *Dicer-dependent pathways regulate chondrocyte proliferation and differentiation.* Proc Natl Acad Sci U S A, 2008. **105**(6): p. 1949-54.
167. Miyaki, S., et al., *MicroRNA-140 plays dual roles in both cartilage development and homeostasis.* Genes Dev., 2010. **24**(11): p. 1173-1185.
168. Sun, H., et al., *MiR-455-3p inhibits the degenerate process of chondrogenic differentiation through modification of DNA methylation.* Cell Death Dis, 2018. **9**(5): p. 537.
169. de Pontual, L., et al., *Germline deletion of the miR-17 approximately 92 cluster causes skeletal and growth defects in humans.* Nat Genet, 2011. **43**(10): p. 1026-30.
170. Ventura, A., et al., *Targeted deletion reveals essential and overlapping functions of the miR-17 through 92 family of miRNA clusters.* Cell, 2008. **132**(5): p. 875-86.
171. Sumiyoshi, K., et al., *Identification of miR-1 as a micro RNA that supports late-stage differentiation of growth cartilage cells.* Biochem Biophys Res Commun, 2010. **402**(2): p. 286-90.
172. Yan, C., et al., *MicroRNA regulation associated chondrogenesis of mouse MSCs grown on polyhydroxyalkanoates.* Biomaterials, 2011. **32**(27): p. 6435-44.
173. Le, L.T., et al., *The microRNA-29 family in cartilage homeostasis and osteoarthritis.* J Mol Med (Berl), 2016. **94**(5): p. 583-96.
174. Kim, D., et al., *MicroRNA-34a regulates migration of chondroblast and IL-1beta-induced degeneration of chondrocytes by targeting EphA5.* Biochem Biophys Res Commun, 2011. **415**(4): p. 551-7.
175. Song, J., et al., *MicroRNA-375, a new regulator of cadherin-7, suppresses the migration of chondrogenic progenitors.* Cell Signal, 2013. **25**(3): p. 698-706.
176. Song, J., D. Kim, and E.J. Jin, *MicroRNA-488 suppresses cell migration through modulation of the focal adhesion activity during chondrogenic differentiation of chick limb mesenchymal cells.* Cell Biol Int, 2011. **35**(2): p. 179-85.
177. Endisha, H., et al., *MicroRNA-34a-5p Promotes Joint Destruction During Osteoarthritis.* Arthritis Rheumatol, 2021. **73**(3): p. 426-439.
178. Chau, M., et al., *Organization of the Indian hedgehog--parathyroid hormone-related protein system in the postnatal growth plate.* J. Mol. Endocrinol., 2011. **47**(1): p. 99-107.

179. Kindblom, J.M., et al., *Expression and localization of Indian hedgehog (Ihh) and parathyroid hormone related protein (PTHrP) in the human growth plate during pubertal development.* J. Endocrinol., 2002. **174**(2): p. R1-6.
180. Lai, L.P. and J. Mitchell, *Indian hedgehog: its roles and regulation in endochondral bone development.* J. Cell. Biochem., 2005. **96**(6): p. 1163-1173.
181. Ehlen, H.W., L.A. Buelens, and A. Vortkamp, *Hedgehog signaling in skeletal development.* Birth Defects Res C Embryo Today, 2006. **78**(3): p. 267-79.
182. Gao, B., et al., *Mutations in IHH, encoding Indian hedgehog, cause brachydactyly type A-1.* Nat Genet, 2001. **28**(4): p. 386-8.
183. Hellemans, J., et al., *Homozygous mutations in IHH cause acrocapitofemoral dysplasia, an autosomal recessive disorder with cone-shaped epiphyses in hands and hips.* Am J Hum Genet, 2003. **72**(4): p. 1040-6.
184. St-Jacques, B., M. Hammerschmidt, and A.P. McMahon, *Indian hedgehog signaling regulates proliferation and differentiation of chondrocytes and is essential for bone formation.* Genes Dev, 1999. **13**(16): p. 2072-86.
185. Tavella, S., et al., *Forced chondrocyte expression of sonic hedgehog impairs joint formation affecting proliferation and apoptosis.* Matrix Biol, 2006. **25**(7): p. 389-97.
186. Ferretti, E., et al., *Concerted microRNA control of Hedgehog signalling in cerebellar neuronal progenitor and tumour cells.* EMBO J., 2008. **27**(19): p. 2616-2627.
187. Xu, H.S., et al., *MiR-324-5p inhibits proliferation of glioma by target regulation of GLI1.* Eur. Rev. Med. Pharmacol. Sci., 2014. **18**(6): p. 828-832.
188. Swingler, T.E., et al., *The expression and function of microRNAs in chondrogenesis and osteoarthritis.* Arthritis Rheum, 2012. **64**(6): p. 1909-19.
189. Lin, A.C., et al., *Modulating hedgehog signaling can attenuate the severity of osteoarthritis.* Nat Med, 2009. **15**(12): p. 1421-5.
190. Sandell, L.J. and T. Aigner, *Articular cartilage and changes in arthritis. An introduction: cell biology of osteoarthritis.* Arthritis Res, 2001. **3**(2): p. 107-13.
191. Wei, F., et al., *Activation of Indian hedgehog promotes chondrocyte hypertrophy and upregulation of MMP-13 in human osteoarthritic cartilage.* Osteoarthritis Cartilage, 2012. **20**(7): p. 755-63.
192. Zhou, J., et al., *Disrupting the Indian hedgehog signaling pathway in vivo attenuates surgically induced osteoarthritis progression in Col2a1-CreERT2; Ihhfl/fl mice.* Arthritis Res Ther, 2014. **16**(1): p. R11.
193. Wilson, N.H. and E.T. Stoeckli, *Sonic hedgehog regulates its own receptor on postcrossing commissural axons in a glypican1-dependent manner.* Neuron, 2013. **79**(3): p. 478-91.
194. Cui, S., et al., *Evidence from human and zebrafish that GPC1 is a biliary atresia susceptibility gene.* Gastroenterology, 2013. **144**(5): p. 1107-1115 e3.
195. Salhotra, A., et al., *Mechanisms of bone development and repair.* Nat Rev Mol Cell Biol, 2020. **21**(11): p. 696-711.
196. Feng, X. and S.L. Teitelbaum, *Osteoclasts: New Insights.* Bone Res, 2013. **1**(1): p. 11-26.
197. Dougall, W.C., et al., *RANK is essential for osteoclast and lymph node development.* Genes Dev, 1999. **13**(18): p. 2412-24.
198. Wiktor-Jedrzejczak, W., et al., *Total absence of colony-stimulating factor 1 in the macrophage-deficient osteopetrotic (op/op) mouse.* Proc Natl Acad Sci U S A, 1990. **87**(12): p. 4828-32.
199. Andersen, T.L., et al., *A physical mechanism for coupling bone resorption and formation in adult human bone.* Am J Pathol, 2009. **174**(1): p. 239-47.
200. Everts, V., et al., *The bone lining cell: its role in cleaning Howship's lacunae and initiating bone formation.* J Bone Miner Res, 2002. **17**(1): p. 77-90.
201. Nakashima, T., et al., *Evidence for osteocyte regulation of bone homeostasis through RANKL expression.* Nat Med, 2011. **17**(10): p. 1231-4.
202. Proff, P. and P. Romer, *The molecular mechanism behind bone remodelling: a review.* Clin Oral Investig, 2009. **13**(4): p. 355-62.

203. Xiong, J., et al., *Matrix-embedded cells control osteoclast formation.* Nat Med, 2011. **17**(10): p. 1235-41.
204. Yamashita, T., N. Takahashi, and N. Udagawa, *New roles of osteoblasts involved in osteoclast differentiation.* World J Orthop, 2012. **3**(11): p. 175-81.
205. Zhao, S., et al., *MLO-Y4 osteocyte-like cells support osteoclast formation and activation.* J Bone Miner Res, 2002. **17**(11): p. 2068-79.
206. Boyce, B.F. and L. Xing, *Biology of RANK, RANKL, and osteoprotegerin.* Arthritis Res Ther, 2007. **9 Suppl 1**: p. S1.
207. Yagi, M., et al., *DC-STAMP is essential for cell-cell fusion in osteoclasts and foreign body giant cells.* J Exp Med, 2005. **202**(3): p. 345-51.
208. Takito, J., S. Inoue, and M. Nakamura, *The Sealing Zone in Osteoclasts: A Self-Organized Structure on the Bone.* Int J Mol Sci, 2018. **19**(4).
209. Zou, W. and S.L. Teitelbaum, *Integrins, growth factors, and the osteoclast cytoskeleton.* Ann N Y Acad Sci, 2010. **1192**: p. 27-31.
210. Blair, H.C., et al., *Isolated osteoclasts resorb the organic and inorganic components of bone.* J Cell Biol, 1986. **102**(4): p. 1164-72.
211. Blair, H.C., et al., *Osteoclastic bone resorption by a polarized vacuolar proton pump.* Science, 1989. **245**(4920): p. 855-7.
212. Boskey, A.L. and A.S. Posner, *Bone structure, composition, and mineralization.* Orthop Clin North Am, 1984. **15**(4): p. 597-612.
213. Manolagas, S.C., *Birth and death of bone cells: basic regulatory mechanisms and implications for the pathogenesis and treatment of osteoporosis.* Endocr Rev, 2000. **21**(2): p. 115-37.
214. Weinstein, R.S. and S.C. Manolagas, *Apoptosis and osteoporosis.* Am J Med, 2000. **108**(2): p. 153-64.
215. Jacome-Galarza, C.E., et al., *Developmental origin, functional maintenance and genetic rescue of osteoclasts.* Nature, 2019. **568**(7753): p. 541-545.
216. McDonald, M.M., et al., *Osteoclasts recycle via osteomorphs during RANKL-stimulated bone resorption.* Cell, 2021. **184**(7): p. 1940.
217. Berendsen, A.D. and B.R. Olsen, *Osteoblast-adipocyte lineage plasticity in tissue development, maintenance and pathology.* Cell Mol Life Sci, 2014. **71**(3): p. 493-7.
218. Ambrosi, T.H., M.T. Longaker, and C.K.F. Chan, *A Revised Perspective of Skeletal Stem Cell Biology.* Front Cell Dev Biol, 2019. **7**: p. 189.
219. Marie, P.J., *Transcription factors controlling osteoblastogenesis.* Arch Biochem Biophys, 2008. **473**(2): p. 98-105.
220. Rahman, M.S., et al., *TGF-beta/BMP signaling and other molecular events: regulation of osteoblastogenesis and bone formation.* Bone Res, 2015. **3**: p. 15005.
221. Calvi, L.M., et al., *Activated parathyroid hormone/parathyroid hormone-related protein receptor in osteoblastic cells differentially affects cortical and trabecular bone.* J Clin Invest, 2001. **107**(3): p. 277-86.
222. Dempster, D.W., et al., *Anabolic actions of parathyroid hormone on bone.* Endocr Rev, 1993. **14**(6): p. 690-709.
223. Mosley, J.R., *Osteoporosis and bone functional adaptation: mechanobiological regulation of bone architecture in growing and adult bone, a review.* J Rehabil Res Dev, 2000. **37**(2): p. 189-99.
224. Udagawa, N., et al., *Osteoprotegerin produced by osteoblasts is an important regulator in osteoclast development and function.* Endocrinology, 2000. **141**(9): p. 3478-84.
225. Chen, X., et al., *Osteocytogenesis: Roles of Physicochemical Factors, Collagen Cleavage, and Exogenous Molecules.* Tissue Eng Part B Rev, 2018. **24**(3): p. 215-225.
226. Compton, J.T. and F.Y. Lee, *A review of osteocyte function and the emerging importance of sclerostin.* J Bone Joint Surg Am, 2014. **96**(19): p. 1659-68.
227. Miller, S.C., et al., *Bone lining cells: structure and function.* Scanning Microsc, 1989. **3**(3): p. 953-60; discussion 960-1.

228. Matic, I., et al., *Quiescent Bone Lining Cells Are a Major Source of Osteoblasts During Adulthood.* Stem Cells, 2016. **34**(12): p. 2930-2942.
229. Bonewald, L.F., *Osteocytes as dynamic multifunctional cells.* Ann N Y Acad Sci, 2007. **1116**: p. 281-90.
230. Semenov, M., K. Tamai, and X. He, *SOST is a ligand for LRP5/LRP6 and a Wnt signaling inhibitor.* J Biol Chem, 2005. **280**(29): p. 26770-5.
231. Li, X., et al., *Sclerostin binds to LRP5/6 and antagonizes canonical Wnt signaling.* J Biol Chem, 2005. **280**(20): p. 19883-7.
232. Bellido, T., et al., *Chronic elevation of parathyroid hormone in mice reduces expression of sclerostin by osteocytes: a novel mechanism for hormonal control of osteoblastogenesis.* Endocrinology, 2005. **146**(11): p. 4577-83.
233. O'Brien, C.A., et al., *Control of bone mass and remodeling by PTH receptor signaling in osteocytes.* PLoS One, 2008. **3**(8): p. e2942.
234. Uda, Y., et al., *Osteocyte Mechanobiology.* Curr Osteoporos Rep, 2017. **15**(4): p. 318-325.
235. Wu, X.T., et al., *The potential role of spectrin network in the mechanotransduction of MLO-Y4 osteocytes.* Sci Rep, 2017. **7**: p. 40940.
236. Zhao, D., et al., *Connexin 43 Channels in Osteocytes Regulate Bone Responses to Mechanical Unloading.* Front Physiol, 2020. **11**: p. 299.
237. Qin, L., et al., *Molecular mechanosensors in osteocytes.* Bone Res, 2020. **8**: p. 23.
238. Choi, J.U.A., et al., *The Mechanosensory Role of Osteocytes and Implications for Bone Health and Disease States.* Front Cell Dev Biol, 2021. **9**: p. 770143.
239. Robling, A.G., et al., *Mechanical stimulation of bone in vivo reduces osteocyte expression of Sost/sclerostin.* J Biol Chem, 2008. **283**(9): p. 5866-75.
240. Li, J., et al., *Dkk1-mediated inhibition of Wnt signaling in bone results in osteopenia.* Bone, 2006. **39**(4): p. 754-66.
241. Morvan, F., et al., *Deletion of a single allele of the Dkk1 gene leads to an increase in bone formation and bone mass.* J Bone Miner Res, 2006. **21**(6): p. 934-45.
242. Kennedy, O.D., et al., *Activation of resorption in fatigue-loaded bone involves both apoptosis and active pro-osteoclastogenic signaling by distinct osteocyte populations.* Bone, 2012. **50**(5): p. 1115-22.
243. Cabahug-Zuckerman, P., et al., *Osteocyte Apoptosis Caused by Hindlimb Unloading is Required to Trigger Osteocyte RANKL Production and Subsequent Resorption of Cortical and Trabecular Bone in Mice Femurs.* J Bone Miner Res, 2016. **31**(7): p. 1356-65.
244. Liu, S., et al., *Pathogenic role of Fgf23 in Dmp1-null mice.* Am J Physiol Endocrinol Metab, 2008. **295**(2): p. E254-61.
245. Feng, J.Q., et al., *Loss of DMP1 causes rickets and osteomalacia and identifies a role for osteocytes in mineral metabolism.* Nat Genet, 2006. **38**(11): p. 1310-5.
246. Yoshiko, Y., et al., *Mineralized tissue cells are a principal source of FGF23.* Bone, 2007. **40**(6): p. 1565-73.
247. Shimada, T., et al., *FGF-23 transgenic mice demonstrate hypophosphatemic rickets with reduced expression of sodium phosphate cotransporter type IIa.* Biochem Biophys Res Commun, 2004. **314**(2): p. 409-14.
248. Shimada, T., et al., *Targeted ablation of Fgf23 demonstrates an essential physiological role of FGF23 in phosphate and vitamin D metabolism.* J Clin Invest, 2004. **113**(4): p. 561-8.
249. Benet-Pages, A., et al., *An FGF23 missense mutation causes familial tumoral calcinosis with hyperphosphatemia.* Hum Mol Genet, 2005. **14**(3): p. 385-90.
250. Larsson, T., et al., *A novel recessive mutation in fibroblast growth factor-23 causes familial tumoral calcinosis.* J Clin Endocrinol Metab, 2005. **90**(4): p. 2424-7.
251. White, K.E., et al., *Autosomal-dominant hypophosphatemic rickets (ADHR) mutations stabilize FGF-23.* Kidney Int, 2001. **60**(6): p. 2079-86.
252. Consortium, A., *Autosomal dominant hypophosphataemic rickets is associated with mutations in FGF23.* Nat Genet, 2000. **26**(3): p. 345-8.

253. Wang, H., et al., *Overexpression of fibroblast growth factor 23 suppresses osteoblast differentiation and matrix mineralization in vitro.* J Bone Miner Res, 2008. **23**(6): p. 939-48.
254. Sitara, D., et al., *Genetic evidence of serum phosphate-independent functions of FGF-23 on bone.* PLoS Genet, 2008. **4**(8): p. e1000154.
255. Rowe, P.S., et al., *MEPE, a new gene expressed in bone marrow and tumors causing osteomalacia.* Genomics, 2000. **67**(1): p. 54-68.
256. Gowen, L.C., et al., *Targeted disruption of the osteoblast/osteocyte factor 45 gene (OF45) results in increased bone formation and bone mass.* J Biol Chem, 2003. **278**(3): p. 1998-2007.
257. Petersen, D.N., et al., *Identification of osteoblast/osteocyte factor 45 (OF45), a bone-specific cDNA encoding an RGD-containing protein that is highly expressed in osteoblasts and osteocytes.* J Biol Chem, 2000. **275**(46): p. 36172-80.
258. Jain, A., et al., *Serum levels of matrix extracellular phosphoglycoprotein (MEPE) in normal humans correlate with serum phosphorus, parathyroid hormone and bone mineral density.* J Clin Endocrinol Metab, 2004. **89**(8): p. 4158-61.
259. McGuire, D., et al., *Intra-articular TPX-100 in knee osteoarthritis: Robust functional response at 6 and 12 months is associated with increased tibiofemoral cartilage thickness.* Arthritis Rhematol, 2018. **70**: p. L16.
260. McGuire, D., et al., *TPX-100 leads to marked, sustained improvements in subjects with knee osteoarthritis: pre-clinical rationale and results of a controlled clinical trial.* Osteoarthritis and Cartilage, 2018. **26**: p. S243.
261. Lerner, U.H., *Bone remodeling in post-menopausal osteoporosis.* J Dent Res, 2006. **85**(7): p. 584-95.
262. Gallagher, J.C. and A.J. Sai, *Molecular biology of bone remodeling: implications for new therapeutic targets for osteoporosis.* Maturitas, 2010. **65**(4): p. 301-7.
263. Downey, P.A. and M.I. Siegel, *Bone biology and the clinical implications for osteoporosis.* Phys Ther, 2006. **86**(1): p. 77-91.
264. Gauthier, A., et al., *Epidemiological burden of postmenopausal osteoporosis in the UK from 2010 to 2021: estimations from a disease model.* Arch Osteoporos, 2011. **6**: p. 179-88.
265. Riggs, B.L. and L.J. Melton, 3rd, *The worldwide problem of osteoporosis: insights afforded by epidemiology.* Bone, 1995. **17**(5 Suppl): p. 505S-511S.
266. Stark, Z. and R. Savarirayan, *Osteopetrosis.* Orphanet J Rare Dis, 2009. **4**: p. 5.
267. Bollerslev, J. and P.E. Andersen, Jr., *Radiological, biochemical and hereditary evidence of two types of autosomal dominant osteopetrosis.* Bone, 1988. **9**(1): p. 7-13.
268. Al-Tamimi, Y.Z., et al., *Patients with autosomal-recessive osteopetrosis presenting with hydrocephalus and hindbrain posterior fossa crowding.* J Neurosurg Pediatr, 2008. **1**(1): p. 103-6.
269. Mohn, A., et al., *Autosomal malignant osteopetrosis. From diagnosis to therapy.* Minerva Pediatr, 2004. **56**(1): p. 115-8.
270. Benichou, O.D., J.D. Laredo, and M.C. de Vernejoul, *Type II autosomal dominant osteopetrosis (Albers-Schonberg disease): clinical and radiological manifestations in 42 patients.* Bone, 2000. **26**(1): p. 87-93.
271. Waguespack, S.G., et al., *Autosomal dominant osteopetrosis: clinical severity and natural history of 94 subjects with a chloride channel 7 gene mutation.* J Clin Endocrinol Metab, 2007. **92**(3): p. 771-8.
272. Kilic, S.S. and A. Etzioni, *The clinical spectrum of leukocyte adhesion deficiency (LAD) III due to defective CalDAG-GEF1.* J Clin Immunol, 2009. **29**(1): p. 117-22.
273. Saftig, P., et al., *Impaired osteoclastic bone resorption leads to osteopetrosis in cathepsin-K-deficient mice.* Proc Natl Acad Sci U S A, 1998. **95**(23): p. 13453-8.
274. Sly, W.S., et al., *Carbonic anhydrase II deficiency identified as the primary defect in the autosomal recessive syndrome of osteopetrosis with renal tubular acidosis and cerebral calcification.* Proc Natl Acad Sci U S A, 1983. **80**(9): p. 2752-6.
275. Guerrini, M.M., et al., *Human osteoclast-poor osteopetrosis with hypogammaglobulinemia due to TNFRSF11A (RANK) mutations.* Am J Hum Genet, 2008. **83**(1): p. 64-76.

276. Sobacchi, C., et al., *Osteoclast-poor human osteopetrosis due to mutations in the gene encoding RANKL.* Nat Genet, 2007. **39**(8): p. 960-2.
277. Yoshida, H., et al., *The murine mutation osteopetrosis is in the coding region of the macrophage colony stimulating factor gene.* Nature, 1990. **345**(6274): p. 442-4.
278. Detheridge, F.M., P.B. Guyer, and D.J. Barker, *European distribution of Paget's disease of bone.* Br Med J (Clin Res Ed), 1982. **285**(6347): p. 1005-8.
279. Ralston, S.H., A.L. Langston, and I.R. Reid, *Pathogenesis and management of Paget's disease of bone.* Lancet, 2008. **372**(9633): p. 155-63.
280. Laurin, N., et al., *Recurrent mutation of the gene encoding sequestosome 1 (SQSTM1/p62) in Paget disease of bone.* Am J Hum Genet, 2002. **70**(6): p. 1582-8.
281. Rea, S.L., et al., *SQSTM1 mutations--bridging Paget disease of bone and ALS/FTLD.* Exp Cell Res, 2014. **325**(1): p. 27-37.
282. Hughes, A.E., et al., *Mutations in TNFRSF11A, affecting the signal peptide of RANK, cause familial expansile osteolysis.* Nat Genet, 2000. **24**(1): p. 45-8.
283. Baron, R., S. Ferrari, and R.G. Russell, *Denosumab and bisphosphonates: different mechanisms of action and effects.* Bone, 2011. **48**(4): p. 677-92.
284. Berg, C., K. Neumeyer, and P. Kirkpatrick, *Teriparatide.* Nat Rev Drug Discov, 2003. **2**(4): p. 257-8.
285. McClung, M.R., et al., *Romosozumab in postmenopausal women with low bone mineral density.* N Engl J Med, 2014. **370**(5): p. 412-20.
286. Ferrari, S.L., *Osteoporosis: Romosozumab to rebuild the foundations of bone strength.* Nat Rev Rheumatol, 2018. **14**(3): p. 128.
287. Hanna, J., G.S. Hossain, and J. Kocerha, *The Potential for microRNA Therapeutics and Clinical Research.* Front Genet, 2019. **10**: p. 478.
288. Inoue, K., et al., *Bone protection by inhibition of microRNA-182.* Nat Commun, 2018. **9**(1): p. 4108.
289. Kim, Y.K., *RNA therapy: rich history, various applications and unlimited future prospects.* Exp Mol Med, 2022. **54**(4): p. 455-465.
290. Roberts, T.C., R. Langer, and M.J.A. Wood, *Advances in oligonucleotide drug delivery.* Nat Rev Drug Discov, 2020. **19**(10): p. 673-694.
291. Ray, K.K., et al., *Inclisiran in Patients at High Cardiovascular Risk with Elevated LDL Cholesterol.* N Engl J Med, 2017. **376**(15): p. 1430-1440.
292. Damase, T.R., et al., *The Limitless Future of RNA Therapeutics.* Front Bioeng Biotechnol, 2021. **9**: p. 628137.
293. Lee, S.W.L., et al., *MicroRNA delivery through nanoparticles.* J Control Release, 2019. **313**: p. 80-95.
294. Dasgupta, I. and A. Chatterjee, *Recent Advances in miRNA Delivery Systems.* Methods Protoc, 2021. **4**(1).
295. Puppo, M., et al., *Non-coding RNAs in bone remodelling and bone metastasis: Mechanisms of action and translational relevance.* Br J Pharmacol, 2021. **178**(9): p. 1936-1954.
296. Cui, Q., et al., *Mmu-miR-185 depletion promotes osteogenic differentiation and suppresses bone loss in osteoporosis through the Bgn-mediated BMP/Smad pathway.* Cell Death Dis, 2019. **10**(3): p. 172.
297. Miguez, P.A., *Evidence of biglycan structure-function in bone homeostasis and aging.* Connect Tissue Res, 2020. **61**(1): p. 19-33.
298. Jongwattanapisan, P., et al., *Identification of the effector domain of biglycan that facilitates BMP-2 osteogenic function.* Sci Rep, 2018. **8**(1): p. 7022.
299. Bruderer, M., et al., *Role and regulation of RUNX2 in osteogenesis.* Eur Cell Mater, 2014. **28**: p. 269-86.
300. Shi, X. and Z. Zhang, *MicroRNA-135a-5p is involved in osteoporosis progression through regulation of osteogenic differentiation by targeting RUNX2.* Exp Ther Med, 2019. **18**(4): p. 2393-2400.

301. Kong, L., et al., *Silencing MicroRNA-137-3p, which Targets RUNX2 and CXCL12 Prevents Steroid-induced Osteonecrosis of the Femoral Head by Facilitating Osteogenesis and Angiogenesis.* Int J Biol Sci, 2020. **16**(4): p. 655-670.
302. Liu, H., et al., *MicroRNA-155 inhibits the osteogenic differentiation of mesenchymal stem cells induced by BMP9 via downregulation of BMP signaling pathway.* Int J Mol Med, 2018. **41**(6): p. 3379-3393.
303. Yang, J.X., et al., *Osteoclast-derived miR-23a-5p-containing exosomes inhibit osteogenic differentiation by regulating Runx2.* Cell Signal, 2020. **70**: p. 109504.
304. Tzeng, Y.S., et al., *Imbalanced Osteogenesis and Adipogenesis in Mice Deficient in the Chemokine Cxcl12/Sdf1 in the Bone Mesenchymal Stem/Progenitor Cells.* J Bone Miner Res, 2018. **33**(4): p. 679-690.
305. Zeng, H.C., et al., *MicroRNA miR-23a cluster promotes osteocyte differentiation by regulating TGF-beta signalling in osteoblasts.* Nat Commun, 2017. **8**: p. 15000.
306. Hassan, M.Q., et al., *A network connecting Runx2, SATB2, and the miR-23a~27a~24-2 cluster regulates the osteoblast differentiation program.* Proc Natl Acad Sci U S A, 2010. **107**(46): p. 19879-84.
307. Armstrong, A.P., et al., *A RANK/TRAF6-dependent signal transduction pathway is essential for osteoclast cytoskeletal organization and resorptive function.* J Biol Chem, 2002. **277**(46): p. 44347-56.
308. Nakasa, T., et al., *The inhibitory effect of microRNA-146a expression on bone destruction in collagen-induced arthritis.* Arthritis Rheum, 2011. **63**(6): p. 1582-90.
309. Ammari, M., et al., *Delivery of miR-146a to Ly6C(high) Monocytes Inhibits Pathogenic Bone Erosion in Inflammatory Arthritis.* Theranostics, 2018. **8**(21): p. 5972-5985.
310. Lee, Y., et al., *MicroRNA-124 regulates osteoclast differentiation.* Bone, 2013. **56**(2): p. 383-9.
311. Nakamachi, Y., et al., *MicroRNA-124 inhibits the progression of adjuvant-induced arthritis in rats.* Ann Rheum Dis, 2016. **75**(3): p. 601-8.
312. Wang, C., et al., *Reduced miR-144-3p expression in serum and bone mediates osteoporosis pathogenesis by targeting RANK.* Biochem Cell Biol, 2018. **96**(5): p. 627-635.
313. Chen, C., et al., *MiR-503 regulates osteoclastogenesis via targeting RANK.* J Bone Miner Res, 2014. **29**(2): p. 338-47.
314. Yin, Y., et al., *MiR-30a attenuates osteoclastogenesis via targeting DC-STAMP-c-Fos-NFATc1 signaling.* Am J Transl Res, 2017. **9**(12): p. 5743-5753.
315. Dou, C., et al., *MiR-7b directly targets DC-STAMP causing suppression of NFATc1 and c-Fos signaling during osteoclast fusion and differentiation.* Biochim Biophys Acta, 2014. **1839**(11): p. 1084-96.
316. Feichtinger, X., et al., *Bone-related Circulating MicroRNAs miR-29b-3p, miR-550a-3p, and miR-324-3p and their Association to Bone Microstructure and Histomorphometry.* Sci Rep, 2018. **8**(1): p. 4867.
317. Kocijan, R., et al., *Circulating microRNA Signatures in Patients With Idiopathic and Postmenopausal Osteoporosis and Fragility Fractures.* J Clin Endocrinol Metab, 2016. **101**(11): p. 4125-4134.
318. Weilner, S., et al., *Differentially circulating miRNAs after recent osteoporotic fractures can influence osteogenic differentiation.* Bone, 2015. **79**: p. 43-51.
319. Liang, M., et al., *Osteoclast-derived small extracellular vesicles induce osteogenic differentiation via inhibiting ARHGAP1.* Mol Ther Nucleic Acids, 2021. **23**: p. 1191-1203.
320. Hayman, D.J., et al., *Increased hippocampal excitability in miR-324-null mice.* Sci Rep, 2021. **11**(1): p. 10452.
321. Labun, K., et al., *CHOPCHOP v2: a web tool for the next generation of CRISPR genome engineering.* Nucleic Acids Res., 2016. **44**(W1): p. W272-6.
322. Montague, T.G., et al., *CHOPCHOP: a CRISPR/Cas9 and TALEN web tool for genome editing.* Nucleic Acids Res., 2014. **42**(Web Server issue): p. W401-7.
323. Schindelin, J., et al., *Fiji: an open-source platform for biological-image analysis.* Nat Methods, 2012. **9**(7): p. 676-82.

324. Franklin, K.B.J. and G. Paxinos, *The mouse brain in stereotaxic coordinates*. 1997, San Diego: Academic Press.
325. Williams, R.W., *Mapping genes that modulate mouse brain development: a quantitative genetic approach.* Results Probl Cell Differ, 2000. **30**: p. 21-49.
326. Wang, F., et al., *RNAscope: a novel in situ RNA analysis platform for formalin-fixed, paraffin-embedded tissues.* J Mol Diagn, 2012. **14**(1): p. 22-9.
327. J. Gan, S.L., Y. Zhang, L. He, L. Bai, R. Liao, J. Zhao, M. Guo, W. Jiang, J. Li, Q. Li, G. Mu, Y. Wu, X. Wang, X. Zhang, D. Zhou, H. Lv, Z. Wang, Y. Zhang, C. Qian, M. Feng, H. Chen, Q. Meng, X. Huang, *MicroRNA-375 is a therapeutic target for castration-resistant prostate cancer through the PTPN4/STAT3 axis.* Experimental & Molecular Medicine, 2022(54): p. 1290–1305.
328. Fanselow, M.S. and H.W. Dong, *Are the dorsal and ventral hippocampus functionally distinct structures?* Neuron, 2010. **65**(1): p. 7-19.
329. Moser, M.B. and E.I. Moser, *Functional differentiation in the hippocampus.* Hippocampus, 1998. **8**(6): p. 608-19.
330. Sun, Q., Y.Q. Jiang, and M.C. Lu, *Topographic heterogeneity of intrinsic excitability in mouse hippocampal CA3 pyramidal neurons.* J Neurophysiol, 2020. **124**(4): p. 1270-1284.
331. Antoniades, A., et al., *Detection of Interictal Discharges With Convolutional Neural Networks Using Discrete Ordered Multichannel Intracranial EEG.* IEEE Trans Neural Syst Rehabil Eng, 2017. **25**(12): p. 2285-2294.
332. Staba, R.J. and A. Bragin, *High-frequency oscillations and other electrophysiological biomarkers of epilepsy: underlying mechanisms.* Biomark Med, 2011. **5**(5): p. 545-56.
333. Staba, R.J., M. Stead, and G.A. Worrell, *Electrophysiological biomarkers of epilepsy.* Neurotherapeutics, 2014. **11**(2): p. 334-46.
334. Mabrouk, O.S., et al., *Automated touch screen device for recording complex rodent behaviors.* J Neurosci Methods, 2014. **233**: p. 129-36.
335. Bray, N.L., et al., *Near-optimal probabilistic RNA-seq quantification.* Nat Biotechnol, 2016. **34**(5): p. 525-7.
336. Church, D.M., et al., *Lineage-specific biology revealed by a finished genome assembly of the mouse.* PLoS Biol, 2009. **7**(5): p. e1000112.
337. Soneson, C., M.I. Love, and M.D. Robinson, *Differential analyses for RNA-seq: transcript-level estimates improve gene-level inferences.* F1000Res, 2015. **4**: p. 1521.
338. Love, M.I., W. Huber, and S. Anders, *Moderated estimation of fold change and dispersion for RNA-seq data with DESeq2.* Genome Biol, 2014. **15**(12): p. 550.
339. Robinson, J.T., et al., *Integrative genomics viewer.* Nat Biotechnol, 2011. **29**(1): p. 24-6.
340. Thorvaldsdottir, H., J.T. Robinson, and J.P. Mesirov, *Integrative Genomics Viewer (IGV): high-performance genomics data visualization and exploration.* Brief Bioinform, 2013. **14**(2): p. 178-92.
341. Plaisier, S.B., et al., *Rank-rank hypergeometric overlap: identification of statistically significant overlap between gene-expression signatures.* Nucleic Acids Res, 2010. **38**(17): p. e169.
342. Rosenblatt, J.D. and J.L. Stein, *RRHO: test overlap using the rank-rank hypergeometric test,* https://www.bioconductor.org/packages/release/bioc/html/RRHO.html. 2014.
343. Schriml, L.M., et al., *Human Disease Ontology 2018 update: classification, content and workflow expansion.* Nucleic Acids Res, 2019. **47**(D1): p. D955-D962.
344. Durinck, S., et al., *Mapping identifiers for the integration of genomic datasets with the R/Bioconductor package biomaRt.* Nat Protoc, 2009. **4**(8): p. 1184-91.
345. Young, M.D., et al., *Gene ontology analysis for RNA-seq: accounting for selection bias.* Genome Biol, 2010. **11**(2): p. R14.
346. Johnson de Sousa Brito, F.M., et al., *Syndecan-3 enhances anabolic bone formation through WNT signaling.* FASEB J, 2021. **35**(4): p. e21246.
347. van 't Hof, R.J., et al., *Open source software for semi-automated histomorphometry of bone resorption and formation parameters.* Bone, 2017. **99**: p. 69-79.

348. Glasson, S.S., T.J. Blanchet, and E.A. Morris, *The surgical destabilization of the medial meniscus (DMM) model of osteoarthritis in the 129/SvEv mouse.* Osteoarthritis Cartilage, 2007. **15**(9): p. 1061-1069.
349. Qing, H., et al., *Demonstration of osteocytic perilacunar/canalicular remodeling in mice during lactation.* J Bone Miner Res, 2012. **27**(5): p. 1018-29.
350. Varani, G. and W.H. McClain, *The G x U wobble base pair. A fundamental building block of RNA structure crucial to RNA function in diverse biological systems.* EMBO Rep, 2000. **1**(1): p. 18-23.
351. Vejnar, C.E. and E.M. Zdobnov, *MiRmap: comprehensive prediction of microRNA target repression strength.* Nucleic Acids Res, 2012. **40**(22): p. 11673-83.
352. Youlten, S.E., et al., *Osteocyte transcriptome mapping identifies a molecular landscape controlling skeletal homeostasis and susceptibility to skeletal disease.* Nat Commun, 2021. **12**(1): p. 2444.
353. Soul, J., et al., *OATargets: a knowledge base of genes associated with osteoarthritis joint damage in animals.* Ann Rheum Dis, 2020.
354. Kato, Y., et al., *Establishment of an osteocyte-like cell line, MLO-Y4.* J Bone Miner Res, 1997. **12**(12): p. 2014-23.
355. Ghali, O., et al., *Dexamethasone in osteogenic medium strongly induces adipocyte differentiation of mouse bone marrow stromal cells and increases osteoblast differentiation.* BMC Cell Biol, 2015. **16**: p. 9.
356. Barter, M.J., et al., *The long non-coding RNA ROCR contributes to SOX9 expression and chondrogenic differentiation of human mesenchymal stem cells.* Development, 2017. **144**(24): p. 4510-4521.
357. R Core Team, *A language and environment for statistical computing*. 2019, R Foundation for Statistical Computing: Vienna, Austria.
358. Bao, J., et al., *MicroRNA-449 and microRNA-34b/c function redundantly in murine testes by targeting E2F transcription factor-retinoblastoma protein (E2F-pRb) pathway.* J Biol Chem, 2012. **287**(26): p. 21686-98.
359. Wu, J., et al., *Two miRNA clusters, miR-34b/c and miR-449, are essential for normal brain development, motile ciliogenesis, and spermatogenesis.* Proc Natl Acad Sci U S A, 2014. **111**(28): p. E2851-7.
360. Zemel, B.M., et al., *A-Type KV Channels in Dorsal Root Ganglion Neurons: Diversity, Function, and Dysfunction.* Front Mol Neurosci, 2018. **11**: p. 253.
361. Falcon-Moya, R., T.S. Sihra, and A. Rodriguez-Moreno, *Kainate Receptors: Role in Epilepsy.* Front Mol Neurosci, 2018. **11**: p. 217.
362. Fisahn, A., *Kainate receptors and rhythmic activity in neuronal networks: hippocampal gamma oscillations as a tool.* J Physiol, 2005. **562**(Pt 1): p. 65-72.
363. Smith, E.H., et al., *Human interictal epileptiform discharges are bidirectional traveling waves echoing ictal discharges.* Elife, 2022. **11**.
364. Kim, H., et al., *A Mechanism for microRNA Arm Switching Regulated by Uridylation.* Mol Cell, 2020. **78**(6): p. 1224-1236 e5.
365. Kozomara, A., M. Birgaoanu, and S. Griffiths-Jones, *miRBase: from microRNA sequences to function.* Nucleic Acids Res, 2019. **47**(D1): p. D155-D162.
366. Kozomara, A. and S. Griffiths-Jones, *miRBase: annotating high confidence microRNAs using deep sequencing data.* Nucleic Acids Res, 2014. **42**(Database issue): p. D68-73.
367. Kandratavicius, L., et al., *Animal models of epilepsy: use and limitations.* Neuropsychiatr Dis Treat, 2014. **10**: p. 1693-705.
368. Wang, C., et al., *Imaging epileptic foci in mouse models via a low-density lipoprotein receptor-related protein-1 targeting strategy.* EBioMedicine, 2021. **63**: p. 103156.
369. Hawkins, N.A., et al., *Screening of conventional anticonvulsants in a genetic mouse model of epilepsy.* Ann Clin Transl Neurol, 2017. **4**(5): p. 326-339.
370. Takeda, Y., et al., *Impaired motor coordination in mice lacking neural recognition molecule NB-3 of the contactin/F3 subgroup.* J Neurobiol, 2003. **56**(3): p. 252-65.

371. Levin, S.I., et al., *Impaired motor function in mice with cell-specific knockout of sodium channel Scn8a (NaV1.6) in cerebellar purkinje neurons and granule cells.* J Neurophysiol, 2006. **96**(2): p. 785-93.
372. O'Leary, T.P., et al., *Motor function deficits in the 12 month-old female 5xFAD mouse model of Alzheimer's disease.* Behav Brain Res, 2018. **337**: p. 256-263.
373. Li, Y., et al., *An inducible transgenic Cre mouse line for the study of hippocampal development and adult neurogenesis.* Genesis, 2011. **49**(12): p. 919-26.
374. Zhou, W., et al., *A transgenic Cre mouse line for the study of cortical and hippocampal development.* Genesis, 2010. **48**(5): p. 343-50.
375. Sun, C., et al., *Astrocytic miR-324-5p is essential for synaptic formation by suppressing the secretion of CCL5 from astrocytes.* Cell Death Dis, 2019. **10**(2): p. 141.
376. Gu, J., et al., *Downregulated miRNA-324-5p aggravates neuronal injury induced by oxygen-glucose deprivation via modulating RAN.* Exp Ther Med, 2020. **19**(1): p. 658-664.
377. Jaeger, B., et al., *Pyridoxine responsive epilepsy caused by a novel homozygous PNPO mutation.* Mol Genet Metab Rep, 2016. **6**: p. 60-3.
378. Wilson, M.P., et al., *Disorders affecting vitamin B6 metabolism.* J Inherit Metab Dis, 2019. **42**(4): p. 629-646.
379. Mills, P.B., et al., *Epilepsy due to PNPO mutations: genotype, environment and treatment affect presentation and outcome.* Brain, 2014. **137**(Pt 5): p. 1350-60.
380. Wang, H.S., et al., *Pyridoxal phosphate is better than pyridoxine for controlling idiopathic intractable epilepsy.* Arch Dis Child, 2005. **90**(5): p. 512-5.
381. Sass, J.O., et al., *Functional deficiencies of sulfite oxidase: Differential diagnoses in neonates presenting with intractable seizures and cystic encephalomalacia.* Brain Dev, 2010. **32**(7): p. 544-9.
382. Haga, K., et al., *Functional receptor molecules CD300lf and CD300ld within the CD300 family enable murine noroviruses to infect cells.* Proc Natl Acad Sci U S A, 2016. **113**(41): p. E6248-E6255.
383. Wilen, C.B., et al., *Tropism for tuft cells determines immune promotion of norovirus pathogenesis.* Science, 2018. **360**(6385): p. 204-208.
384. Graziano, V.R., et al., *CD300lf is the primary physiologic receptor of murine norovirus but not human norovirus.* PLoS Pathog, 2020. **16**(4): p. e1008242.
385. Lee, S.M., et al., *CD300F blocks both MyD88 and TRIF-mediated TLR signaling through activation of Src homology region 2 domain-containing phosphatase 1.* J Immunol, 2011. **186**(11): p. 6296-303.
386. Visse, R. and H. Nagase, *Matrix metalloproteinases and tissue inhibitors of metalloproteinases: structure, function, and biochemistry.* Circ Res, 2003. **92**(8): p. 827-39.
387. Page-McCaw, A., A.J. Ewald, and Z. Werb, *Matrix metalloproteinases and the regulation of tissue remodelling.* Nat Rev Mol Cell Biol, 2007. **8**(3): p. 221-33.
388. Bronisz, E. and I. Kurkowska-Jastrzebska, *Matrix Metalloproteinase 9 in Epilepsy: The Role of Neuroinflammation in Seizure Development.* Mediators Inflamm, 2016. **2016**: p. 7369020.
389. Reinhard, S.M., K. Razak, and I.M. Ethell, *A delicate balance: role of MMP-9 in brain development and pathophysiology of neurodevelopmental disorders.* Front Cell Neurosci, 2015. **9**: p. 280.
390. Rempe, R.G., et al., *Matrix Metalloproteinase-Mediated Blood-Brain Barrier Dysfunction in Epilepsy.* J Neurosci, 2018. **38**(18): p. 4301-4315.
391. Takacs, E., et al., *Matrix metalloproteinase-9 activity increased by two different types of epileptic seizures that do not induce neuronal death: a possible role in homeostatic synaptic plasticity.* Neurochem Int, 2010. **56**(6-7): p. 799-809.
392. Jen, Y.H., M. Musacchio, and A.D. Lander, *Glypican-1 controls brain size through regulation of fibroblast growth factor signaling in early neurogenesis.* Neural Dev, 2009. **4**: p. 33.
393. Guo, H., et al., *Mammalian microRNAs predominantly act to decrease target mRNA levels.* Nature, 2010. **466**(7308): p. 835-40.

394. Thalman, C., et al., *Synaptic phospholipids as a new target for cortical hyperexcitability and E/I balance in psychiatric disorders.* Mol Psychiatry, 2018. **23**(8): p. 1699-1710.
395. Stern, S., et al., *Neurons derived from patients with bipolar disorder divide into intrinsically different sub-populations of neurons, predicting the patients' responsiveness to lithium.* Mol Psychiatry, 2018. **23**(6): p. 1453-1465.
396. Mertens, J., et al., *Differential responses to lithium in hyperexcitable neurons from patients with bipolar disorder.* Nature, 2015. **527**(7576): p. 95-9.
397. Behrendt, R.P. and C. Young, *Hallucinations in schizophrenia, sensory impairment, and brain disease: a unifying model.* Behav Brain Sci, 2004. **27**(6): p. 771-87; discussion 787-830.
398. Abulseoud, O.A., et al., *Lateral hypothalamic kindling induces manic-like behavior in rats: a novel animal model.* Int J Bipolar Disord, 2014. **2**(1): p. 7.
399. Del Arco, A., et al., *Hyperactivity to novelty induced by social isolation is not correlated with changes in D2 receptor function and binding in striatum.* Psychopharmacology (Berl), 2004. **171**(2): p. 148-55.
400. Dalley, J.W., et al., *Specific abnormalities in serotonin release in the prefrontal cortex of isolation-reared rats measured during behavioural performance of a task assessing visuospatial attention and impulsivity.* Psychopharmacology (Berl), 2002. **164**(3): p. 329-40.
401. Silva-Gomez, A.B., et al., *Decreased dendritic spine density on prefrontal cortical and hippocampal pyramidal neurons in postweaning social isolation rats.* Brain Res, 2003. **983**(1-2): p. 128-36.
402. Fone, K.C., et al., *Increased 5-HT2C receptor responsiveness occurs on rearing rats in social isolation.* Psychopharmacology (Berl), 1996. **123**(4): p. 346-52.
403. Jones, C.A., D.J. Watson, and K.C. Fone, *Animal models of schizophrenia.* Br J Pharmacol, 2011. **164**(4): p. 1162-94.
404. Jang, Y., et al., *Dysregulated long non-coding RNAs in the temporal lobe epilepsy mouse model.* Seizure, 2018. **58**: p. 110-119.
405. Srivastava, P.K., et al., *Genome-wide analysis of differential RNA editing in epilepsy.* Genome Res, 2017. **27**(3): p. 440-450.
406. Simkin, D., et al., *Aging-Related Hyperexcitability in CA3 Pyramidal Neurons Is Mediated by Enhanced A-Type K+ Channel Function and Expression.* J Neurosci, 2015. **35**(38): p. 13206-18.
407. Oh, M.M., D. Simkin, and J.F. Disterhoft, *Intrinsic Hippocampal Excitability Changes of Opposite Signs and Different Origins in CA1 and CA3 Pyramidal Neurons Underlie Aging-Related Cognitive Deficits.* Front Syst Neurosci, 2016. **10**: p. 52.
408. Ortiz-Gonzalez, X.R., et al., *Focal cortical dysplasia is more common in boys than in girls.* Epilepsy Behav, 2013. **27**(1): p. 121-3.
409. Taylor, I., et al., *Is photosensitive epilepsy less common in males due to variation in X chromosome photopigment genes?* Epilepsia, 2007. **48**(9): p. 1807-1809.
410. McHugh, J.C. and N. Delanty, *Epidemiology and classification of epilepsy: gender comparisons.* Int Rev Neurobiol, 2008. **83**: p. 11-26.
411. Scharfman, H.E. and N.J. MacLusky, *Sex differences in the neurobiology of epilepsy: a preclinical perspective.* Neurobiol Dis, 2014. **72 Pt B**: p. 180-92.
412. Li, N., et al., *Up-regulation of key microRNAs, and inverse down-regulation of their predicted oxidative phosphorylation target genes, during aging in mouse brain.* Neurobiol Aging, 2011. **32**(5): p. 944-55.
413. Li, X., et al., *Circulatory miR34a as an RNAbased, noninvasive biomarker for brain aging.* Aging (Albany NY), 2011. **3**(10): p. 985-1002.
414. Bernardo, B.C., et al., *Sex differences in response to miRNA-34a therapy in mouse models of cardiac disease: identification of sex-, disease- and treatment-regulated miRNAs.* J Physiol, 2016. **594**(20): p. 5959-5974.
415. Duque, G., et al., *Age-related bone loss in the LOU/c rat model of healthy ageing.* Exp Gerontol, 2009. **44**(3): p. 183-9.
416. Colman, R.J., et al., *Skeletal effects of aging in male rhesus monkeys.* Bone, 1999. **24**(1): p. 17-23.

417. Glatt, V., et al., *Age-related changes in trabecular architecture differ in female and male C57BL/6J mice.* J Bone Miner Res, 2007. **22**(8): p. 1197-207.
418. Ferguson, V.L., et al., *Bone development and age-related bone loss in male C57BL/6J mice.* Bone, 2003. **33**(3): p. 387-98.
419. Halloran, B.P., et al., *Changes in bone structure and mass with advancing age in the male C57BL/6J mouse.* J Bone Miner Res, 2002. **17**(6): p. 1044-50.
420. Bucay, N., et al., *osteoprotegerin-deficient mice develop early onset osteoporosis and arterial calcification.* Genes Dev, 1998. **12**(9): p. 1260-8.
421. Komori, T., et al., *Targeted disruption of Cbfa1 results in a complete lack of bone formation owing to maturational arrest of osteoblasts.* Cell, 1997. **89**(5): p. 755-64.
422. Dallas, S.L., M. Prideaux, and L.F. Bonewald, *The osteocyte: an endocrine cell ... and more.* Endocr Rev, 2013. **34**(5): p. 658-90.
423. Powell, W.F., Jr., et al., *Targeted ablation of the PTH/PTHrP receptor in osteocytes impairs bone structure and homeostatic calcemic responses.* J Endocrinol, 2011. **209**(1): p. 21-32.
424. Bivi, N., et al., *Cell autonomous requirement of connexin 43 for osteocyte survival: consequences for endocortical resorption and periosteal bone formation.* J Bone Miner Res, 2012. **27**(2): p. 374-89.
425. Lu, Y., et al., *DMP1-targeted Cre expression in odontoblasts and osteocytes.* J Dent Res, 2007. **86**(4): p. 320-5.
426. Xiong, J., et al., *Osteocyte-derived RANKL is a critical mediator of the increased bone resorption caused by dietary calcium deficiency.* Bone, 2014. **66**: p. 146-54.
427. Ritman, E.L., *Current status of developments and applications of micro-CT.* Annu Rev Biomed Eng, 2011. **13**: p. 531-52.
428. Flannery, B.P., et al., *Three-Dimensional X-ray Microtomography.* Science, 1987. **237**(4821): p. 1439-44.
429. Stock, S.R., *Trends in micro- and nanoComputed Tomography 2008-2010.* Developments in X-Ray Tomography, 2010. **VII**.
430. Filgueira, L., *Fluorescence-based staining for tartrate-resistant acidic phosphatase (TRAP) in osteoclasts combined with other fluorescent dyes and protocols.* J Histochem Cytochem, 2004. **52**(3): p. 411-4.
431. Iwaniec, U.T., T.J. Wronski, and R.T. Turner, *Histological analysis of bone.* Methods Mol Biol, 2008. **447**: p. 325-41.
432. Villanueva, A.R., *A New Goldner's One-Step Trichrome Stain for Identification of Osteoid Seams, Bone and Cells in Undecalcified, Plastic Embedded Sections of Bone.* Journal of Histotechnology, 1988. **11**(4): p. 249-251.
433. Gruber, H.E., *Adaptations of Goldner's Masson trichrome stain for the study of undecalcified plastic embedded bone.* Biotech Histochem, 1992. **67**(1): p. 30-4.
434. Salmon, P.L., et al., *Structure Model Index Does Not Measure Rods and Plates in Trabecular Bone.* Front Endocrinol (Lausanne), 2015. **6**: p. 162.
435. Sheng, M.H., et al., *Histomorphometric studies show that bone formation and bone mineral apposition rates are greater in C3H/HeJ (high-density) than C57BL/6J (low-density) mice during growth.* Bone, 1999. **25**(4): p. 421-9.
436. Carpenter, T.O., et al., *Rickets.* Nat Rev Dis Primers, 2017. **3**: p. 17101.
437. Jamsa, T., et al., *Comparison of three-point bending test and peripheral quantitative computed tomography analysis in the evaluation of the strength of mouse femur and tibia.* Bone, 1998. **23**(2): p. 155-61.
438. Langdahl, B., S. Ferrari, and D.W. Dempster, *Bone modeling and remodeling: potential as therapeutic targets for the treatment of osteoporosis.* Ther Adv Musculoskelet Dis, 2016. **8**(6): p. 225-235.
439. Epker, B.N. and H.M. Frost, *Periosteal appositional bone growth from age two to age seventy in man. A tetracycline evaluation.* Anat Rec, 1966. **154**(3): p. 573-7.
440. Myers, E.R. and S.E. Wilson, *Biomechanics of osteoporosis and vertebral fracture.* Spine (Phila Pa 1976), 1997. **22**(24 Suppl): p. 25S-31S.

441. Chen, Q., et al., *An osteopontin-integrin interaction plays a critical role in directing adipogenesis and osteogenesis by mesenchymal stem cells.* Stem Cells, 2014. **32**(2): p. 327-37.
442. Sen, B., et al., *mTORC2 regulates mechanically induced cytoskeletal reorganization and lineage selection in marrow-derived mesenchymal stem cells.* J Bone Miner Res, 2014. **29**(1): p. 78-89.
443. Moon, Y.S., et al., *Mice lacking paternally expressed Pref-1/Dlk1 display growth retardation and accelerated adiposity.* Mol Cell Biol, 2002. **22**(15): p. 5585-92.
444. Tian, F., et al., *Core binding factor beta (Cbfbeta) controls the balance of chondrocyte proliferation and differentiation by upregulating Indian hedgehog (Ihh) expression and inhibiting parathyroid hormone-related protein receptor (PPR) expression in postnatal cartilage and bone formation.* J Bone Miner Res, 2014. **29**(7): p. 1564-1574.
445. Kurosaka, H., et al., *Core binding factor beta functions in the maintenance of stem cells and orchestrates continuous proliferation and differentiation in mouse incisors.* Stem Cells, 2011. **29**(11): p. 1792-803.
446. Yoshida, C.A., et al., *Core-binding factor beta interacts with Runx2 and is required for skeletal development.* Nat Genet, 2002. **32**(4): p. 633-8.
447. Wu, M., et al., *Cbfbeta governs osteoblast-adipocyte lineage commitment through enhancing beta-catenin signaling and suppressing adipogenesis gene expression.* Proc Natl Acad Sci U S A, 2017. **114**(38): p. 10119-10124.
448. Park, N.R., et al., *Core Binding Factor beta Plays a Critical Role During Chondrocyte Differentiation.* J Cell Physiol, 2016. **231**(1): p. 162-71.
449. Nguyen, K.H., et al., *SWI/SNF-Mediated Lineage Determination in Mesenchymal Stem Cells Confers Resistance to Osteoporosis.* Stem Cells, 2015. **33**(10): p. 3028-38.
450. Kim, G.W., et al., *CXC chemokine ligand 12a enhances chondrocyte proliferation and maturation during endochondral bone formation.* Osteoarthritis Cartilage, 2015. **23**(6): p. 966-74.
451. Lu, W., et al., *CXCL12/CXCR4 Axis Regulates Aggrecanase Activation and Cartilage Degradation in a Post-Traumatic Osteoarthritis Rat Model.* Int J Mol Sci, 2016. **17**(10).
452. Asagiri, M., et al., *Autoamplification of NFATc1 expression determines its essential role in bone homeostasis.* J Exp Med, 2005. **202**(9): p. 1261-9.
453. Matsuo, K., et al., *Nuclear factor of activated T-cells (NFAT) rescues osteoclastogenesis in precursors lacking c-Fos.* J Biol Chem, 2004. **279**(25): p. 26475-80.
454. Kim, J.H. and N. Kim, *Regulation of NFATc1 in Osteoclast Differentiation.* J Bone Metab, 2014. **21**(4): p. 233-41.
455. Jonason, J.H. and R.J. O'Keefe, *Isolation and culture of neonatal mouse calvarial osteoblasts.* Methods Mol Biol, 2014. **1130**: p. 295-305.
456. Bakker, A.D. and J. Klein-Nulend, *Osteoblast isolation from murine calvaria and long bones.* Methods Mol Biol, 2012. **816**: p. 19-29.
457. van den Bos, T., et al., *Differences in matrix composition between calvaria and long bone in mice suggest differences in biomechanical properties and resorption: Special emphasis on collagen.* Bone, 2008. **43**(3): p. 459-68.
458. Soejima, K., et al., *Different responsiveness of cells from adult and neonatal mouse bone to mechanical and biochemical challenge.* J Cell Physiol, 2001. **186**(3): p. 366-70.
459. Langenbach, F. and J. Handschel, *Effects of dexamethasone, ascorbic acid and beta-glycerophosphate on the osteogenic differentiation of stem cells in vitro.* Stem Cell Res Ther, 2013. **4**(5): p. 117.
460. Jeon, M.J., et al., *Activation of peroxisome proliferator-activated receptor-gamma inhibits the Runx2-mediated transcription of osteocalcin in osteoblasts.* J Biol Chem, 2003. **278**(26): p. 23270-7.
461. Khan, E. and Y. Abu-Amer, *Activation of peroxisome proliferator-activated receptor-gamma inhibits differentiation of preosteoblasts.* J Lab Clin Med, 2003. **142**(1): p. 29-34.
462. Jackson, S.M. and L.L. Demer, *Peroxisome proliferator-activated receptor activators modulate the osteoblastic maturation of MC3T3-E1 preosteoblasts.* FEBS Lett, 2000. **471**(1): p. 119-24.

463. Lecka-Czernik, B., et al., *Inhibition of Osf2/Cbfa1 expression and terminal osteoblast differentiation by PPARgamma2.* J Cell Biochem, 1999. **74**(3): p. 357-71.
464. Akune, T., et al., *PPARgamma insufficiency enhances osteogenesis through osteoblast formation from bone marrow progenitors.* J Clin Invest, 2004. **113**(6): p. 846-55.
465. Ashburner, M., et al., *Gene ontology: tool for the unification of biology. The Gene Ontology Consortium.* Nat Genet, 2000. **25**(1): p. 25-9.
466. Gene Ontology, C., *The Gene Ontology resource: enriching a GOld mine.* Nucleic Acids Res, 2021. **49**(D1): p. D325-D334.
467. Sato, K. and H. Takayanagi, *Osteoclasts, rheumatoid arthritis, and osteoimmunology.* Curr Opin Rheumatol, 2006. **18**(4): p. 419-26.
468. He, Y., et al., *Erk1 positively regulates osteoclast differentiation and bone resorptive activity.* PLoS One, 2011. **6**(9): p. e24780.
469. Aliprantis, A.O., et al., *NFATc1 in mice represses osteoprotegerin during osteoclastogenesis and dissociates systemic osteopenia from inflammation in cherubism.* J Clin Invest, 2008. **118**(11): p. 3775-89.
470. Boyce, B.F. and L. Xing, *Functions of RANKL/RANK/OPG in bone modeling and remodeling.* Arch Biochem Biophys, 2008. **473**(2): p. 139-46.
471. Park, J.H., N.K. Lee, and S.Y. Lee, *Current Understanding of RANK Signaling in Osteoclast Differentiation and Maturation.* Mol Cells, 2017. **40**(10): p. 706-713.
472. Zhao, B., et al., *Interferon regulatory factor-8 regulates bone metabolism by suppressing osteoclastogenesis.* Nat Med, 2009. **15**(9): p. 1066-71.
473. Miyauchi, Y., et al., *The Blimp1-Bcl6 axis is critical to regulate osteoclast differentiation and bone homeostasis.* J Exp Med, 2010. **207**(4): p. 751-62.
474. Hu, Y., et al., *Tartrate-Resistant Acid Phosphatase 5/ACP5 Interacts with p53 to Control the Expression of SMAD3 in Lung Adenocarcinoma.* Mol Ther Oncolytics, 2020. **16**: p. 272-288.
475. Reithmeier, A., et al., *Tartrate-resistant acid phosphatase (TRAP/ACP5) promotes metastasis-related properties via TGFbeta2/TbetaR and CD44 in MDA-MB-231 breast cancer cells.* BMC Cancer, 2017. **17**(1): p. 650.
476. Bian, Z.Q., et al., *Overexpressed ACP5 has prognostic value in colorectal cancer and promotes cell proliferation and tumorigenesis via FAK/PI3K/AKT signaling pathway.* Am J Cancer Res, 2019. **9**(1): p. 22-35.
477. Nichogiannopoulou, A., et al., *Defects in hemopoietic stem cell activity in Ikaros mutant mice.* J Exp Med, 1999. **190**(9): p. 1201-14.
478. Umemoto, Y., et al., *Leptin stimulates the proliferation of murine myelocytic and primitive hematopoietic progenitor cells.* Blood, 1997. **90**(9): p. 3438-43.
479. Bennett, B.D., et al., *A role for leptin and its cognate receptor in hematopoiesis.* Curr Biol, 1996. **6**(9): p. 1170-80.
480. DiMascio, L., et al., *Identification of adiponectin as a novel hemopoietic stem cell growth factor.* J Immunol, 2007. **178**(6): p. 3511-20.
481. Wang, H., Y. Leng, and Y. Gong, *Bone Marrow Fat and Hematopoiesis.* Front Endocrinol (Lausanne), 2018. **9**: p. 694.
482. Lorenz, R., et al., *ViennaRNA Package 2.0.* Algorithms Mol Biol, 2011. **6**: p. 26.
483. Gruber, A.R., et al., *The Vienna RNA websuite.* Nucleic Acids Res, 2008. **36**(Web Server issue): p. W70-4.
484. Mathews, D.H., et al., *Incorporating chemical modification constraints into a dynamic programming algorithm for prediction of RNA secondary structure.* Proc Natl Acad Sci U S A, 2004. **101**(19): p. 7287-92.
485. Bournat, J.C. and C.W. Brown, *Mitochondrial dysfunction in obesity.* Curr Opin Endocrinol Diabetes Obes, 2010. **17**(5): p. 446-52.
486. de Mello, A.H., et al., *Mitochondrial dysfunction in obesity.* Life Sci, 2018. **192**: p. 26-32.
487. Brand, M.D. and D.G. Nicholls, *Assessing mitochondrial dysfunction in cells.* Biochem J, 2011. **435**(2): p. 297-312.

488. Wang, Z., et al., *MicroRNA-200b suppresses arsenic-transformed cell migration by targeting protein kinase Calpha and Wnt5b-protein kinase Calpha positive feedback loop and inhibiting Rac1 activation.* J Biol Chem, 2014. **289**(26): p. 18373-86.
489. Nam, J.W., et al., *Global analyses of the effect of different cellular contexts on microRNA targeting.* Mol Cell, 2014. **53**(6): p. 1031-1043.
490. Panda, A.C., *Circular RNAs Act as miRNA Sponges.* Adv Exp Med Biol, 2018. **1087**: p. 67-79.
491. Lou, W., B. Ding, and P. Fu, *Pseudogene-Derived lncRNAs and Their miRNA Sponging Mechanism in Human Cancer.* Front Cell Dev Biol, 2020. **8**: p. 85.
492. Jeggari, A., D.S. Marks, and E. Larsson, *miRcode: a map of putative microRNA target sites in the long non-coding transcriptome.* Bioinformatics, 2012. **28**(15): p. 2062-3.
493. Salmena, L., et al., *A ceRNA hypothesis: the Rosetta Stone of a hidden RNA language?* Cell, 2011. **146**(3): p. 353-8.
494. Brennecke, J., et al., *Principles of microRNA-target recognition.* PLoS Biol, 2005. **3**(3): p. e85.
495. Doench, J.G. and P.A. Sharp, *Specificity of microRNA target selection in translational repression.* Genes Dev, 2004. **18**(5): p. 504-11.
496. Riffo-Campos, A.L., I. Riquelme, and P. Brebi-Mieville, *Tools for Sequence-Based miRNA Target Prediction: What to Choose?* Int J Mol Sci, 2016. **17**(12).
497. Kertesz, M., et al., *The role of site accessibility in microRNA target recognition.* Nat Genet, 2007. **39**(10): p. 1278-84.
498. Mathews, D.H., et al., *Expanded sequence dependence of thermodynamic parameters improves prediction of RNA secondary structure.* J Mol Biol, 1999. **288**(5): p. 911-40.
499. Schnall-Levin, M., et al., *Unusually effective microRNA targeting within repeat-rich coding regions of mammalian mRNAs.* Genome Res, 2011. **21**(9): p. 1395-403.
500. Betel, D., et al., *Comprehensive modeling of microRNA targets predicts functional non-conserved and non-canonical sites.* Genome Biol, 2010. **11**(8): p. R90.
501. Enright, A.J., et al., *MicroRNA targets in Drosophila.* Genome Biol, 2003. **5**(1): p. R1.
502. John, B., et al., *Human MicroRNA targets.* PLoS Biol, 2004. **2**(11): p. e363.
503. Peterson, S.M., et al., *Common features of microRNA target prediction tools.* Front Genet, 2014. **5**: p. 23.
504. Chi, S.W., et al., *Argonaute HITS-CLIP decodes microRNA-mRNA interaction maps.* Nature, 2009. **460**(7254): p. 479-86.
505. McNabb, D.S., R. Reed, and R.A. Marciniak, *Dual luciferase assay system for rapid assessment of gene expression in Saccharomyces cerevisiae.* Eukaryot Cell, 2005. **4**(9): p. 1539-49.
506. van Dongen, S., C. Abreu-Goodger, and A.J. Enright, *Detecting microRNA binding and siRNA off-target effects from expression data.* Nat Methods, 2008. **5**(12): p. 1023-5.
507. Garcia, D.M., et al., *Weak seed-pairing stability and high target-site abundance decrease the proficiency of lsy-6 and other microRNAs.* Nat Struct Mol Biol, 2011. **18**(10): p. 1139-46.
508. Janowski, M., *Functional diversity of SDF-1 splicing variants.* Cell Adh Migr, 2009. **3**(3): p. 243-9.
509. Shi, Y., D.J. Riese, 2nd, and J. Shen, *The Role of the CXCL12/CXCR4/CXCR7 Chemokine Axis in Cancer.* Front Pharmacol, 2020. **11**: p. 574667.
510. Doring, Y., et al., *The CXCL12/CXCR4 chemokine ligand/receptor axis in cardiovascular disease.* Front Physiol, 2014. **5**: p. 212.
511. Laguri, C., et al., *The novel CXCL12gamma isoform encodes an unstructured cationic domain which regulates bioactivity and interaction with both glycosaminoglycans and CXCR4.* PLoS One, 2007. **2**(10): p. e1110.
512. Yu, L., et al., *Identification and expression of novel isoforms of human stromal cell-derived factor 1.* Gene, 2006. **374**: p. 174-9.
513. Liu, C., et al., *CXCL12/CXCR4 signal axis plays an important role in mediating bone morphogenetic protein 9-induced osteogenic differentiation of mesenchymal stem cells.* Int J Med Sci, 2013. **10**(9): p. 1181-92.
514. Bernhardt, A., et al., *Triple Culture of Primary Human Osteoblasts, Osteoclasts and Osteocytes as an In Vitro Bone Model.* Int J Mol Sci, 2021. **22**(14).

515. Huang, J., et al., *Crosstalk between MLO-Y4 osteocytes and C2C12 muscle cells is mediated by the Wnt/beta-catenin pathway.* JBMR Plus, 2017. **1**(2): p. 86-100.
516. Bliziotes, M., et al., *Serotonin transporter and receptor expression in osteocytic MLO-Y4 cells.* Bone, 2006. **39**(6): p. 1313-21.
517. Cheng, B., et al., *Expression of functional gap junctions and regulation by fluid flow in osteocyte-like MLO-Y4 cells.* J Bone Miner Res, 2001. **16**(2): p. 249-59.
518. Rosser, J. and L.F. Bonewald, *Studying osteocyte function using the cell lines MLO-Y4 and MLO-A5.* Methods Mol Biol, 2012. **816**: p. 67-81.
519. Cui, S., et al., *APPswe/Abeta regulation of osteoclast activation and RAGE expression in an age-dependent manner.* J Bone Miner Res, 2011. **26**(5): p. 1084-98.
520. Guo, H.H., et al., *Hepcidin contributes to Swedish mutant APP-induced osteoclastogenesis and trabecular bone loss.* Bone Res, 2021. **9**(1): p. 31.
521. Islam, R., et al., *Pin1 regulates osteoclast fusion through suppression of the master regulator of cell fusion DC-STAMP.* J Cell Physiol, 2014. **229**(12): p. 2166-74.
522. Rahman, M.M., et al., *Secretion of PDGF isoforms during osteoclastogenesis and its modulation by anti-osteoclast drugs.* Biochem Biophys Res Commun, 2015. **462**(2): p. 159-64.
523. Wang, Y., et al., *Inhibition of PTGS1 promotes osteogenic differentiation of adipose-derived stem cells by suppressing NF-kB signaling.* Stem Cell Res Ther, 2019. **10**(1): p. 57.
524. Andrae, J., R. Gallini, and C. Betsholtz, *Role of platelet-derived growth factors in physiology and medicine.* Genes Dev, 2008. **22**(10): p. 1276-312.
525. Chen, P.H., X. Chen, and X. He, *Platelet-derived growth factors and their receptors: structural and functional perspectives.* Biochim Biophys Acta, 2013. **1834**(10): p. 2176-86.
526. Tysiewicz-Dudek, M., F. Pietraszkiewicz, and B. Drozdzowska, *Alzheimer's disease and osteoporosis: common risk factors or one condition predisposing to the other?* Ortop Traumatol Rehabil, 2008. **10**(4): p. 315-23.
527. Melton, L.J., 3rd, et al., *Fracture risk in patients with Alzheimer's disease.* J Am Geriatr Soc, 1994. **42**(6): p. 614-9.
528. Shin, J., et al., *Swedish mutation within amyloid precursor protein modulates global gene expression towards the pathogenesis of Alzheimer's disease.* BMB Rep, 2010. **43**(10): p. 704-9.
529. Yu, J.H., C.Y. Im, and S.H. Min, *Function of PIN1 in Cancer Development and Its Inhibitors as Cancer Therapeutics.* Front Cell Dev Biol, 2020. **8**: p. 120.
530. Pu, W., Y. Zheng, and Y. Peng, *Prolyl Isomerase Pin1 in Human Cancer: Function, Mechanism, and Significance.* Front Cell Dev Biol, 2020. **8**: p. 168.
531. Shen, Z.J., et al., *Pin1 null mice exhibit low bone mass and attenuation of BMP signaling.* PLoS One, 2013. **8**(5): p. e63565.
532. Lee, T.H., et al., *Essential role of Pin1 in the regulation of TRF1 stability and telomere maintenance.* Nat Cell Biol, 2009. **11**(1): p. 97-105.
533. Yoon, W.J., et al., *Pin1-mediated Runx2 modification is critical for skeletal development.* J Cell Physiol, 2013. **228**(12): p. 2377-85.
534. Zsurka, G. and W.S. Kunz, *Mitochondrial dysfunction in neurological disorders with epileptic phenotypes.* J Bioenerg Biomembr, 2010. **42**(6): p. 443-8.
535. Andreasen, M. and S. Nedergaard, *Effect of acute mitochondrial dysfunction on hyperexcitable network activity in rat hippocampus in vitro.* Brain Res, 2021. **1751**: p. 147193.
536. Hadley, S.H., P.K. Bahia, and T.E. Taylor-Clark, *Sensory nerve terminal mitochondrial dysfunction induces hyperexcitability in airway nociceptors via protein kinase C.* Mol Pharmacol, 2014. **85**(6): p. 839-48.
537. Souri, M., et al., *Very-long-chain acyl-CoA dehydrogenase subunit assembles to the dimer form on mitochondrial inner membrane.* FEBS Lett, 1998. **426**(2): p. 187-90.
538. Andresen, B.S., et al., *Cloning and characterization of human very-long-chain acyl-CoA dehydrogenase cDNA, chromosomal assignment of the gene and identification in four patients of nine different mutations within the VLCAD gene.* Hum Mol Genet, 1996. **5**(4): p. 461-72.
539. Vaux, D.L. and J. Silke, *HtrA2/Omi, a sheep in wolf's clothing.* Cell, 2003. **115**(3): p. 251-3.

540. Kang, S., T. Fernandes-Alnemri, and E.S. Alnemri, *A novel role for the mitochondrial HTRA2/OMI protease in aging.* Autophagy, 2013. **9**(3): p. 420-1.
541. Hance, N., M.I. Ekstrand, and A. Trifunovic, *Mitochondrial DNA polymerase gamma is essential for mammalian embryogenesis.* Hum Mol Genet, 2005. **14**(13): p. 1775-83.
542. Dobson, P.F., et al., *Mitochondrial dysfunction impairs osteogenesis, increases osteoclast activity, and accelerates age related bone loss.* Sci Rep, 2020. **10**(1): p. 11643.
543. Long, Q., et al., *Assessing Mitochondrial Bioenergetics in Isolated Mitochondria from Mouse Heart Tissues Using Oroboros 2k-Oxygraph.* Methods Mol Biol, 2019. **1966**: p. 237-246.
544. Kuhn, R., et al., *Inducible gene targeting in mice.* Science, 1995. **269**(5229): p. 1427-9.
545. Guo, S., et al., *MicroRNA miR-125a controls hematopoietic stem cell number.* Proc Natl Acad Sci U S A, 2010. **107**(32): p. 14229-34.
546. Bernstein, E., et al., *Role for a bidentate ribonuclease in the initiation step of RNA interference.* Nature, 2001. **409**(6818): p. 363-6.
547. Bernstein, E., et al., *Dicer is essential for mouse development.* Nat Genet, 2003. **35**(3): p. 215-7.
548. O'Connell, R.M., et al., *MicroRNAs enriched in hematopoietic stem cells differentially regulate long-term hematopoietic output.* Proc Natl Acad Sci U S A, 2010. **107**(32): p. 14235-40.
549. Han, Y.C., et al., *microRNA-29a induces aberrant self-renewal capacity in hematopoietic progenitors, biased myeloid development, and acute myeloid leukemia.* J Exp Med, 2010. **207**(3): p. 475-89.
550. Rosales, C. and E. Uribe-Querol, *Phagocytosis: A Fundamental Process in Immunity.* Biomed Res Int, 2017. **2017**: p. 9042851.
551. Rosales, C., *Neutrophil: A Cell with Many Roles in Inflammation or Several Cell Types?* Front Physiol, 2018. **9**: p. 113.
552. Dzierzak, E. and S. Philipsen, *Erythropoiesis: development and differentiation.* Cold Spring Harb Perspect Med, 2013. **3**(4): p. a011601.
553. Takarada, T., et al., *Genetic analysis of Runx2 function during intramembranous ossification.* Development, 2016. **143**(2): p. 211-8.
554. Takarada, T., et al., *An analysis of skeletal development in osteoblast-specific and chondrocyte-specific runt-related transcription factor-2 (Runx2) knockout mice.* J Bone Miner Res, 2013. **28**(10): p. 2064-9.
555. Bonewald, L.F., *Establishment and characterization of an osteocyte-like cell line, MLO-Y4.* J Bone Miner Metab, 1999. **17**(1): p. 61-5.
556. Divieti Pajevic, P., *New and Old Osteocytic Cell Lines and 3D Models.* Curr Osteoporos Rep, 2020. **18**(5): p. 551-558.
557. Kato, Y., et al., *Establishment of an osteoid preosteocyte-like cell MLO-A5 that spontaneously mineralizes in culture.* J Bone Miner Res, 2001. **16**(9): p. 1622-33.
558. Asangani, I.A., et al., *MicroRNA-21 (miR-21) post-transcriptionally downregulates tumor suppressor Pdcd4 and stimulates invasion, intravasation and metastasis in colorectal cancer.* Oncogene, 2008. **27**(15): p. 2128-36.
559. Hu, C.H., et al., *miR-21 deficiency inhibits osteoclast function and prevents bone loss in mice.* Sci Rep, 2017. **7**: p. 43191.
560. Yang, N., et al., *Tumor necrosis factor alpha suppresses the mesenchymal stem cell osteogenesis promoter miR-21 in estrogen deficiency-induced osteoporosis.* J Bone Miner Res, 2013. **28**(3): p. 559-73.
561. Tang, Y., et al., *TGF-beta1-induced migration of bone mesenchymal stem cells couples bone resorption with formation.* Nat Med, 2009. **15**(7): p. 757-65.
562. Xian, L., et al., *Matrix IGF-1 maintains bone mass by activation of mTOR in mesenchymal stem cells.* Nat Med, 2012. **18**(7): p. 1095-101.
563. Ichikawa, S., et al., *A Phex mutation in a murine model of X-linked hypophosphatemia alters phosphate responsiveness of bone cells.* J Bone Miner Res, 2012. **27**(2): p. 453-60.
564. Owen, C., et al., *A novel Phex mutation in a new mouse model of hypophosphatemic rickets.* J Cell Biochem, 2012. **113**(7): p. 2432-41.

565. Li, X., et al., *Targeted deletion of the sclerostin gene in mice results in increased bone formation and bone strength.* J Bone Miner Res, 2008. **23**(6): p. 860-9.
566. Knoth, R., et al., *Murine features of neurogenesis in the human hippocampus across the lifespan from 0 to 100 years.* PLoS One, 2010. **5**(1): p. e8809.
567. Clark, R.E. and L.R. Squire, *Similarity in form and function of the hippocampus in rodents, monkeys, and humans.* Proc Natl Acad Sci U S A, 2013. **110 Suppl 2**: p. 10365-70.
568. Grone, B.P. and S.C. Baraban, *Animal models in epilepsy research: legacies and new directions.* Nat Neurosci, 2015. **18**(3): p. 339-43.
569. Brady, R.D., et al., *Modelling traumatic brain injury and posttraumatic epilepsy in rodents.* Neurobiol Dis, 2019. **123**: p. 8-19.
570. Seyfried, T.N. and G.H. Glaser, *A review of mouse mutants as genetic models of epilepsy.* Epilepsia, 1985. **26**(2): p. 143-50.
571. Prideaux, M., et al., *SaOS2 Osteosarcoma cells as an in vitro model for studying the transition of human osteoblasts to osteocytes.* Calcif Tissue Int, 2014. **95**(2): p. 183-93.
572. Wang, K., et al., *A Novel Osteogenic Cell Line That Differentiates Into GFP-Tagged Osteocytes and Forms Mineral With a Bone-Like Lacunocanalicular Structure.* J Bone Miner Res, 2019. **34**(6): p. 979-995.